Numerical and experimental investigations of instabilities in electron beams in plasmas

Martin King

(MSci., MSc., The University of Strathclyde)

Department of Physics

The University of Strathclyde

Thesis Submitted for the Degree of Ph.D.

September 2013

Abstract

Beam-plasma interactions can produce highly non-linear effects that can influence the dynamics of a system. Two-such systems have been investigated: Plasma moderated cyclotron instabilities relevant to the mechanisms of Auroral Kilometric Radiation (AKR) and the non-linear behaviour of the two-stream beam-plasma instability. In the first case numerical simulations were undertaken and compared to the measurements of a laboratory experiment conducted previously.

Radio emissions from the Earth's polar regions, known as Auroral Kilometric Radiation (AKR) have been measured at a frequency of ~300kHz with an efficiency of ~1%.This emission is generated when particles are accelerated downwards along the Earth's increasing magnetic field. As they propagate they undergo magnetic compression and form a horseshoe distribution in velocity space. As these particles travel through an area of plasma depletion known as the auroral density cavity, it is believed that a form of cyclotron resonance maser (CRM) instability causes them to emit the radio waves detected by a range of satellites. The University of Strathclyde has previously undertaken laboratory experiments to investigate this behaviour. This work numerically simulated the previous experimental setup with and without a background plasma. The simulated electron beam distribution was matched analytically to the measured beam in the previous laboratory experiment. This beam was then injected into a simulation of the laboratory geometry and predicted wave generation efficiency of ~1% which closely matched the previous measurements. The impact of adding a background plasma to the simulation was also investigated and successfully showed that the efficiency of the CRM instability falls off as the plasma frequency approaches a tenth of the cyclotron frequency (400MHz in these simulations). This again was in good agreement to the previous experimental measurements.

Further work was undertaken to investigate the instabilities that form when a rectilinear electron beam is propagated through a plasma column. This is of potential relevance to fast-ignition inertial confinement fusion as in this form of fusion, a

deuterium-tritium fuel pellet is compressed using uniform laser irradiation while a secondary laser pulse is then utilised to accelerate a highly relativistic electron beam into the core of the pellet to provide the heating necessary to initiate fusion. As the beam propagates it can potentially undergo the beam-plasma instability. This work presents a numerical study of the beam-plasma instability in a low-density environment using a 2.5D particle-in-cell code. This numerical model is then used to as a basis around which to construct a similar laboratory apparatus to ultimately benchmark the code. This will enhance confidence in the use of PiC codes in the simulation of these instabilities. The simulated beam-plasma instability correlated well to the predicted analytic growth rates in the linear regime. Typically after ~20-80ns of beam propagation, when the beam-plasma instability is saturated, periodic plasma cavities are formed. The spacing between these cavities increased linearly from ~2 to 6cm as the voltage of a 10A electron beam was increased from 10kV to 100kV, in a background hydrogen plasma of density $9x10^{16}m^{-3}$. Ion density perturbations were found to propagate from these cavities in both the positive and negative axial directions, at speeds close to the local ion sound speed observed inside the cavity but faster than the mean ion sound speed (averaged across the plasma column). Spectra of the longitudinal electric field shows oscillations close to the electron plasma and ion acoustic frequencies close to these cavity structures suggesting that this behaviour relates to the modulational instability.

An experimental apparatus was developed to reproduce major features of the numerical simulations. A low pressure ($7x10^{-4}$mB) helium gas discharge was formed in a Penning like configuration in a 50mm diameter anode, 1m in length, featuring specially designed insulators. This proved capable of supporting a 40mA discharge with a plasma density estimated at $1.2x10^{16}m^{-3}$ at 20mA. An electron gun was developed (supported by numerical modelling) which was able to deliver an electron beam of 4-12A through the central 15mm section of the plasma column at an energy of some 60kV. Initial experiments have been undertaken passing this electron beam through the plasma column, leading to recommendations for further development of the apparatus.

Acknowledgements

I would like to thank my supervisor Dr Kevin Ronald for all of his help and support during the course of this work, without who this work would not be possible. I would also like to thank the rest of the ABP group, particularly Dr David Speirs for all of his help during the experiments and maintaining the computing cluster, and Mr Barclay for the construction of the apparatus. I would also like to thank my family for being encouraging and supportive. Finally I'd like to thank my wonderful girlfriend Angela who has kept me going through the final years of this work.

Table of contents

Chapter 1 : Introduction and background

1 Introduction and background

Beam-plasma interactions can have an important impact on any plasma system where there is a distribution of particles propagating through one or more other particle distributions. This work focuses on three specific areas of beam-plasma interactions:

- Modelling computationally the dynamics of the laboratory experiments investigating the mechanisms for auroral kilometric radiation conducted previously at the University of Strathclyde.

- Studying the non-linear behaviour of the two-stream/beam-plasma instability that may be of relevance to fast-ignition inertial confinement fusion through the use of numerical codes.

- Designing, constructing and initial testing of a laboratory experiment to create the conditions for the two-stream/beam-plasma instability to eventually provide a benchmark for the numerical codes.

1.1 Auroral kilometric radiation

Emissions from the polar regions of the Earth's magnetosphere, known as auroral kilometric radiation (AKR) [Delory, et al., 1998; Ergun, et al., 1998b; 2000], have been detected by multiple satellite observations from approximately 1974. This process as the name suggests is a strong radio emission with a wavelength on the order of a kilometre. AKR has a narrow bandwidth and occurs at frequencies of between 50kHz and 800kHz [Mutel, et al., 2004]. The emission occurs in short duration bursts and can occur between 0.5 and 3 earth radii above the Earth's surface. From the measurements of the emitted radiation it was found that the frequency corresponds closely to the local cyclotron frequency with a peak in emission intensity at ~300kHz. The wave polarisation and propagation was also observed to be perpendicular to the Earth's magnetic field lines which would indicate the excitation of the plasma X-mode

[Benson, 1985]. The peak power of the emission has been suggested to be in the region of 1GW which would correspond to a radiation efficiency of ~1% from the kinetic energy of the electrons [Gurnett, 1974; Pritchett and Strangeway, 1985]. As this efficiency is considered large for a naturally occurring phenomenon, it has led to considerable research in the field to understand the process [Bingham, et al., 1999; 2004; Vorgul, et al., 2004; 2005; Burinskaya and Rauch, 2007].

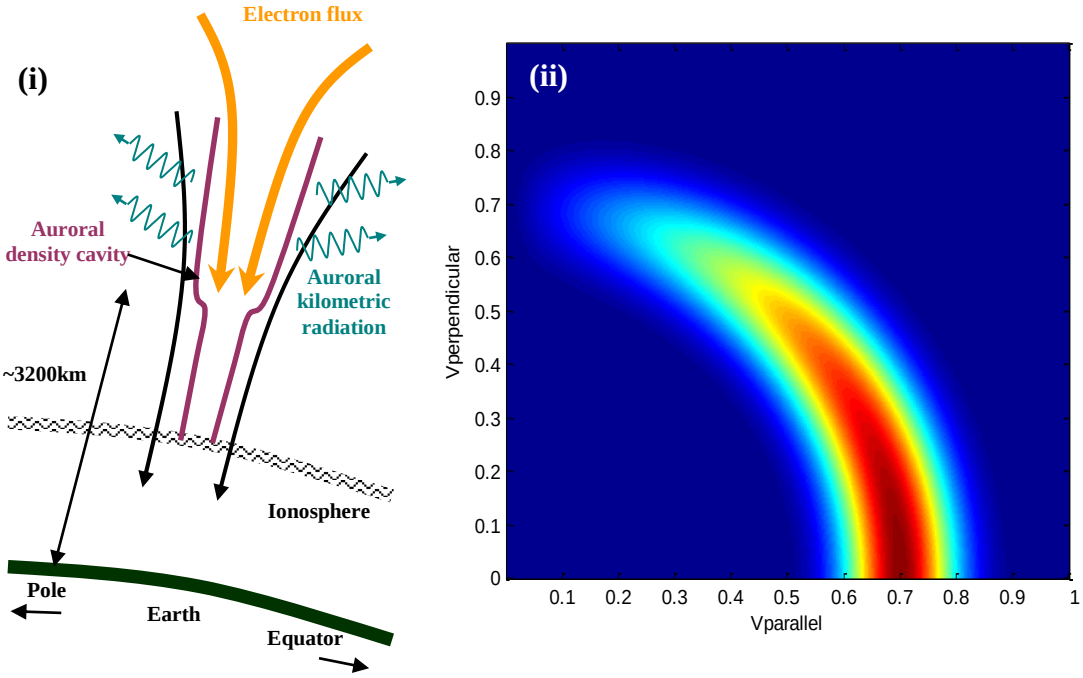

Figure 1.1 (i) Schematic of the AKR process (ii) Example horseshoe velocity distribution

The mechanism behind the AKR emission occurs in a region of plasma depletion above the polar regions of the Earth's magnetosphere, known as the auroral density cavity. This region spans approximately 9000km with peak emissions at an altitude of about 3200km and has a plasma frequency that is roughly 30 times less than that of the cyclotron resonance frequency of the electrons in the Earth's magnetic field. As particles enter this region, they are accelerated by electric fields above the auroral density cavity into the increasing magnetic field region. Due to the adiabatic conservation of the magnetic moment, the pitch angle ($\tan\theta = \frac{v_\perp}{v_\parallel}$) of the electron is increased. As there will be an initial spread of velocity where the electrons enter the

convergent magnetic field region, the electrons with a velocity component perpendicular to the magnetic field lines will experience an increase in rotational velocity. This forms the velocity of the incoming stream of electrons into what is known as a horseshoe distribution, shown in figure 1.1. This particular type of velocity distribution has been shown to be unstable to a cyclotron resonance maser type interaction [Bingham and Cairns, 2000; 2002] and it has therefore been proposed that this is the mechanism that generates the AKR emissions in this region.

As well as the Earth, other astrophysical bodies may also produce radio emissions due to the cyclotron resonance maser interaction. There have been investigations into other magnetised planets in the solar system which show similar behaviour in their polar regions, for example Jupiter (including its moon Io), Saturn, Uranus and Neptune [Ergun, et al., 2000; Pritchett, et al., 2002; Zarka, 2001]. Outwith the solar system, it has been suggested that microwave emission from certain stars, including CU Viginis [Kellett, et al., 2007] and UV Ceti [Bingham, Cairns and Kellett, 2001] may also be explained by the cyclotron maser instability.

1.2 Two-stream/beam-plasma instability

The two-stream instability is a very common plasma instability and was first studied using a cold plasma theory in 1948-1949 [Pierce, 1948; Nergaard, 1948; Haeff, 1949]. The theory was then extended to warm plasmas in 1959-1960 [Buneman, 1959; Jackson, 1960]. The two-stream instability occurs when there is an interpenetration of two or more moving particle distributions, for example an electron beam flowing through another electron beam or a background plasma [Davidson, 2002]. The cause of this instability can be thought of as originating from a point source disturbance within a two-beam plasma [Stix, 1992]. If a density fluctuation arises from this disturbance in one stream of particles, then the electric field will initiate a plasma oscillation at that location. However, these fields can modulate the electron densities of the second stream and the drift of these density modulations through each other can result in energy exchange. This leads to growth of the energy associated with the electric fields feeding from the energy of the initial particle streams.

The initial rationale behind investigating this well understood instability was in the potential impact the non-linear behaviour of this instability may have on fast-ignition inertial confinement fusion (ICF). This particular type of fusion is an alternate method to the more conventional direct or indirect-drive ICF. The concept of conventional direct-drive ICF [McCrory, et al., 2008], shown in figure 1.2, is that a small, frozen, pellet formed of a mixture of deuterium and tritium is uniformly irradiated with high intensity laser radiation. This laser radiation would cause ablation of the outer layer of the frozen pellet. As the material is ablated off of the surface, this produces a force on the inner material causing it to compress to extreme densities (up to ~1000g/cm^{-3}, approximately 100 times the density of lead). As the material compresses, shockwaves also propagate towards the core of the pellet, inducing heating in the now dense plasma. If both the density and the temperature of the plasma ions satisfy the Lawson criterion [Lawson, 1957] then there will be a self-sustaining fusion reaction that will propagate out from the centre of the pellet as a 'burn' wave.

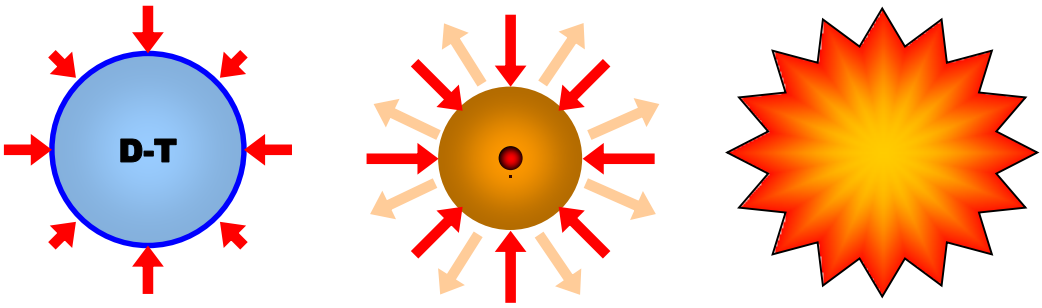

Figure 1.2 Schematic of direct-drive inertial confinement fusion

Indirect-drive ICF functions in much the same way, except that the deuterium-tritium pellet is placed in the centre of a gold cylinder known as a hohlraum [Lindl, 1995]. The laser radiation is used to irradiate the interior of the hohlraum to generate X-rays. It is the X-rays that then produce the ablation pressure on the pellet to cause the compression and heating. The benefit of this method over direct-drive ICF is that it may produce a more uniform compression that inhibits potential geometric instabilities.

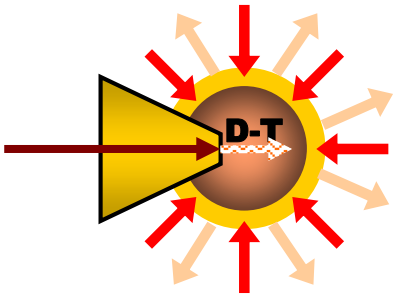

Figure 1.3 Schematic of fast-ignition inertial confinement fusion

Fast-ignition ICF has similarities with direct-drive ICF [Key, 2007], and is illustrated in figure 1.3. High intensity laser pressure is again used to compress the deuterium-tritium pellet. However, the heating mechanism is not provided by the compression but by a secondary 'ignition' laser pulse that generates a highly relativistic electron beam that propagates through the compressed plasma, providing heat to the ions by way of electron-ion collisions. In most fast-ignition experiments the 'ignition' laser is focussed into a gold cone that is initially inserted into the deuterium-tritium pellet, with the tip close to the core. The electron beam is then produced at the cone tip and can transfer its energy more efficiently to the core of the compressed pellet.

In laser-plasma interaction experiments, measured laser energy transfer to the deuterium-tritium ions was found to be much higher than that expected for purely collisional electron-ion heating [Kodama, et al., 2001; 2002]. It was proposed that as the electron beam propagates into the highly compressed plasma, the two-stream instability can occur, producing very large electrostatic fields [Sircombe, et al., 2008]. These electrostatic fields can then parametrically decay into longitudinal ion acoustic waves which are subsequently damped by ion-ion collisions which cause additional heating of the ions and would account for the increased laser energy transfer [Mendonça, et al., 2005].

A complication in this potential approach is that the fast electrons can be broken up into filaments due to transverse instabilities [Hill, et al., 2005] which would limit the efficiency of the energy transfer. A new technique of applying an external axial magnetic field across the pellet prior to the compression may aid in preventing these

transverse instabilities [Gotchev, et al., 2008; Chang, et al., 2011; Hohenberger, et al., 2012]. When compression of the pellet occurs, the applied magnetic field is itself compressed with the pellet due to the conductive nature of the plasma, boosting the field strength into the kiloTesla range (illustrated in figure 1.4). As the electrons will now be radially confined, due to their cyclotron motion in this compressed field, the transverse instabilities will be suppressed. This compressed magnetic field may therefore be of use during fast-ignition experiments [Yang, et al., 2011; Zhuo, et al., 2014]. Understanding the predictive capacity of computer simulations to predict streaming instabilities in such magnetised plasmas motivated a significant part of this research.

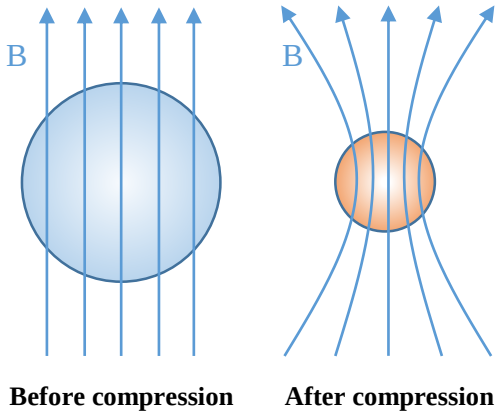

Figure 1.4 Illustration of magnetic compression in inertial confinement targets

1.3 Prior relevant research at the University of Strathclyde

This work was undertaken within the Atoms, Beams and Plasma (ABP) group at the University of Strathclyde. This group has experience in various research fields such as beam-wave interactions, vacuum devices, free electron physics and plasma physics [Cross, Sparks and Phelps, 1995; Ronald, et al., 1998]. Research in the group is conducted utilising a variety of methods including experiments and numerical simulations.

Previous work has been conducted at Strathclyde into the investigation of the AKR mechanism by both experimental and computational means [McConville, et al., 2008; McConville, 2009; Gillespie, et al., 2008; Speirs, et al., 2005; 2008; and Ronald, et al.,

2008]. A scaled laboratory experiment was used to recreate the conditions that occur in the magnetosphere by proportionally increasing the plasma density, magnetic fields and electron current density. The streaming electrons were produced from an annular cathode emitter and magnetically compressed to form the required horseshoe distribution. These electrons were then passed through a Penning plasma discharge confined by the magnetic field required for electron cyclotron resonance. The generated RF signal was then detected and compared with the magnetospheric case. This experimental programme provides the basis for the numerical investigation presented in this work, of the effects of beam-plasma interactions as the horse-shoe distributed electrons transit through the plasma discharge.

The experience gained through the use of a Penning discharge to generate a low density plasma is also used in the design and construction of the experiment to ultimately investigate the non-linear regime of the two-stream/beam-plasma instability.

1.4 Objectives

Following on from previous experiments on the laboratory demonstration of the auroral kilometric radiation emission mechanisms, numerical simulations were required to understand the dynamical behaviour of an electron beam undergoing the cyclotron resonance maser instability whilst in the presence of a background plasma. This work will therefore present simulation results of the interaction region of the experiment with an electron beam that has a horseshoe velocity distribution close to that observed in the previous experiments. The impact of the addition of a background plasma within the interaction region will then also be investigated with the predicted output from the simulations compared to that of the previous experimental measurements.

To investigate the potential heating mechanisms proposed for utilising the beam-plasma instability in fast-ignition inertial confinement fusion experiments, a 2D numerical study will be conducted with the main conclusions shown. This will involve simulations of a low density plasma and electron beam that can be reproduced in a

laboratory environment which could then be used to benchmark the code predictions. The study will focus upon and show the ion behaviour that is predicted during the non-linear regime of the beam-plasma instability.

Confidence in the ability of numerical codes to simulate this dynamical plasma behaviour is required for the use of these codes at fusion relevant density regimes. To this end, the simulations conducted in the previously mentioned numerical study will be used to design and construct a laboratory apparatus in order to provide a benchmark for these codes. The design and performance of the components of this experimental apparatus, including an electron accelerator, solenoids, probes and a Penning trap, will be discussed with preliminary measurements presented of the interaction of the electron beam propagating through the background plasma.

Chapter 2 : Theory

2 Theory

2.1 Plasma definition

A plasma can be defined as a "quasi-neutral gas of charged and neutral particles that exhibit collective behaviour" [Chen, 2005]. Such a collection may also be referred to (somewhat more generally) as an ionised gas. For a gas in equilibrium, the degree of ionisation is given by the Saha equation,

$$\frac{n_i n_e}{n_a} = \left(\frac{g_i g_e}{g_a}\right)\left(\frac{2\pi m k_B T}{h^2}\right)^{3/2} e^{-eV_i/2kT} \qquad \textbf{EQ 2.1}$$

where n_e, n_i and n_a are the number densities of electrons, ionised atoms and neutral atoms respectively, g_e, g_i and g_a are statistical constants, T is the temperature, m is the mass of an electron, h is Planck's constant, k_B is Boltzmann's constant and V_i is the ionisation potential.

As a plasma is quasi-neutral it can be assumed that $n_i \approx n_e$ therefore the Saha equation can be written,

$$\frac{n_i}{n_a} = \frac{n_e}{n_a} \propto \left(\frac{1}{n_a^{1/2}}\right) T^{3/4} e^{-eV_i/2k_B T} \qquad \textbf{EQ 2.2}$$

From this equation it can be seen that a high degree of ionisation in a gas requires a high temperature, a low ionisation potential and a low number density of neutral atoms. The majority of the plasmas in this thesis will not however be in thermal equilibrium.

2.1.1 Concept of temperature

It is possible to relate temperature to the mean translational energy of the particles in a plasma, such that the average thermal energy (for a 3-dimensional monatomic plasma) is given by,

$$E_{av} = \frac{3}{2} k_B T \qquad \textbf{EQ 2.3}$$

In plasma physics, it is sometimes convenient to refer to temperature in terms of eV. The conversion factor is given as approximately 1eV = 11,600K. Note that it is the energy corresponding to k_BT rather than E_{av} that is being converted.

2.1.2 Debye length

To understand the principles behind the plasma maintaining charge neutrality, we introduce a test charge of magnitude *Ze* into a neutral plasma. This test charge will cause the electrons to be attracted to it while the ions are repelled which results in a neutralising 'cloud' surrounding the test charge. Assuming the number density of electrons in this cloud has a Boltzmann distribution $n_c = n_e \exp(e\phi / kT_e)$ and ignoring ion motion, the electrostatic potential $\phi(r)$ in the plasma can be solved by applying Poisson's Equation.

Since $\phi(r) \rightarrow 0$ as $r \rightarrow \infty$ Poisson's Equation for large r and spherical symmetry gives,

$$\frac{1}{r^2}\frac{d}{dr}\left(r^2\frac{d\phi}{dr}\right) = \frac{n_e e^2}{\varepsilon_0 k_B T_e}\phi = \frac{\phi}{{\lambda_D}^2} \qquad \textbf{EQ 2.4}$$

From the solution of equation 2.4 for $\phi(r)$ and given that, as $r \rightarrow 0$, $\phi(r) \rightarrow Ze/4\pi\varepsilon_0 r$ we get,

$$\phi(r) = \frac{Ze}{4\pi\varepsilon_0 r}\exp(-r/\lambda_D) \qquad \textbf{EQ 2.5}$$

where,

$$\lambda_D = \left(\frac{\varepsilon_0 k_B T_e}{n_e e^2}\right)^{1/2} \qquad \textbf{EQ 2.6}$$

is the Debye Length. From this result, it can be seen that outwith a sphere of radius significantly exceeding λ_D centred on the test charge (the region within λ_D is called the Debye sphere), the perturbation in the potential is strongly damped by the screening cloud within the sphere, and the plasma remains effectively neutral. Similarly, the Debye Length can be considered to be a scale length for the penetration of external electrostatic fields.

In order for an ionised gas to be considered a plasma one requires the condition $\lambda_D << L$ be met, where L is the dimension of the system.

2.1.3 Plasma parameter

In order for the result of equation 2.6 to be valid, there must be a sufficient number of electrons within the Debye sphere, such that $n_e\lambda_D^3 >> 1$. Taking the inverse of this, we can define the plasma parameter g,

$$g = \frac{e^2}{\varepsilon_0 k_B T_e \lambda_D} = \frac{1}{n_e \lambda_D^{\ 3}} << 1 \qquad \textbf{EQ 2.7}$$

From this result it can be seen that increasing the number of particles within the Debye sphere will reduce the importance of direct interaction between any particular pair of particles. The plasma parameter can therefore be considered to be a measure of the dominance of the collective interactions over collisions, it is this condition that defines a weakly coupled plasma.

2.2 Fundamental plasma concepts

2.2.1 Plasma Frequency

The current density of the plasma can be given by [Lorrain, Corson and Lorrain, 1988],

$$\underline{J} = \varepsilon_0 \frac{\partial \underline{E}}{\partial t} + \sigma \underline{E} \qquad \textbf{EQ 2.8}$$

where $\underline{E}$ is the electric field associated with the an electromagnetic wave and σ is the conductivity. It is possible to define $\varepsilon_0 \frac{\partial \underline{E}}{\partial t}$ as the displacement current density, associated with the usual polarisation of the vacuum and $\sigma \underline{E}$ as the conduction current density. Assuming the electric field varies with $e^{i(\omega t)}$, the conductivity can be rewritten as $\sigma = -\frac{in_e e^2}{\omega m_e}$ (ignoring any ionic currents), giving a current density,

$$\underline{J} = i\omega\varepsilon_0 \underline{E} - \frac{in_e e^2}{\omega m_e}\underline{E} \qquad \textbf{EQ 2.9}$$

The displacement current density leads the electric field by 90° while the conduction current density lags 90°. When there is no net current density ($\underline{J} = 0$), the displacement and conduction current densities balance and the electric field oscillates at a frequency known as the plasma frequency ω_p, given by,

$$\omega_{pe} = \left(\frac{n_e e^2}{\varepsilon_0 m_e} \right)^{1/2} \qquad \textbf{EQ 2.10}$$

Physically, the electrons in the plasma are moved by the electric field to restore charge neutrality. This results in the electrons oscillating in the plasma at the plasma frequency ω_p around an equilibrium position.

2.2.2 Collision processes in plasmas

Through the application of an external electric field E to an unmagnetised plasma and ignoring the displacement current, a current density of J flows, given by,

$$\underline{J} = \sigma \underline{E} = \frac{\underline{E}}{\eta} \qquad \textbf{EQ 2.11}$$

where η is the electrical resistivity.

The current density J can be related to both the drift velocity of the electrons u_e and the drift velocity of the ions u_i in the following form,

$$\underline{J} = -n_e e \underline{u_e} + n_i e \underline{u_i} \approx -n_e e \underline{u_e} \qquad \textbf{EQ 2.12}$$

As the current density of the ion term is typically negligible due to the relative mass of the ions compared to that of the electrons (combined with the greater propensity for collisions associated with the larger ions) it is common to assume that $u_e >> u_i$. If the electric field is removed at a particular time $t = 0$, then the drifting electrons will decrease in velocity due to collisions and the lack of driving electric field. The electron drift velocity will decrease with a characteristic time constant τ_c. Therefore the electron drift velocity can be assumed to be,

$$\underline{u_e} = \underline{u_{e0}} e^{-t/\tau_c} \qquad \textbf{EQ 2.13}$$

where u_{e0} is the electron drift velocity at time t = 0.

From this, the collision frequency υ_c is given by $1/\tau_c$ and we can define the mean free path λ_{mfp} as,

$$\lambda_{mfp} = v_{rms}\tau_c \qquad \textbf{EQ 2.14}$$

where v_{rms} is the root mean squared velocity of the electrons, i.e. their thermal velocity, typically greater than the drift velocity in most cases.

It is now possible to describe a plasma as "collisionless" if the mean free path is greater than that of the linear size of the plasma and "collisional" if the mean free path is less than the linear size of the plasma.

2.2.3 Plasma sheath

In a plasma that is bounded by a solid surface, there exists a region between the plasma and the solid, known as the boundary sheath region. The electrons in the plasma typically have a much higher speed than that of the ions, therefore there is initially greater flux of electrons on the boundaries.

The result of this is that the solid surface acquires a negative electric potential in comparison to the plasma. This electric potential reflects enough of the electrons back into the plasma, thus equalising the flux of the negative and positive charges on to the solid surface, resulting in a steady electrostatic potential. The ions in this sheath region are accelerated through the potential difference and impact with significant directed energy on the solid surface. In general, the thickness of this sheath region is of the order of a few Debye lengths.

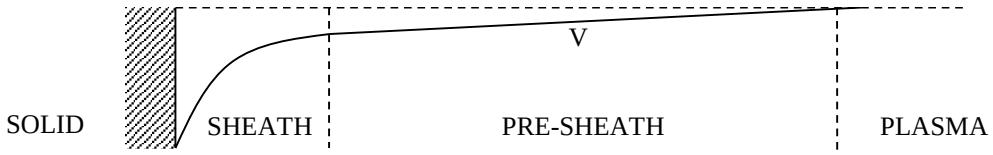

Figure 2.1 Plasmas regions close to a solid boudary

Between the sheath region and the plasma there is a pre-sheath region, as shown in figure 2.1. In this region there is a small electric field caused by a small charge imbalance. This leads to a potential difference, V_0, between the boundaries of the pre-

sheath and the sheath where the Bohm sheath criterion gives the minimum value of V_0 (assuming the pre-sheath and sheath to be collisionless) as,

$$|eV_0| \geq \frac{1}{2} k_B T_e \qquad \textbf{EQ 2.15}$$

At the boundary of the pre-sheath and sheath regions, the ions have this amount of directed energy and will continue to be accelerated through the sheath region towards the solid.

2.3 Plasma models

2.3.1 Particle orbit model

One of the simplest methods for understanding particle behaviour in plasmas is to consider the orbit of a single particle in a given electric and magnetic field. Whilst this model does not describe any collective particle behaviour in the plasma, it does describe the some of the important effects of an externally applied magnetic field on a plasma.

In the simple case of non-relativistic motion of the charged particle in a constant spatially uniform magnetic field, with no applied electric field, the electrons and ions both perform helical orbits which, when projected on to a plane transverse to the axis of the magnetic field, form circles. The centre of each projected circle is known as the guiding centre for that particular particle's motion. This motion arises simply from the Lorentz force equation,

$$\underline{F} = q(\underline{E} + \underline{v} \times \underline{B}) \qquad \textbf{EQ 2.16}$$

For a charged particle of charge q and mass m moving in a circle, from force balance between the expressions for the central force and the Lorentz force we get,

$$\frac{m v_\perp^{\,2}}{r_L} = |q| v_\perp B \qquad \textbf{EQ 2.17}$$

where $v_\perp$ is the magnitude of the perpendicular component of the particle's velocity and r_L is the Larmor radius of the particle's orbit. Therefore,

$$r_L = \frac{mv_\perp}{|q|B} \qquad \textbf{EQ 2.18}$$

It can therefore be seen that for ions with a larger mass, their Larmor radii will be larger than that of electrons for comparable velocities. Following from this we may define the electron cyclotron frequency ω_{ce} and the ion cyclotron frequency ω_{ci} (corrected for relativity),

$$\omega_{ce} = \frac{eB}{\gamma m_e} \qquad \textbf{EQ 2.19}$$

$$\omega_{ci} = \frac{eB}{\gamma m_i} \qquad \textbf{EQ 2.20}$$

where $\gamma = \left(1 - \frac{v^2}{c^2}\right)^{-1/2}$ is the Lorentz correction factor.

This model also allows the description of the trapping of particles due to inhomogeneous magnetic fields. Equation 2.21 below defines the magnetic moment of a gyrating particle,

$$\underline{\mu}_m = \pi r^2 I \underline{z} = \frac{mv_\perp^2}{2B} \underline{z} \qquad \textbf{EQ 2.21}$$

where $\underline{\mu}_m$ is the magnetic dipole moment of an electron orbit, I is the current associated with the electron rotational orbit and r is the radius of the electron orbit. The magnetic moment is an invariant quantity over the scale of the thermal particle motion and therefore must remain constant (assuming B changes relatively slowly). If a particle moves from a weak magnetic field to a strong magnetic field region it must increase its perpendicular velocity to ensure the magnetic moment remains constant. Due to the conservation of energy the parallel momentum must therefore decrease. This result is effectively the conservation of angular momentum. The minimum pitch angle of a confined particle is given by,

$$\sin^2 \theta_m = \frac{B_0}{B_m} \equiv \frac{1}{r_m} \qquad \textbf{EQ 2.22}$$

where the pitch angle is defined as $\tan\theta = \frac{v_{\perp}}{v_{\parallel}} \equiv \alpha$, and r_m is the magnetic mirror ratio.

At the initial condition in the weak magnetic field region, if a particle has a pitch angle between 90° and θ_m it will be reflected back into the weak magnetic field region.

2.3.2 Fluid description of a plasma

In order to understand a plasma that has a significant amount of electric and magnetic fields produced through the motion of the particles, describing the behaviour of the plasma with each individual particle rapidly becomes analytically difficult. To mitigate this, it is possible to describe the plasma in terms of a continuous fluid. This method allows the individual particles to be ignored and the motion of fluid elements can be considered instead. Unlike conventional hydrodynamics however, describing a plasma in this way is complicated by the fluid elements containing electrical charges. This has led to the development of magneto-hydrodynamics model which considers Maxwell's equations, the continuity equation and the conservation of momentum together to describe the plasma behaviour.

Maxwell's equations

$$\underline{\nabla} \cdot \underline{E} = \frac{\rho}{\varepsilon_0} \qquad \textbf{EQ 2.23}$$

$$\underline{\nabla} \cdot \underline{B} = 0 \qquad \textbf{EQ 2.24}$$

$$\underline{\nabla} \times \underline{E} = -\frac{\partial \underline{B}}{\partial t} \qquad \textbf{EQ 2.25}$$

$$\underline{\nabla} \times \underline{B} = \varepsilon_0 \mu_0 \frac{\partial \underline{E}}{\partial t} + \mu_0 \underline{J} \qquad \textbf{EQ 2.26}$$

Where

$\underline{E}$ is the electric field	ρ is the charge density
$\underline{B}$ is the magnetic field	ε_0 is the permittivity of free space
$\underline{J}$ is the current density	μ_0 is the permeability of free space

Maxwell's equations determine the electric and magnetic fields produced due to moving charged fluid elements as well as any externally applied fields.

Continuity equation	$\frac{\partial n_\alpha}{\partial t} + \nabla \cdot (n_\alpha \underline{u}_\alpha) = 0$	**EQ 2.27**
Conservation of momentum equation	$m_\alpha n_\alpha (\frac{\partial}{\partial t} + u_\alpha \cdot \nabla) u_\alpha = q_\alpha n_\alpha (\underline{E} + \underline{u}_\alpha \times \underline{B}) - \nabla p_\alpha$	**EQ 2.28**

where α is the particle species, m is the mass, u is the velocity and q is the particle charge.

The continuity equation above assumes that the rate of change of the particles of each species at some point in space is correlated to the net flux of particles out from that point with no particle sources or sinks. The conservation of momentum equation takes into account the combined effects of pressure, Newton's second law and the Lorentz force.

2.3.3 Kinetic theory

While the fluid model is convenient in the description of macroscopic plasma systems, it does not consider the velocity distributions of the particles within each fluid element. In a fluid model the particle density is considered as a variable in time and space only. Therefore, in order to achieve a more complete understanding of the microscopic plasma behaviour, it is necessary to consider the plasma in six-dimensional *(r,v)* space and to consider the evolution of the distribution functions *f(r,v,t)* of the particles in an infinitesimally small volume element. Describing a plasma in such a way is known as kinetic theory. By integrating over the distribution function, the fluid equations are obtained allowing kinetic theory to describe both the macroscopic aspects of the plasma as well as the microscopic details.

The evolution of the distribution functions is given be the equation,

$$\frac{\partial f}{\partial t} + \underline{v} \cdot \frac{\partial}{\partial \underline{r}} + \frac{\underline{\underline{F}}}{m} \cdot \frac{\partial f}{\partial \underline{v}} = \left(\frac{\partial f}{\partial t} \right)_c \qquad \textbf{EQ 2.29}$$

where $\underline{F}$ is the force acting on the particles and $\left(\frac{\partial f}{\partial t} \right)_c$ is the change in the distribution function f due to collisions. When this parameter is present this equation is known as the collisional kinetic equation. However, when this parameter is set to zero and $\underline{F}$ is represented by the Lorentz force equation, it has become known as the Vlasov equation.

A key result that emerges from considering the solution of the Vlasov equation, where the electric field of the Lorentz force equation has been created by the perturbation of a homogenous plasma that was in equilibrium, is the effect of the damping of longitudinal space charge waves. This phenomenon was first discovered by Landau and is therefore known as Landau damping.

2.4 Plasma waves

Due to the inhomogeneous, anisotropic, dispersive and dissipative nature of plasmas, a multitude of different wave behaviours can be generated within a plasma system. These waves tend to act in a non-linear fashion but can be adequately defined (for certain circumstances) using a linear theory and a few assumptions. Initially ignoring plasma pressure and thermal effects can aid in understanding electromagnetic waves modes such as the R and L modes that can propagate parallel to magnetic field lines or the X mode which can propagate perpendicular to the field. By then considering a warm plasma and the effects of pressure, it is possible to observe electrostatic wave modes such as the longitudinal electron plasma waves (known as Langmuir waves) or ion acoustic waves [Boyd and Sanderson, 1969; 2003; Rosenbluth and Sagdeev, 1984a;1984b; Stix, 1992].

2.4.1 Basic wave theory

It is important to understand the underlying concepts used to describe electromagnetic wave propagation. It is possible to express the electric field of any plane wave as the superposition of two linearly independent solutions of the plane wave equation (corresponding to orthogonal polarisations). The complex amplitudes of which are given below,

$$E_x = E_{x0} \exp i(kz - \omega t + \alpha) \quad \textbf{EQ 2.30}$$

$$E_y = E_{y0} \exp i(kz - \omega t + \beta) \quad \textbf{EQ 2.31}$$

This then leads to an electric field equation of,

$$E(z,t) = (E_{x0}\hat{x} + E_{y0}e^{i\delta}\hat{y}) \exp i(kz - \omega t + \alpha) \quad \textbf{EQ 2.32}$$

In this equation, the wave vector $\underline{k}$ is aligned along the z-axis, and E_{x0} and E_{y0} are real and $\delta=\beta-\alpha$. [Allen and Phelps, 1977].

The electric field vector's rotation describes that of an ellipse if $\delta=\pm\pi/2$. Therefore such an electromagnetic wave is generally described as being elliptically polarised. There are special cases when E_{x0} or E_{y0} (or δ) are equal to zero, which makes the wave linearly polarised and when $E_{x0}=E_{y0}$ with $\delta=\pm\pi/2$ which makes the wave circularly polarised. The direction of rotation around the axis is dictated by the choice of positive or negative sign. For circularly polarised waves, when the sign is positive the rotation is anticlockwise and the wave is said to be right-circularly polarised. Conversely when negative the wave is clockwise and said to be left-circularly polarised.

This description of electromagnetic waves has only considered monochromatic waves. In practically all waves there will be a spread in frequency and wavenumber. This leads to dispersive effects in a plasma as the wave envelope changes as it propagates as shown in the dispersion relation of figure 2.2.

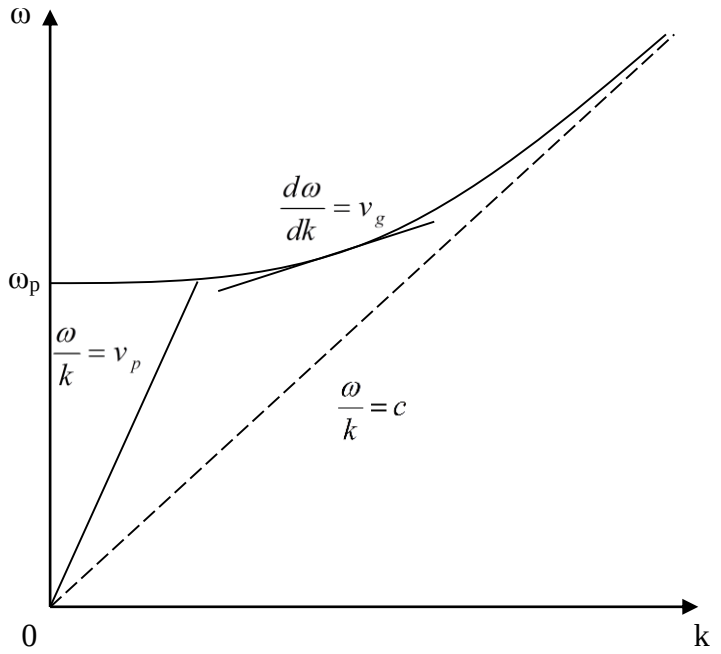

Figure 2.2 Dispersion relation of an electromagnetic wave in a plasma

As can be seen in Figure 2.2, the phase velocity v_p of a wave is given by $\omega/k=v_p$ and the group velocity v_g is given by $d\omega/dk=v_g$.

2.4.2 Wave oscillations in a cold plasma

A plasma is defined as being cold when the thermal speeds of the particles are much less than that of the phase speed of the propagating waves. This approach provides a good initial description of wave behaviour in a plasma. The problem may be further simplified by the assumption that the plasma is collisionless. The cold plasma wave equations are described purely by the ion and electron continuity equations, the Lorentz force equation and Maxwell's equations. The linearised versions of these equations are given below [Boyd and Sanderson, 2003],

$$\frac{\partial n_1}{\partial t} + \nabla \cdot (n_0 \underline{u}_1) = 0 \qquad \textbf{EQ 2.33}$$

$$\frac{\partial \underline{u}_1}{\partial t} = \frac{e}{m}(\underline{E}_1 + \underline{u}_1 \times \underline{B}_0) \qquad \textbf{EQ 2.34}$$

$$\underline{\nabla} \times \underline{E}_1 = -\frac{\partial \underline{B}_1}{\partial t} \qquad \textbf{EQ 2.35}$$

$$\underline{\nabla} \times \underline{B}_1 - \frac{1}{c^2}\frac{\partial \underline{E}_1}{\partial t} = \mu_0 \underline{J} = \mu_0 \sum_i q_i n_0 \underline{u}_1 \qquad \textbf{EQ 2.36}$$

$$\underline{\nabla} \cdot \underline{E}_1 = \frac{\rho}{\varepsilon_0} = \frac{1}{\varepsilon_0}\sum_i q_i n_1 \qquad \textbf{EQ 2.37}$$

$$\underline{\nabla} \cdot \underline{B}_1 = 0 \qquad \textbf{EQ 2.38}$$

For these equations, the initial conditions $\underline{E_0}$ and $\underline{u_0}$ are equal to zero and $\underline{B}_0$ and n_0 are constant in space and time. $\underline{E_1}$ and $\underline{B_1}$ are the AC fields arising from a small perturbation from the plasma equilibrium. Likewise $\underline{u_1}$ and n_1 are the particle velocity and density perturbed from equilibrium for each species. The summations are then performed over each particle species *i*. The total particle density, velocity and field strengths are,

$$\begin{aligned} n &= n_0 + n_1 \\ \underline{u} &= \underline{u}_1 \\ \underline{E} &= \underline{E}_1 \\ \underline{B} &= \underline{B}_0 + \underline{B}_1 \end{aligned} \qquad \textbf{EQ 2.39}$$

By assuming that all these variables vary as $\exp i(\underline{k} \cdot \underline{r} - \varpi t)$ and that the current $\underline{J}$ is defined in terms of the conductivity tensor (i.e. $\underline{J} = \bar{\sigma} \cdot \underline{E}_1$), the wave equation can be written as,

$$\underline{n} \times (\underline{n} \times \underline{E}_1) = -\underline{E}_1 - \frac{i}{\varepsilon_0 \omega}\bar{\sigma} \cdot \underline{E}_1 = -\bar{\varepsilon} \cdot \underline{E}_1 \qquad \textbf{EQ 2.40}$$

where $\bar{\varepsilon}$ is the cold plasma dielectric tensor and $n = c\underline{k} / \omega$ is the dimensionless wave propagation vector.

By defining the dielectric tensor as below, with $\underline{B}_0$ defined to be in the z direction,

$$\bar{\varepsilon} = \begin{bmatrix} S & -iD & 0 \\ iD & S & 0 \\ 0 & 0 & P \end{bmatrix} \quad \textbf{EQ 2.41}$$

This gives the components of the cold plasma dielectric tensor as,

$$S = \frac{1}{2}(R+L) = 1 - \frac{\omega_p^2(\omega^2 + \Omega_i\Omega_e)}{(\omega^2 - \Omega_i^2)(\omega^2 - \Omega_e^2)} \quad \textbf{EQ 2.42}$$

$$D = \frac{1}{2}(R-L) = \frac{\omega_p^2\omega(\Omega_i + \Omega_e)}{(\omega^2 - \Omega_i^2)(\omega^2 - \Omega_e^2)} \quad \textbf{EQ 2.43}$$

$$R = 1 - \frac{\omega_p^2}{(\omega + \Omega_i)(\omega + \Omega_e)} \quad \textbf{EQ 2.44}$$

$$L = 1 - \frac{\omega_p^2}{(\omega - \Omega_i)(\omega - \Omega_e)} \quad \textbf{EQ 2.45}$$

$$P = 1 - \frac{\omega_p^2}{\omega^2} \quad \textbf{EQ 2.46}$$

where Ω_e is < 0 and $\Omega_i > 0$ associated with the opposite rotational direction of the cyclotron motion. The direction of the wave propagation is given such that $\underline{n} = (n\sin\theta, 0, n\cos\theta)$ and therefore equation 2.40 can be rewritten without any loss of generality as,

$$\underline{n}(\underline{n}\cdot\underline{E}) - n^2\underline{E} + \varepsilon\cdot\underline{E} = 0 \quad \textbf{EQ 2.47}$$

and therefore

$$\begin{bmatrix} S - n^2\cos^2\theta & -iD & n^2\cos\theta\sin\theta \\ iD & S - n^2 & 0 \\ n^2\cos\theta\sin\theta & 0 & P - n^2\sin^2\theta \end{bmatrix} \begin{bmatrix} E_x \\ E_y \\ E_z \end{bmatrix} = 0 \quad \textbf{EQ 2.48}$$

with the general dispersion relation of cold plasma waves given by,

$$An^4 - Bn^2 + C = 0 \quad \textbf{EQ 2.49}$$

where,

$$A = S\sin^2\theta + P\cos^2\theta \quad \textbf{EQ 2.50}$$

$$B = RL\sin^2\theta + PS(1+\cos^2\theta) \quad \textbf{EQ 2.51}$$

$$C = PRL \quad \textbf{EQ 2.52}$$

θ in these equations is the angle between that of the direction of propagation of the wave and the static bias magnetic field.

The solutions to *n* can only be purely real or purely imaginary as in a cold plasma with no particle streaming there is no source of free energy that will allow instabilities to grow. When the solution to *n* is real then the waves will propagate. If the solution is imaginary then the waves are evanescent. When n^2 goes through zero or infinity, it corresponds to a transition between propagation and evanescence. When n tends towards zero as the frequency is tuned, then the transition is known as a cut-off as no wave above (or below as appropriate) the defined frequency will propagate. This occurs if P, R or L = 0. As such it is possible to define the cut-off frequencies of each case as follows (only considering positive ω),

$$\omega = \omega_p \quad \textbf{EQ 2.53}$$

$$\omega = \sqrt{\left(\omega_p^2 + \frac{(\Omega_i - \Omega_e)^2}{4}\right)} - \frac{\Omega_i + \Omega_e}{2} \equiv \omega_R \quad \textbf{EQ 2.54}$$

$$\omega = \sqrt{\left(\omega_p^2 + \frac{(\Omega_i - \Omega_e)^2}{4}\right)} + \frac{\Omega_i + \Omega_e}{2} \equiv \omega_L \quad \textbf{EQ 2.55}$$

At a cut-off, the wavevector tends towards zero while the phase velocity tends to infinity. The alternative extreme propagation condition, where *n* goes to infinity, requires that A transit through zero. This corresponds to a resonance as the wavevector tends to infinity and the phase velocity to zero. In this case it is possible to define a hollow cone with a resonance angle of θ_{res}. This cone separates angles where propagation is possible from angles where it is not. This angle is defined as,

$$\tan^2\theta_{res} = -\frac{P}{S} \quad \textbf{EQ 2.56}$$

θ_{res} lies between 0 and $\pi/2$, since the problem is symmetric with regard to the propagation direction. There are two distinct cases, where propagation is possible for

angles less that θ_{res} and where propagation is possible for angles greater than θ_{res}. The principal resonances (where no propagation is possible for any angle) occur according to equation 2.57, for the first case, and equation 2.58 for the second,

$$\theta_{res} = 0 \rightarrow P = 0 \text{ or } S = 0.5(R+L) \rightarrow \infty \quad \textbf{EQ 2.57}$$

$$\theta_{res} = \frac{\pi}{2} \rightarrow S = 0 \quad \textbf{EQ 2.58}$$

The first resonance condition in equation 2.57 is a degenerate case, i.e. all coefficients of equation 2.49 disappear. However, for the second resonance condition in equation 2.58,

$$R \rightarrow \infty \text{ as } \omega \rightarrow -\Omega_e = |\Omega_e| \quad \textbf{EQ 2.59}$$

$$L \rightarrow \infty \text{ as } \omega \rightarrow \Omega_i \quad \textbf{EQ 2.60}$$

which defines the electron cyclotron resonance and the ion cyclotron resonance respectively, which are important for waves travelling along the magnetic field lines. In addition to these, at the second resonance, given by equation 2.58, there are also hybrid resonances associated with perpendicular propagation given by,

$$\omega_{UH}^2 \approx (\omega_p^2 + \Omega_e^2 + \Omega_i^2) \approx (\omega_{pe}^2 + \Omega_e^2) \quad \textbf{EQ 2.61}$$

$$\omega_{LH}^2 \approx -\frac{\Omega_e\Omega_i(\omega_p^2 - \Omega_e\Omega_i)}{(\omega_p^2 + \Omega_e^2 + \Omega_i^2)} \approx \begin{cases} |\Omega_e\Omega_i| & \text{for } \omega_p^2 >> \Omega_e^2 \\ \omega_{pi}^2 + \Omega_i^2 & \text{for } \omega_p^2 << \Omega_e^2 \end{cases} \quad \textbf{EQ 2.62}$$

The subscripts UH define the upper hybrid resonance and LH define the lower hybrid resonance. These different resonances and cut-offs affect the different special cases of waves that will now be discussed.

For a plasma without a magnetic field, $B_0=0$ and $\theta=0$, equation 2.49 results in two simple wave solutions,

$$\omega^2 = \omega_p^2 \quad \textbf{EQ 2.63}$$

$$\omega^2 = \omega_p^2 + k^2c^2 \quad \textbf{EQ 2.64}$$

The first solution corresponds to the simple longitudinal ($\underline{k} \parallel \underline{E}$) plasma oscillation. In the cold plasma limit, this wave has no group velocity and therefore does not propagate. The second wave solution is a transverse wave ($\underline{k} \perp \underline{E}$) that cannot propagate in the range $0 < \omega < \omega_p$. The dispersion curve for this wave is given in figure 2.2. When the plasma has a finite temperature, the first solution becomes modified by the

thermal velocity of the particles resulting in what are known as Langmuir waves, given by,

$$\omega^2 = \omega_p^2 + k^2\left(V_i^2 + V_e^2\right) \qquad \textbf{EQ 2.65}$$

where *V* represents the thermal velocity of the ion and electron species, given by the subscripts *i* and *e* respectively, and are defined as,

$$V_i^2 = \frac{\gamma_i k_B T_{i0}}{m_i} \text{ and } V_e^2 = \frac{\gamma_e k_B T_{e0}}{m_e} \qquad \textbf{EQ 2.66}$$

where T_0 is the temperature of the species, *m* is the species mass and γ is the ratio of the specific heats, related to the degrees of freedom, *s*, of the species by *(s+2)/s*. A further solution for ion waves also appears when there is a finite temperature, given by,

$$\frac{\omega^2}{k^2} = V_i^2 + \frac{Z\gamma_e k_B T_{e0}}{m_i(1+k^2\lambda_D^2)} \qquad \textbf{EQ 2.67}$$

where *Z* is the charge of the ion species. This wave solution is known as the ion acoustic wave. This is analogous to a sound wave in a neutral gas, except that where a sound wave is a longitudinal wave driven by particle collisions, the ion acoustic wave is a longitudinal wave driven by the electrostatic potentials that arise due to the difference in amplitudes of the ion and electron oscillations. These waves propagate at the ion sound speed which is defined as,

$$c_s = \sqrt{\frac{Z\gamma_e k_B T_{e0}}{m_i}} \qquad \textbf{EQ 2.68}$$

Note that these warm plasma wave solutions make the assumption that the electrons in the plasma are typically hotter than the ions such that $V_i << V_e$.

Returning now to the cold plasma model, in the presence of a magnetic field but considering $\theta=\pi/2$, one solution to the dispersion relation is a transverse wave with $\underline{E} \perp \underline{k}$ which corresponds to a perpendicular propagating wave with an electric field parallel to the magnetic field vector $\underline{B}_0$. This wave is identical to the field free case described above and is known as the ordinary or O mode. Of particular interest in this work, another solution for $\theta=\pi/2$ is given by,

$$n^2 = \frac{RL}{S} \rightarrow \frac{\omega^2}{k^2c^2} = \frac{S}{RL} = \frac{1}{2}\left(\frac{1}{R} + \frac{1}{L}\right) \qquad \textbf{EQ 2.69}$$

This wave solution is known as the extraordinary or X mode. This mode has cut-offs, where $k \rightarrow 0$, at ω_R and ω_L as well as resonances, where $k \rightarrow \infty$, at ω_{UH} and ω_{LH}. Figure 2.3 shows the dispersion relation for the X-mode.

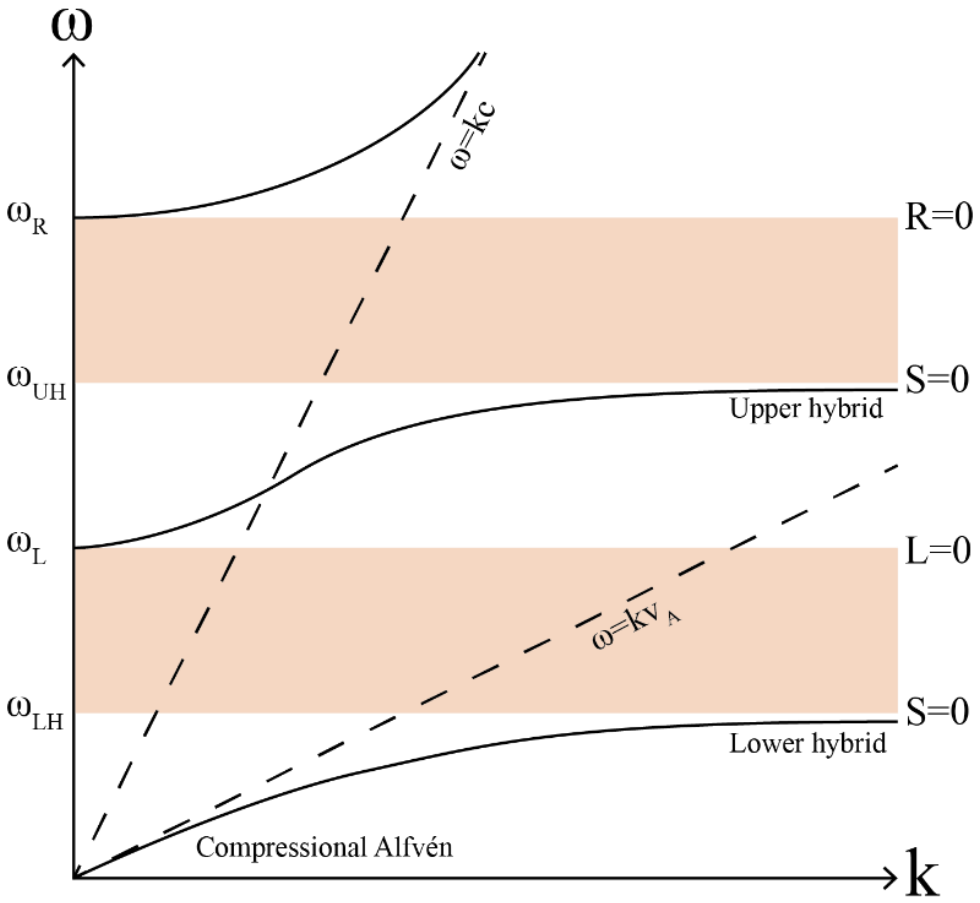

Figure 2.3 Dispersion relation of the X-mode

2.5 Instabilities

2.5.1 Two-stream / Beam-plasma instability

Considering a simple cold, unmagnetised plasma in the steady state with streaming components it is possible to describe the two-stream instability. Starting with just one component species of this plasma, the cold plasma equations can be linearised similarly to before but now,

$$
\begin{aligned}
n &= n_0 + n_1 \\
\underline{u} &= \underline{u}_0 + \underline{u}_1 \\
\underline{E} &= \underline{E}_1 \\
\underline{B} &= \underline{B}_1
\end{aligned}
\qquad \textbf{EQ 2.70}
$$

Where n_0 and $\underline{u_0}$ are constants defining the initial number density and initial velocity of the species respectively and n_1 and $\underline{u_1}$ are the perturbations in the number density and velocity respectively. As there are no initial electric and magnetic fields, the only fields arise from the perturbation. Therefore the equations of continuity and motion can be written,

$$\frac{\partial n_1}{\partial t} + \underline{\nabla} \cdot (n_0 \underline{u}_1 + n_1 \underline{u}_0) = 0 \qquad \textbf{EQ 2.71}$$

$$\frac{\partial \underline{u}_1}{\partial t} + (\underline{u}_0 \cdot \underline{\nabla})\underline{u}_1 = \frac{q}{m}(\underline{E}_1 + \underline{u}_0 \times \underline{B}_1) \qquad \textbf{EQ 2.72}$$

Considering only longitudinal waves, then from Maxwell's equations $\underline{\nabla} \times \underline{E}_1 = 0$ therefore there is no change in magnetic field component from the perturbation. As the initial magnetic field is zero, only Poisson's equation is required,

$$\underline{\nabla} \cdot \underline{E}_1 = \frac{1}{\varepsilon_0} \sum_i q_i n_1 \qquad \textbf{EQ 2.73}$$

From these equations, and assuming that all the perturbed quantities vary as $\exp i(\underline{k} \cdot \underline{r} - \omega t)$ it is possible to solve for the non-trivial case of $\underline{E}_1 \neq 0$ and obtain the generalised dispersion relation of longitudinal waves for all species in the plasma,

$$\sum_\alpha \frac{\omega_{p\alpha}^2}{(\omega - \underline{k} \cdot \underline{u}_\alpha)^2} = 1 \qquad \textbf{EQ 2.74}$$

where $\omega_{p\alpha}$ is the plasma frequency and α is the species. Considering the dispersion relation given by equation 2.74 for two beams of electrons, it can be seen that this equation is a quartic with four solutions. For $|k| > k_c$ there are four real solutions, where the critical value is given by $k_c^2 = \left(\omega_{p1}^{2/3} + \omega_{p2}^{2/3}\right)^3 / (u_1 - u_2)^2$. However, for $|k| < k_c$ the solutions become a pair of complex conjugate solutions. It is the imaginary part of these solutions which represent the exponentially growing and damped waves in the system, with the growing wave being associated with the two-stream instability. For the case where there is one population with a finite drift velocity streaming into a

secondary population with zero drift velocity, this is known as the beam-plasma instability [Thode and Sudan, 1975].

2.5.2 Modulational instability

In a system where there is the propagation of both Langmuir waves and ion acoustic waves, it is possible for these two waves to couple and modify their propagation behaviours. Due to the large difference in response time between the electrons and the ions, the electron wave essentially sees the ions as a static background whereas the ion wave perceives the fast electron behaviour as a neutralising medium. If an ion density fluctuation is formed, this can introduce perturbations in the electron wave dispersion. Similarly, the electrons affect the ion acoustic wave as the pondermotive force of the slowly varying electric field can displace the electrons. This coupling is given by the Zakharov equations [Zakharov, 1972; Dendy, 2002],

$$2i\omega_{pe}\frac{\partial \underline{E}}{\partial t}+\frac{\gamma_e k_B T_e}{m_e}\nabla(\nabla\cdot\underline{E})-c^2\nabla\times(\nabla\times\underline{E})=\omega_{pe}^2\left(\frac{n_s}{n_0}\right)\underline{E} \qquad \textbf{EQ 2.75}$$

$$\left(\frac{\partial^2}{\partial t^2}-c_s^2\nabla^2\right)n_s=\frac{\varepsilon_0}{4m_i}\nabla^2\left|\underline{E}\right|^2 \qquad \textbf{EQ 2.76}$$

Where n_s is the perturbation in density introduced by the slow time-scale wave. These two equations describe the coupling between the slow-time scale density perturbations and the resultant electric field. They show that if there is a slow perturbation in the ion density, there is a corresponding slow perturbation in the electron density which moderates the evolution of the amplitude of the electric field associated with the electron plasma frequency. For electrons oscillating in an inhomogeneous electric field E (and assuming the simple case where the electric field and its gradient are aligned), as the electrons oscillate in the direction of the increasing field strength they will experience a stronger reverse force, -eE, in the opposite half of the cycle. This has the result of moving the electrons out of the region of high electric field amplitudes. A similar analogue occurs for the magnetic component of the Lorentz force, when the electron motion is perpendicular to the field gradient. As these electrons move out of these high field regions, the ions follow resulting in areas of plasma depletion which

leads to what is known as the modulational instability [Nishikawa, Hojo and Mima, 1974; Rosenbluth and Sagdeev, 1984b].

In the example of a wave propagating with constant amplitude through a homogenous plasma, a small perturbation in density can lead to plasma depletion. This will in turn lead to an increase in the wave amplitude, which will drive more electrons from this plasma cavity. This modulation of the wave profile can grow, resulting in plasma cavities that are several Debye lengths in dimension.

To determine the regime where the modulation instability can occur, it is important to consider the turbulence parameter which determines the threshold for the instability,

$$W = \frac{\varepsilon_0 \left\langle \left| \underline{E} \right|^2 \right\rangle}{2} \frac{1}{n_0 k_B T_e} = \frac{\varepsilon_0 \left| \underline{E} \right|^2}{4 n_0 k_B T_e} \qquad \textbf{EQ 2.77}$$

This parameter gives the ratio of the average electric field energy associated with an electrostatic or electromagnetic wave in the plasma to the thermal energy density of the particles. With this parameter defined, it is possible to show that if $W > \frac{3k^2}{k_D^2}$ where k is the wavenumber of the wave and k_D is the Debye wavenumber $k_D = \frac{2\pi}{\lambda_D}$, then it is possible for waves to become trapped and the modulational instability to grow.

2.5.3 Cyclotron resonance maser instability

The cyclotron resonance maser (CRM) instability grows when an electron beam gyrates around an external magnetic field and couples to an electromagnetic wave. [Twiss, 1958; Sprangle and Drobot, 1977; Chu 1978]. It is the main process that is utilised to extract energy from a gyrating electron beam and use it to produce radiation, such as in a gyrotron.

The CRM instability consists of the gyrating electron beam interacting with the AC components of an electromagnetic wave, such as those in a waveguide, which results

in the electron beam forming azimuthal bunches which provides an efficient mechanism for the transfer of energy to the electromagnetic wave.

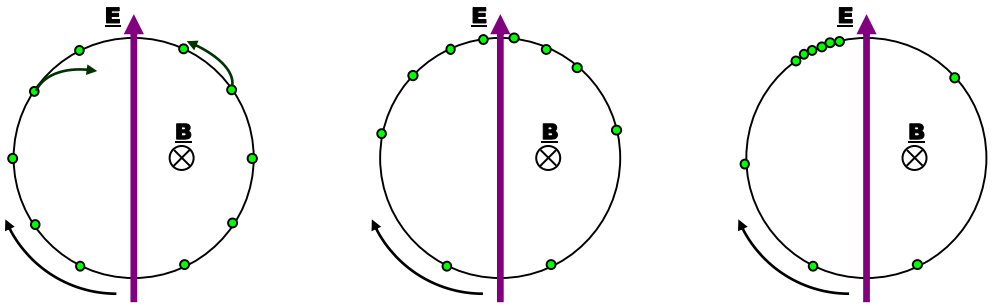

Figure 2.4 Schematic of azimuthal bunching due to CRM instability

Figure 2.4 shows schematically how the cyclotron resonance maser instability operates [Granatstein and Alexeff, 1987]. Initially the electrons are uniformly distributed around the magnetic field axis at the Larmor radius. The electrons and the electric field both co-rotate in the same clockwise direction. As the electrons continue to orbit they begin to interact with the transverse electric field components of the electromagnetic wave. This leads to a deceleration on the left side of the field line, illustrated in figure 2.4, and an acceleration on the right. As the electrons exchange energy with the transverse electric field, the modulated relativistic factor begins to modify their cyclotron frequency i.e. the decelerating electrons increase their cyclotron frequency and advance in phase whereas the accelerating electrons decrease their cyclotron frequency and retard in phase. This ultimately leads to an azimuthal bunch forming. When the bunch is in a suitable phase with the electric field, they can emit radiation coherently. This occurs when the wave frequency slightly exceeds the cyclotron frequency, the resulting phase drift moves the electrons into the decelerating phase as indicated in the third image in figure 2.4.

In the Earth's magnetosphere, the AKR emissions are thought to be produced by a related CRM mechanism [Delory, et al., 1998; Ergun, et al., 1998b; 2000]. In this case, the emitted radiation has been observed to be polarised in the X-mode. It has been shown that the horseshoe velocity distribution of electrons is also unstable to the CRM mechanisms [Bingham and Cairns, 2000; 2002]. To approximate this process in the

laboratory, a waveguide with a circular cross-section was previously used to support near cut-off transverse-electric modes which would be able to simulate the properties of an X-mode, see section 2.6. Likewise the numerical simulations in this work would use the same waveguide approximation of the plasma X-mode.

2.6 Waveguide theory

From Maxwell's equations (2.35-2.38), it is possible to derive the equation for a propagating electromagnetic wave as,

$$\nabla^2 \underline{E} = \mu\varepsilon \frac{\partial^2 \underline{E}}{\partial t^2} \qquad \textbf{EQ 2.78}$$

$$\nabla^2 \underline{B} = \mu\varepsilon \frac{\partial^2 \underline{B}}{\partial t^2} \qquad \textbf{EQ 2.79}$$

The solutions to these equations require careful consideration of the boundary conditions of the system being considered. Within a hollow conducting waveguide, the electric field component parallel to the structure boundary must become zero as the conduction path in the boundary will short out this field. Similarly, the AC magnetic field component perpendicular to the boundary must also be zero as there would be a current flow in the boundary that would cancel the field. A free-space wave has purely transverse electric and magnetic field components known as a TEM wave. In a hollow conducting waveguide, it is not possible for both of these fields to be transverse to the waveguide axis (and therefore the propagation direction) due to the boundary conditions. Therefore the only allowed waves that can propagate through the structure have either axial magnetic fields and are called transverse electric field modes (TE) or have axial electric fields and are referred to as transverse magnetic field modes (TM). The general (Cartesian) solutions for these waves are given,

$$E_x = -\frac{j}{k_c^2}\left(k_z \frac{\partial E_z}{\partial x} + \omega\mu \frac{\partial H_z}{\partial y} \right) \qquad \textbf{EQ 2.80}$$

$$E_y = -\frac{j}{k_c^2}\left(-k_z \frac{\partial E_z}{\partial y} + \omega\mu \frac{\partial H_z}{\partial x} \right) \qquad \textbf{EQ 2.81}$$

$$H_x = \frac{j}{k_c^2}\left(\omega\varepsilon \frac{\partial E_z}{\partial y} - k_z \frac{\partial H_z}{\partial x} \right) \qquad \textbf{EQ 2.82}$$

$$H_y = -\frac{j}{k_c^2}\left(\omega\varepsilon \frac{\partial E_z}{\partial x} + k_z \frac{\partial H_z}{\partial y} \right) \qquad \textbf{EQ 2.83}$$

Where $k_z = \sqrt{k^2 - k_c^2}$ is the propagation constant and k_c is the cut-off wavenumber with these parameters dependant on the geometry of the waveguide and frequency of the wave ($k = \frac{2\pi f}{c}$). These equations describe TE waves when E_z=0 and TM waves H_z=0.

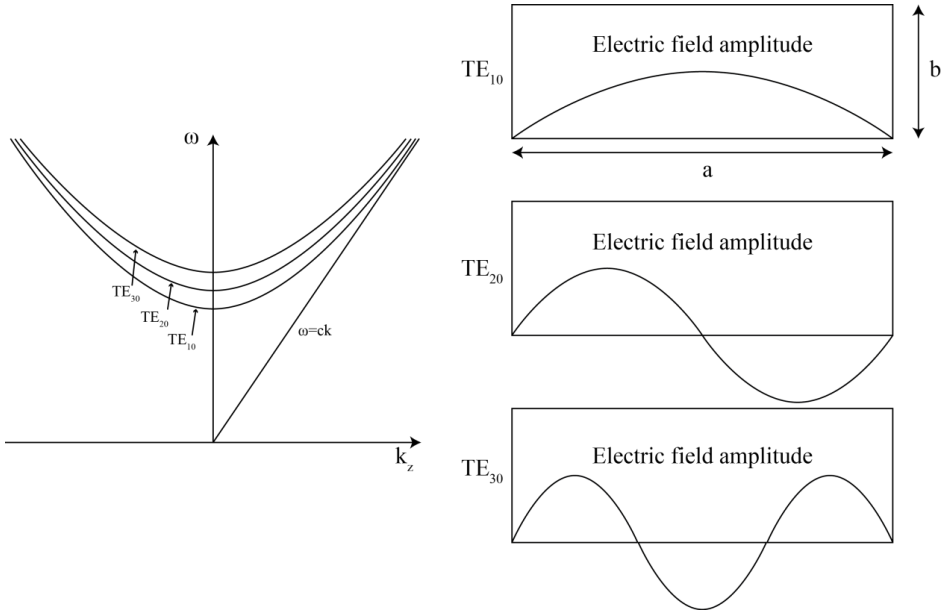

Figure 2.5 Dispersion of rectangular waveguide TE modes and cross-section examples of TE electric field behaviour for TE modes

For a waveguide of rectangular cross-section the H_z and E_z components for TE and TM waves respectively are given by,

$$H_Z = A\cos\frac{m\pi x}{a}\cos\frac{n\pi y}{b}e^{-jk_z z} \qquad \textbf{EQ 2.84}$$

$$E_Z = B\sin\frac{m\pi x}{a}\sin\frac{n\pi y}{b}e^{-jk_z z} \qquad \textbf{EQ 2.85}$$

And the different modes of propagation cut-off wavenumbers are given by,

$$k_c = \sqrt{\left(\frac{m\pi}{a}\right)^2 + \left(\frac{n\pi}{b}\right)^2} \qquad \textbf{EQ 2.86}$$

Where A is an arbitrary amplitude, a and b are the waveguide dimensions and m and n are the waveguide mode numbers. For TE modes, m=n=0 is a forbidden mode whereas for TM modes m=0 or n=0 is a trivial solution. The graphical form of the dispersion relation for example TE modes are given in figure 2.5. One can see that in

a smooth waveguide the dispersion had a hyperbolic form with a minimum (cut-off) frequency of $\omega = ck_c$.

For a cylindrical waveguide of circular cross-section, the equations 2.80-2.83 can be represented in cylindrical coordinates,

$$E_r = -\frac{j}{k_c^2}\left(k_z \frac{\partial E_z}{\partial r} + \frac{\omega\mu}{r}\frac{\partial H_z}{\partial \phi}\right) \quad \textbf{EQ 2.87}$$

$$E_\phi = -\frac{j}{k_c^2}\left(-\frac{k_z}{r}\frac{\partial E_z}{\partial \phi} + \omega\mu\frac{\partial H_z}{\partial r}\right) \quad \textbf{EQ 2.88}$$

$$H_r = \frac{j}{k_c^2}\left(\frac{\omega\varepsilon}{r}\frac{\partial E_z}{\partial \phi} - k_z\frac{\partial H_z}{\partial r}\right) \quad \textbf{EQ 2.89}$$

$$H_\phi = -\frac{j}{k_c^2}\left(\omega\varepsilon\frac{\partial E_z}{\partial r} + \frac{k_z}{r}\frac{\partial H_z}{\partial \phi}\right) \quad \textbf{EQ 2.90}$$

And again the H_z and E_z components for TE and TM modes respectively,

$$H_Z = [A\sin(n\phi) + B\cos(n\phi)]J_n(k_c r)e^{-jk_z z} \quad \textbf{EQ 2.91}$$

$$E_Z = [A\sin(n\phi) + B\cos(n\phi)]J_n(k_c r)e^{-jk_z z} \quad \textbf{EQ 2.92}$$

Where A and B are arbitrary amplitudes of the sin and cosine terms which can be independent of each other corresponding to two degenerate, orthogonal polarisations of the wave. J_n is a Bessel function of the first kind of order n.

To find the cut-off wavenumber for TE modes, we require that $E_\phi = 0$ when r = a, the radius of the waveguide which gives,

$$k_c = \frac{P'_{nm}}{a} \quad \textbf{EQ 2.93}$$

Where P'_{nm} is the m^{th} root of the derivative of the Bessel function, J'_n. The first few roots are shown in table 2.1,

n	P'_{n1}	P'_{n2}	P'_{n3}
0	3.832	7.016	10.174
1	1.841	5.331	8.536
2	3.054	6.706	9.970

Table 2.1 First values for the roots of the derivative of the ordinary Bessel function of the first kind J'_n

For the cut-off wavenumbers of the TM modes, $E_z = 0$ when r = a, which gives

$$k_c = \frac{P_{nm}}{a} \qquad \textbf{EQ 2.94}$$

Where P_{nm} is the m^{th} root of the Bessel function, J_n. Again the first few values for this root is shown in table 2.2,

n	P_{n1}	P_{n2}	P_{n3}
0	2.405	5.520	8.654
1	3.832	7.016	10.174
2	5.135	8.417	11.620

Table 2.2 First values for the roots of the ordinary Bessel function of the first kind J_n

As the propagation constant $k_z \rightarrow 0$ (i.e. near cut-off), a TE wave propagates perpendicular to the waveguide axis with a polarisation direction perpendicular to the waveguide axis. At the same condition, this leads to the magnetic field component of the wave tending to become purely axial. This particular type of wave has propagation and polarisation properties that are similar to a plasma X-mode as discussed in section 2.4.2. Observations of the radiation generated in the magnetosphere show that it is polarised in the plasma X-mode and at a frequency close to the electron cyclotron frequency. The laboratory models relate to the AKR emission from the earth's magnetosphere where there is an area of plasma depletion known as the auroral density cavity that has boundaries where the plasma frequency is greater than the electron cyclotron frequency. It has been supposed that these boundaries function in a similar manner to a conducting cylindrical waveguide of circular cross-section [Burinskaya and Rauch, 2007]. For the simulations presented in this work, the near cut-off TE modes are used for the laboratory models of the X-mode.

2.7 Electron emission

In order to generate an electron beam propagating in a vacuum, an emissive cathodic electrode is required in the system. The electron emission process from this cathode is enabled by a number of mechanisms, of particular importance are field emission, thermionic-Schottky emission and explosive electron emission (that is an extreme

consequence of the first two). The dense electron population within the conduction band of metals (and other conductors) is prevented from leaving the cathode due to a potential barrier that forms on the surface of the material. The different emission mechanisms describe ways in which this potential barrier can be traversed or penetrated. The mechanism which dominates is typically determined by the strength of the applied electric field across the cathode surface, along with the temperature and composition of the underlying material. The limit of the emission current is determined by the laws of electromagnetism and in particular the Child-Langmuir or space-charge limit.

2.7.1 Space-charge limit

For a relatively weak electric field applied to the surface of a warm cathode, the current can be found to increase in proportion with $V_a^{3/2}$, where V_a is the applied voltage. The cause of this limit arises due to the relative ease with which the electrons escape the cathode material. As the electron beam current is required to be continuous across the diode gap, at relatively low velocities near the cathode, the electron cloud density is high which depresses the local electrostatic potential, shown in figure 2.6. This density is large enough that the electric field on the cathode surface tends to zero.

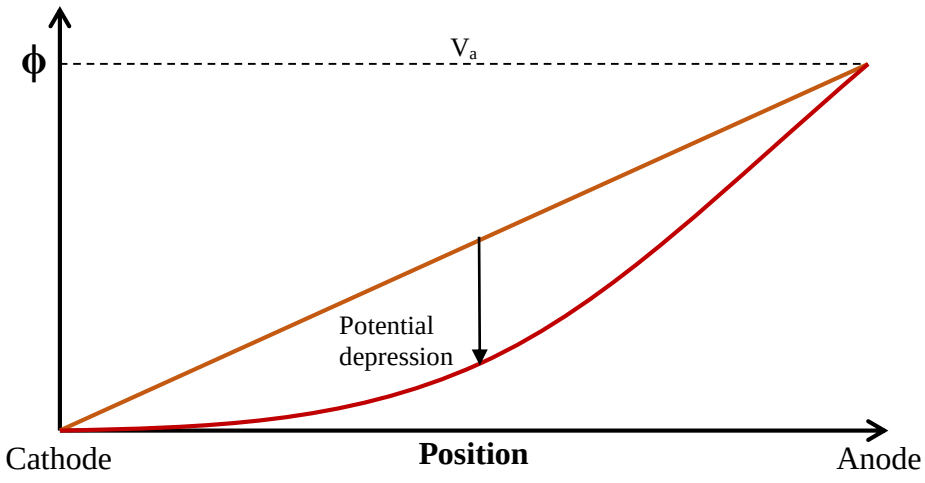

Figure 2.6 Electrostatic potential between the cathode and the anode

This is known as the space charge limit and it determines the maximum current that can be drawn from a cathode in vacuum. Whilst this behaviour is dependent on the geometry of the system, it always has the form,

$$I = PV^{3/2} \qquad \textbf{EQ 2.95}$$

Where P is the perveance. This equation is referred to as the Child-Langmuir law, or alternatively the three-half power law. For a plane parallel diode in the sub- relativistic limit, the perveance is defined as,

$$P = \frac{4}{9}\frac{A\varepsilon_0\sqrt{\frac{2e}{m_e}}}{d^2} \qquad \textbf{EQ 2.96}$$

Where A is the area of the electrodes and d the electrode gap spacing [Gilmour, 1986; 2011; Lorrain, Corson and Lorrain 1988; Humphries, 1990]

2.7.2 Thermionic-Schottky emission

For all cathode temperatures above absolute zero, there will exist a population of electrons in the high energy tail of the electron distribution function that have sufficient energy to escape over the potential barrier. The density of this population will be predominately controlled by the cathode temperature. If a weak electric field is applied to this cathode material, then these electrons will be allowed to leave the surface. This is known as the thermal emission current, given by the Richardson Dushman equation [Gilmour, 1986],

$$J = A_0 T^2 e^{-\frac{e\phi}{k_B T}} \qquad \textbf{EQ 2.97}$$

Where T is the temperature of the cathode and ϕ is the surface barrier potential. The constant A_0 is given as $1.20\text{x}10^6$ $\text{Am}^{-2o}\text{K}^{-2}$.

However, the effect of an externally applied electric field modifies the work function, which acts to reduce the maximum value of the barrier potential. This is known as the

Schottky effect and is described by a modified version of the Richardson Dushman equation,

$$J = A_0 T^2 e^{-\frac{e(\phi-\Delta\phi)}{k_B T}} = A_0 T^2 e^{-\frac{e(\phi-\sqrt{\frac{eE}{4\pi\varepsilon_0}})}{k_B T}} \qquad \textbf{EQ 2.98}$$

Where E is the applied electric field. For a warm cathode, as the applied electric field is increased, this mechanism will reach a point where it can no longer support the space-charge limit of the current which can be carried by the vacuum diode. This will result in the current reaching a plateau at the so-called temperature limit. The current as a function of applied voltage is shown in figure 2.7.

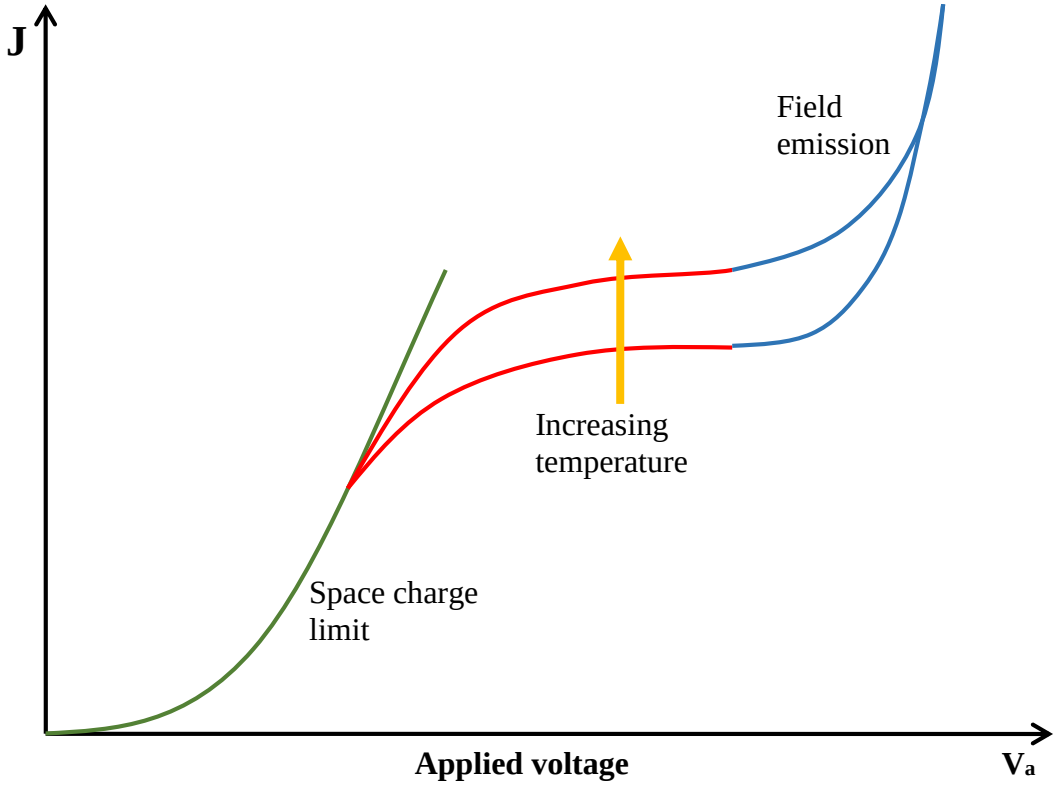

Figure 2.7 Emission current as a function of applied voltage

2.7.3 Field emission and field enhancement

As the applied electric field is increased further, more electrons will begin to be emitted than can be explained by the thermionic mechanism. This behaviour is due to the surface potential barrier becoming narrow enough that the dense electron population at or near the Fermi level in the conduction band has a finite probability of surface barrier tunnelling from the metal to the vacuum. This tunnelling current rapidly becomes dominant over the thermionic current. It should be noted, however, that this process cannot raise the current to the space charge limit as by definition this would result in no field on the cathode. This tunnelling current is given by the Fowler-Nordheim relation,

$$J = \frac{AE^2}{\phi} e^{-\frac{B\phi^{3/2}}{E}} \qquad \textbf{EQ 2.99}$$

Where A is given as $1.54 \times 10^{-6}(10^{4.54/\sqrt{\phi}})$ and B is $6.53 \times 10^{9} eV^{-3/2}$, with E the electric field (Vm^{-1}), J the current density (Am^{-2}) and ϕ the work function (eV) [Ronald, 1996; Noer, 1982].

For real plane cathode materials, the onset of field enhanced emission occurs orders of magnitude lower than would be expected. This is due to the surface containing many discontinuities and, in particular, extreme whiskers of material that can result in local enhancement of the electric field. This enhancement is typically on the order of the aspect ratio of the discontinuities. For very thin whiskers with tips ~nm across, this can result in particularly high enhancement. Field emission from only a few such microscopic sites can dominate the bulk thermal emission from the entire cathode when the applied electric field is sufficiently high.

2.7.4 Dielectric enhanced breakdown

Field enhancement is no longer thought to provide a complete explanation for the experimental observations from surfaces in high field environments (though it does explain the potential for significant field emission at macroscopic fields well below

the critical value predicted by the Fowler-Nordheim relationship). Other additional mechanisms associated with dielectric surface coatings have been identified. Above a certain critical field, small currents that flow from the metal to the empty conduction band of the insulator, avalanche through the dielectric which provides a large supply of electrons at the vacuum edge of the dielectric [Latham, 1983].

2.7.5 Explosive electron emission

The operation of a velvet cathode depends upon a mix of the previous effects that result in electron emission. The surface is initially a dielectric that is covered in uniform fibrous tufts. These tufts perturb the electric field, leading to the enhanced emission process. This is further enhanced by the breakdown along the length of the fibres from the underlying metal which provides a large electron density at the cathode tips.

All of these field enhanced emission processes (see sections 2.7.3 - 2.7.4) are generally unstable in reality. Rapid, localised heating typically results in the vaporisation of the cathode material which creates a gas cloud at the cathode surface. The intense thermionic current from the hot underlying material can ionise this gas, forming a dense plasma. This plasma then supports space charge limited emission in the vacuum gap. This process is known as explosive electron emission [Ronald, 1996; Mesyats and Proskurovsky, 1989; Tsimring, 2007]. This is a highly dynamic process, due to the non-static nature of the plasma cloud. This cloud can expand with a velocity determined primarily by the specific energy of vaporisation of the bulk material, although this is affected by the electric and magnetic fields present. An estimate of this expansion velocity has been given by [Mesyats and Proskurovsky, 1989] as,

$$V_{\exp} = \sqrt{\frac{4\gamma_1 J^2 t_v \kappa}{(\gamma_1 - 1)\pi^2 \rho}} \qquad \textbf{EQ 2.100}$$

Where γ_1 is an adiabatic parameter, typically ~1.24 [Mesyats and Proskurovsky, 1989], t_v is the time taken for the tip to vaporise, κ the resistivity and ρ the material density.

Typical values of the expansion velocity are in the range of 1-7 cm/μs [Mesyats and Proskurovsky, 1989; Ronald, 1996] for metals from lead to stainless steel (slow to fast respectively). This limits the operation of such cathodes to systems that have pulse durations significantly less than the time taken for the plasma cloud to traverse the anode-cathode gap. A cathode immersed in a magnetic field will also exhibit more uniform emission as the magnetic field prevents the space charge cloud at an emission site from suppressing the electric field in a neighbouring potential site.

2.8 Gas discharges

For the beam-plasma laboratory experiment, it is necessary to produce a low density plasma from a low pressure background of helium gas. To achieve this, the gas has to be ionised in a sustained discharge which is the result of a process similar to that of Townsend discharge.

In its simplest form, the Townsend discharge is created between two parallel conducting plates (an anode and cathode) and a potential difference is applied between the electrodes, illustrated in figure 2.8. Initially as the voltage is raised above zero, the anode and cathode collect randomly produced charge carriers formed in the gap [von Engel 1965; 1983]. The cathode also emits a weak electron current (which can be enhanced by UV irradiation or heating) which propagates towards the anode (figure 2.8(i)). Whereas in a vacuum, where the electrons propagate all the way to the anode with little disruption, in the presence of a background gas the propagating electrons can begin to collide with the neutral atoms or molecules of the gas. The likelihood of this event is dictated by the mean free path. Typically these collisions are elastic and scatter the directed drifting electrons whilst conserving the bulk of their energy, hence the electric field effectively ‘heats’ the electron thermal motion. If the colliding electron’s kinetic energy exceeds that of the ionisation threshold of the neutral gas particles, then an electron can be stripped from that neutral resulting in both a positive ion and now two electrons (figure 2.8(ii)).

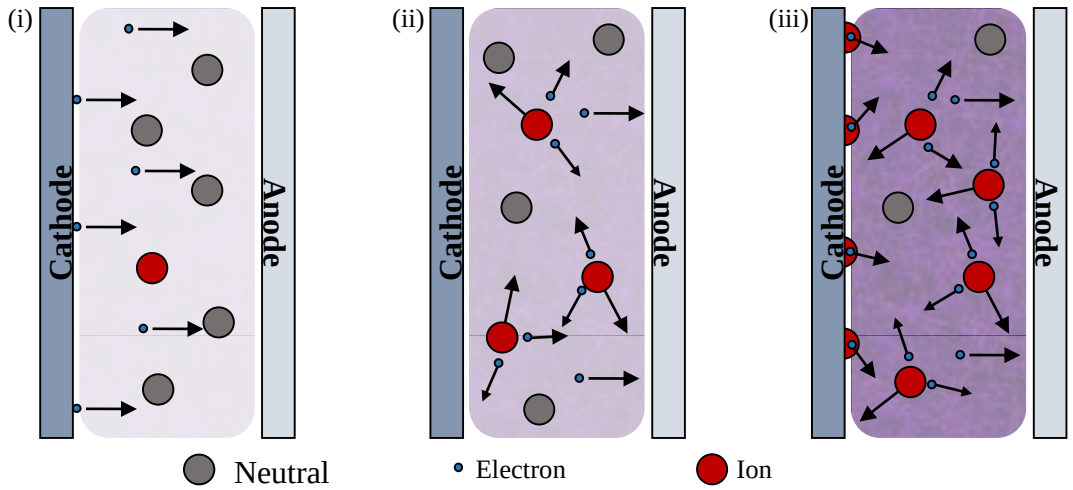

Figure 2.8 Townsend discharge schematic

The colliding electron deflects in a different direction and with a reduced kinetic energy due to the inelastic nature of the collision. The secondary electrons which are stripped from the neutrals are also accelerated and drift towards the anode, again leading to further collisions resulting in an exponential avalanche of ionisation. In addition, the ions that are created accelerate back and impact upon the cathode surface which can result in secondary electron emission (as the ion delivers it's kinetic and potential energy locally) (figure 2.8(iii)). In order for the discharge to be self-sustaining, the following expression must be satisfied,

$$\gamma\left(e^{\alpha d}-1\right)=1 \qquad \textbf{EQ 2.101}$$

Where α is known as the first Townsend coefficient which relates the number of electron-ion pairs produced by an electron over a unit path length as it moves from the cathode to anode, d is the distance between the anode and cathode and γ is the second Townsend coefficient related to the number of secondary electrons generated per ion impacting on the cathode.

Unfortunately this particular type of discharge does not work well at low gas pressures. This is due to the mean free path of the electrons which increases as the pressure of the gas is reduced. This typically results in the electrons travelling from the cathode to anode without colliding with any neutral particles leading to a very low ionisation rate and no sustained discharge. For the laboratory beam-plasma experiment we instead use a Penning-like discharge.

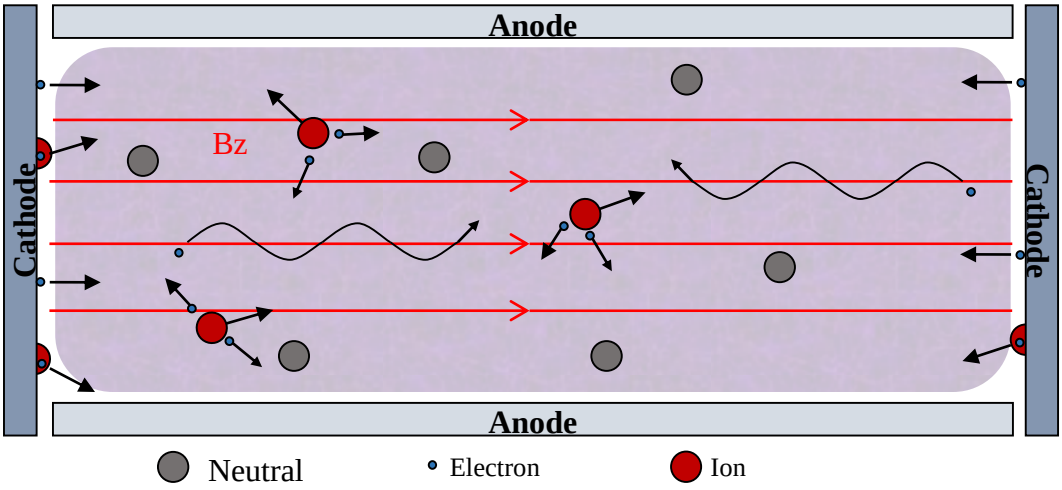

Figure 2.9 Penning discharge schematic

For the Penning trap geometry [Chambers, Fitch and Halliday 1998; Eichmeier and Thumm 2008], the anode consists, instead of a conducting plate, of a conducting cylinder and there are now two cathode plates or discs at either end of the anode, figure 2.9. A static magnetic field is applied parallel to the length of the anode. For this discharge, a voltage is again applied to the cathode and, similar to the Townsend discharge, electrons will either be formed by random statistical ionisation in the bulk of the gas, or begin to be emitted from the cathode surface. In this geometrical configuration, the electrons are again attracted towards the anode but the applied magnetic field prevents the electrons from reaching it. Instead the electrons gyrate along the magnetic field lines until they are repelled by the second cathode. The electrons will therefore 'bounce' back and forth between the cathodes greatly increasing their path length. As would be expected, this results in many more collisions between the electrons and the neutral gas particles, increasing the amount ionisation. The ions are still attracted to the cathodes and are still able to impact upon the cathode surfaces, producing secondary electrons. The specific designs of the traps used in the beam-plasma experiment are described in Chapter 5.

2.9 Plasma probe theory

In order to obtain a measurement of the characteristic parameters of a plasma, such as the number density and electron temperature, probes are typically inserted into the plasma [Huddlestone and Leonard, 1965; Hutchinson, 2002]. When a plasma is incident upon a surface, such as the probe, a sheath forms as described in section 2.2.3. By applying a varying bias voltage to the probe, the amount of current flowing in the probe changes due to changes in the particle distribution in the sheath due to the probe potential. Through the measurement of the current-voltage (I-V) characteristics of the plasma it may be possible to obtain an estimate for the electron temperature as the collected current density, J, on the probe is related to the probe voltage, V_p, as follows,

$$J = J_0 e^{\left(\frac{eV_p}{kT_e}\right)} \qquad \textbf{EQ 2.102}$$

By taking the natural logarithm of equation 2.102,

$$\ln J = \ln J_0 + \frac{eV_p}{kT_e} \qquad \textbf{EQ 2.103}$$

Therefore the gradient of a plot of ln J vs V_p is $\frac{e}{kT_e}$ allowing the electron temperature to be determined. From this it is possible to use equation 2.103 to determine the thermal velocity of the electrons and from this the number density by,

$$n_e = \frac{4J_0}{ev_{th}} \qquad \textbf{EQ 2.104}$$

The value for J_0 can be determined again by the plot of J vs V_p, as it will occur at the plasma potential V_{pot} and correspond to the electron saturation region. A typical plot of the I-V characteristics of a probe inserted into a plasma is shown in figure 2.10,

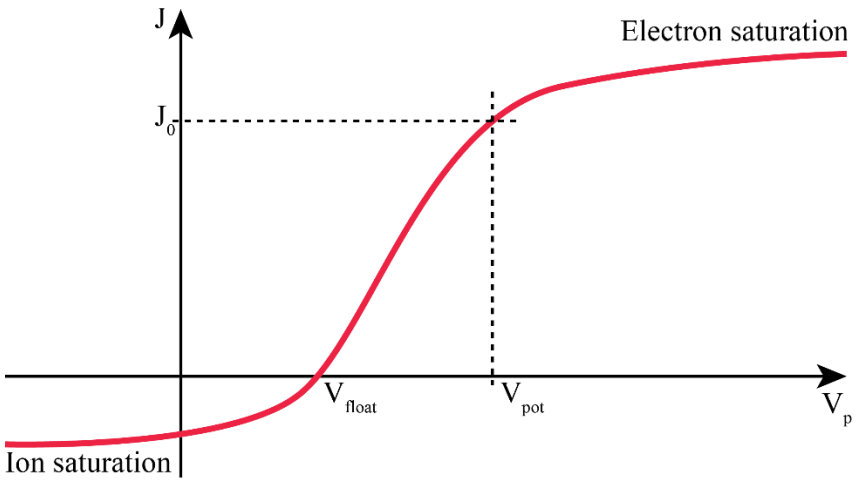

Figure 2.10 Typical plasma probe I-V characteristics

From this curve it can be seen that there are various charge collection regimes on the probe. When the probe is biased increasingly positive, the probe is in the electron saturation regime. Here the electron current is predominantly collected as the electrons are attracted and the ions are repelled from the probe surface. The plasma potential, V_{pot}, is the point at which the probe is at the same potential as the plasma and there is no particular attraction to the probe for either the electrons or ions. Here the current is determined predominately by the thermal motion of the electrons. As the voltage is decreased below the plasma potential, electrons are increasingly repelled (reducing their density according to the Boltzmann distribution) until there is no net current flow at the floating potential V_{float}. Continuing to decrease the voltage will result in the current being predominately generated from the ion flow to the probe, whereby the probe reaches the ion saturation regime. Due to the larger mass of the ions compared to the electrons, the magnitude of the ion saturation current is less than that of the electron saturation current. In the presence of a magnetic field, the probe sheath behaviour can become more complicated as the electron trajectories through the sheath will gyrate along the field lines. The ions on the other hand do not respond as strongly to the bias magnetic field, typically having a larger Larmor radii (even for a significant temperature decrement over the electrons) which may therefore adversely affect the collection current balance. Moreover, the assumed temperature anisotropy of equation 2.102 may be challenged in the presence of a strong magnetic field.

Chapter 3 : Computational methodology

3 Computational methodology

3.1 Particle-in-cell finite difference time-domain solver

Due to the inherent complexity of the non-linear dynamics of a plasma system, computational codes have been employed to model the systems of interest. One approach, followed in this thesis, utilises a finite difference time-domain (FDTD) method to solve Maxwell's equations in their partial differential forms by splitting the space of the system into an array of 1, 2 or 3-dimensional grid points.

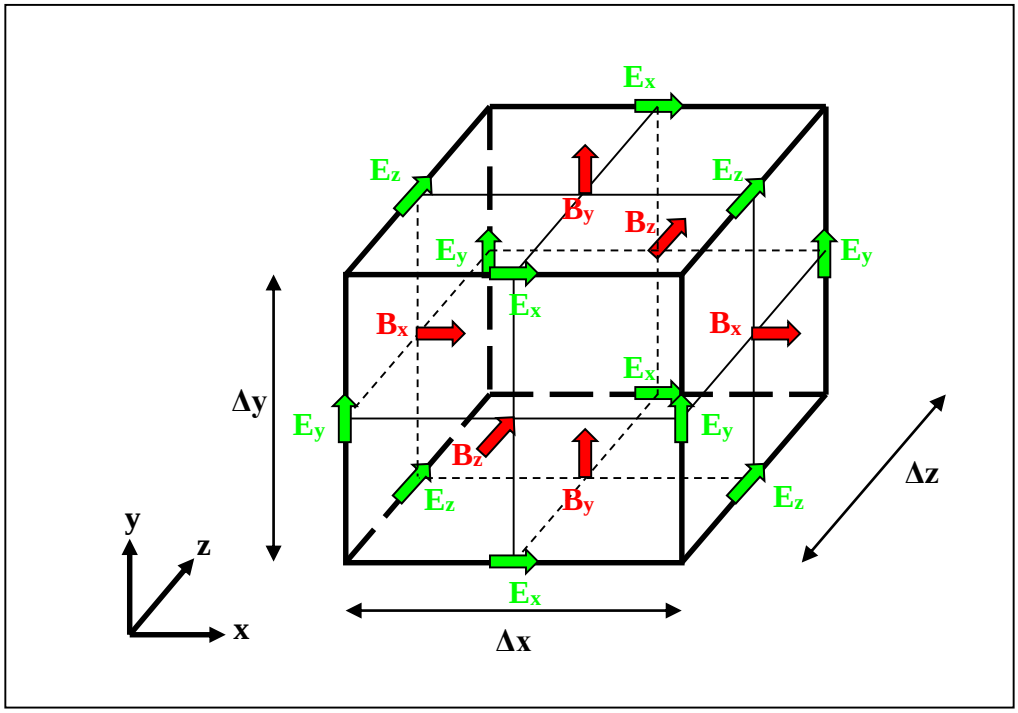

Figure 3.1 Cartesian 3D Yee-cell

In this method, the electric and magnetic field components are arranged around a rectangular cell element formed by the normal planes to three orthogonal vectors defined by 6 grid points, as proposed by [Yee 1966]. The electric field components are defined along the edges of the cell whereas the magnetic field components are located at the centre of each of the cell faces. Note that if one transposes half a cell in each direction one may perceive that there is a mesh structure which inverts these

alignments. This arrangement of field components is known as a Yee-cell, shown in figure 3.1 for Cartesian coordinates. The minimum length of the Yee-cell is required to be substantially less than the smallest simulated wavelength.

The fields are solved at fixed integers of time, or time-steps, which are defined at the start of the code. This time-step is required to satisfy the Courant criterion,

$$c\Delta t < \frac{1}{\sqrt{\frac{1}{\Delta x^2} + \frac{1}{\Delta y^2} + \frac{1}{\Delta z^2}}} \qquad \textbf{EQ 3.1}$$

The electric and magnetic field components are calculated at each time-step and at each grid point using a leapfrog method. This is done by calculating the electric fields at one instance of time and then calculating the magnetic fields half a time-step later. Another half time-step later, the electric fields are calculated again and this process is then iterated over the whole simulation run-time.

In order to investigate plasma systems or beam dynamics, particles must also be considered in the computational codes. As the electric and magnetic field components are determined across an array of grid nodes, the charged particles in the system are moved according to the Lorentz force equation and the relativistic equations of motion. These particles are tracked through the system irrespective of the grid nodes giving rise to the name particle-in-cell (PiC). Quantities such as charge density and current are calculated and are fed back for use in the calculation of the electric and magnetic field components at the grid nodes.

As modelling all the particles in even a typical tenuous plasma would be computationally expensive, the concept of macro-particles is introduced. A macro-particle is a larger effective particle that approximates the mass and charge of a combined number of particles of a given species defined by the code. The fewer particles that make up the macro-particle, the more accurate the system becomes therefore there is a trade-off between accuracy and computational speed to be considered. Normally a minimum of 3 macro-particles (per species) to one grid cell is desirable to have a low numerical noise floor.

3.2 xOOPIC numerical code

The PiC code used predominately in this work is the freely available xOOPIC written in C++ and developed by the University of Berkley [Verboncoeur, 1995]. This code implements the finite difference method over 2.5-dimensions (2-dimensions in space and 3-dimensions in phase-space) and can be run using either a Cartesian coordinate system or a cylindrical coordinate system.

xOOPIC is a parallelisable code and for this work has been compiled and configured to run on up to 96 threads split between four Linux-based machines. This parallelisation functions by splitting the defined grid point array and macro-particles axially between each of the computational threads. Each thread then calculates the field components and particle positions and velocities independently within its own computational zone. To maintain cohesion across the system, shared boundaries are setup where the grid point array is split, and the code then makes use of the standardised message passing interface (MPI) to transfer the calculated boundary fields and the data of the macro-particles that traverse the shared boundaries between the adjacent computational zones. xOOPIC can only divide the computational mesh in one spatial dimension, a scheme which is well suited to problems which are long in that dimension.

For this work, three simulation boundary conditions were utilised. The first is a simple conducting boundary which assumes a perfect conductor and therefore sets tangential electric field component to zero and absorbs particles that impact upon it (without secondary emission). The second is the symmetry boundary which maintains Maxwell's equations for cylindrical systems and allows particles to be retransmitted back into the system in line with cylindrical geometry. The final boundary is the output wave boundary. This boundary uses a surface impedance method to set the ratio of the tangential electric and magnetic field components to the impedance of the boundary medium. In all cases in this work, the boundary medium is free-space. While it is possible to inject waves in via this boundary this was not required, however using a

similar method the output ports were set at a fixed potential in some scenarios to mimic electrostatic confinement potentials.

Modifications to the xOOPIC source was necessary for some of the investigations performed in this work.

3.2.1 Injecting beams with required velocity distributions

xOOPIC as distributed does not provide the functionality to inject a particle beam with a user-defined velocity distribution. Therefore, in order to match the velocity distribution of the electron beam in the computational simulation of the laboratory AKR experiment, without simulating the full magnetic compression region, required the modification of the xOOPIC source.

Initial modification was required to allow the injection of a phase asynchronous gyrating beam at a fixed Larmor orbit, offset from the axis of the simulation system. Due to the cylindrical nature of the simulations this required conversion between the perpendicular velocity of the beam reference frame (i.e. the azimuthal velocity of the electron about its own guiding centre) to the radial and azimuthal velocities of the overall simulation reference frame (i.e. about the symmetry axis of the entire simulation volume). This can be achieved through the use of simple trigonometry.

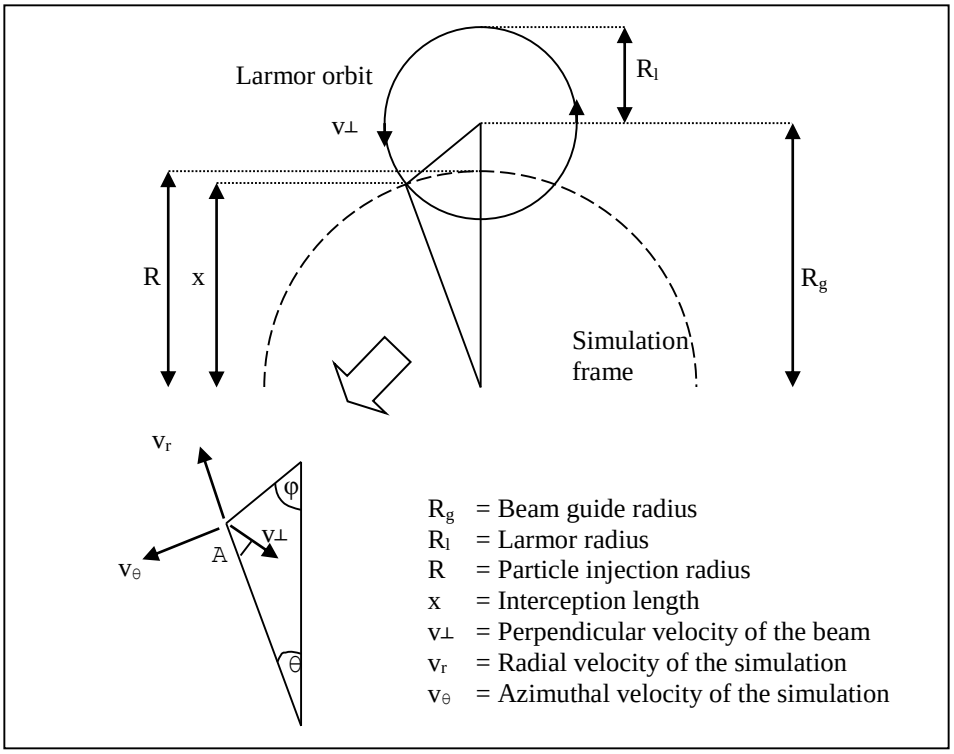

Figure 3.2 Conversion from beam-frame to cylindrical simulation frame

From Figure 3.2, it can be shown that for a known magnetic field, injected particle radial position, guiding centre radius and beam perpendicular momentum,

$$v_r = v_\perp \cos(A) \qquad \textbf{EQ 3.2}$$

$$v_\theta = v_\perp \sin(A) \qquad \textbf{EQ 3.3}$$

Where $A = \frac{\pi}{2} - \theta - \varphi$, $\theta = \cos^{-1}\left(\frac{x}{R}\right)$, $\phi = \cos^{-1}\left(\frac{R_g - x}{R_l}\right)$ and $x = \frac{R_g^2 - R_l^2 + R^2}{2R_g}$

With this conversion mechanism in place it is possible to apply any distribution to the injected particles pitch angle as once the perpendicular velocity is known; it can be converted as above. However, to apply a distribution function to each particle the corresponding random variate must be calculated.

Random variates are calculated based on the application of a probability density function to a uniform random sample. In xOOPIC there already exists a uniform pseudo-random number generator that is used for particle loading and a Gaussian variate generator for temperature distributions.

For a specific distribution function it is therefore necessary to code in the appropriate random variate generator. For this work, a gamma distribution function (illustrated in figure 3.3) was chosen as it allowed for a variety of different forms for the distribution (such as the Maxwell-Boltzmann distribution which exists as a special case of the Gamma distribution) to be produced by changing two constant values k and θ in the function,

$$F(x;k,\theta) = \frac{1}{\Gamma(k)\theta^k} x^{k-1} e^{-\frac{x}{\theta}} \qquad \textbf{EQ 3.4}$$

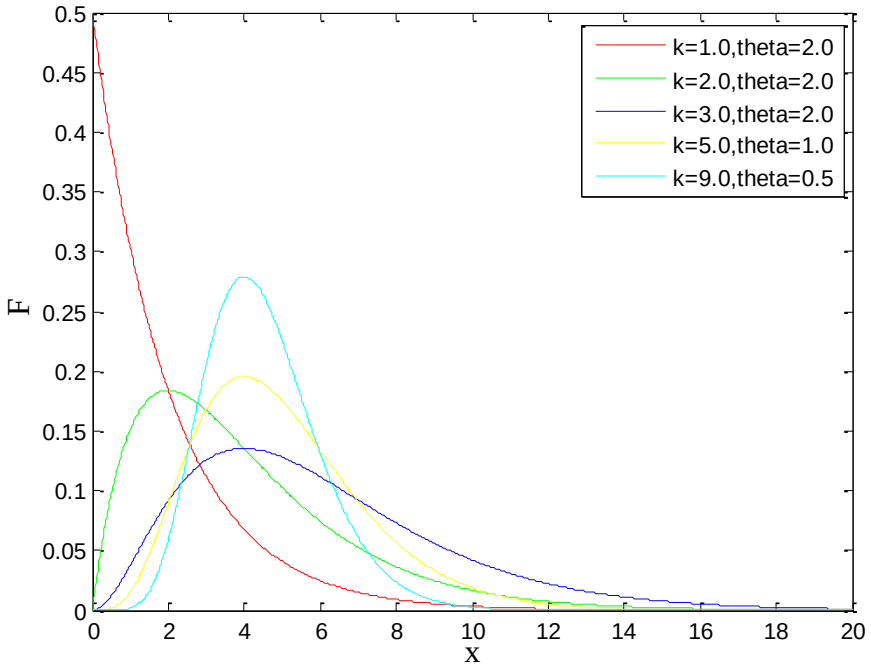

Figure 3.3 Gamma distribution function

Fast generation of this variate was implemented as laid out by [Marsaglia and Tsang, 2000].

3.2.2 Output diagnostics

The output from xOOPIC is produced via user-defined data dump-steps, defined as a fixed number of time-steps. However, at each dump-step all information within the system is output, including the fields at all grid points and macro-particle positions,

phase-velocities and charge. This makes the output data very large and difficult to analyse if the data-dump frequency is high. In order to observe temporal behaviour of the fields and the particle quantities it was necessary to build new diagnostic outputs into the code. To this end, a new diagnostic routine was introduced that would only output one single variable into its own dump file. This new feature allows the user to select specific variables to be output at a frequency independent of the simulation's overall data-dump rate.

An additional data output problem arises due to the parallelisation of the code. As the simulation is split up between the computational nodes, each node is independent of the others with the exception of the shared split boundaries. As a result, each node produces an output file for the variables only for the grid points that particular node is processing. As such, the output data needs to be collated into a single output file for future post-processing. This was achieved by writing a C++ program to combine all of the individual nodes output files at each dump-step.

3.3 Overview of xOOPIC Simulations

3.3.1 Simulations of laboratory experiments investigating AKR mechanisms

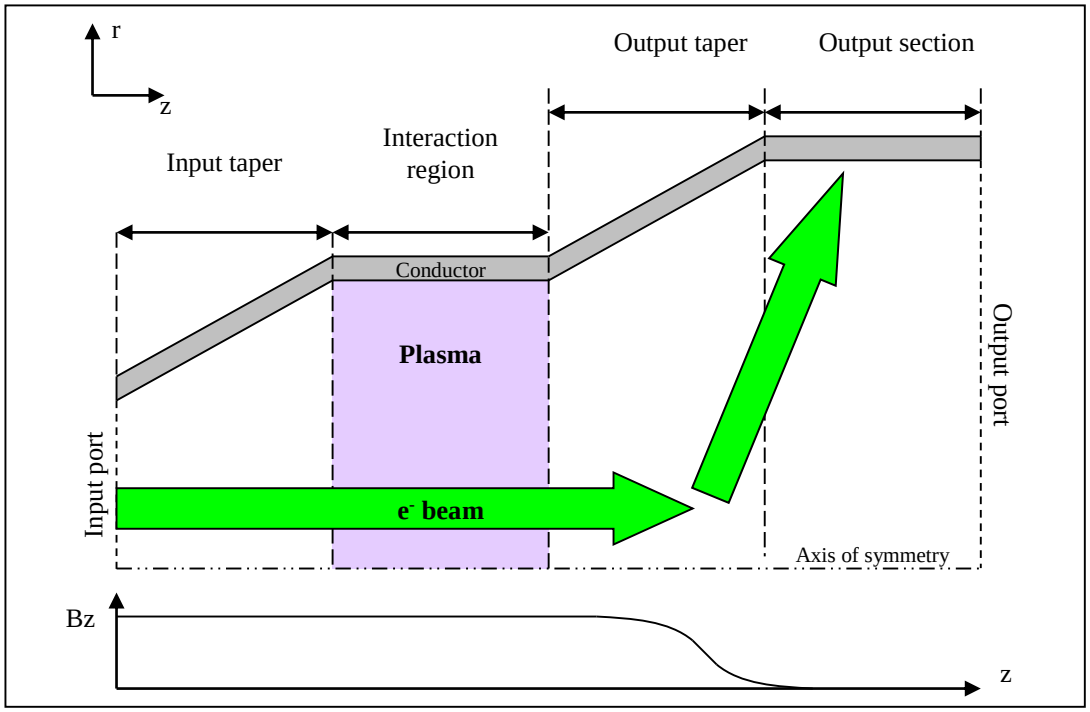

Figure 3.4 Schematic of AKR simulations

Numerical simulations have been constructed in xOOPIC to model the CRM behaviour seen in laboratory experiments conducted in [McConville, 2009]. To this end the simulation has been designed to model the laboratory experiment as closely as possible as shown in Figure 3.4. A uniform axial magnetic field is applied across the input taper and interaction region. This confines both the beam and plasma radially. At the output taper, the axial magnetic field is ramped down to prevent the electron beam from intercepting the output port. As B_z is ramped down, B_r is modified to ensure that $\nabla \cdot B = 0$. In the experiment, the electron beam velocity distribution is created via a long magnetic compression region. This region of the laboratory experiment has not been modelled, and an input taper has been included in the simulation to prevent backwards waves from reaching the electron beam injection region. The experiment also included a reflecting structure here which formed an electrode of the discharge used to produce the plasma.

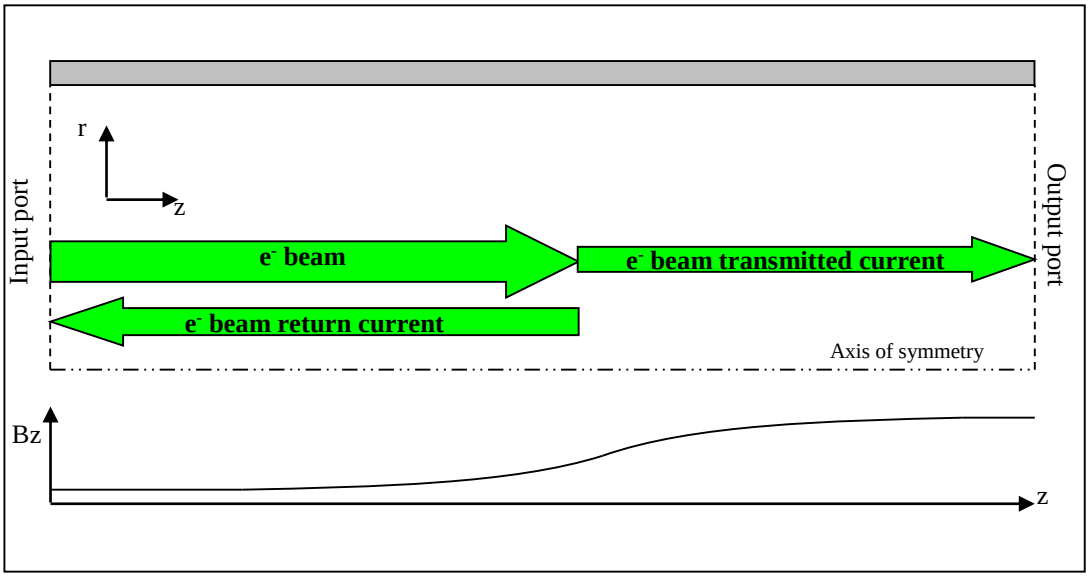

Figure 3.5 Schematic of magnetic mirror simulation

Prior to undertaking the CRM simulation described in the preceding section, it was necessary to test and optimise the electron beam that would be injected with a user defined velocity distribution. This distribution was matched to the experimental electron beam velocity distribution as it enters the interaction region. To achieve this, a secondary simulation was designed to determine the transmission of the simulated electron beam through a magnetic mirror and compare it to that of the experimental measurements.

This secondary simulation consists simply of injecting the electron beam with the selected velocity distribution into a straight cylindrical waveguide with an axially increasing magnetic field, see Figure 3.5. Experimental measurements of the transmitted beam current have been recorded with varying amplitudes of maximum magnetic field in the interaction region. Applying a profiled magnetic field in the simulation, rising from the resonant magnetic field to the same maximum magnetic field amplitude as in the experiment, allowed the velocity distribution of the simulated beam to be optimised to provide as close a match as possible to the experimental beam.

3.3.2 Two-stream/Beam-plasma simulations

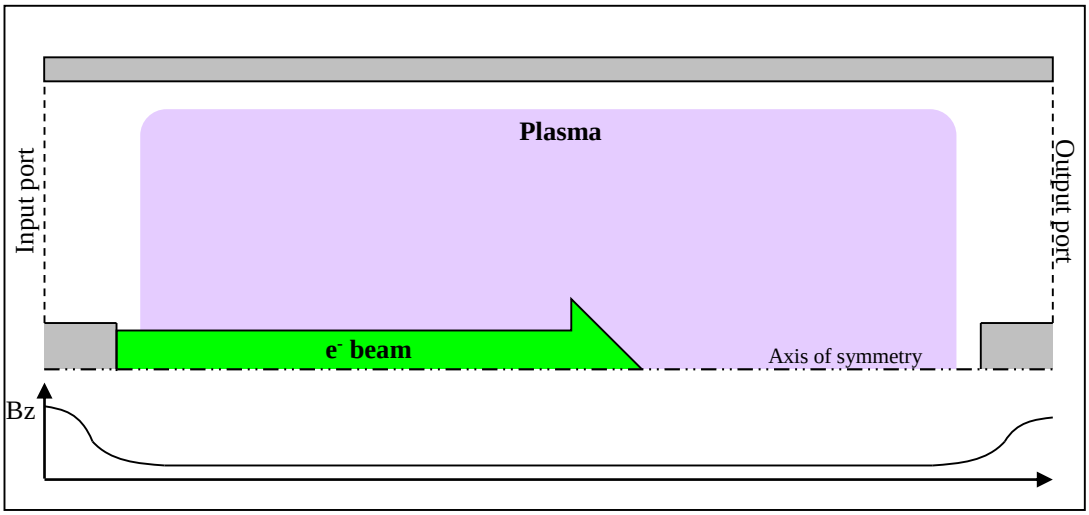

Figure 3.6 Schematic of magnetically confined two-stream simulation

In order to investigate the non-linear behaviour that occurs during a beam-plasma interaction, simulations have been created that can be duplicated in a laboratory experiment. These simulations consist of an electron beam, injected from a perfectly conducting surface propagating through a confined plasma column. A secondary conducting surface is also in place to intercept the beam and prevent it interacting with the computational exit port. To confine the plasma radially, an axial magnetic field is applied over the plasma column but to confine the plasma axially, two schemes have been investigated numerically. The first, shown in Figure 3.6, is a magnetic bottle arrangement that relies purely on the applied magnetic field. At both exit ports of the simulation, the axial magnetic field is ramped up to a higher level than the plateau field over the plasma column. As the axial field rises, approaching particles are mirrored back into the plasma column.

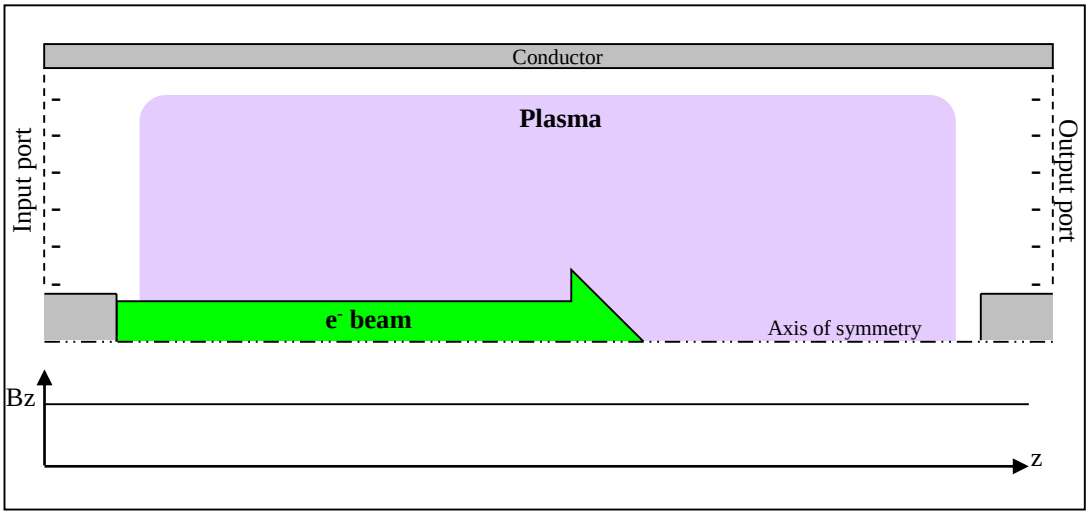

Figure 3.7 Schematic of electro-statically confined two-stream simulation

In the second scheme, shown in Figure 3.7, a constant negative electric potential is applied to the exit ports while the axial magnetic field is uniform across the whole simulation. This negative potential repels the negatively charged electrons back into the plasma column, the space-charge effects of which attract the positive ions keeping the plasma confined. This scheme is similar in style to the Penning discharge that would be utilised in the laboratory experiment. For all of the beam-plasma simulations, each particle species was initialised with 108 macro-particles per cell.

3.4 MAGIC simulation overview

A second finite-difference PiC code was used for this project known as MAGIC. This code is commercially available and has been designed primarily to model vacuum electronic devices. For this work, this particular code was used to design and simulate the electron emitter that would be used in the laboratory experiment. Like xOOPIC, this code is 2.5-dimensional but also has full 3-dimensional capabilities. However, unlike xOOPIC, it is not easily parallelisable which makes plasma simulations with a large amount of macro-particles highly time consuming. The boundary conditions in MAGIC are similar to xOOPIC but the output port boundaries operate based on a matched phase-velocity scheme [Ludeking and Woods, 2010]. The advantage of this code is that it has a variety of inbuilt electron emission models and magnetic field input

and creation features that make it ideal for the design of vacuum electronic components.

3.4.1 Electron generation and propagation simulation

For the laboratory experiment, a means to generate a laminar, rectilinear electron beam, similar to the one used in the two-stream instability simulations, was required. To this end, numerical simulations in MAGIC were undertaken in order to design the components necessary for such a device.

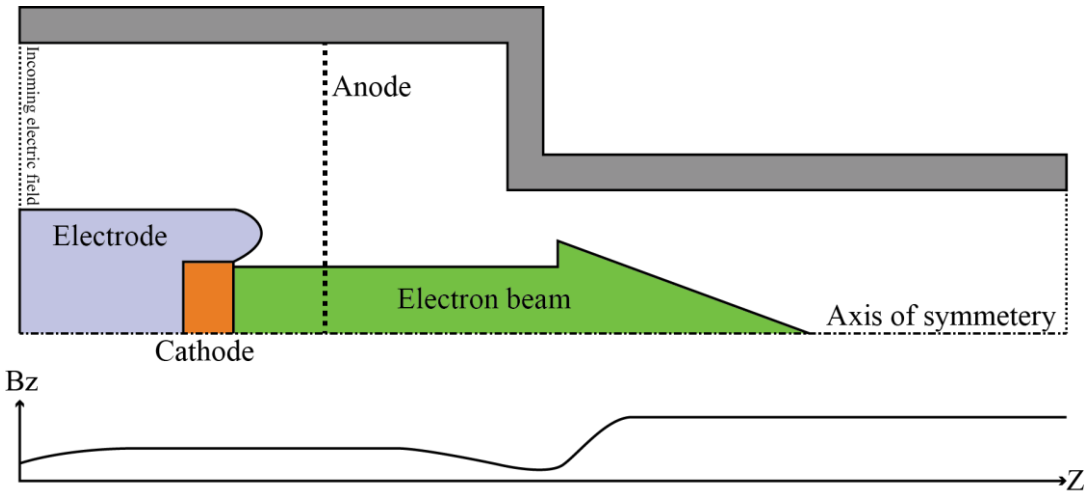

Figure 3.8 Schematic of the electron generation simulation

Figure 3.8 shows the schematic of the numerical simulation created in MAGIC. The cathode utilises a simple, inbuilt explosive emission model that simulates the electron emission from the cathode surface. This model does not contain the complexities of a realistic explosive emission, instead when the electric field on a region of the cathode surface (pre-defined as the emitter surface) reaches a critical level (~30kV/cm), that region will begin to emit electrons continuously, even if the field subsequently drops below the critical level. As MAGIC does not support applying fixed voltages to conducting surfaces, in order to produce the electric field between the cathode and anode, an electric field is injected as a TEM wave along the coaxial line from behind

the cathode from a free-space boundary. This creates the necessary electric field to start to produce and accelerate the electrons.

The magnetic field profile was determined theoretically from an analytical model of the magnet solenoids, benchmarked against measurements with a Hall probe. This field was then recreated using MAGICs own magnetic field coil algorithms. The spacing between the two magnet coils creates a depression in the axial magnetic field, which may lead to unwanted effects in the electron beam, such as mirroring or scalloping. By modifying the shape of the electrode and adjusting the anode-cathode gap spacing, it is possible to compensate for this dip in magnetic field and simulate the production an electron beam with a similar current and beam diameter to that which was used in the two-stream numerical simulations.

3.5 Post-processing

In order to analyse the raw data output from xOOPIC and MAGIC, it was sometimes necessary to write a variety of MATLAB scripts to process the data.

- **Animations**
  Scripts were made to take each combined output dump and produce image frames that were used to generate an animation file for the corresponding output variable.
- **Fourier analysis**
  As each output variable is saved across all of the grid points of the entire simulation and output at regular time intervals, it was possible to write automated scripts to perform both spatial and temporal Fourier analysis on the output data. This enables the visualisation of the variation of the spectrum of the system across space and similarly any change in the spatial structures with time.

- **Temporal evolution**

  In addition to animations, scripts were written to analyse the temporal evolution of plasma and field structures, either at a point in the simulation or across a line through the simulation.

- **Histograms**

  Scripts had to be written to generate histograms of macro-particle information, such as velocity, temperature etc. In addition, scripts were made to create animated histograms over time or space.

Chapter 4 : Numerical results

4 Numerical results

4.1 Simulation of plasma mediated cyclotron instabilities

Experiments have been undertaken at the University of Strathclyde [McConville, et al., 2008] where an electron beam has been formed into a horseshoe distribution in electron velocity space by adiabatic magnetic compression. The cyclotron maser emissions from this electron beam have been studied to aid in the understanding of the mechanism of Auroral Kilometric Radiation [Gurnett and Green, 1978; Delory, et al., 1998; Ergun, et al., 2000; Bingham and Cairns, 2000; 2002]. These prior experiments were used to test the predictions of numerical simulation tools which may be used to simulate cyclotron wave emission in the environments similar to the magnetosphere [Ronald, et al., 2011; Bingham, el al., 2013]. Three dimensional ray-tracing has also been used to model the mechanism and the radiation propagation, feedback and escape processes with a ring-like distribution of electrons [Burinskaya, 2013]. A recent addition to these experiments, to more realistically reproduce the magnetospheric environment was the introduction of a background plasma. This work therefore focused on extending the numerical models to consider the impact of this background plasma on the evolution of the CRM instability (which was seen in the experiment to be rather substantial). This demanded a parallel PiC code as the serial codes used to model the electron beam-wave interaction were insufficient to address the complex problem when the plasma was added to the system. In many ways the 2D PiC code xOOPIC is well suited to this task, however it was not capable of injecting gyrating electron beams as distributed. As indicated in section 3.2.1, a scheme was devised which allowed such beams to be injected into the system, and new software routines were introduced to the xOOPIC source code to enable this. Sections 4.1.1-4.1.2 demonstrates the functionality of these new routines incorporated into the xOOPIC source. Section 4.1.3 shows the matching and optimisation of the numerical electron beam distribution to the experimentally measured distribution by means of magnetic compression simulations. Finally, section 4.14 presents the results obtained from the numerical modelling of the auroral radio wave simulation experiments.

4.1.1 Gyro-orbit beam injection/Gyrotron test

To test the electron beam injection routines added to the xOOPIC source code, it was first necessary to ensure that the code was correctly injecting a simple arbitrary gyrating electron beam at a set gyro-orbit. As this was a test of beam behaviour, the simulation size was set to a short section 3cm in length and 2cm in radius. The beam was injected from a conducting boundary using the set of parameters given in table 4.1,

Current	60A		Confining B-field	0.4T
Voltage	75kV		Beam guide radius	0.07m
Beam α	1.0		Current rise time	4ns

Table 4.1 Simulation parameters for gyro-beam test

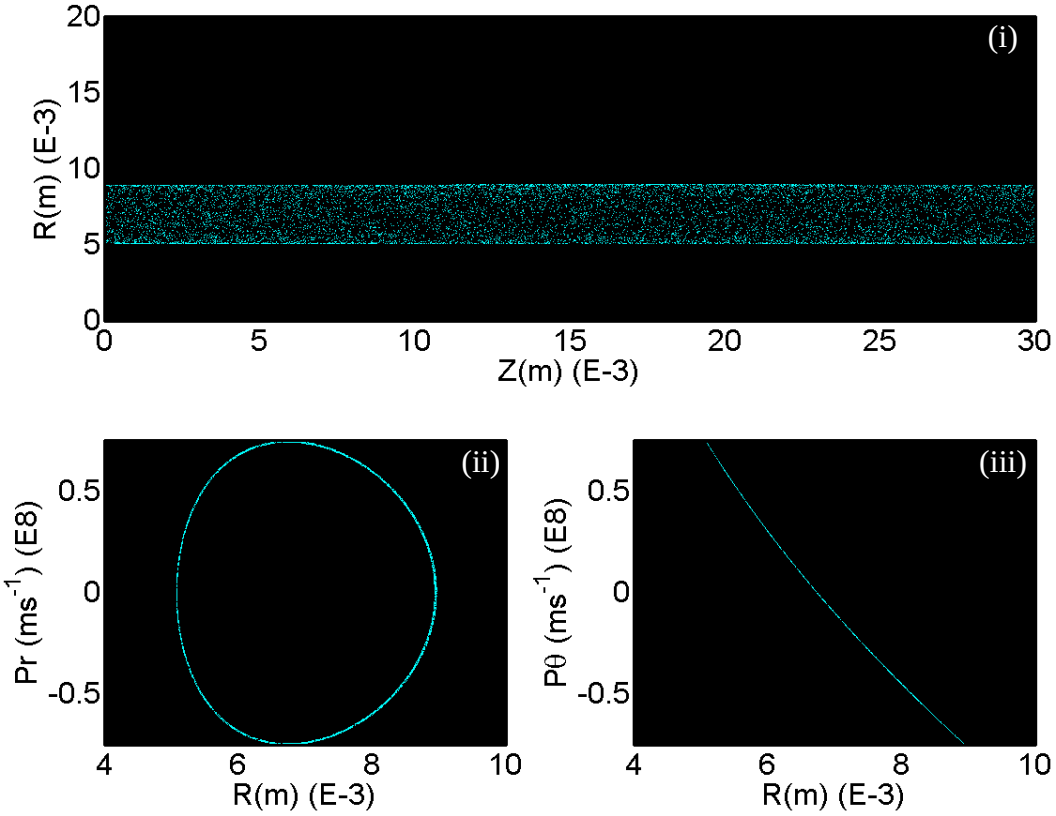

Figure 4.1 Gyrating beam generated by xOOPIC (i) Z-R space (ii) Pr-R space (iii) Pθ-R space

Figure 4.1 shows the gyrating beam that is produced by the newly created routines in xOOPIC. The radial and azimuthal velocity components that are generated can be compared directly to that of a gyro beam produced in a different 2D code (MAGIC) with the same parameters, shown in figure 4.2. This code has inbuilt functionality that allows the generation of gyrating particle beams and was therefore used as a control for the new routine. MAGIC 2D is not capable of parallel execution and therefore was not suitable for the complex plasma calculations required.

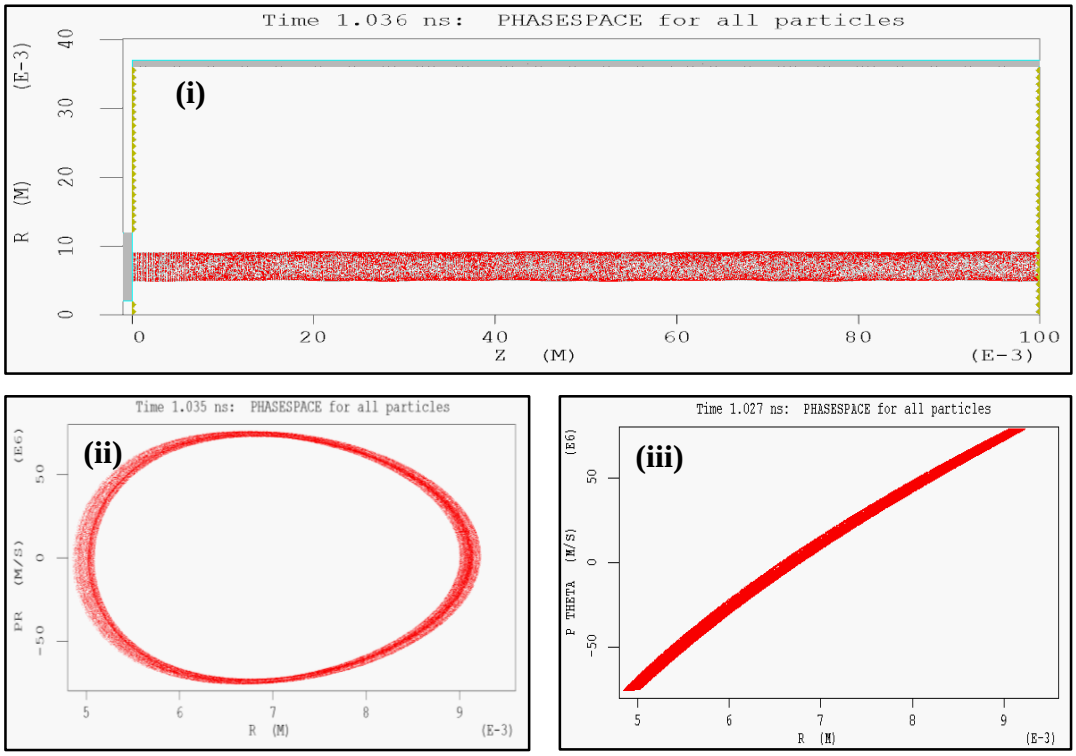

Figure 4.2 Gyrating beam generated by MAGIC (i) Z-R space (ii) Pr-R space (iii) Pθ-R space

As can be seen, the particle injection routines added to xOOPIC creates very similar particle trajectories to those generated by MAGIC for matched input parameters. The azimuthal component from the MAGIC simulation is in the alternate direction as the axial magnetic field and gyration direction were inverted. However, the values for both the radial and azimuthal velocities are a close match. Note that in both codes the azimuthal and radial components of the velocity are determined relative to the simulation axis of symmetry. This leads to a visual distortion in the beam momentum plots. If the radial and azimuthal components were relative to the beam gyro-centre,

figures 4.1(ii) and 4.2(ii) would be perfectly circular while figures 4.1(iii) and 4.2(iii) would be a straight line.

To further test the growth of the cyclotron instabilities excited by the gyrating electron beam in the xOOPIC code, a simulation of a simple non-optimised gyrotron was run in MAGIC and was then recreated in xOOPIC. The simulations output power is broadly consistent with this type of device, and MAGIC is known to provide a reasonable simulation of these systems. Shown in figure 4.3 below is the comparison between the predicted output power from each of the codes.

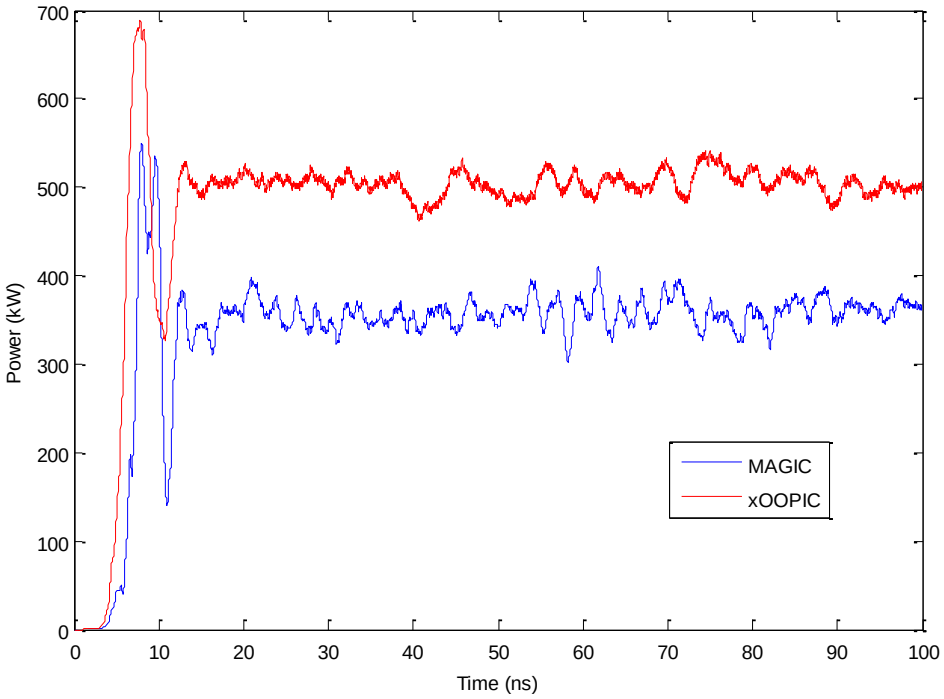

Figure 4.3 Simple non-optimised gyrotron output power

It is interesting to note that the switch on dynamics predicted by the two codes is quite consistent. The difference between the output power predicted by the two codes is approximately 30%. This disparity may be due to the differences in the meshing algorithms used between the codes. This may lead to slight differences in the cut-off frequency of the resonant cavity, and hence to slightly different cyclotron detuning (the difference between the wave frequency and the cyclotron frequency). To show

this, the generated frequency between the codes was also compared. Figure 4.4 shows the frequency of the azimuthal electric field predicted from both the MAGIC and xOOPIC simulations.

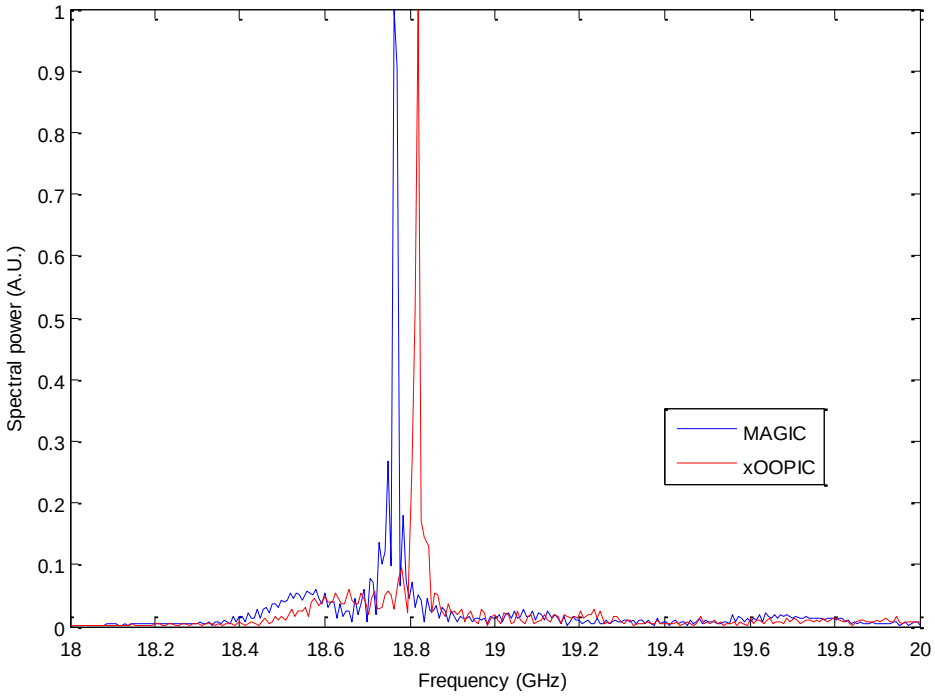

Figure 4.4 Simple non-optimised gyrotron output frequency

As can be seen, there is a small frequency difference between the predictions of the two codes. Given the sensitivity of gyrotron operation to the shift between the waveguide cut-off frequency and the cyclotron frequency, this small shift in frequency may move the MAGIC simulation further from the optimal magnetic field for that frequency. With detailed optimisation of the mesh it may be possible to decrease the power and frequency disparity however, the similarity in the overall growth and saturation of the CRM instability in the two codes provided satisfactory confidence.

Benchmarking the specially written particle injection subroutines written for the parallelisable xOOPiC package against a known stable (though serial) PiC code with inbuilt gyro-injection algorithms, which have been used previously to design experimental apparatus, gives confidence in the use of the custom algorithms added to

xOOPIC. This will allow these algorithms to be used to simulate the CRM instability in the complex electron beams and plasmas used in the experiments reported by McConville [McConville, et al., 2008; McConville, 2009].

4.1.2 Horse-shoe beam injection

As the previous benchmark showed, the gyro-beam injection code is correctly generating gyrating realistic electron beams. Tests were then carried out on the injection of a beam with the horse-shoe like distribution function that would be created using the gamma function (as shown in section 3.2.1) to describe the electron distribution in pitch angle, $\arctan(v_{\perp}/v_z)$. To begin with, a test beam with its current and energy selected to match experimental values, was again propagated along a simulation of length 3cm and radius 2cm with the parameters given in table 4.2.

Current	60A		Confining B-field	0.21T
Voltage	75kV		Beam guide radius	0.07m
Gamma fn k value	3		Current rise time	4ns
Gamma fn θ value	4			

Table 4.2 Simulation parameters for beam gamma function distribution tests

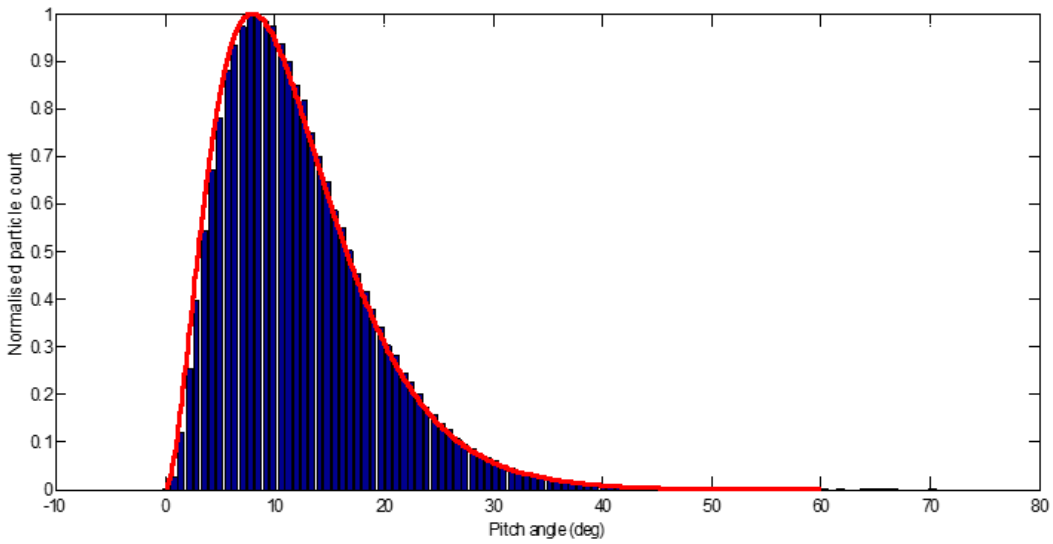

Figure 4.5 Particle pitch angle distribution of a horseshoe beam generated by xOOPIC at the point of injection

Shown in figure 4.5 is a histogram of the distribution of the beam particles in pitch angle produced by the simulation at the instant of injection normalised to the maximum particle bin count in the system at the time of injection. The overlaid red line is the analytical function (subject to the same normalisation) of the gamma distribution used to define the electron beam. From this it can be seen that there is good agreement between the analytic function and the distribution produced by the simulations showing that the code is injecting the beam requested.

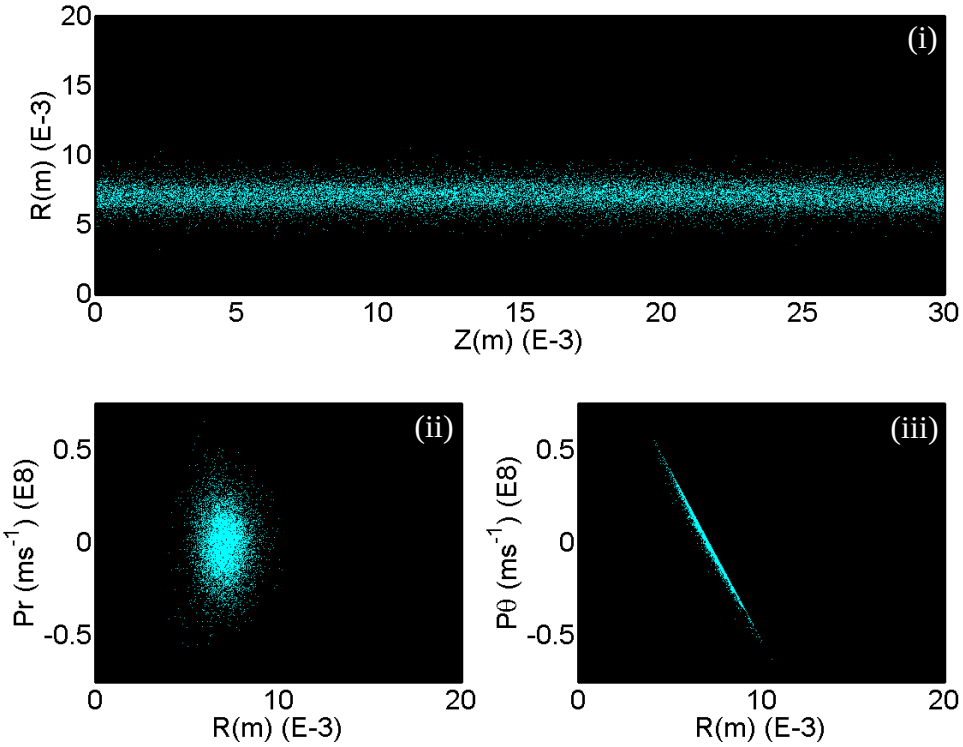

Figure 4.6 Horseshoe beam generated by xOOPIC (i) Z-R space (ii) Pr-R space (iii) Pθ-R space

The plots shown in Figure 4.6 show the properties of the beam propagating after 5ns. At this time, the beam has reached its full current along the entire axial extent of the beam, meaning essentially that the highest pitch angle particles have had time to propagate along the length of the simulation. Further from figure 4.7, it can be seen that injecting with a gamma distribution, with these configuration parameters, yields a beam with a horseshoe-like distribution in axial and perpendicular momentum.

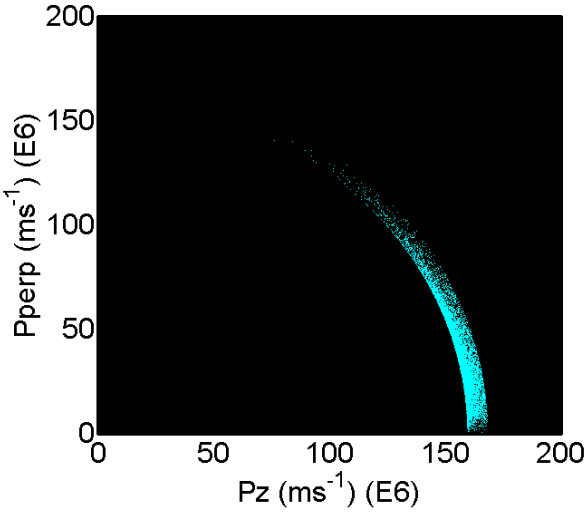

Figure 4.7 Horseshoe distribution of Pz vs P⊥

Figure 4.8 shows a histogram of the beams particle density against pitch angle after 5 ns again normalised to the maximum particle bin count in the system at 5 ns. What this shows is that the differing axial and perpendicular velocities can slightly skew the distribution filling a finite volume away from the pre-defined configuration as the beam propagates. This arises essentially because it takes longer for the high pitch particles to traverse the system, hence their population density becomes slightly higher.

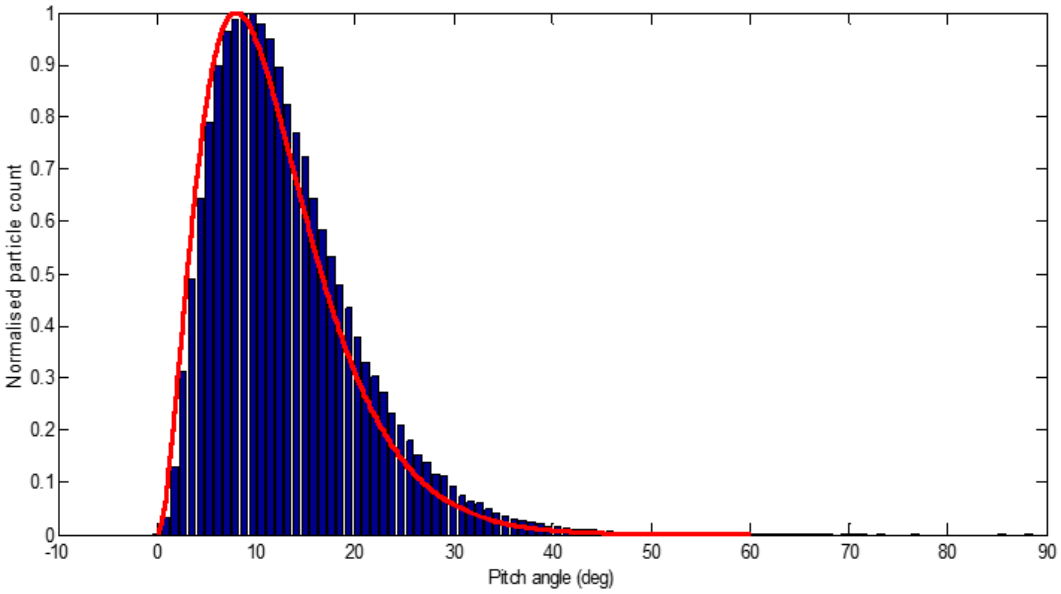

Figure 4.8 Particle pitch angle distribution of a horseshoe beam generated by xOOPIC after 5 ns

4.1.3 Magnetic compression tests

Given that the beam is being defined with a mathematical function, to ensure maximum comparability between the simulations and experimental measurements of the radiation excitation induced by the beam, it is appropriate find a method to match the numerical beam distribution to the measured electron beam. It is possible to attempt to match the beam distribution to the experimental setup by optimising the distribution to give the same magnetic mirroring behaviour seen in the experimental measurements (see section 3.3.1).

Figure 4.9 shows the beam behaviour and axial magnetic field profile of a typical magnetic mirror simulation. The electron beam is injected into a static B-field with a magnitude of ~0.21T, comparable with the experiments resonant plateau field. The magnitude of the axial B-field is increased progressively along z (modifying the radial magnetic field to ensure that $\underline{\nabla} \cdot \underline{B} = 0$ from Maxwell's second equation) to a higher value. As the beam, with the gamma pitch angle distribution, propagates into the area of increasing axial magnetic field, the beam follows the magnetic field lines and compresses radially. Any particles with a perpendicular velocity component start to convert axial velocity to perpendicular velocity, due to the conservation of the magnetic moment. If a particle loses all of its axial velocity, magnetic mirroring will occur and the particle will begin to propagate back towards the injection point. The non-mirrored particles continue to propagate forward and this transmitted current of the beam can be measured once the system has reached a steady state (example shown in figure 4.10) and compared to the experimental current measurements. This is analogous to the method used in the experiment to map the electron distribution function in pitch angle. Note that in the simulations the axial magnetic field is aligned in the negative z-direction.

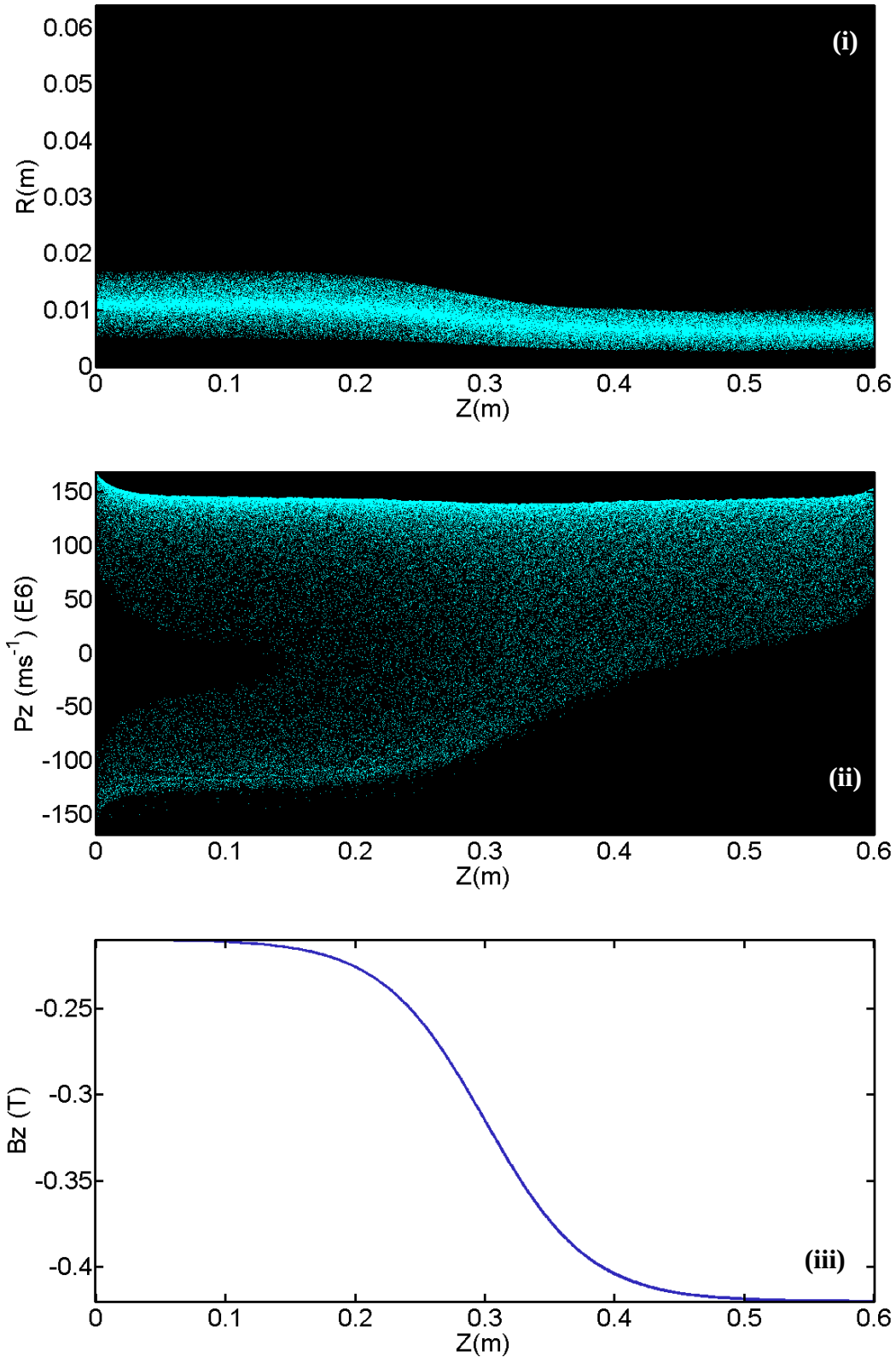

Figure 4.9 Example beam behaviour during a magnetic mirror simulation Z-R (ii) Pz-Z (iii) Axial magnetic field profile

The experimental current measurements were made at a number of maximum plateau magnetic fields and for multiple different cathode magnetic field strengths induced by the currents flowing in the insulating magnet coils. These results are shown in figure 4.11. Each of the beams yielded by these different cathode magnetic fields were modelled in the xOOPIC magnetic mirror simulations. To do this, different distribution parameters were selected and optimised for each experimental beam. As the xOOPIC simulations would not be modelling the magnetic compression region of the AKR experiment, the beam would be injected at the magnetic field corresponding to the cyclotron resonance condition. Therefore, for these magnetic mirror simulations, the magnetic mirror ratio was calculated from the resonant magnetic field.

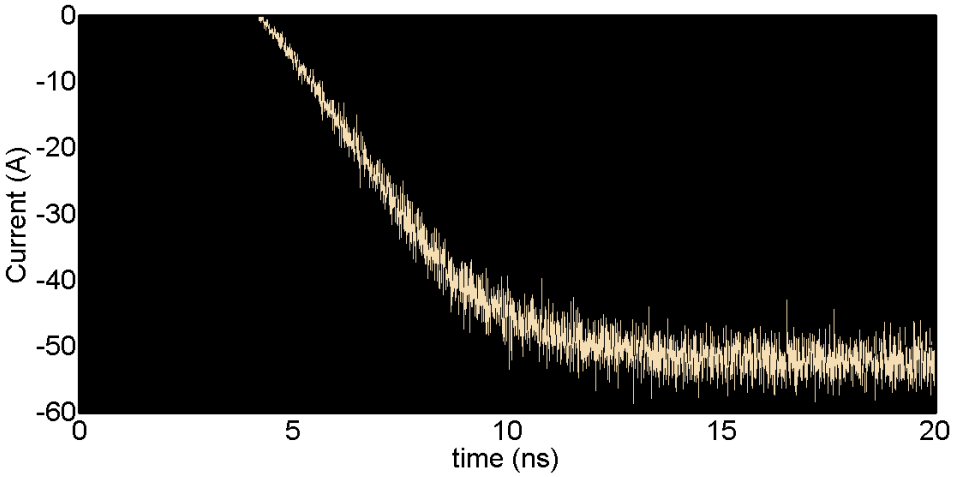

Figure 4.10 Example transmitted current in magnetic mirror simulation

It was discovered, unsurprisingly, that as the magnetic field in the electron emitter was changed in the experiment a different pitch angle distribution was required in the simulations. Table 4.3 shows the optimised parameters for the gamma pitch angle distribution:

Experimental cathode B-field	xOOPIC injection current	Gamma k value	Gamma θ value
0.01T	11A	2	32
0.02T	35A	2	20
0.063T	60A	1.5	12

Table 4.3 Optimised beam distribution parameters for different experimental cathode currents

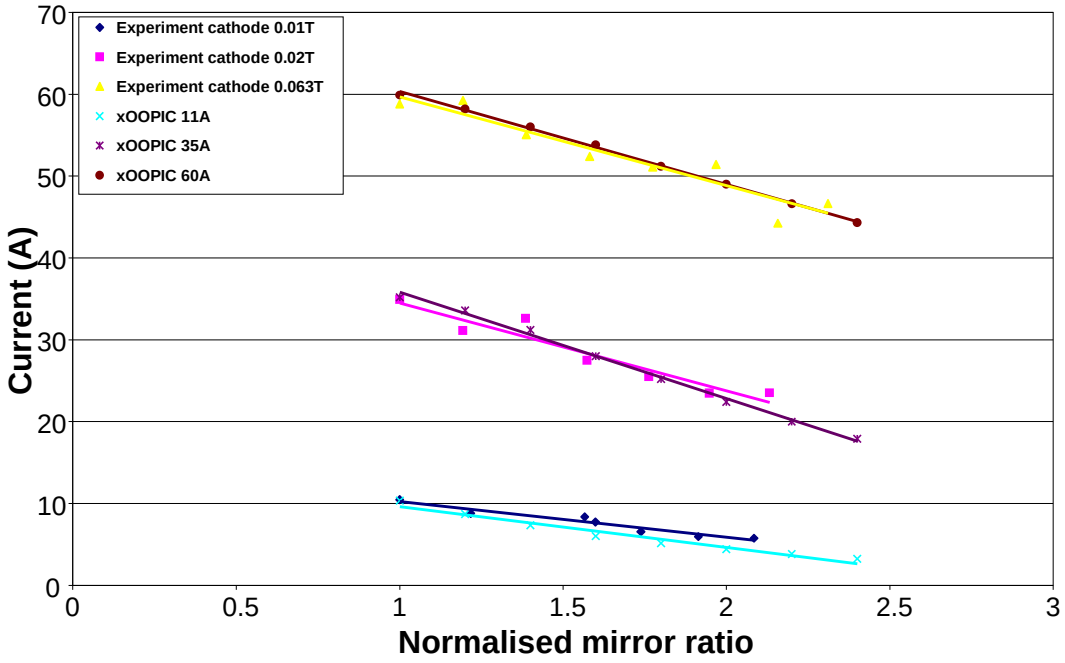

Figure 4.11 Experimental magnetic mirror results for different cathode magnetic fields [McConville, 2009] compared with optimised xOOPIC magnetic mirror simulation results

The experimental data shown in figure 4.11 was conducted in a previous work [McConville, 2009]. It was obtained by injecting an annular electron beam into a magnetic compression region in order to form the necessary horseshoe distribution. The magnetic field is increased from the electron emitter region to the plateau magnetic field in the interaction region. The plateau field was adjusted and the transmitted beam current was measured with a Faraday cup. As the magnetic field is increased, more electrons with perpendicular momentum will be reflected due to the magnetic mirror effect, just as in the simulations. The transmitted current data was initially recorded against the ratio of the magnetic field at the electron beam emitter and the plateau magnetic field.

The simulation does not model the experiments primary magnetic compression region (between the electron emitter and the plateau field in the solenoid) and the pitch angle distribution has been configured for a specific magnetic field (0.21T). The initial magnetic field in the magnetic mirror simulation is always set to this value and the maximum field is varied downstream. Therefore to compare both experimental and

simulation results, the maximum experimental field is re-normalised to this plateau magnetic field for the x-axis of figure 4.11.

Three different beam currents were optimised and are plotted in figure 4.11, however only the beams produced with cathode magnetic fields of 0.02T and 0.063T were used further. As can be seen, the optimisation of the velocity distribution resulted in reasonably good agreement at all beam currents.

4.1.4 Experimental AKR simulation

The optimised beam distributions, were injected into a numerical representation of the laboratory experiments interaction region. In each case, the beam is injected through a short taper section to allow the beam to stabilise after injection and prevent backward wave propagation. This can be important in preventing the electron beam being subject to non-physical modulation at the injection point if electromagnetic waves can exist at this artificial region. The beam then enters the resonant cavity where the beam's cyclotron frequency is approximately the same as the cut-off of the waveguide TE_{01} mode. Resonance between the beam's cyclotron oscillations and the electromagnetic oscillations of the cavity mode allow the growth of the CRM instability. There is then another tapered section into the output waveguide where the beam is dissipated on the wall due to the decrease in axial magnetic field. Shown in figure 4.12 is an example of the beam behaviour at times before (20ns) and after (340ns) the CRM instability has grown to saturation. The azimuthal bunching and energy modulation due to the CRM instability can be seen in the trajectories shown in the latter case but not in the former. Figures 4.13 and 4.14 show the corresponding temporal evolution of the output signal and spectral content of the radiation.

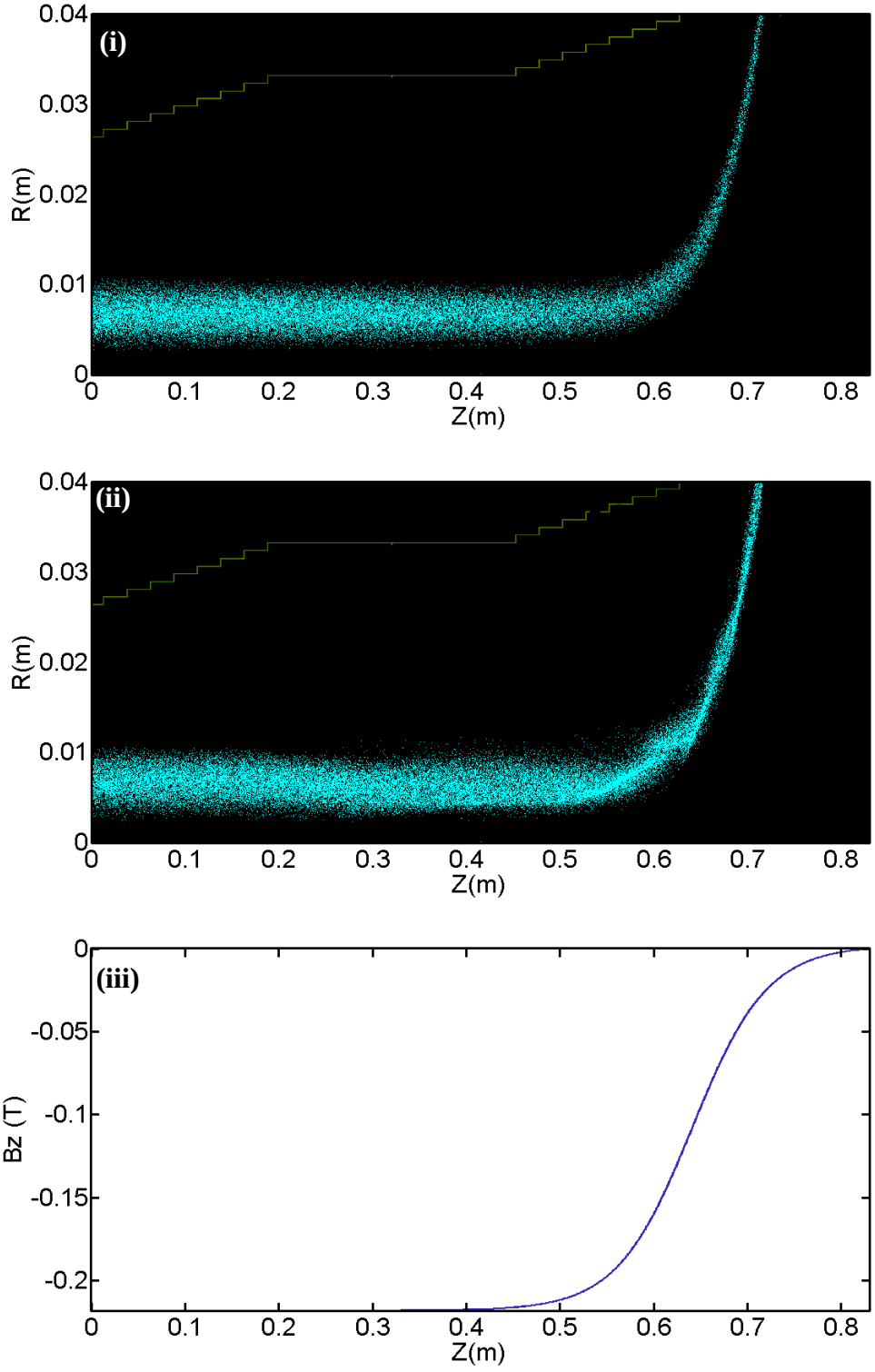

Figure 4.12 35A beam current AKR simulation Z-R plots (i) 20ns (ii) 340ns (iii) Axial magnetic field profile

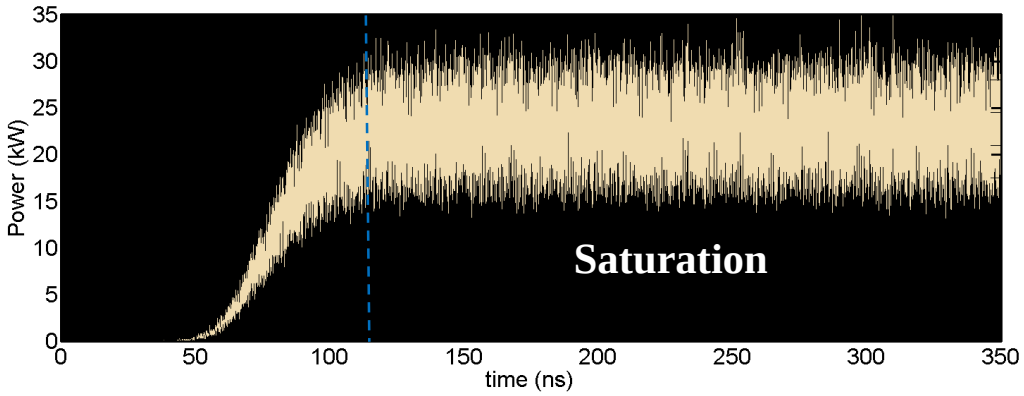

Figure 4.13 Output power predicted a for 35A beam in the AKR simulation

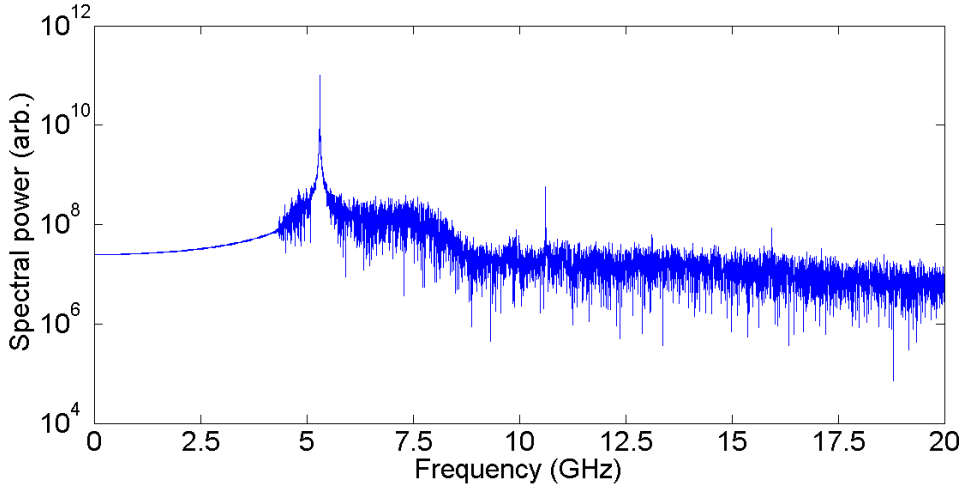

Figure 4.14 Output frequency predicted for a 35A beam in the AKR simulation

Figure 4.13 shows that after ~110ns, the energy being extracted from the electron beam is approaching saturation and subsequently produces near constant output power. These results may be compared to the experimental performance which has shown that the frequency generated is typically around the relativistic cyclotron frequency (5.4GHz) with an efficiency of ~1.5%. Here the wave is shown to be generated at a frequency of 5.31GHz and an efficiency of ~1% when the system is optimally tuned (fine adjustment of the magnetic field). Kinetic modelling of the astrophysical case shows approximate wave efficiencies of a few percent [Kuznetsov and Vlasov, 2012]. By increasing the mesh resolution of the simulation there is negligible change in either the output frequency or the power giving confidence in the numerical robustness of the predictions of the simulations.

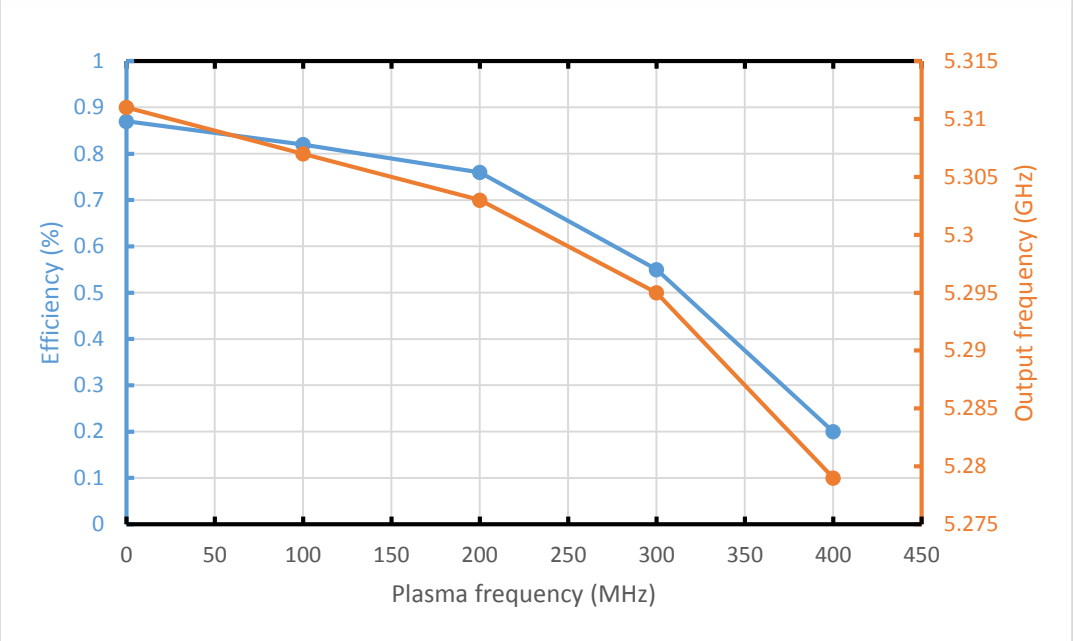

Figure 4.15 Output efficiency/frequency for the 60A beam current at varying background plasma frequencies

By running the simulation again for the higher current 60A beam, again the efficiency is predicted to be ~1% at 5.31GHz. This configuration of electron beam was used in the laboratory experiments to test the sensitivity of the instability to the presence of a background plasma. These experiments revealed that the plasma caused significant damping to the maximum wave production efficiency, falling from 1.5% to zero as the background plasma frequency was increased from 0Hz to 300MHz. While this is higher than the efficiency seen in the simulations, it is relevant to note that the experimental measurement of the output power is a complex process and subject to a degree of uncertainty. Therefore the simulations are deemed to be in reasonable agreement. Exploiting the parallel execution features of xOOPIC, it was possible to introduce a background plasma to investigate the efficiency decrease numerically. Figure 4.15 shows the output efficiency and output frequency as a function of the background plasma frequency. As the background plasma frequency is increased the efficiency of the predicted CRM instability decreases as expected from the theory [Cairns, et al., 2011], geophysical observations and the laboratory experimental results. As background ω_p approaches $\omega_{ce}/10$ the efficiency falls off very strongly. This simulation therefore provides good agreement with this aspect of the experimental results.

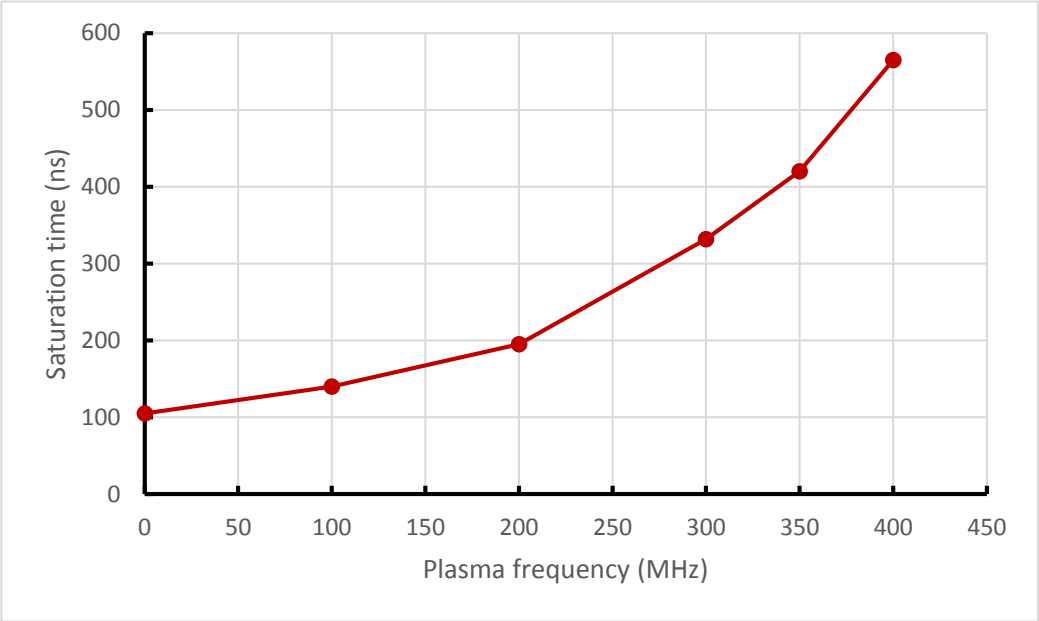

Figure 4.16 Saturation time of output power for a 60A beam current for varying background plasma frequencies

When operating with the background plasma present, the experiment showed statistical variability whereby there would be no output power detected when the electron beam was injected. No similar 'critical' or 'threshold' effects were seen in the simulations. It had been considered that the essential electron velocity distribution for driving the cyclotron instability was being affected by the near to threshold streaming instability, however these simulations provided no evidence of such an effect. Figure 4.16 shows the time that the simulations predict it would take for the CRM instability to become saturated and provide constant power output. As can be seen, as the background plasma frequency is increased, the time until saturation increases. It is possible that in the experimental setup, the instability growth rate may be having an effect as the duration of the electron beam pulse is finite (~100ns in the experiment). It has been observed that during the Penning discharge, the plasma column can operate in different spatial modes. This could result in variations in plasma density across the radial dimension of the trap. Therefore, during the transit of the electron beam, if the Penning trap has switched to a different mode, the electron beam may experience a temporarily higher or lower plasma frequency that could affect the instability growth. Ultimately this will require further work.

4.2 Two-stream simulations

4.2.1 Linear computational solutions

Following from the linear two-stream instability theory 2.5.1 it is possible to solve equation 2.74 computationally for differing plasma stream scenarios yielding their dispersion relations.

The dispersion relations shown in figure(s) 4.17 contain either four real solutions or two real solutions and two complex conjugate solutions. The solutions that are always real are shown in red while the blue and green curves correspond to solutions that switch between real and complex values, where the blue curve shows the real component and the green curve shows the imaginary. It is the imaginary component of the complex solutions that show the growth of the instability. Shown in table 4.4 below is a summary of the approximate growth rates predicted by the linear analysis for each of the two-stream scenarios.

Scenario	Maximum temporal growth rate	Wavenumber of maximum growth	Corresponding angular wave frequency
Co-propagating	$1.73 \times 10^{9} rads^{-1}$	$160 m^{-1}$	$1.5 \times 10^{10} rads^{-1}$
Counter-propagating	$1.5 \times 10^{9} rads^{-1}$	$22 m^{-1}$	$8 \times 10^{7} rads^{-1}$
Beam-plasma	$1.78 \times 10^{9} rads^{-1}$	$78 m^{-1}$	$7.7 \times 10^{9} rads^{-1}$

Table 4.4 Linear theory predictions of the two-stream growth rates

Co-propagating

ω_1=3.27x10^{9}rads^{-1}
ω_2=4.02x10^{9}rads^{-1}
u_1=1.11x10^{8}ms^{-1}
u_2=0.73x10^{8}ms^{-1}

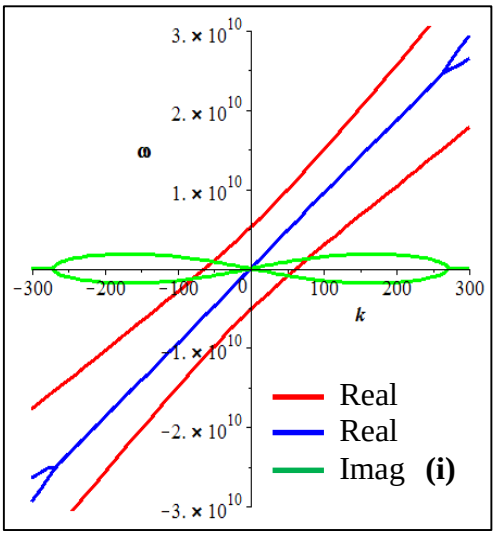

Counter-propagating

ω_1=3.14x10^{9}rads^{-1}
ω_2=3.14x10^{9}rads^{-1}
u_1=1.2x10^{8}ms^{-1}
u_2=-1.2x10^{8}ms^{-1}

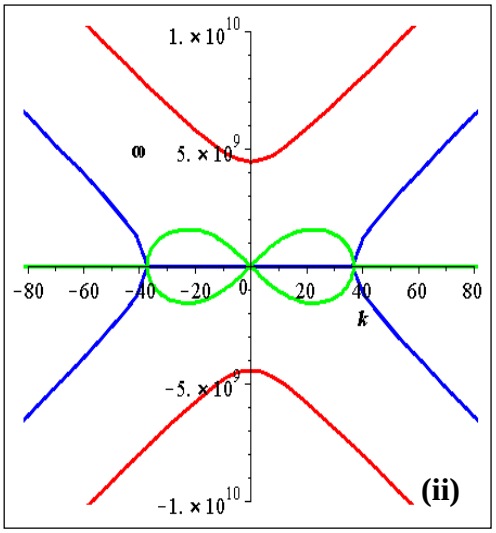

Beam-plasma

ω_1=1.8x10^{9}rads^{-1}
ω_2=8.73x10^{9}rads^{-1}
u_1=1.2x10^{8}ms^{-1}
u_2=0ms^{-1}

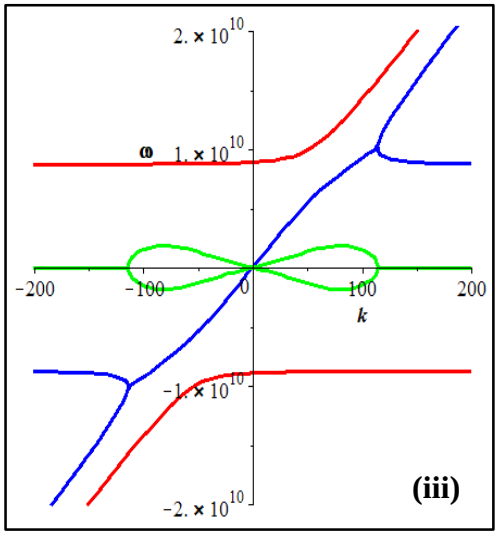

Figure 4.17 Linear theory two-stream dispersion relations (i) co-propagating beams (ii) counter propagating beams (iii) beam-plasma, here ω and u represent the plasma angular frequency and drift velocity of each component

4.2.2 Co-propagating two-beam simulation

While the two-stream instability growth has been investigated numerically in the past [Bret, Gremillet and Dieckmann, 2010], it was important to test the numerical code xOOPIC against the linear theory. The simple case of two spatially overlapped, co-propagating electron beams was used with the same parameters as the linear theory in table 4.4. This case allowed the growth of the two-stream instability to be observed without the complication of plasma confinement problems or neutralising ion populations. The two-beams are injected from the same conducting surface with a beam radius of 0.008m. The simulation is 1.2m long in the beam propagation direction and 0.03m in radius. The total simulation time is 20ns.

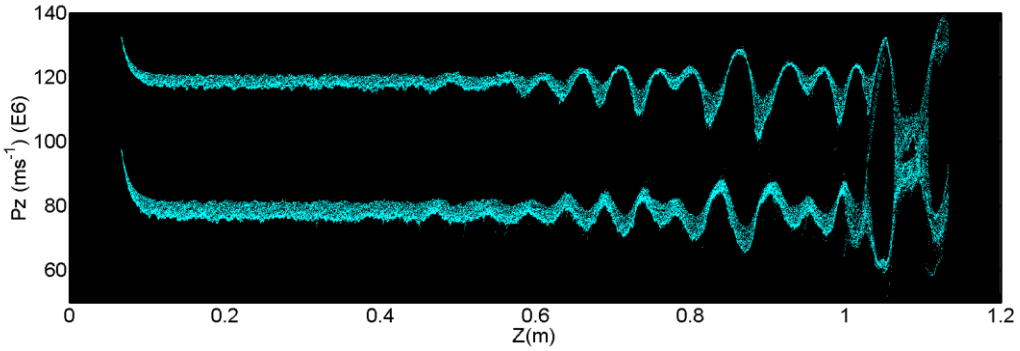

Figure 4.18 Axial momentum along beam propagation axis at 20ns

Figure 4.18 shows the axial momentum of the two co-propagating electron beams along the beam propagation axis after 20ns. As can be seen, there is substantial modulation of the axial momentum of each of the beams after they have propagated together over a distance of approximately 0.6m. Phase-mixing of the electron beam velocities can be seen at a position of approximately 1m.

To compare these numerical results to the linear theory the axial electric field must be analysed. A snapshot in time of this field at 10ns is shown in figure 4.19. The spatial oscillation of the axial electric field produced from the two-stream instability can be

seen clearly from 0.6m. To show the growth and spatial movement of this axial wave, the temporal behaviour of the axial electric field has been plotted in figure 4.20.

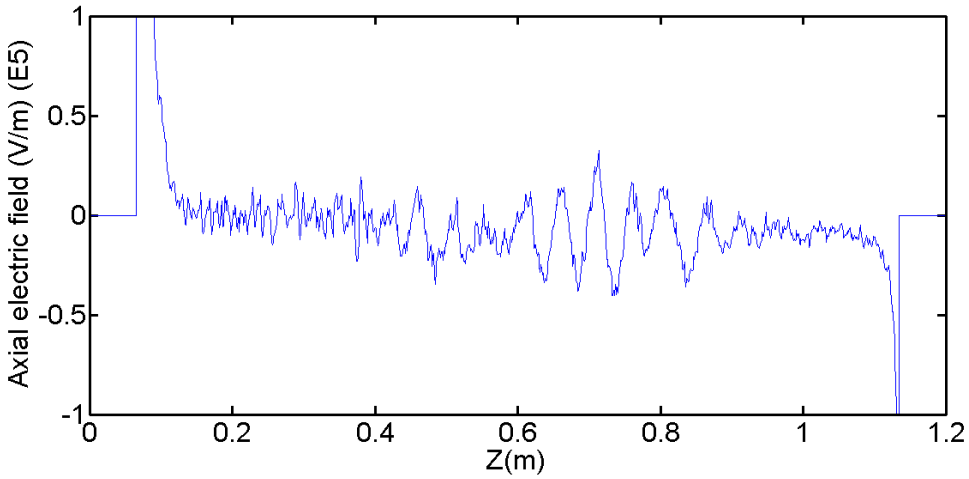

Figure 4.19 Axial electric field along beam propagation axis at 10ns

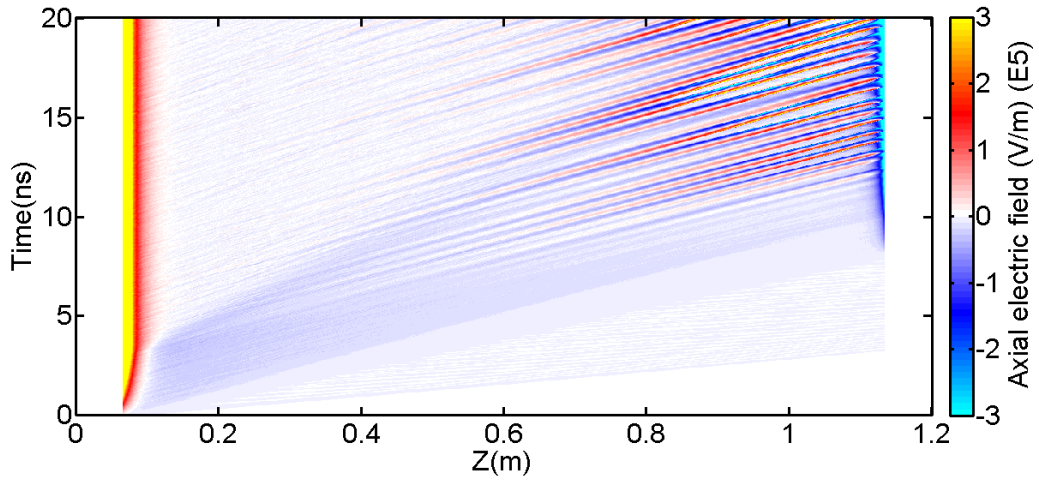

Figure 4.20 Axial electric field temporal evolution along electron beam axis

As can be seen, the electric field oscillations propagate axially in the beam propagation direction at a velocity between that of the two beams (approximately $1x10^{8}ms^{-1}$ in this case). From this data it is possible to perform Fourier analysis to obtain plots of the wave frequency and spatial structure.

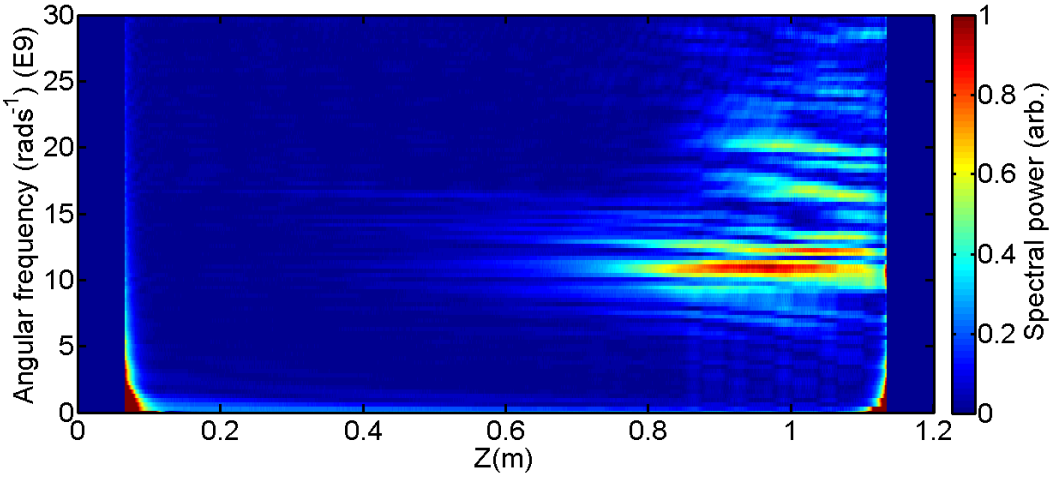

Figure 4.21 Axial E-field angular frequency ω against axial position

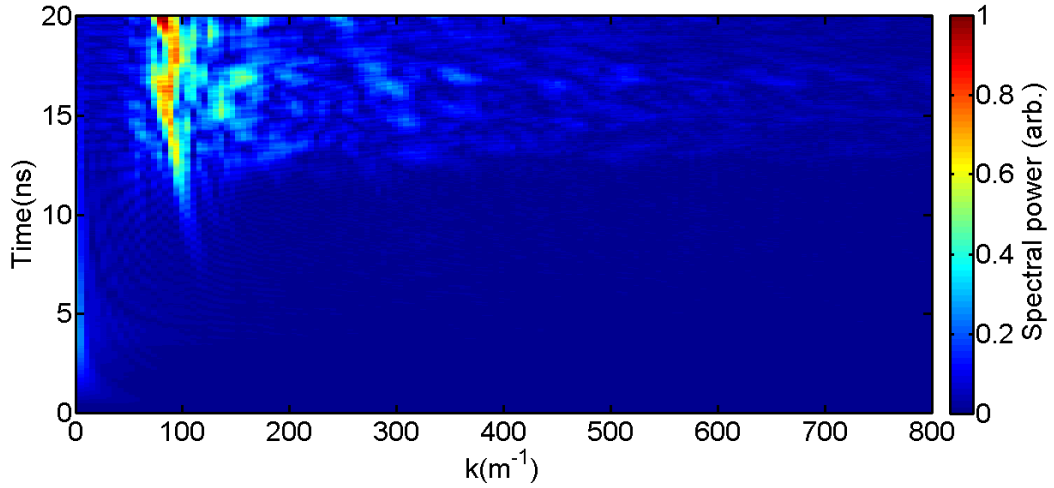

Figure 4.22 Axial wavenumber k against time

From figure 4.21, the strongest oscillations are seen to occur at an angular frequency of 1.09×10^{10} rads^{-1}. This is ~30% less than that predicted from the real component of the complex solution for the frequency (Re(ω(k)) at the wavevector corresponding to the maximum instability growth rate (Im(ω(k)) of the linear dispersion shown in figure 4.17. Similarly from figure 4.22, the strongest spatial Fourier structure is observed at a wavenumber 'k' of 104m^{-1}. Again this is approximately 25% less than the wavenumber predicted corresponding to the maximum temporal growth rate of the instability. Even in this simple scenario there is large amplitude, nonlinear behaviour observable from the phase mixing of the two species [Roberts and Berk, 1967]. The difference in predicted frequency and wavenumber may be due to this nonlinear

behaviour beginning to affect the electron densities and velocities. When reducing the temporal window of the Fourier transform, to only include the first 10ns where the electric field amplitude is small, the primary frequency observed is ~$1.5x10^{10}rads^{-1}$ which is comparable to the frequency predicted by the linear theory.

4.2.3 Beam plasma magnetic mirror confinement simulations

Satisfied the co-propagating scenario reproduces the predicted linear theory behaviour, the beam-plasma scenario can now be explored. Numerical simulations of this are relevant in fields including astrophysics [Ratcliffe, et al., 2014] (1D PiC simulations) and fast-ignition ICF [Sircombe, et al., 2008] (1D Vlasov simulations). While this work focuses on PiC methods to model the instability, the weak turbulence method has previously been used in the limit where the turbulence parameter W is small in homogeneous and inhomogeneous plasma [Kontar and Pécseli, 2002]. In the first scheme of beam-plasma simulations, the plasma is confined using the magnetic mirror arrangement shown in section 3.3.2. The increasing axial magnetic field at the simulation exit ports confines the plasma axially however, as the electron beam enters the simulation the beam expands in radius due to the changing axial magnetic field. This does not hinder the beam-plasma interaction but does reduce the overall beam number density. Table 4.5 lists the parameters that are initially used to define the beam-plasma simulation.

n_e	2.4 x 10^{16}m-3		Mesh cell	0.4mm
T_e	100eV		ω_{pe}	$8.73x10^{9}rads^{-1}$
T_i	10eV		ω_{pi}	$2.04x10^{8}rads^{-1}$
Beam current	36A		Plateau B_z	0.4T
Beam voltage	50kV		Expanded radius	24mm
Beam radius	8mm		Ion species	H^+
Simulation radius	64mm			

Table 4.5 Simulation parameters for beam-plasma magnetic mirror confinement

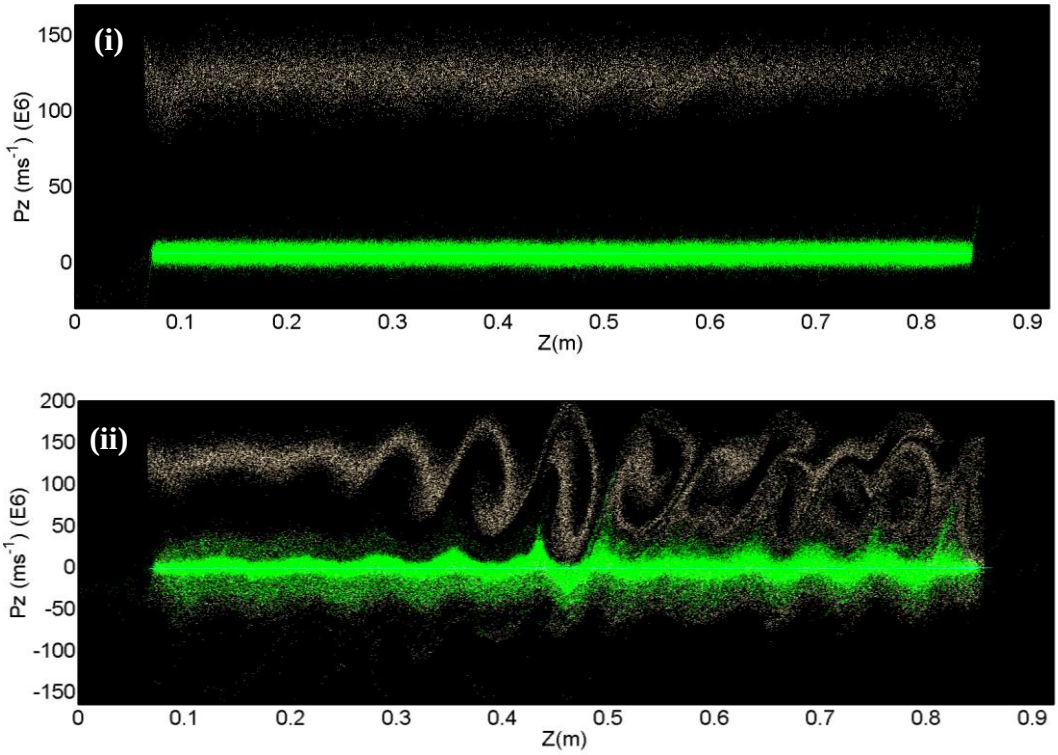

Figure 4.23 Beam-plasma instability, magnetic mirror confinement, axial momentum of all particles – orange = beam electrons, green = plasma electrons, blue = plasma ions (i) at 7ns (ii) at 50ns

The entire simulation is run for 440ns in order to investigate the non-linear effects of the saturation of the two-stream instability. At 7ns the two-stream instability is still growing as seen in figure 4.23, however, by 50ns the instability is well saturated as can also be seen in figure 4.23. At 50ns the electron beam axial momentum has formed multiple phase-space vortices that continue to propagate in the positive axial direction. This phase trapping leads to large axial electrostatic fields that can be seen in figure 4.24.

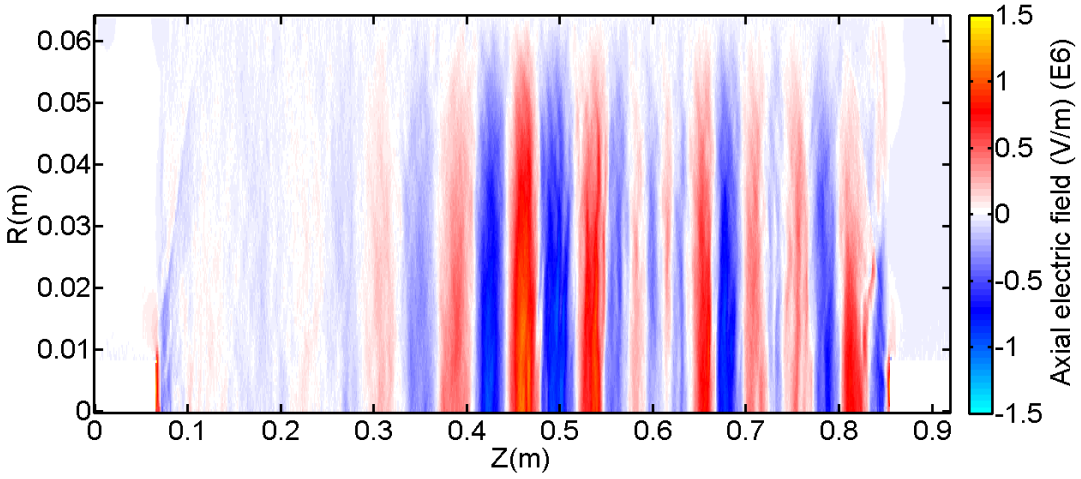

Figure 4.24 Beam-plasma instability, magnetic mirror confinement, axial electric field at 50ns

The behaviour of analogous individual phase-space vortices has been investigated previously in both theory and in numerical simulations [Eliasson and Shukla, 2006]. However, before looking into the effects of the non-linear behaviour it is necessary to first analyse the linear behaviour of the system.

Linear regime

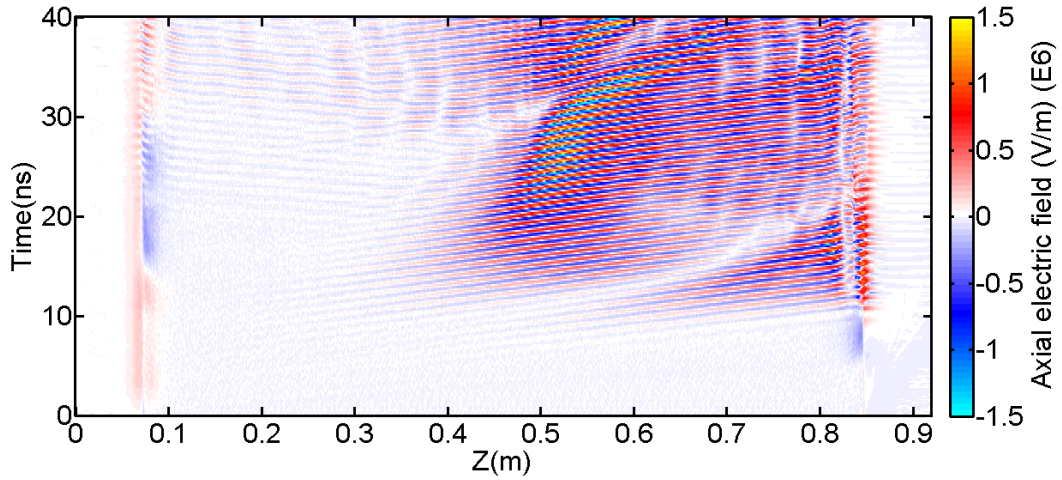

Figure 4.25 Beam-plasma instability, magnetic mirror confinement, axial electric field temporal behaviour in the linear regime at a radius of 32mm

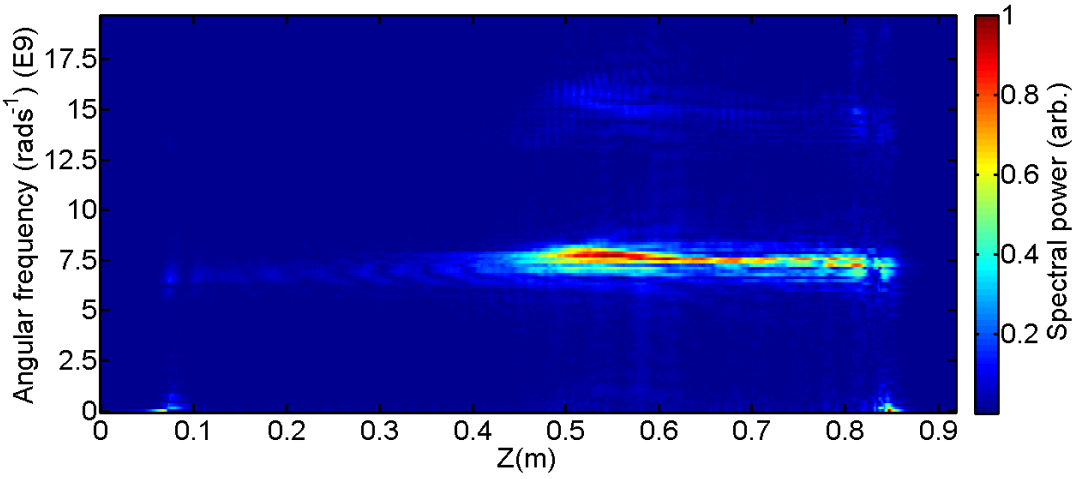

Figure 4.26 Beam-plasma instability, magnetic mirror confinement, axial E-field angular frequency over axial position at a radius of 32mm for a window of 0ns to 40ns

Using the same approach as in the co-propagating scenario, it is possible to plot the temporal behaviour of the axial electric field, shown in figure 4.25, and perform Fourier analysis on it. The angular frequency of the axial electric field, taken from figure 4.26, is approximately $7x10^{9}rads^{-1}$ which is close to the predication of the linear theory. Likewise, the axial wavenumber from figure 4.27 is $80m^{-1}$ which also closely matches the linear theory prediction presented in table 4.4.

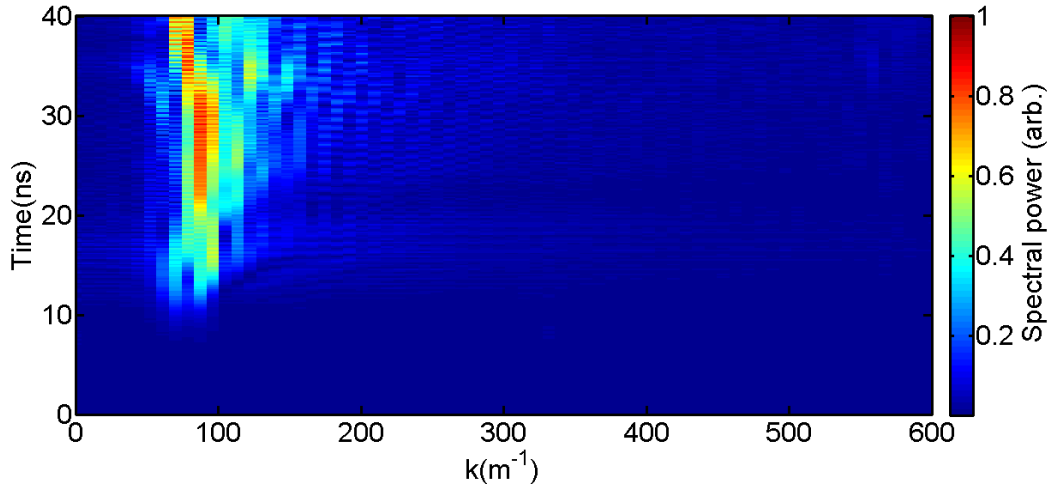

Figure 4.27 Beam-plasma instability, magnetic mirror confinement, axial wavenumber evolution over time for the linear regime of the two-stream instability at a radius of 32mm

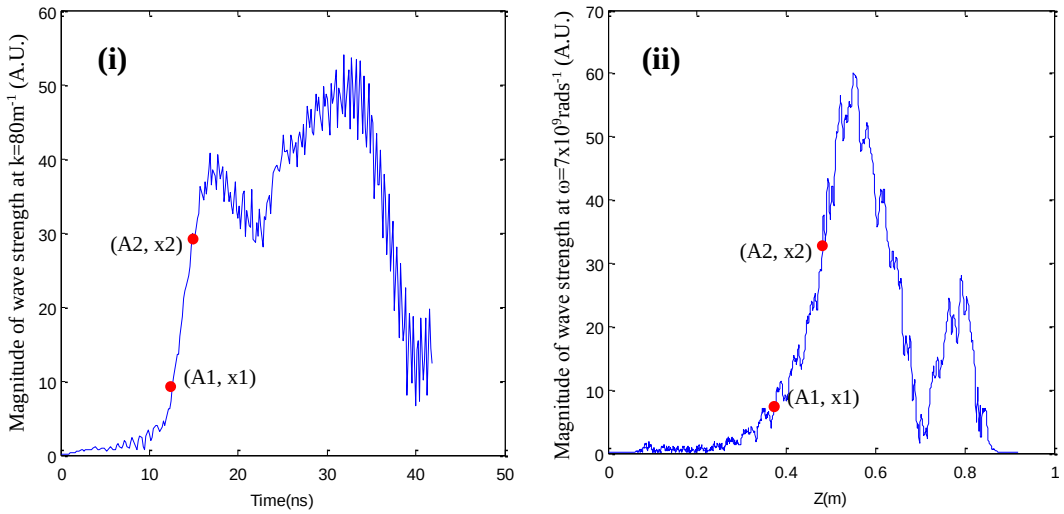

Figure 4.28 (i) Growth in time of the wave with a wavenumber of 80m^{-1} (ii) Growth in space of the wave at an angular frequency of 7x10^{9}rads^{-1}

Figure 4.28 shows the spatial and temporal growth of the signal with the strongest wavenumber and angular frequency. During the initial phase of the growth both of these curves approximate an exponential. For each of these plots, by taking two points of the amplitude and time/space it is possible to work out the exponential time/space constant by,

$$\tau = \frac{(x2 - x1)}{\ln(A2/A1)}$$

From these time and space constants the growth rates can be determined. The spatial growth rate is found to be ~92m^{-1} and the temporal growth rate ~3.3x10^{9}rads^{-1}. This is approximately twice as fast as the linear theory predictions of the temporal growth rate. Like the co-propagating case, non-linear behaviour may be present within the 40ns Fourier window that may result in this faster growth.

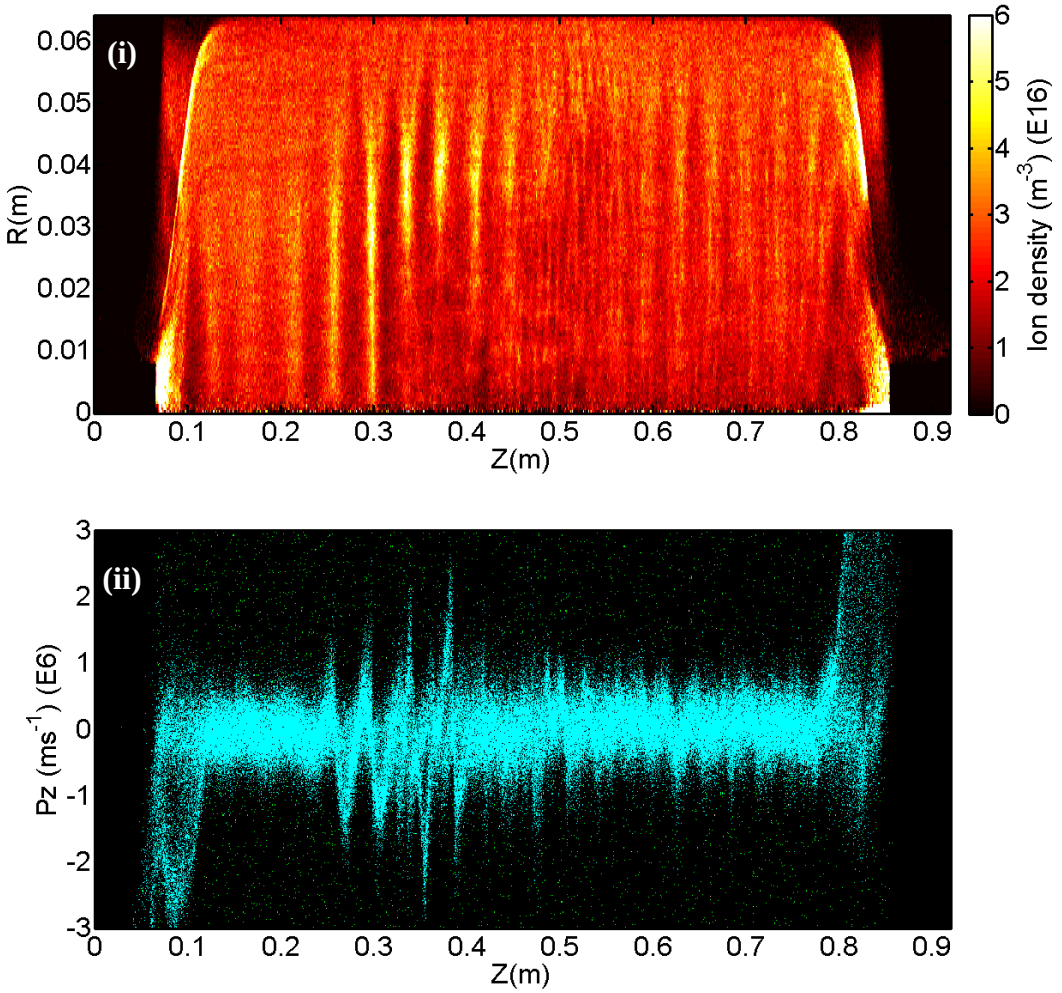

Figure 4.29 Ion behaviour at 140ns (i) Ion density Z-R (ii) Plasma phasespace Pz-Z (where the blue particles are the plasma ions and green are plasma electrons)

As an objective of this research was to look at the long time scale, multi-dimensional evolution of the instability, particularly with a view to considering the impact on the ions, the simulations were run for some 400ns. It was observed that after approximately 80ns, the ions and electrons begin to form strong axial bunches at an axial position of approximately 0.25 to 0.45m. The formation of these bunches appear similar to regions of plasma depletion that have been observed in prior PiC investigations of the two-stream behaviour [Dieckmann, Shukla and Drury, 2006]. Following the formation of these bunches, they appear to form two streams of particles drifting along the beam propagation axis in both the positive and negative directions.

A snapshot of this behaviour at 140ns is shown in the upper frame in figure 4.29 while particle axial phase-space behaviour is shown in the lower frame. Figure 4.30 shows the evolution of these bunches in time at a given radial position of 32mm. Similar propagation of ion density modulations have been seen in the experiments conducted in [Franck, et al., 2001] where periodic ion bunches are injected into a plasma discharge.

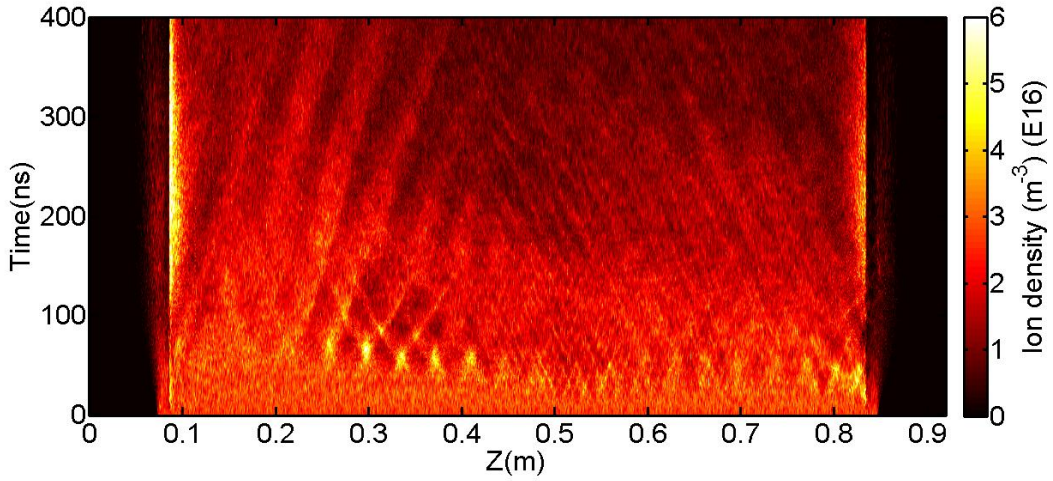

Figure 4.30 Ion temporal behaviour at 32mm radius

The macroscopic background electron density behaviour during these late time periods in the simulation maps closely to that of ion behaviour. For all intents and purposes, the ion density figures shown also relate to the macroscopic electron behaviour. Investigating the axial electric field at this point suggests that the cause of this ion behaviour is the presence of a standing wave structure along the beam propagation axis. Figure 4.31 shows the temporal behaviour of the axial electric field again but this time observing the behaviour when the ion/electron bunches start to form. It should be noted that the background plasma electron density oscillates weakly with the high frequency (~1GHz) component of the axial electric field standing wave structure.

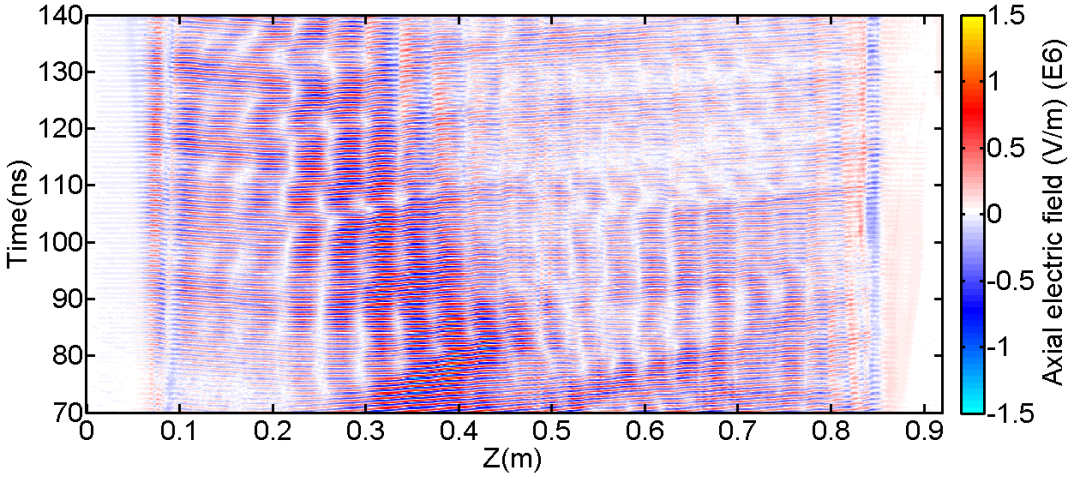

Figure 4.31 Beam-plasma instability, magnetic mirror confinement, axial electric field temporal behaviour at 70ns to 140ns at a radius of 32mm

The standing wave structure can be seen at an axial position of approximately 0.273m in figure 4.31. In figure 4.32, more detail of the temporal behaviour can be seen in the line plot of the axial electric field at an axial position 0.273m and radial position of 32mm. As can be seen the axial electric field associated with the standing wave begins to grow at approximately 70ns and grows to a maximum at 95ns. The signal then oscillates with a beat period of ~10-20ns before declining after ~140ns. This wave has an angular frequency of $7.14 \times 10^{9} rads^{-1}$ which is near the frequency identified in the linear limit of the two-stream instability. The temporal Fourier transform of the axial electric field can be seen in figure 4.33 and shows periodic variation of the strength of the $7.14 \times 10^{9} rads^{-1}$ spectral component with spatial location.

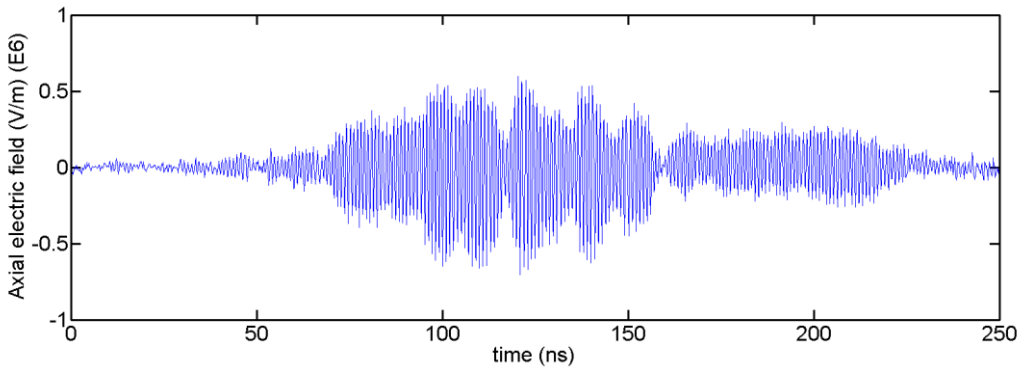

Figure 4.32 Beam-plasma instability, magnetic mirror confinement, temporal behaviour of the axial electric field at Z=0.273m and R=32mm

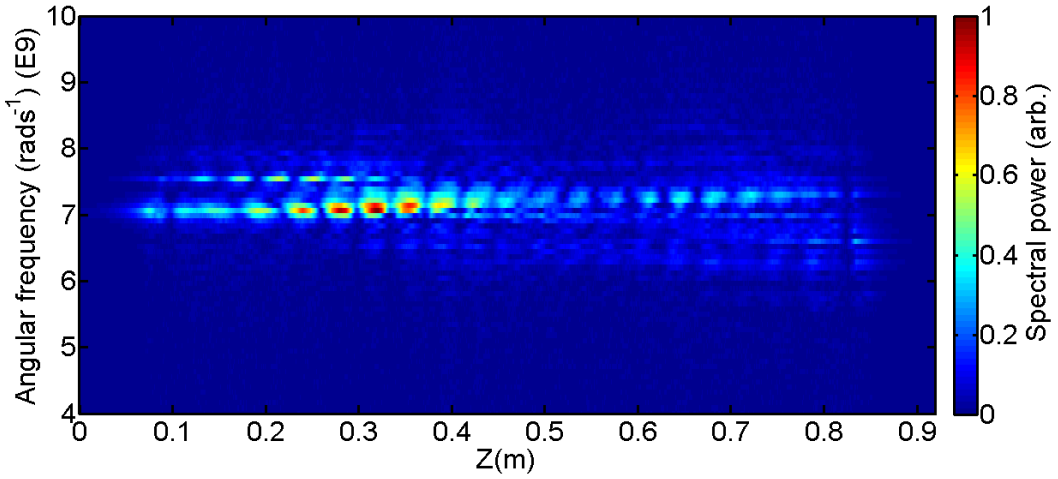

Figure 4.33 Beam-plasma instability, magnetic mirror confinement, axial E-field (high angular frequency component) over axial position at a radius of 32mm over a temporal window of 64ns to 154ns

A possible explanation behind the formation of these standing wave structures can be that the beam-plasma instability is generating a series of Langmuir oscillations as the beam transits through the plasma, as the beam-plasma instability frequencies are close to that of the electron plasma frequency. The superposition of these Langmuir oscillations appear to build in strength in the region near where the first phase-vortices have formed. These oscillations extend across the radial extent of the waveguide before being suppressed close to the conducting boundary. The wavelength of these electrostatic-like oscillations are below the vacuum cut-off of the waveguide and can therefore only be supported within the plasma. These oscillations lead to a depletion of the electrons, forming a cavity, forcing the electrons out in both the positive and negative longitudinal directions. As there are periodic cavities being formed, the displaced electrons merge with the electrons displaced from the adjacent depletion regions, forming density bunches. Due to the increase in electron density in these regions, the ions are drawn towards them to maintain quasi-neutrality. This mechanism appears to be similar to that of the modulational instability discussed in section 2.5.2.

As these bunches form, they appear to have a dampening effect upon the large electric fields generated by the beam-plasma instability, leading to the standing waves being

the dominant electric field structure in the system. The phase-space vortices are still present but tend to move through the system to regions less perturbed by the spatial bunching of the plasma particles (typically downstream and deeper into the plasma column). The electron and ion density bunches that were formed from the cavities continue to evolve at a constant velocity in their initial displacement direction. They can then propagate through oppositely directed bunches and through the adjacent cavities before eventually beginning to dissipate. As they begin to dissipate, this allows the beam-plasma instability to begin to grow once again in its original location.

When examining the lower frequencies shown in figure 4.34, there appear to be frequencies that would correspond to that of the waves associated with the ion behaviour. At an axial position of 0.27m-0.4m, in a location where there is significant ion bunching and strong, higher frequency standing wave oscillations, there exists a spatially modulated low frequency ion oscillation as well, at a frequency of ~$50x10^{6}rads^{-1}$. These oscillations may be ion-acoustic related [Sircombe, et al., 2009] as the density bunch velocities correspond closely to the ion-acoustic velocities of the plasma. As the modulational instability theory [Dendy, 2002] describes a coupling between Langmuir and ion-acoustic waves, it may be possible for ion-acoustic waves to build up in the cavities formed by the strong higher frequency oscillations which would explain the spatial modulation of the electric field at this low frequency closely matching the spatial modulation of the strength of the high frequency signals.

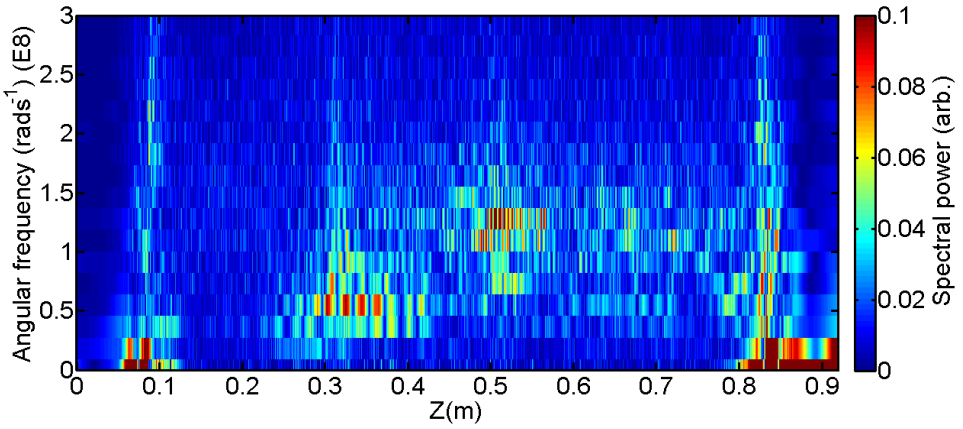

Figure 4.34 Beam-plasma instability, magnetic mirror confinement, low axial E-field (low angular frequency component) over axial position at a radius of 32mm over a temporal window of 64ns to 440ns

Similar behaviour in frequency has been observed in observations of type III solar radio bursts [Thejappa,et al., 2012] relating the behaviour to the two-stream instability, although this hypothesis has been challenged [Graham et al., 2012].

As an aside, a simulation was run with similar parameters as above but with a periodic density profile applied to the plasma along the axial length of the system, at a similar spatial frequency to the cavities that were predicted by the streaming instability simulations described in section 4.2.3. This resulted in the suppression of the beam-plasma instability. This suggests that the beam-plasma instability may be self-limiting as it induces an axial bunching of the particles that will inhibit its own growth. Similar suppression was seen by [Nakamura, 1970] when applying a density modulation to an electron beam propagating in a background plasma.

4.2.4 Beam plasma electrostatic confinement simulations

It was decided to develop an experiment to attempt to observe the features of the two-stream instability and potentially the low frequency ion oscillations. The magnetic mirror simulations provided a good starting point to investigate the non-linear behaviour of the beam-plasma two-stream instability. The experimental design proposed however, utilises electrostatic axial confinement rather than that of a magnetic mirror system. To better match the experimental design it was necessary to remove the magnetic mirror elements of the simulation and replace it with a constant axial magnetic field that provided the field required for radial confinement. The axial confinement was then created by applying a constant negative voltage onto the ports of the simulation as seen in section 3.3.2. This is actually the inverse of the experimental design. In the experimental design, the anode wall is set at a positive potential whilst the cathode(s) are grounded, allowing the electron beam to pass through unperturbed by the Penning trap cathode, and moreover ensures that should the cathodes intercept the electron beam, this charge would immediately be diverted to ground, rather than the terminals of the power supply. Unfortunately, the means to apply a voltage to a conducting boundary is not supported in xOOPIC. This inverse method results in a very slight acceleration of the electron beam as it enters the system

and a deceleration as it reaches the end (which can also be expected in the experiments due to the slightly positive anode since only the potential difference is relevant). Ultimately this did not result in any obvious impact upon the mechanisms being investigated.

To further match the experimental setup, the radius of the system had to be reduced. This constraint was imposed by the design of the magnet coils in order that they could achieve an adequate magnetic field with the power supplies realistically available. Re-optimisation of the numerical simulations was required as it was discovered that when the radius was reduced it was necessary to increase the plasma density in order to completely observe similar non-linear ion behaviour as seen previously in the magnetic mirror simulations. While there was some evidence of ion bunch formation, the bunches formed close to the conducting boundary at the density used in the first, magnetically confined simulations. This results in the interception of the ions at the conducting boundary removing the macro-particles from the simulation leading to a change in the long term plasma dynamics. By increasing the plasma density, the bunches form closer to the electron beam reducing the impact of this boundary interception. These new simulation parameters are given in table 4.6.

n_e	9×10^{16}m-3		Mesh cell	0.4mm
T_e	100eV		ω_{pe}	16.9×10^{9}rads^{-1}
T_i	10eV		ω_{pi}	3.94×10^{8}rads^{-1}
Beam current	10A / 35A		Axial B_z	0.4T
Beam voltage	10-100kV		Ion species	H^+
Beam radius	8mm		Simulation radius	25mm

Table 4.6 Simulation parameters for beam-plasma electro-static confinement

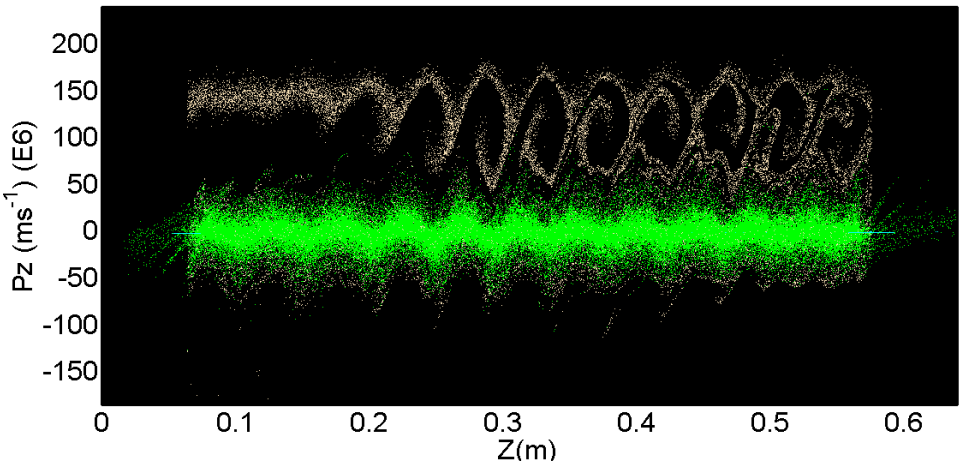

Figure 4.35 Beam-plasma electrostatic confinement axial momentum of all particles – orange = beam electrons, green = plasma electrons, blue = plasma ions at 70ns

Figure 4.35 shows that the simulations of electrostatic confinement with a smaller radius (but higher background density) exhibit the same saturated axial momentum behaviour as seen in the magnetic mirror confinement scenario. Again, by 70ns the two-stream instability seems to be fully saturated and is exhibiting regular phase-trapping along the axis of propagation. The background plasma electrons also appear to be being modulated in axial velocity by the phase-space vortices formed in the electron beam.

Observing the axial electric field behaviour shown in figure 4.36, the instability exhibits similar growth behaviour despite the change in the confinement arrangements. However, in this case the temporal growth rates are faster due to the increased background plasma frequency. In addition, as there is no magnetic decompression of the electron beam, its overall density was higher, thus the plasma frequency of the electron beam was also increased. The non-linear behaviour therefore begins much sooner due to the faster saturation of the linear regime of the two-stream instability.

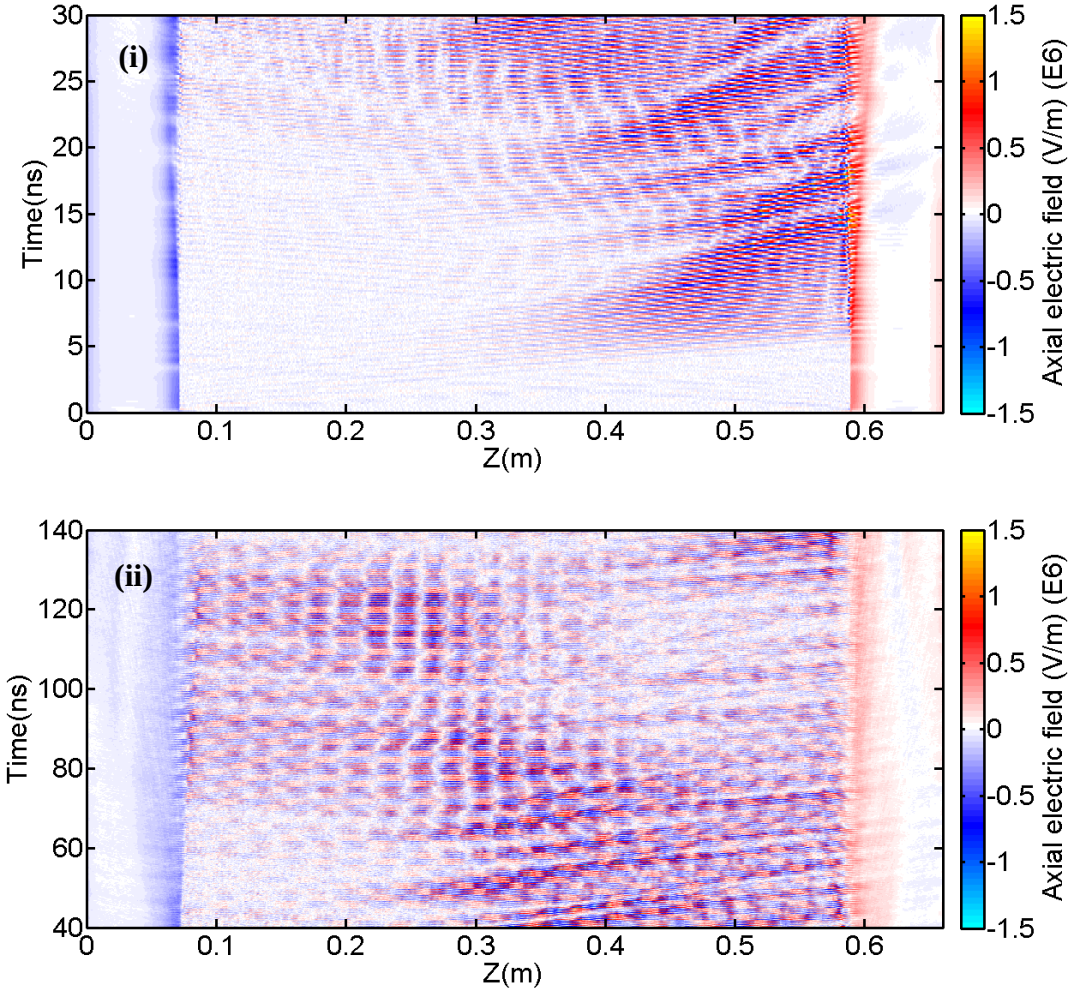

Figure 4.36 Beam-plasma electrostatic confinement temporal evolution of the axial electric field at a radius of 16mm for 10A beam current (i) linear regime (ii) non-linear regime

Satisfied that the electrostatic confinement simulation is exhibiting the same overall behaviour as the magnetic mirror confinement calculations, it was now possible to investigate the effects of changing the beam current on the non-linear ion behaviour.

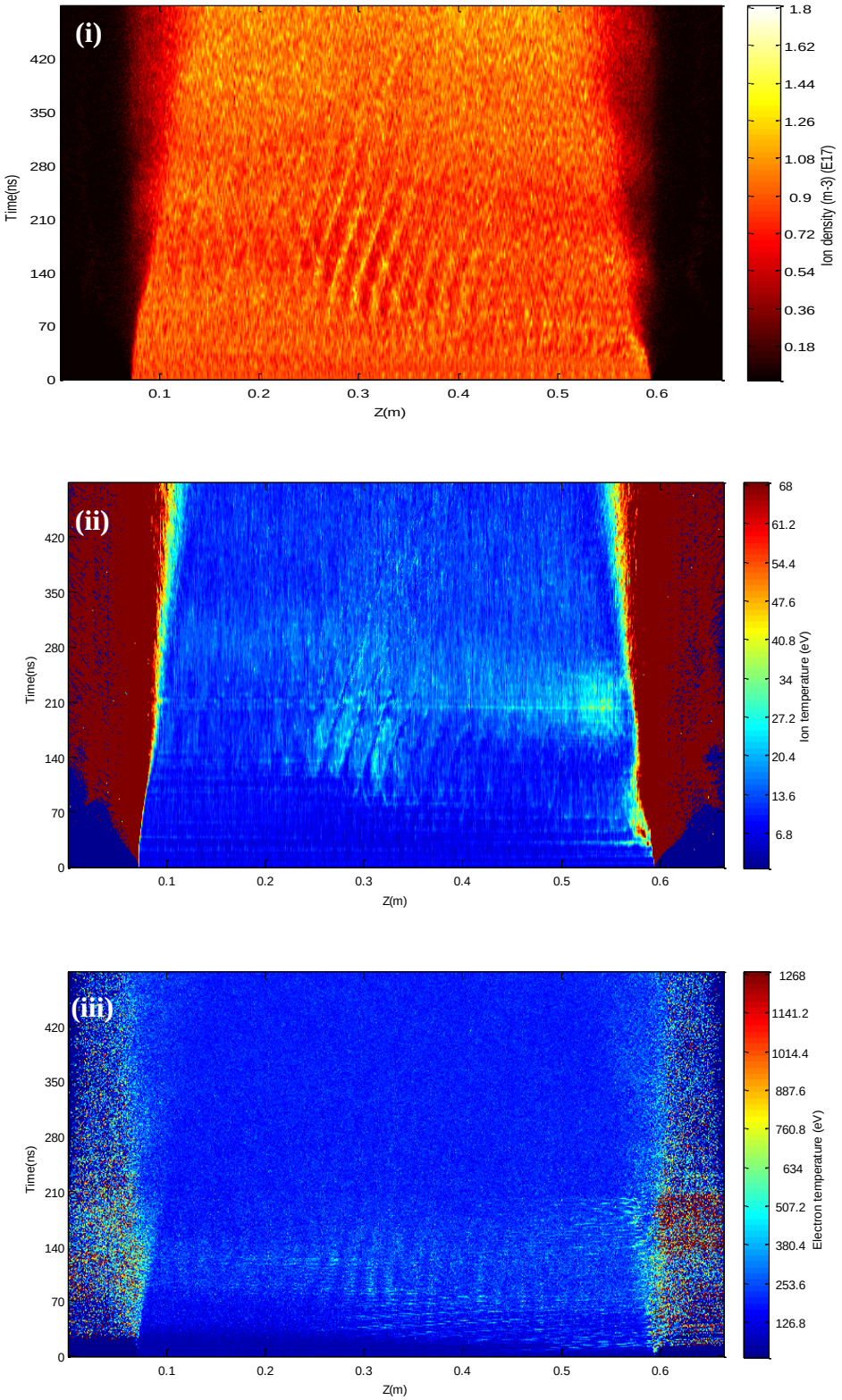

Figure 4.37 Evolution of the beam-plasma electrostatic confinement simulation at a radius of 16mm for a 50 kV 10A electron beam (i) ion density (ii) ion temperature (iii) electron temperature

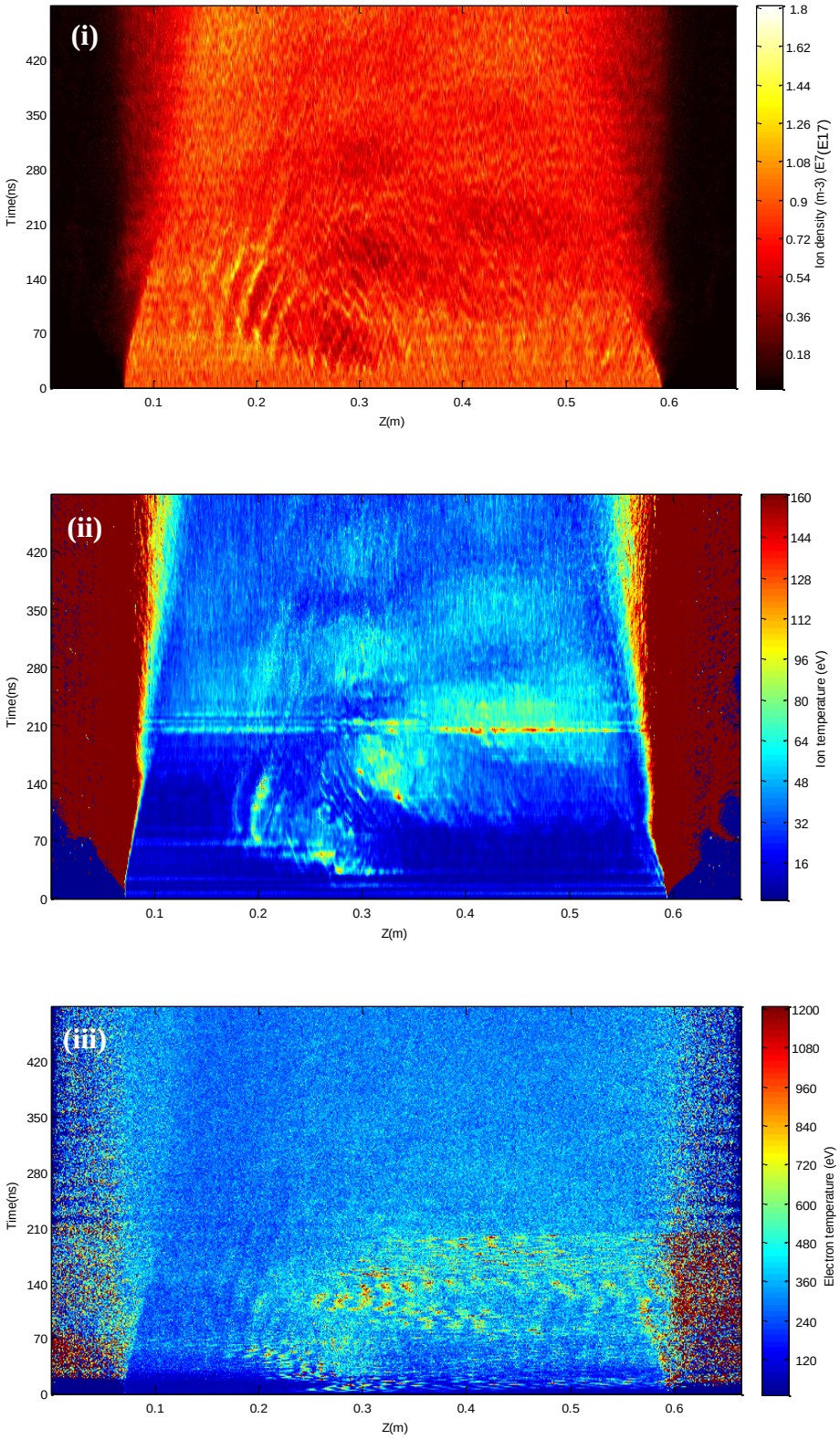

Figure 4.38 Evolution of the beam-plasma electrostatic confinement simulation at a radius of 16mm for a 50kV 35A electron beam (i) ion density (ii) ion temperature (iii) electron temperature

Figures 4.37 and 4.38 show the different temporal evolutions of the ion density and the ion and electron temperatures predicted for a beam current at 10A and 35A respectively at a radius of 16mm. Note that in both figures 4.37 and 4.38, a small fraction of the particles can traverse the gap between the plasma edge and the confining electrostatic boundaries leading to anomalous temperatures. These can be ignored due to the very low particle density and distance from the region of interest.

At 10A beam current the ion bunches form at an axial position of ~0.25m after approximately 70ns and have a relatively uniform structure size of ~0.02m. They appear to propagate predominately in the positive axial direction. In the vicinity of these bunches the ion temperature is noticeably higher than the background ion temperature. The electron temperature has hot spots that roughly correspond to the regions where strong axial electric field standing waves are seen in figure 4.36.

Raising the current to 35A, results in high density ion bunches forming after a shorter drift length in the plasma at an axial position of ~0.15m again after ~70ns. The structure is not as uniform and they appear to propagate towards an area of ion depletion at an axial position ~0.25m which seems to have been formed by a similar weaker process which commenced after 30ns. Again the ion temperature appears to increase near the bunch formations, however additional hotspots in the electron temperature appear to form after 100ns near axial electric field standing wave structures at a position of ~0.3m, but there does not seem to be such a close correlation between the electron temperature spatial structure in this case and the relatively weak ion density modulations. It should be noted that these temperatures are approximated utilising the mean of the macro-particle speeds within each mesh cell.

One can clearly see that in both simulations, the precursor for the ion modulation is the observation of rather energetic electron populations, indicating the development of strong axial electric fields. This is clearly visible in the development of Figure 4.38 where hot electrons are observed close to z=0.25m very early in the simulation which precede the first ion spatial structures observed after 35ns. Subsequently after some

50ns, energetic electrons are observed near z=0.2m which are shortly followed with the formation of a second, stronger modulation in the ion density and temperature at ~75ns.

Taking the values of the electrostatic fields to be approximately 10^6 V/m with an electron temperature of 500eV and density of $5x10^{16}m^{-3}$, it is possible to determine that the turbulence parameter W~0.55 (from equation 2.77, [Dendy, 2002]). Given the same electron density and temperature the Debye wavenumber is k_D~$8442m^{-1}$. This suggests that within this system it is possible for waves to become trapped and the modulational instability to grow for k values less than $3614m^{-1}$ (i.e. for wavelengths exceeding ~2mm). As the cavity size observed in these numerical simulations are on the order of ~20mm, it is possible for waves to have become trapped and the instability to grow.

It should be noted that in both of these simulations there is a large increase of ion temperature when the beam turns off at 200ns. This was due to rather abrupt termination of the beam current giving rise to strong E-fields due to sudden step change in the charge balance.

Increasing the current further causes extremely strong disruption to the ion density distribution but there is little in the way of ion structure and the particles do not exhibit the same collective behaviour as seen in the lower current scenarios.

It is also possible to investigate the effects of changing the beam voltage on the non-linear ion behaviour, with example behaviour shown for voltages of 10kV and 100kV in figures 4.39 and 4.40 respectively. In order to observe the full behaviour at higher beam voltages (where the growth rate is rather lower) the total simulation length was doubled for all of the simulations investigating the impact of the beam voltage on the development of the instability. Similarly, in order ensure saturation of the instability over the larger plasma length, the electron beam current was maintained after 200ns.

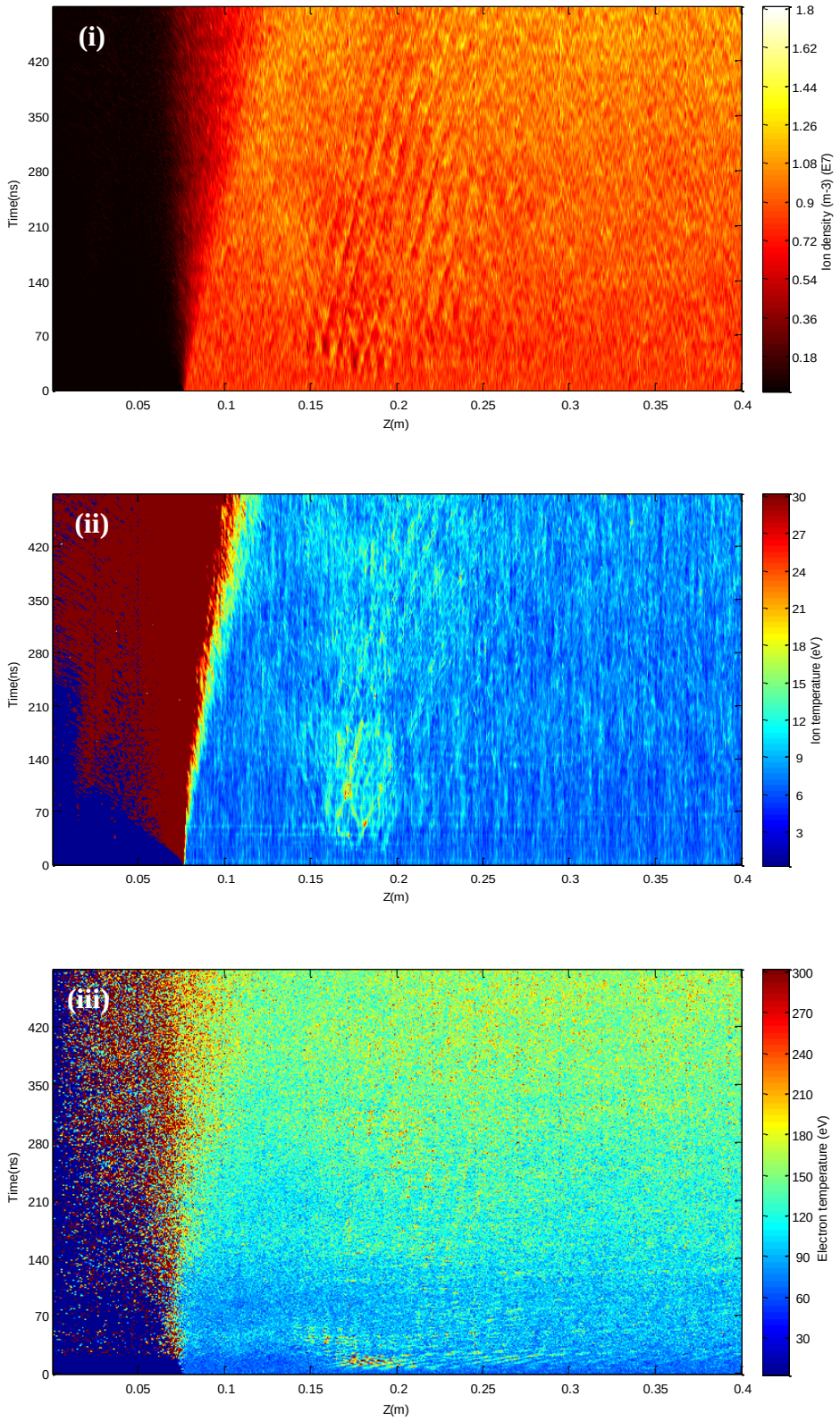

Figure 4.39 Beam-plasma electrostatic confinement temporal behaviour at a radius of 16mm for a 10kV 10A electron beam (i) ion density (ii) ion temperature (iii) electron temperature

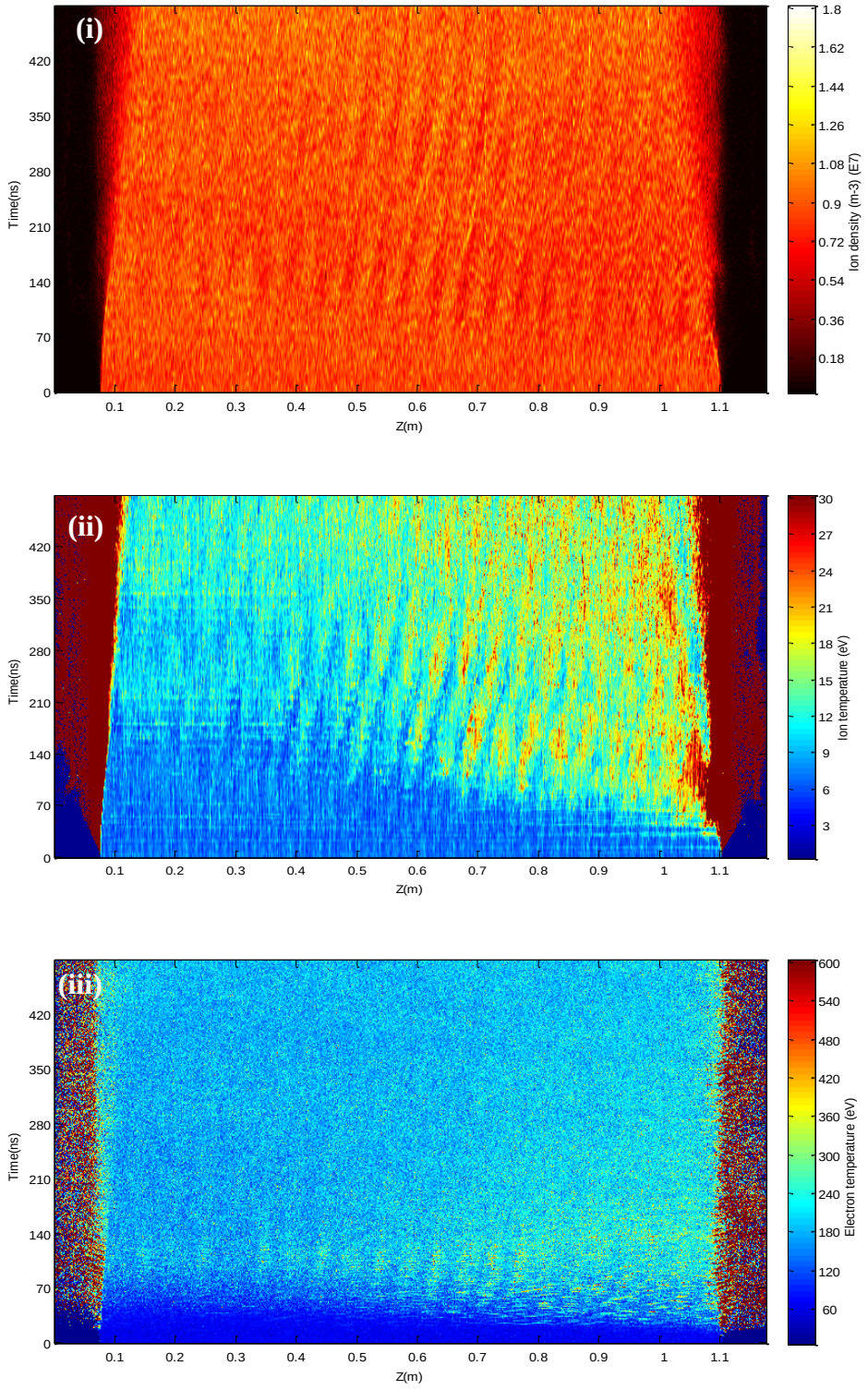

Figure 4.40 Beam-plasma electrostatic confinement temporal behaviour at a radius of 16mm for a 100kV 10A electron beam (i) ion density (ii) ion temperature (iii) electron temperature

For a beam voltage of 10kV, the phase-space vortices, and hence the strong axial E-field that proceed to modulate the particle positions, now develop after the beam has propagated a distance of ~0.15m after 35ns. In comparison, the 50kV beam simulation showed the formation of ion spatial bunching after a propagation distance of 0.3m and after 70ns whilst raising the voltage to 100kV requires the beam to traverse a distance of 0.6m before the ion spatial bunching is observed after some 100ns.

As the ion bunching process at a beam current of 10A, for all beam voltages, is relatively uniform and well defined it is possible to plot the ion bunch spacing and ion bunch velocity as a function of the beam voltage.

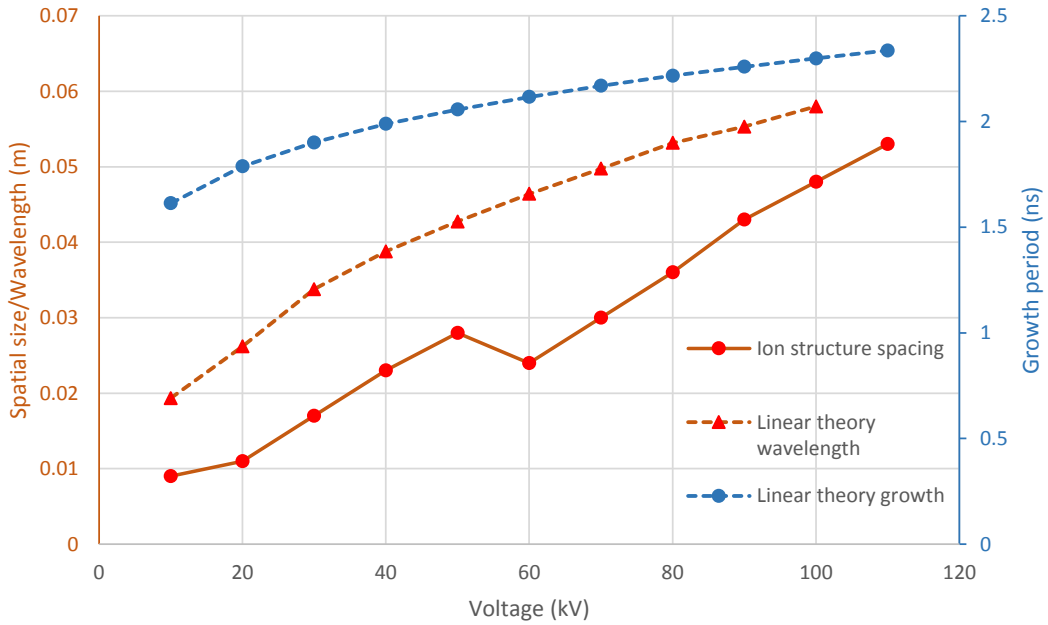

Figure 4.41 Beam-plasma electrostatic confinement - ion structure spacing as a function of beam voltage

As seen from figure 4.41 as the beam voltage is increased the ion bunch spacing increases relatively linearly. However, at a beam voltage of 60kV the ion bunch spacing trend seems to offset by ~0.003m. The ion bunch spacing seems to behave linearly again after this offset. This kink appears reproducible but has not been linked to a physical process and may warrant further investigation. Also plotted is the wavelength corresponding to the maximum growth for the beam-plasma instability,

derived from the linear theory. It can be seen that the ion bunch spacing scales approximately at the same rate as the wavelength of the electron beam-plasma instability. This suggests that the spatial wave-vector favoured by the beam-plasma instability determines the length of the standing oscillations that appear to be the driver for the ion and electron bunching.

Test simulations with no electron beam or very high beam voltages which results in no beam-plasma instability growth (i.e. no particle phase trapping) shows no indication of plasma cavity formation. This suggests that these cavities are directly related to the phase-trapping behaviour associated with the beam-plasma instability. Reducing the overall longitudinal dimension of the simulations also showed the cavities formed at the same absolute spatial location further suggesting that neither reflections at the boundaries, nor any backwards growing instabilities are involved in the cavity formation.

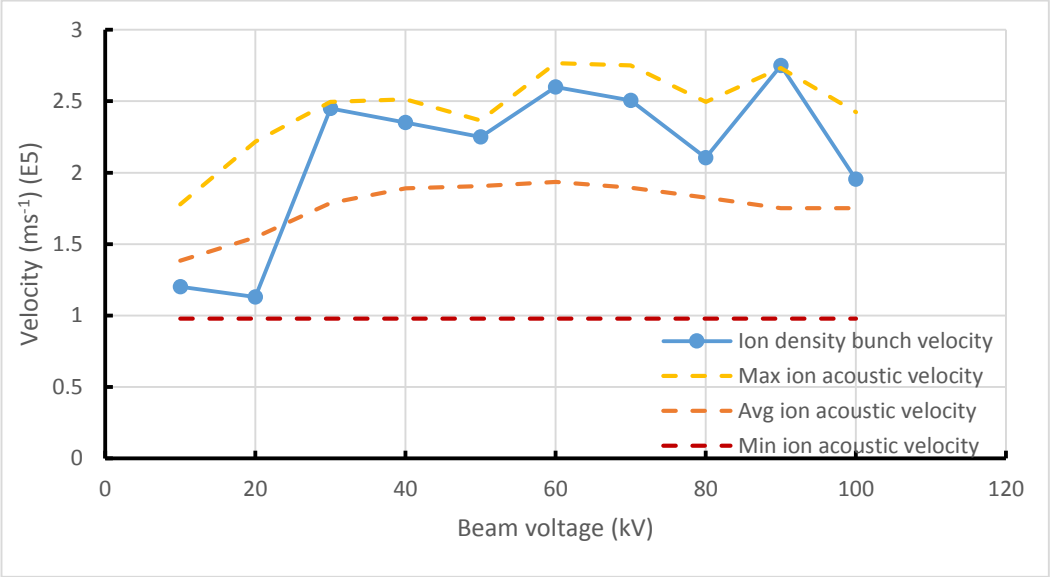

Figure 4.42 Beam-plasma electrostatic confinement ion bunch velocity as a function of beam voltage

Figure 4.42 shows the approximate ion bunch velocity as a function of beam voltage. For voltages < 20kV, the ion bunches seem to propagate quite slowly at ~$1.2 \times 10^5 ms^{-1}$. For higher beam energies the ion bunch velocity seems to increase to ~$2.4 \times 10^5 ms^{-1}$ and seems to remain close to that value for all beam voltages > 30kV. When compared

to the ion acoustic velocities in the system, dictated by the electron temperatures, typically the ion bunch velocity is larger than that of the average acoustic speed, based on the electron temperature averaged over the system, with the exception of beam voltages less than 20kV. However for beam voltages above 30kV, the bunch velocities appear to move close to the maximum localised ion acoustic velocities predicted in the system. These local maxima correspond to the hot spots within the density cavities formed in the system. This suggests that the ion density bunches are leaving the depleted cavity regions at the local ion acoustic velocity and are continuing to propagate through the system at that particular velocity.

These 2D simulations show the development and growth of a two stream instability and show the saturation of the instability with the formation of phase-space vortices [Roberts and Berk, 1967]. The strong E-fields established by the two stream instability appear in the non-linear regime to give rise to spatial modulation of the plasma density [Dieckmann, Shukla, and Drury, 2006] in a manner similar to the modulational instability [Dendy, 2002] and with low frequency wave oscillations as anticipated by [Sircombe, et al., 2008]. The density perturbations appear to drift at the ion acoustic velocity. Similar excitation of low frequency signals have been interpreted in type III solar bursts as being associated with ion acoustic oscillations [Thejappa, et al., 2012]. Although using a different excitation model, ion acoustic oscillations have been observed experimentally to be excited by modulation of the plasma density [Franck, et al., 2002].

4.3 Electron beam simulations

To produce the electron beam required to drive the beam-plasma instability described in sections 4.2 in a laboratory experiment, it was necessary to design the emitter system using numerical simulations in the PiC code MAGIC as outlined in section 3.4.1.

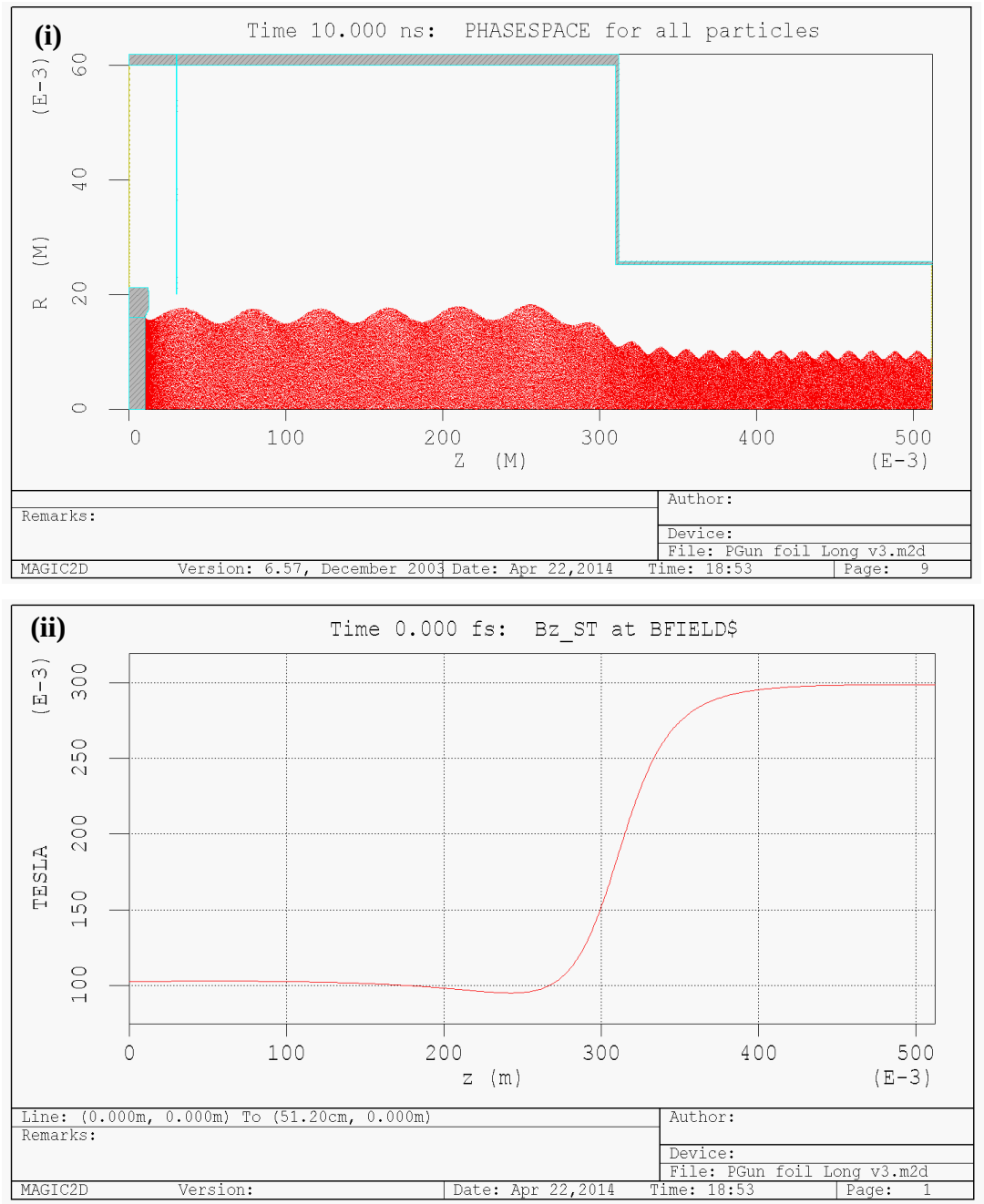

Figure 4.43 (i) Z-R plot showing particle positions after 10ns (ii) Axial magnetic field profile

Figure 4.43 shows the particle positions after 10ns from the start of the simulation along with the magnetic field profile that was produced by the MAGIC coil function. The initial electron emission has a radius of ~16mm and the magnetic field profile used introduces a degree of scalloping to the beam radius. Within the larger diameter cathode region, this scalloping is on the order of 2mm in radius variation. As the beam transits from the cathode region to the interaction waveguide region, the magnetic field rises due to the stronger field created by the main interaction region solenoid. This has the effect of magnetically compressing the electron beam down to a radius of ~8mm with a beam radius fluctuation of ~1mm. Removing all scalloping effects from the electron beam proved difficult therefore 1mm of beam radius fluctuation was deemed acceptable. As the emission model implemented in the simulations is a simplistic representation of the explosive electron emission cathode to be used, the beam generated by the real cathode will not be as uniform and experimental optimisation will be required in any event.

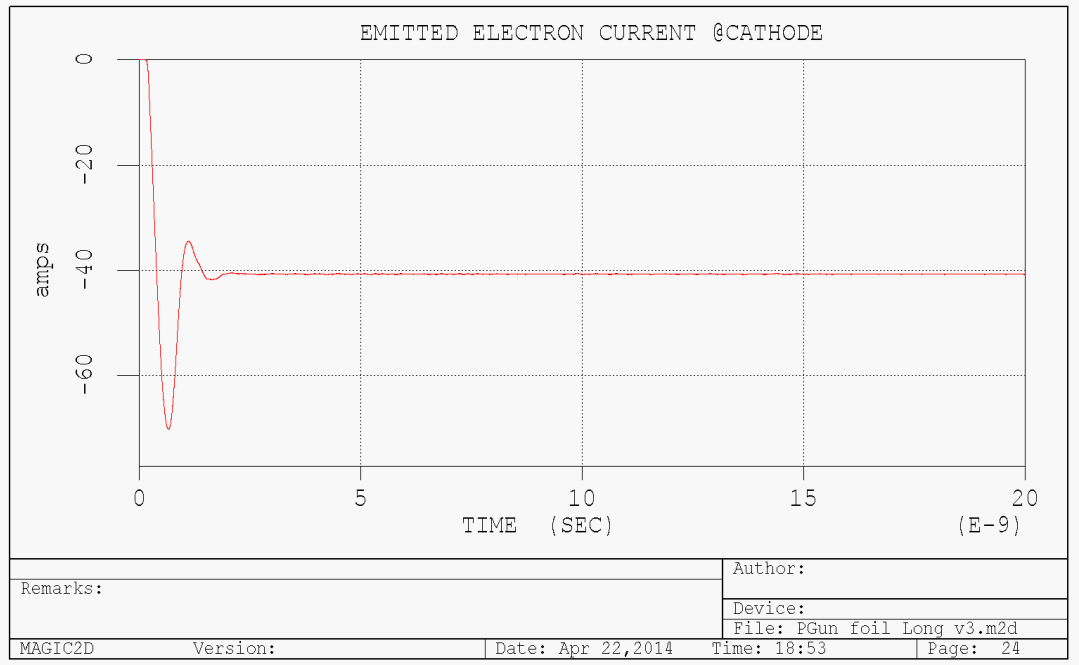

Figure 4.44 Emitted current from the cathode

For an anode gap spacing of 1.5cm, the numerical simulations predict a beam current of ~40A for an applied voltage of 50kV. Figure 4.44 shows the predicted current emitted from the cathode surface. There is a brief oscillation in the emitted current as

the accelerating electric field is introduced into the system (as a TEM wave from the LHS of the geometry) but after 2ns the current is constant. As no magnetic mirroring occurs and there is no interception between the particles and any of the conducting boundaries this emitted current will translate directly to beam current in the interaction region. This gives scope for experimental tuning of the beam current, given the realities of the experiment, in the energy range of interest by using beam collimators, filtering meshes and the magnetic compression from the emitter to the plasma column.

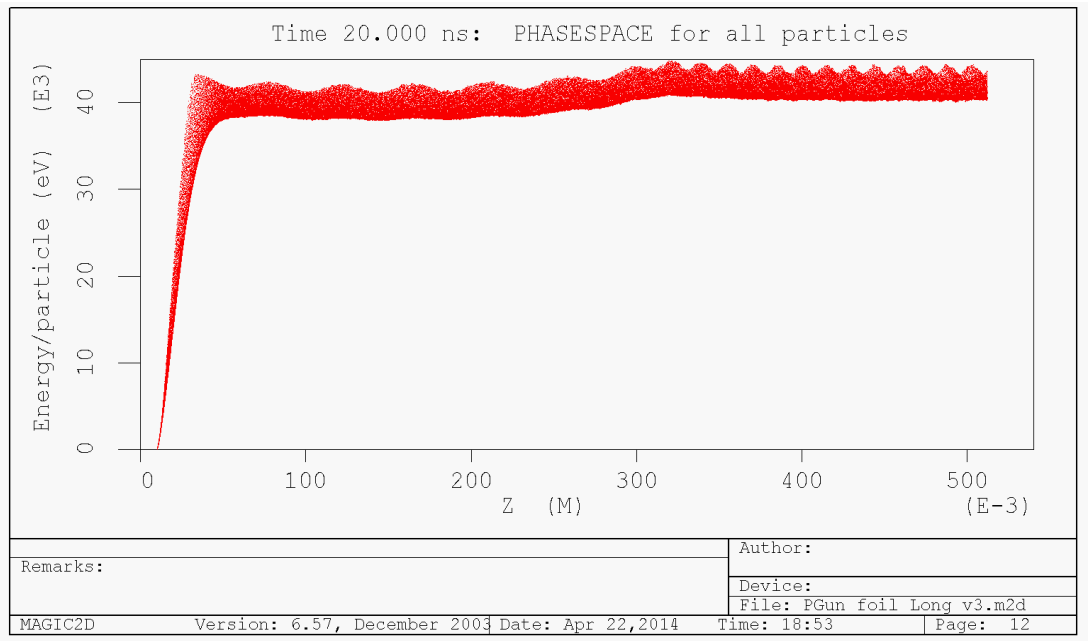

Figure 4.45 Particle energy along the propagation axis after 20ns

The TEM wave injected into the system corresponds to an applied voltage pulse of amplitude 50kV on the cathode. Figure 4.45 shows that after 20ns, when the beam is in a state of equilibrium, the electrons are accelerated to ~40kV with an energy spread of ~3kV. As the accelerating potential is produced by the injected TEM wave, mismatching (due to reflections) on the accelerator of the simulation may slightly reduce the field applied across the anode-cathode gap and therefore result in the lower beam energy, combined with space-charge depression induced by the beam itself.

Chapter 5 : Laboratory experimental apparatus

5 Laboratory experimental apparatus

5.1 Experiment overview

In order to verify the results of the numerical simulations of the beam-plasma two-stream instability, a laboratory experiment was constructed. Prior experiments have shown that the quasi-linear theory of the beam-plasma instability holds [Roberson, Gentle and Nielsen, 1971] and that ion acoustic trapping of the electron-plasma waves can occur in an unmagnetised plasma [Ikezi, Chang and Stern, 1976]. The design of this experiment is intended to realise a parameter space similar to that described in Section 4.2.4 and achieve the correct regime for the turbulence parameter W. To this end, the laboratory experiment consists broadly of an electron accelerator, a Penning trap plasma discharge region which provides the low temperature background plasma, and a range of diagnostic instruments to determine the electron beam energy and current, the plasma density and the impact the beam has on the plasma. The electron emitter generates a rectilinear beam that propagates into the Penning trap which contains a helium plasma discharge with a pressure on the order of $7x10^{-4}$ mbar. The mean free path for helium at this pressure is ~30cm [von Engel, 1965], so collisions should not severely affect the movement of the ions predicted by the simulations. The beam is expected to perturb the plasma as seen in the numerical simulations and the behaviour is measured utilising the diagnostic instruments. A schematic showing the experimental setup is shown in figure 5.1.

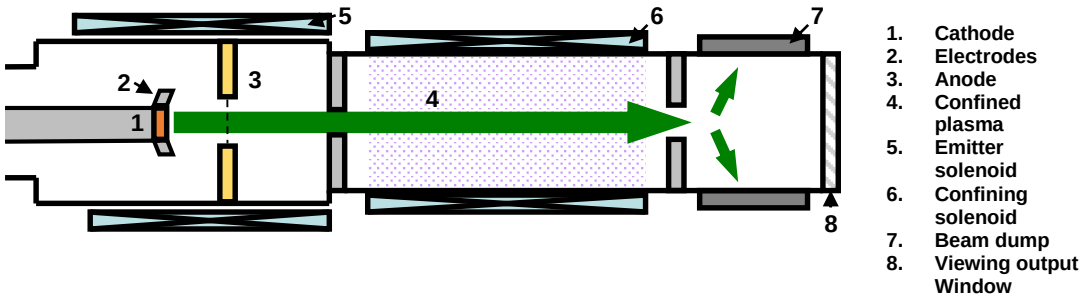

Figure 5.1 Experimental schematic showing the roles of key components

5.2 Vacuum system

In order to ensure a collisionless path for the electron beam and to ensure a collisionless plasma environment, the electron accelerator and the plasma discharge operate at a relatively low pressure. It is necessary therefore to first evacuate the entire system of atmospheric gases. The system is vacuum sealed primarily using nitrile gaskets in o-ring grooves and is pumped down using both a roughing fore pump and a high vacuum pump, shown in figure 5.2.

The roughing pump used is an Edwards RV12 two-stage rotary vane pump that is first used to reduce the internal pressure of the system down to approximately $1x10^{-3}$ mbar. During this regime the pressure is monitored through the use of two Pirani gauges, one of which is located in the foreline which links the roughing pump to the vacuum system, the other is on the high vacuum side of the high vacuum pump. Once the pressure has reached the maximum inlet pressure for high vacuum pump (~10^{-2}mbar), this 'fore' pump is then used as a backing pump for the high vacuum pump.

Figure 5.2 Vacuum system at the downstream end of the apparatus

The high vacuum pump used in this case is an Edwards 100/300M oil vapour diffusion pump. This pump allows the system pressure to be further reduced down to approximately $1x10^{-6}$mbar. In this regime the Pirani gauges can no longer operate effectively therefore ion gauges are now used, one located in the accelerator region, the other above the high vacuum pump on the downstream end of the apparatus. Once the required vacuum has been reached, helium is fed into the system via a high accuracy vacuum needle valve. This allows the pressure of the helium in the system to be set according to requirements.

As the vacuum pumps are located only at one (downstream) end of the system, it is necessary to ensure that all components are constructed in such a way that they do not significantly impede the pumping path of the system. In addition, to aid in the uniform evacuation of the system, an auxiliary flexible hose is connected from the vacuum pumps to the accelerator (upstream) part of the experiment in order to provide a secondary pumping path to mitigate against the restrictions introduced by parts of the beam line apparatus. This is particularly important to ensure adequate evacuation of the accelerator when the discharge components are introduced into the principle axis of the apparatus.

5.3 Solenoids

Strong magnetic fields are required for the plasma confinement and to ensure that the electron beam does not expand due to space charge effects. To provide the necessary field, water cooled solenoids were employed. These solenoids were constructed by wrapping oxygen-free high conductivity copper tubing coated in a plastic electrical insulator around a non-magnetic metallic former. The winding density is 1 turn every 7mm both axially and radially. The windings are always in paired layers with opposite helical pitch ensuring axial orientation of the magnetic field. For the two distinct solenoids, a different number of layers of this copper tubing was used determined by the required magnetic field. When high currents flow through the copper tubing, the heat generated has to be removed by circulating water through the tubes at a high flow rate. This is provided by a water cooling system operating at 23Bar.

For this experiment, two main solenoids were used, as shown in figure 5.3. To provide the necessary high field for plasma confinement, a coil was used that has an overall length of approximately 1.5m and an internal diameter of 64mm formed of 6 layers of windings as described above. To insulate the electron emitter and to ensure a smooth magnetic transition for the electron beam leaving the emitter region in to the main plasma confinement coil, a secondary coil was used. This coil had a length of 0.5m and an internal diameter of 210mm and was formed of 4 layers. The electron emitter cathode was immersed in the field near the centre of this coil.

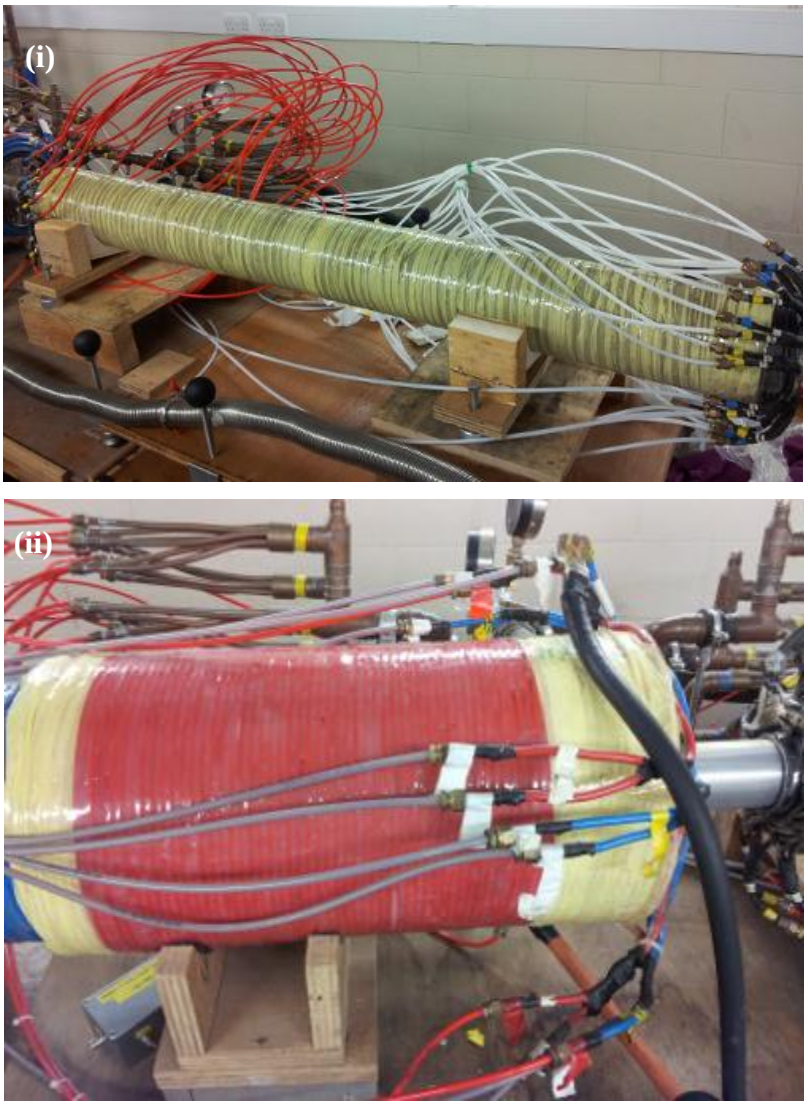

Figure 5.3 Solenoids (i) Main coil for plasma confinement (ii) Secondary coil for electron beam emission region and transition into the main coil

Before the above solenoid setup was built, initial plasma measurements were undertaken using a previously designed Penning trap which used a different solenoid arrangement. This solenoid arrangement utilised a series of three coils, a primary coil of 0.5m length, 10cm inner diameter and wound in ten layers with two shim coils, each 10cm long and formed of 2 layers on each end of the primary coil. The shim coils allowed a longer plateau field than would be possible with a single solenoid. In the case of the initial plasma measurements these coils were all driven by the same current and provided a uniform magnetic field over a length of 20cm.

5.4 Preliminary low current Penning trap design

To aid in the design of the final Penning trap, it was necessary to investigate the performance of a previously designed trap at higher currents. This previous design was constructed to operate at a much lower current (approximately 2.5mA) for use in the laboratory investigation of AKR [McConville, 2009].

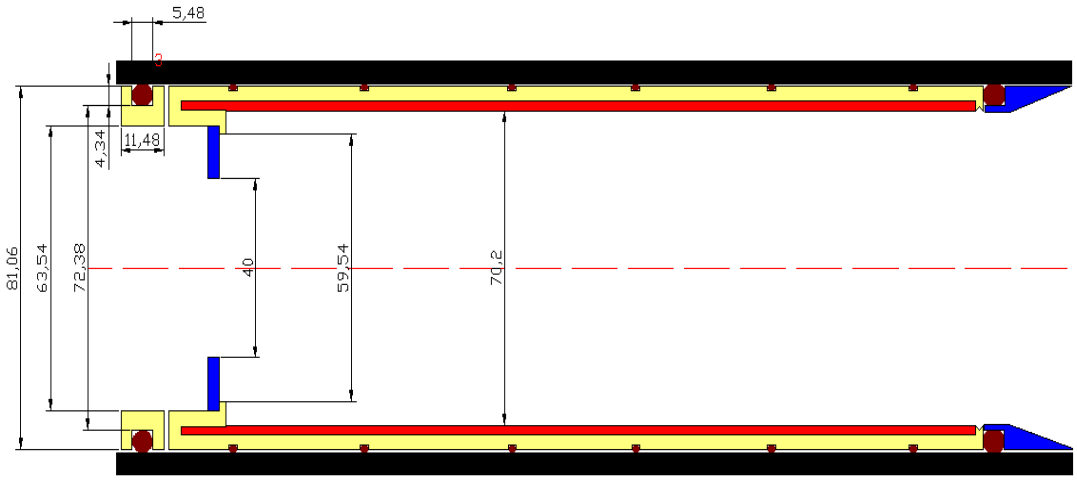

Figure 5.4 Preliminary Penning trap design (yellow=insulator, blue = cathode, red=anode and black = waveguide) [McConville, 2009]

The trap is constructed as shown in Figure 5.4. The anode is a copper tube 0.2m long with an internal diameter of 70.8mm. This is surrounded by electrically insulating nylon interconnecting rings that cover the entire length of the anode, held in place by

two nylon end-caps that the anode edge slots into. This is then wrapped in a film of mylar to aid insulation and insertion into the waveguide cavity. An electrical connection is made by connecting the inner conductor of a coaxial cable to the anode through a gap in the insulating nylon. This coaxial cable is then connected to a custom manufactured HT-BNC vacuum feed-through that allows a potential to be supplied by an external power supply. The power supply circuit schematic can be seen in figure 5.5.

The first cathode is held by one of the nylon end caps and is made of a hollow copper disc with an internal diameter of 40mm and outside diameter of 63mm, approximately 5mm thick. The second cathode consists of a separate spoked copper mesh held in place by a copper ring. These cathodes are electrically grounded to the system waveguide.

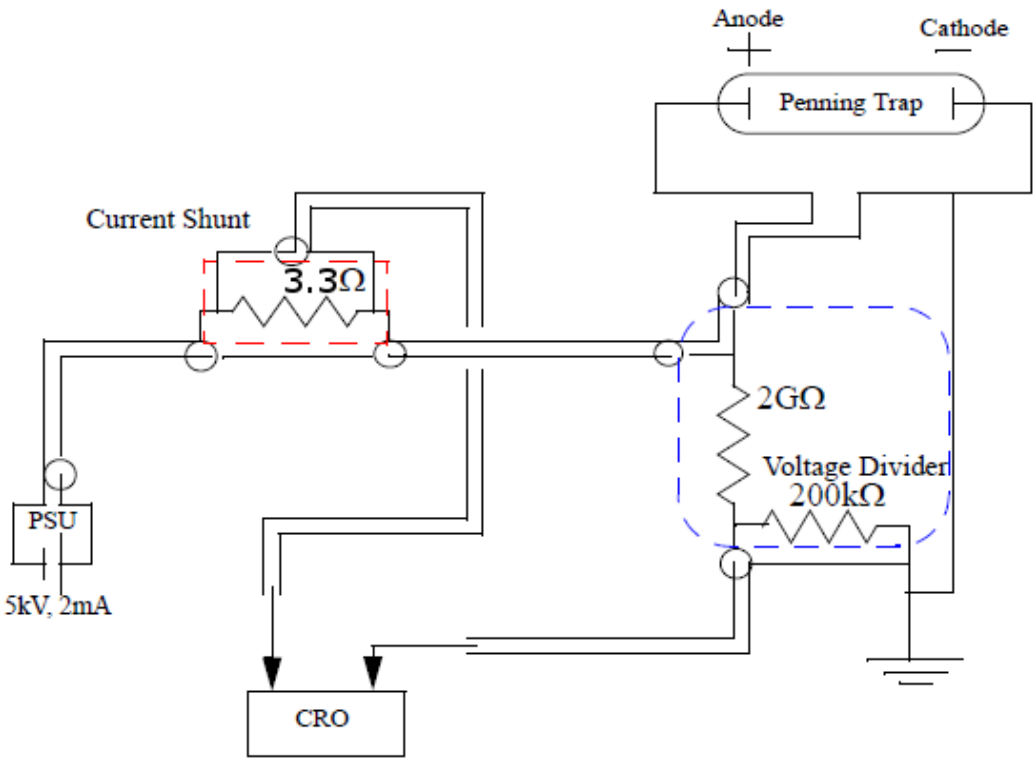

Figure 5.5 Initial Penning trap power supply circuit

For this experiment a background pressure of helium gas is injected into the system, at ~10^{-4} mbar. A voltage is then applied to the anode wall of the Penning trap. This

voltage is ramped up to ~1-2kV whereupon breakdown of the gas occurs between the anode and the cathode which begins to draw current from the power supply. This current can then be regulated by the power supply, allowing a degree of control of the discharge.

The experiments with this apparatus allowed investigation into a range of issues that may arise when applying a higher current to a design of this type. It also allowed for the testing of the trap in a pulsed discharge current configuration.

5.5 Redesigned high current Penning trap design

For the main beam-plasma interaction experiment, a longer trap was required to match the numerical simulations. After testing the previous Penning trap design, it was found that the design had a problem with metallic deposition on the insulators at high current. This would ultimately lead to an electrical short circuit between the anode and the cathodes, circumventing the discharge path. To counter this, the Penning trap insulators were redesigned.

Figure 5.6 Modified Penning trap design

Figure 5.6 shows the redesigned Penning trap. The anode has now been elongated to 1m in length and reduced in inner diameter to 50.8mm to match a reduced waveguide inner diameter of 54.8mm (this was necessary in order that the power supplies could magnetise an adequate column length). It was decided that the interlocking nylon rings were not necessary for the voltage hold-off between the waveguide wall and the Penning anode. Instead, the length of the anode was simply wrapped in multiple layers of Mylar. This Mylar was slotted underneath two nylon end-caps which hold the anode in place in the waveguide and are tapered to increase the tracking length between the anode and the grounded outer waveguide. More importantly this ensures that the main

insulator surface is shielded from metallic deposition from the plasma. The design of the nylon end-cap is shown in figure 5.7 along with the first cathode.

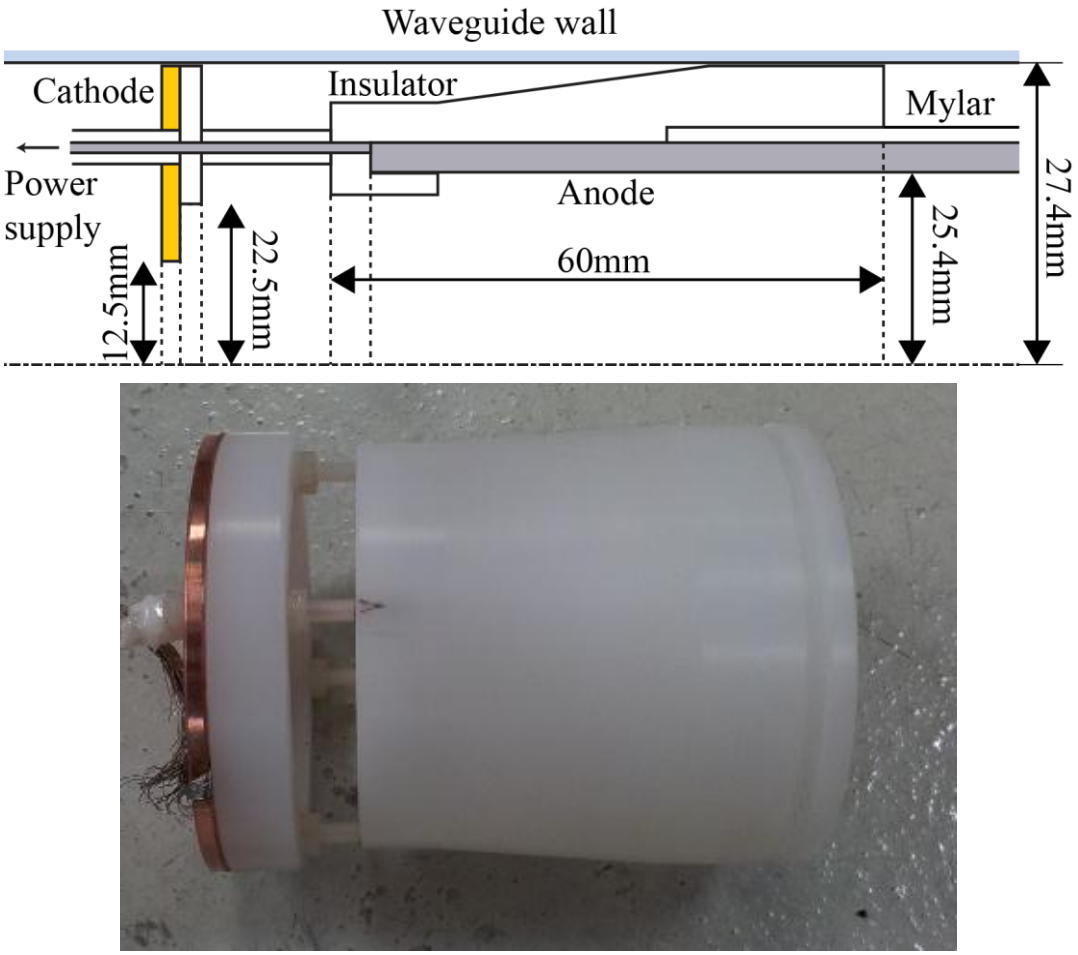

Figure 5.7 Nylon insulators

The first cathode now consists of a hollow copper disc with an external diameter of 59.5mm and internal diameter of 25mm with a thickness of approximately 3mm. An insulating nylon ring is placed in front of the cathode with the same external diameter but inner diameter of 45mm. These two pieces are then spaced 5mm away from the anode edge and held in place by way of four nylon screws. This means that the tracking distance between the anode and cathode is increased with the only path being obliged to follow the thread of the nylon screws.

The anode connection is made again with the inner conductor of a coaxial cable, however, this is now fed through a longitudinal hole drilled through one of the connecting nylon screws.

Initially the second cathode was still the same spoked design as before but constructed from stainless steel and reduced in inner radius to fit in the reduced size waveguide. This cathode was then spaced 5mm away from the anode edge with no physical connection between them. Ultimately this second cathode was removed as the discharge could ignite irrespective of whether it was installed or not. Removing the spoked cathode allowed for easier insertion of the diagnostic probes.

5.6 Penning trap anode power supply

In order to drive a current of up to 400mA into the Penning trap, it is necessary to use a high voltage regulated DC power supply. In this experiment a Glassman PK10R400 was used, capable of providing 10kV and 400mA. As this is a very powerful, regulated supply it was important to place a reasonable resistor stack with high power handling in series between the power supply and the Penning trap. When the discharge in the trap ignites, the resistance becomes variable and potentially 'negative dynamic' which would cause the power supply to be constantly adjusting its output as it attempts to control the current, and the control logic could find problems associated with the highly non-resistive behaviour of the load. By placing a resistance in series with the plasma load, seen in figure 5.8, one effectively reduces the percentage of variation in resistance compared with directly connecting the supply to the trap. The resistors used were 68kΩ wire-wound ceramic resistors. These were typically used in parallel banks of 10, giving a 6.8kΩ resistance per bank with up to 4 banks in series or parallel operation.

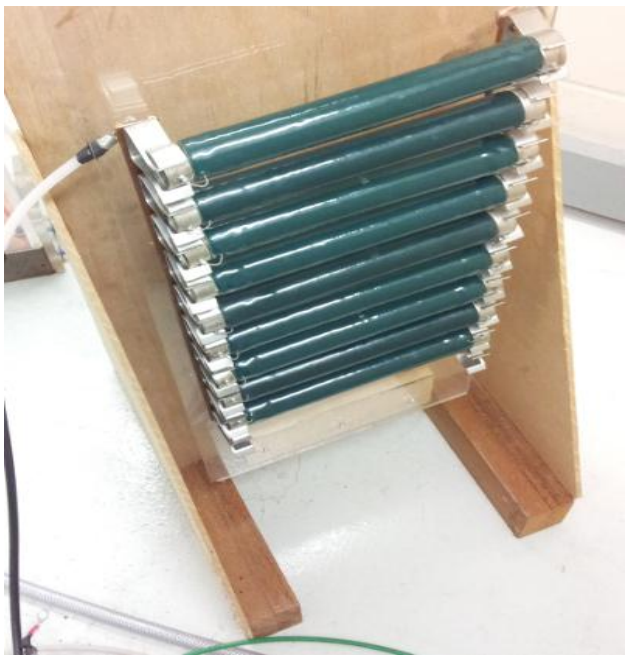

Figure 5.8 Resistor bank

To further reduce degradation of the Penning trap due to heating and/or deposition, it is possible to pulse the current output of the power supply. This allows the plasma discharge to ignite and be maintained at a low baseline current (~5mA) and then only pulsed to higher current (up to 400mA) for a short time (≤~1s) when required.

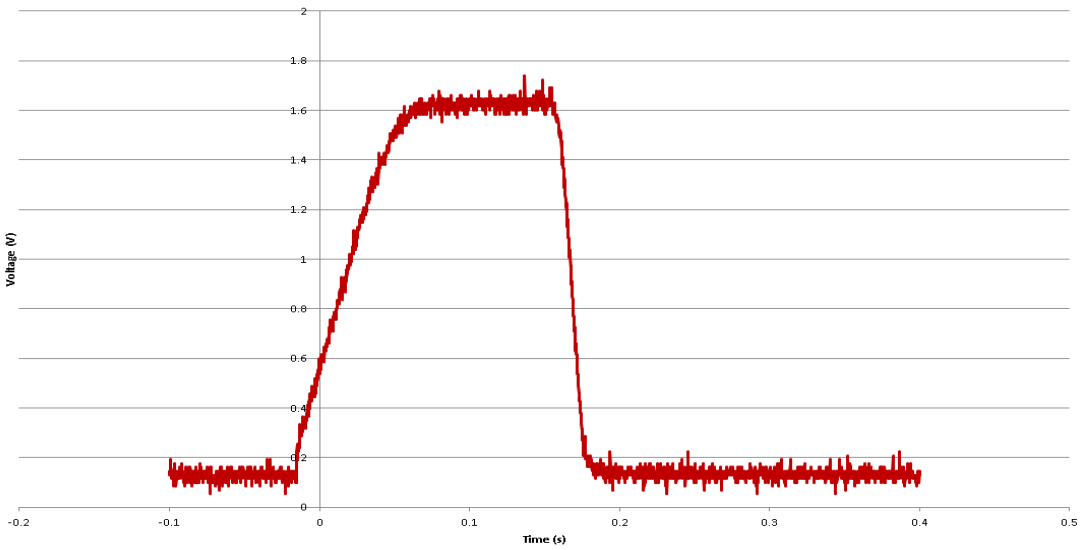

Figure 5.9 Pulse generator pulse shape

To facilitate this modulation of the power supply, a pulse generator was used to generate a pulse that provided a sufficiently long rise time that the power supply could track, shown in figure 5.9. The pulse generator supplied a voltage between 0-10V to the power supply via a serial interface (10V representing full scale deflection). The power supply then produces a current proportional to the pulse voltage between 0-400mA. This pulse generator was ultimately switched for arbitrary waveform generator which provided a better control of the pulse rise and fall times. This could provide computer controlled pulses to the power supply that would ensure a greater discharge stability and control of the ramp rates of the current through the pulse. This had the drawback of only being able to generate a pulse of 1V, giving a maximum discharge current of 40mA for the experiments reported here.

5.7 Electron beam generation

The electron beam is produced by a cathode and anode arrangement that was designed using the numerical results shown in section 4.8. The cathode and emitter surface are mounted on a long aluminium cathode stalk that extends the cathode close to the interaction region of the Penning trap. The cathode itself is constructed from a solid disc of copper with a velvet emitter surface secured to the front face. The anode is constructed as a stainless steel mesh positioned at a distance of 20mm in front of the cathode surface. The mesh spokes are chemically etched to a fine scale to ensure that the electrons can stream through with minimal interception. Both the cathode and anode can be seen in figure 5.10

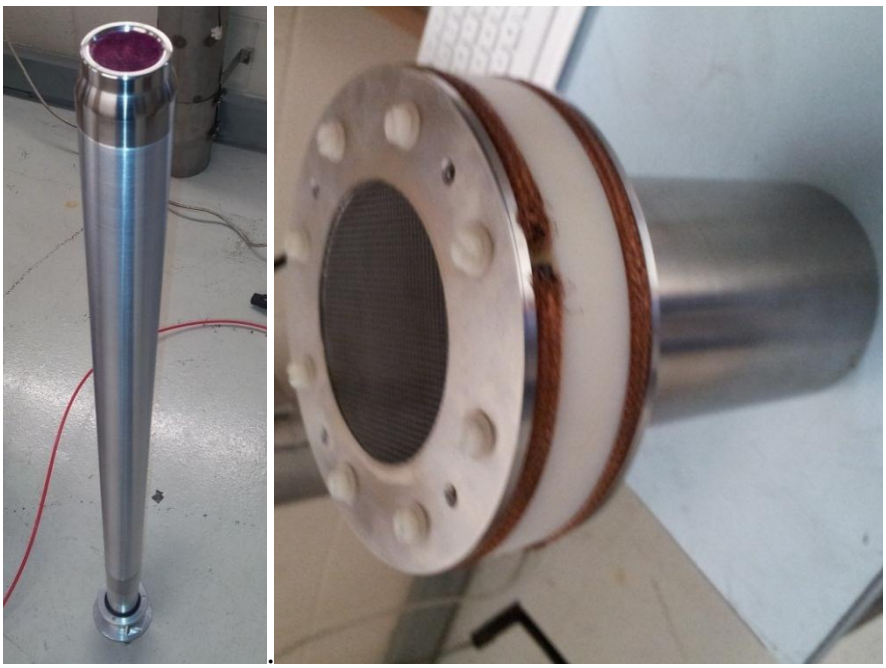

Figure 5.10 Electron emitter cathode and anode

By applying an electric field to the cathode, greater than the critical field (>30kV/cm) necessary for electrical breakdown, and keeping the anode at ground potential, the fibres of the velvet material will begin to emit electrons due to field enhancement. The fibre material sublimates to form a plasma on the cathode face which expands outward at a velocity of ~$2x10^{6}ms^{-1}$. Electrons are then emitted from this plasma surface towards and through the anode mesh. For this type of emitter, if the applied voltage pulse length is too long, the plasma will expand fully to the anode causing the system to short in a vacuum arc. Around the cathode are rounded wings constructed from 316L grade stainless steel. Aluminium is used to keep the weight down in the cathode stalk, but for the emitter 'wings', stainless steel is essential due to the relatively aggressive environment created during the cathode discharge. These 'wings' shape the electric field in the vicinity of the emitter surface, ensuring that the electrons are emitted perpendicular to the cathode surface. In addition, the cathode is also fully immersed in the magnetic field produced from the secondary coil assisting in preventing the emitted electrons from expanding beyond the radius of the emitter surface.

5.8 Electron emitter firing circuit

In order to apply high voltage rectangular pulses of ~100ns to the electron emitter, a special type of double stacked Blumlein [Somerville, MacGregor and Farish, 1990] system is utilised, as pictured in figure 5.11.

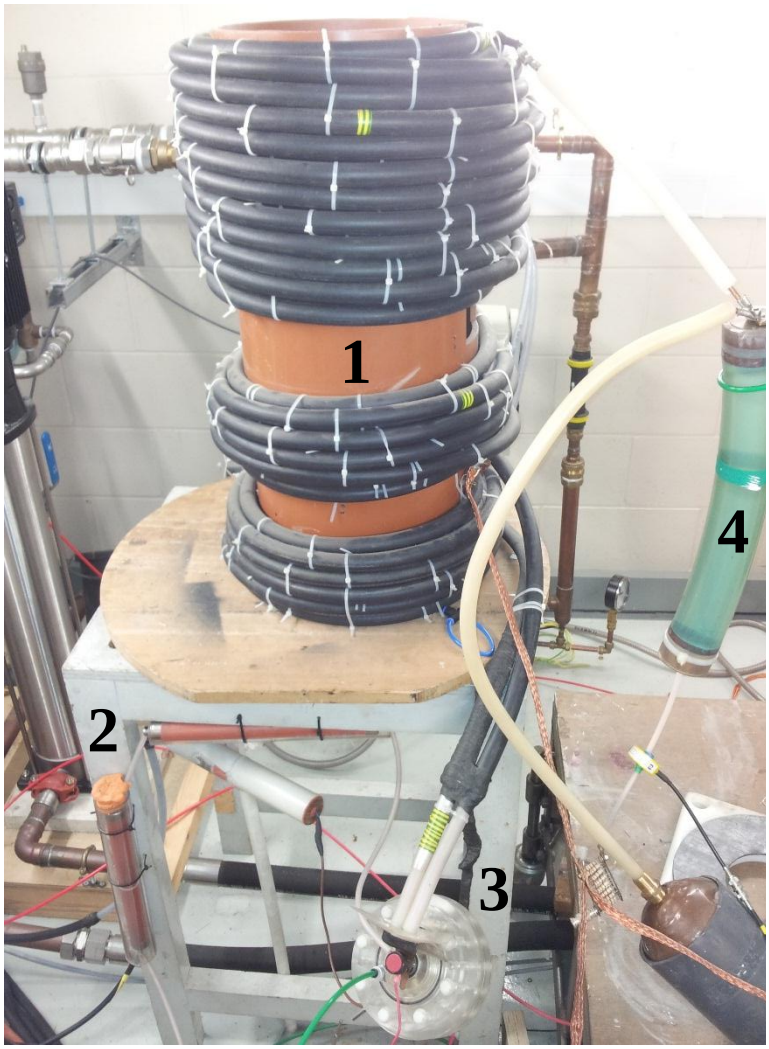

1. Pulse forming cables

2. Charging resistors

3. Spark gap

4. Ionic resistor

Figure 5.11 Blumlein system

This system operates through the use of four cables that are each charged in parallel to a voltage V_{charge}. These cables are then discharged in series through the electron emitter in parallel with an ionic resistor that is connected to ground, producing a voltage of $2V_{charge}$ (the resistor/accelerator combination is similar to the 200Ω impedance of the 4 cables in serial configuration, so half of the 4 V_{charge} signal amplitude appears over

the power supply and half over the load). This resistor is made using a saturated copper sulphate ($CuSO_4$) solution which is capable of withstanding the high peak powers that are used to generate the electron beam. In order to trigger this system, a mid-plane spark gap was used in conjunction with a Thyratron.

This spark gap is constructed as three conducting electrodes that are separated by a pair of gaps filled with a pressurised gas (Nitrogen). When a sufficiently high voltage is applied across the gaps, a spark is generated that ionises the gas. This has the effect of rapidly reducing the electrical resistance between the electrodes to virtually zero. The central electrode is initially kept at an intermediate DC potential to provide the same field strength in each half of the gap. The middle electrode is perforated so that when either half of the gap fires, the plasma can easily fill the other half, completing the circuit. A thyratron is used to short the middle electrode of the spark gap to ground which induces breakdown in the other side of the spark gap. Closing of this switch converts the Blumlein cables from parallel to series. The schematic for this is shown in figure 5.12.

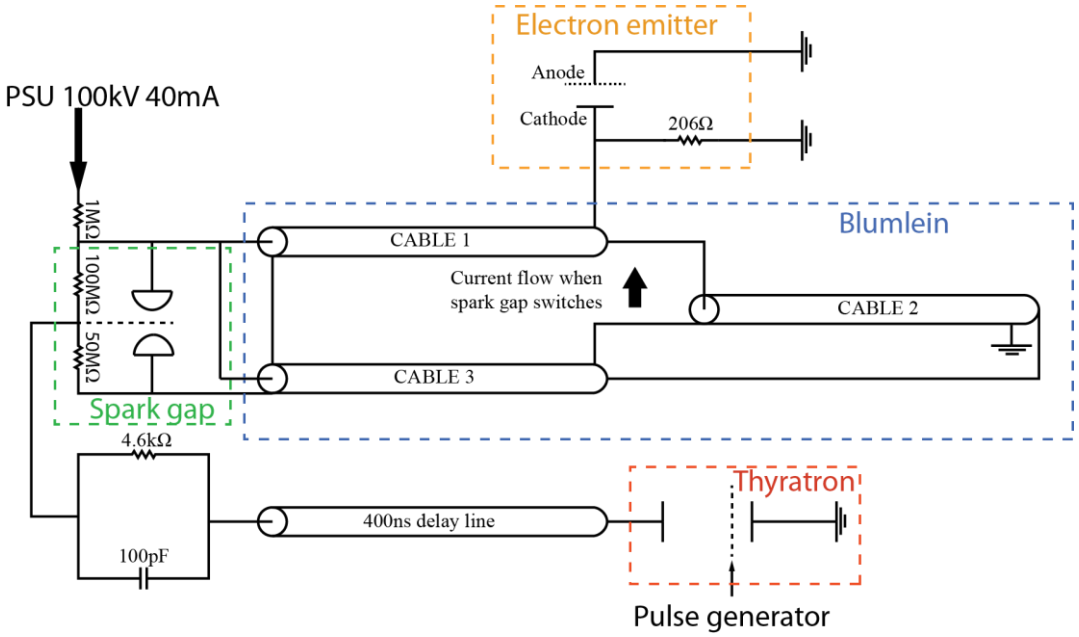

Figure 5.12 Blumlein circuit schematic

In order to monitor the voltage and current applied to the cathode during the pulse, two Rogowski coils were used (see section 5.9.2). The first monitored the current drawn through the 206Ω ionic resistor and could therefore be used to indirectly measure the cathode voltage. The second monitored the current flowing from the anode to ground allowing the total cathode current to be measured. The role of the 206Ω resistor was twofold. In the first instance it permitted measurement of the electron energy via the current flowing in this circuit branch. Its primary role however, was to define the maximum output impedance perceived by the pulsed power generator (the output impedance of which is 4 x 50Ω, from the serial superposition of the four co-axial lines). This prevents reflections and strong pulse distortion that could otherwise corrupt the form of the HT pulse applied to the cathode of the accelerator, since the accelerator initially presents a capacitive load which switches rapidly to resistive behaviour. The resistor achieves the latter effect at the price of halving the output voltage for any given charging voltage.

5.9 Diagnostics

5.9.1 Faraday cup

In order to diagnose the current of the generated electron beam, a Faraday cup was used, pictured in figure 5.13. This device is placed directly in the beam path and is used to capture the electron beam and from this determine it's current. The Faraday cup has been designed with a conical cross-sectional beam collector which aids in the collection of any secondary electron emission due to beam impact. The collector is mounted to a nylon support structure that has multiple holes drilled to allow for a vacuum pumping path. The cup is grounded through a 50Ω resistance and then the output is shunted by a 50Ω co-axial line to an oscilloscope which was also terminated in a 50Ω impedance. This gives a total impedance of 25Ω to ground enabling the beam current to be measured from the voltage developed across the resistance.

Figure 5.13 Photograph showing the Faraday cup used in the experiments, illustrating the 50Ω resistors, copper sliding contact, conical beam receiver and the nylon support structure with vacuum pumping apertures

5.9.2 Rogowski Coils

In order to measure the current flowing at different points in the system without making physical contact to the apparatus, Rogowski coils are utilised. These coils consist of a coil of wire wound around a torodial former (the secondary), constructed from a mu-metal magnetic material, which are placed around a wire (the primary) carrying a current flow (though in principle they can also be used to measure currents flowing in free space). When the primary current changes, the change in the magnetic field produced by the primary current linking the secondary coil induces a voltage around the windings of the secondary which can be monitored. This voltage is nominally proportional to the differential of the primary current due to Faraday's law. However, the coils in these experiments are operated in the self-integrating mode, whereby the dominant impedance in the output circuit is the self-inductance of the secondary winding itself. This means that by measuring the voltage across a resistor in parallel with the secondary winding one obtains a signal that is proportional to the current in the primary. This constrains the minimum frequency (maximum pulse length) for the validity of the calibration. By ensuring that the coil is wound as uniformly as possible, other sources of magnetic fields may be prevented from inducing undesired voltages. These coils were commercially sourced from Ion Physics

and should therefore have a reasonable degree of coil uniformity. Their specification was that they had a sensitivity of 1.0 V/A into a 50Ω termination for a maximum pulse duration of ~10μs.

5.9.3 Plasma probes

For a plasma discharge, it is important to be able to measure electron temperature and density. To achieve this, a Langmuir type probe was inserted into the plasma discharge region, whilst an ionisation gauge was used to measure the background gas density. The initial probe design, used on the low current Penning trap, was constructed simply by stripping back the outer insulator and outer conductor of a solid core coaxial cable leaving only the inner conductor and insulator. This was then cut to produce a planar face, giving a near circular collection area on the inner conductor, as shown in figure 5.14.

Figure 5.14 Photograph of a simple probe fabricated from co-axial cable

In the initial measurements using the Penning trap designed for low currents, this probe was held in place by a rigid nylon support structure. The probe is then connected to a high voltage supply that drives current through the probe tip to achieve a chosen electrical potential. By measuring the current drawn at a variety of voltages it is possible to obtain the I-V characteristics of the Langmuir probe. From this measurement it is possible to achieve an estimate of the plasma electron temperature and electron density as shown in section 2.9.

Figure 5.15 Tungsten probe with glass insulator surround

For the high-current Penning trap, more robust probes were found to be required. To this end, custom probes were constructed from tungsten wire of various thicknesses that were surrounded by a glass insulator, an example of which can be seen in figure 5.15. These materials are able to withstand the higher currents and temperatures produced by the higher density, higher power plasma. These probes function as Langmuir probes in a similar manner to the previous low current examples. A range of probe tip configurations were manufactured, including probes with barrel tips where the collection surface is the tip and 'waist' of a cylinder, and probes where the tungsten wire was completely enclosed by the glass except for the tip. A third configuration was a so called 'baffled' probe where the tip of the probe was blocked by a dielectric and the collection surface was exclusively the waist of the cylinder. The key difference between these configurations arises from the fact that the probe can only be practically inserted into the Penning trap orientated along the axis of the magnetic field system. This means that the tip will tend to collect particles travelling across the magnetic field. Baffling the tip of the probe would be expected to change the relative collection of the ions and electrons since the electron orbital size is likely to be less than the ions. In addition, these probes can be used as an RF pickup antenna that can be connected to a spectrum analyser to observe the RF fields that are produced longitudinally due to the plasma oscillations. This will give an approximate measure of the plasma frequency and as such an alternative measurement of the plasma density. The RF signals were measured on an Anritsu MS2036A spectrum analyser.

Chapter 6 : Laboratory experimental measurements

6 Laboratory experimental measurements

In order to build upon the numerical simulations showing the complicated behaviour of the particles in the saturated regime of the beam-plasma simulations, it was decided to construct an experimental apparatus to ultimately investigate the long-time evolution of the beam-plasma instability. The experiment would aim to achieve similar beam currents, beam diameters and energies to those used in the simulations, with comparable densities. Key differences between the simulations and the experiment were that the experiment would (at least initially) use helium, not hydrogen gas, which would tend to increase the time scales of the ion processes, whilst the electron temperature is expected to be initially cooler. The previous chapter shows the key features of the apparatus. Here preliminary measurements of the performance of the components of the apparatus, specifically the solenoid magnet coils, the gas discharge column, electron accelerator and beam are presented with some preliminary measurements of the transport of the electron beam through the plasma column.

6.1 Magnetic field generation

As the experiment was to depend on a high current Penning trap configuration to confine the plasma electrons, as well as require magnetic confinement for the formation and transit of the electron beam, it was necessary to confirm that the axial profile of the magnetic field generated by the new 1.5m long solenoid, defined in section 5.3, was adequately smooth and to calibrate the magnetic field generated as a function of the current flowing through the windings. To conduct this measurement, a nylon cylindrical disc was manufactured to fit inside the inner diameter of the main solenoid. This disc had a hole drilled through the centre into which a Hall effect probe was inserted. This enabled the probe to slide through the length of the coil allowing axial magnetic field measurements to be taken through the end section of the solenoid to the plateau region (the area approximately one diameter inside the coil end).

The magnetic field was generated in the coil by allowing a relatively small 31.6A current to flow through the coil, which required a voltage of approximately 20V

(dependant on temperature) using a spectroscopy grade linear regulator power supply. This produced an adequate field to allow accurate measurement with the Hall effect sensor.

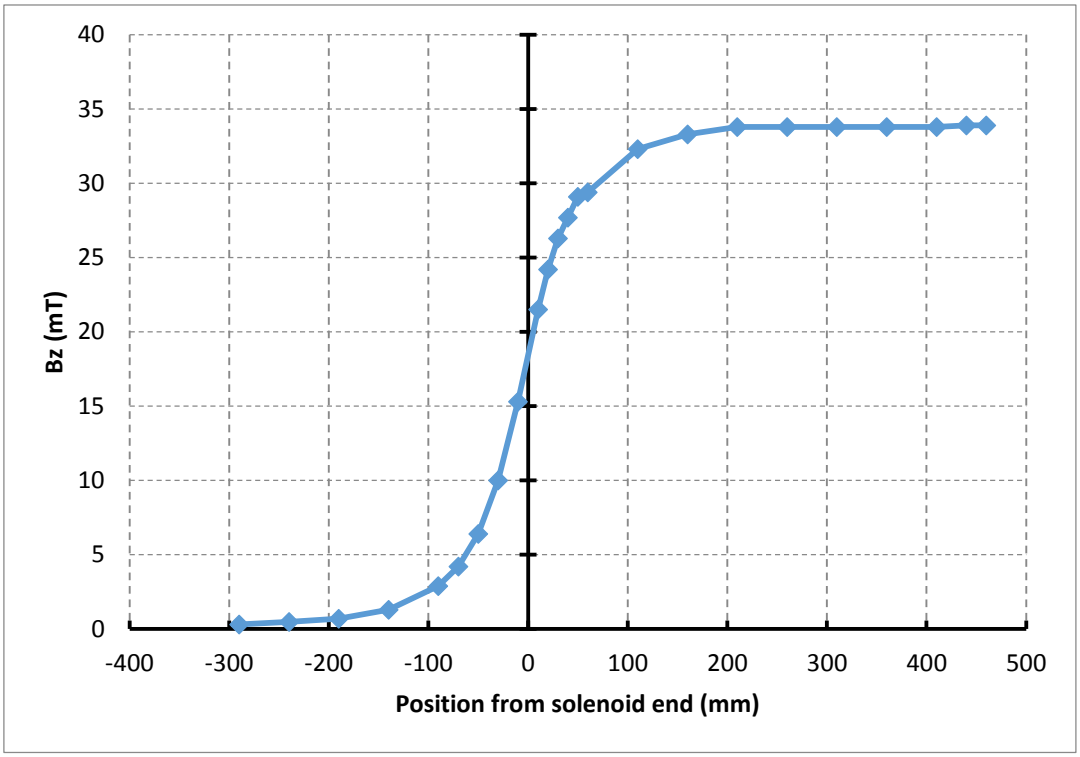

Figure 6.1 Axial magnetic field profile of the plasma confinement coil

Figure 6.1 shows that by moving in approximately 15-20cm from the end of the coil the magnetic field reaches a stable plateau. This gives a maximum plateau field of 0.322T at the maximum current of 300A of the power supply.

6.2 Preliminary DC plasma I-V characteristics tests

To understand the issues that might arise when attempting to operate a Penning trap at a higher plasma density (which is assumed to imply a higher operating current), the initial low-current design [McConville, et al., 2008] was first investigated, initially using a lower current, relatively simple power supply. This was the supply originally intended for use with this Penning trap. Figure 6.2 shows the I-V characteristic plots for the external electrical circuit at different background gas pressures. These tests

were conducted with a magnetic field of 0.32T generated by a magnet coil current of 200A. Note that the magnet coil used for these tests had a different winding configuration from the coil described in section 6.1.

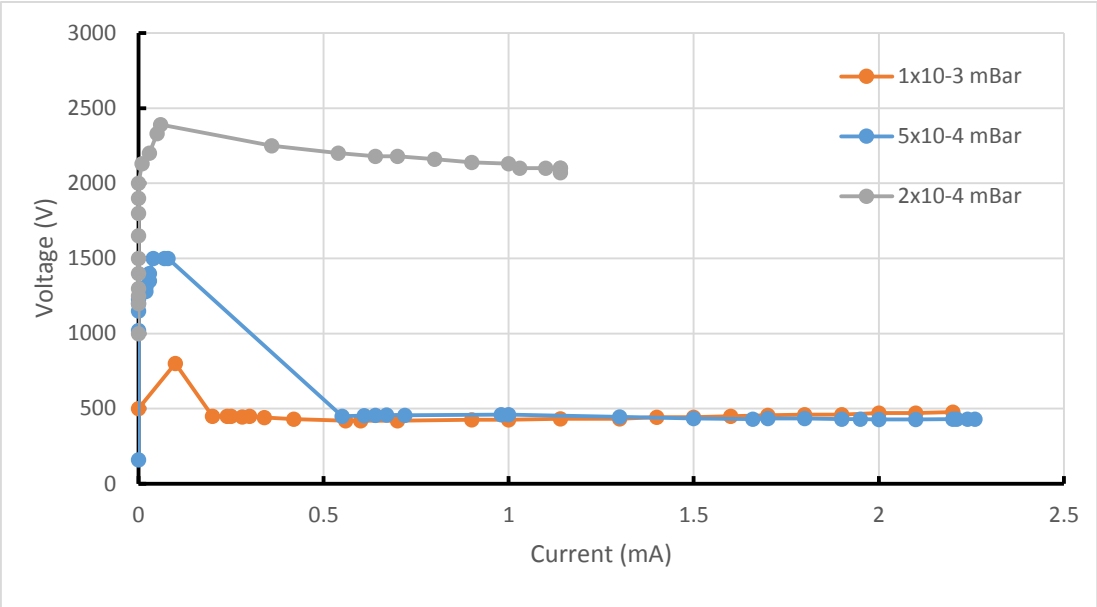

Figure 6.2 Preliminary plasma discharge I-V characteristics using a non-regulated anode power supply at different helium gas pressures

As can be seen, at all pressures, before the Penning discharge fully ignites, the system presents a relatively high approximately resistive load with the voltage increasing quickly for relatively little increase in current (of course at the very lowest voltage settings, the current is zero). Once the discharge ignites, the voltage drops sharply and the current increases. After this point there are typically regions where the voltage drops as the current is increased, with the exception of the higher pressure $1x10^{-3}$ mBar case. Here the voltage drops but then begins to rise slightly again with increasing current. With this power supply, the two higher pressures show relatively stable operation at approximately 0.5 to 2 mA with a higher voltage required to drive the discharge at lower pressures limiting its range in current to 1mA (over which range it was also stable).

For the beam-plasma two-stream experiments however, the Penning trap must be operated at a much higher anode current to achieve the required plasma density, the

previous experiment having achieved a density of ~$10^{15}m^{-3}$ with a current of 2.5mA. Using the same trap design as before, a higher current (400mA, 10kV), switched mode, current and voltage regulated power supply was connected to the anode in series with a 13.6kΩ load resistance. The I-V characteristics of the resultant discharge are again plotted for a range of different gas pressures in figure 6.3.

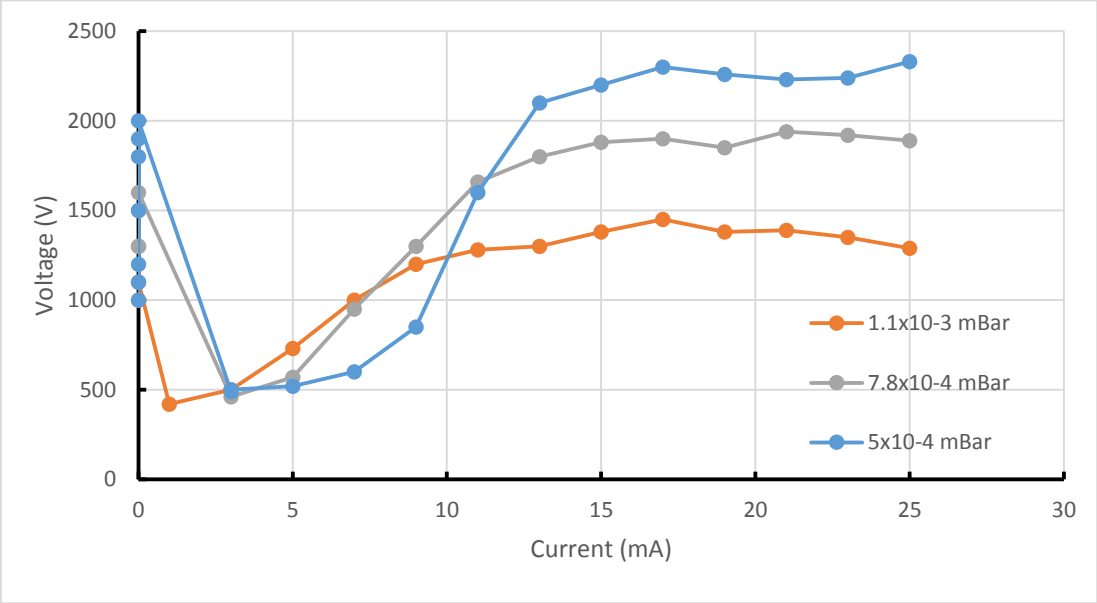

Figure 6.3 Preliminary plasma discharge I-V characteristics using a regulated anode power supply at different helium gas pressures

Similar behaviour is observed as the voltage rises with little current flowing before the discharge ignites. Again the voltage drops and the current rapidly rises once the discharge lights. For this supply configuration however, the discharge was rather unstable between 2-5mA, making measurements in that range difficult. Higher background gas pressures produced a more stable discharge in that low current range. At higher currents (i.e. > 5mA) the current and voltage were stable, and the voltage quickly rises with increasing current before reaching an apparent plateau.

For these pressures the helium ions will be collisionless over the scale lengths of interest found from the numerical simulations (~3cm). The mean free-path of the helium for $1x10^{-3}$mbar will be ~23cm. The drift of the ion perturbations was

approximately 10cm which would give an upper limit to the pressure of ~$2x10^{-3}$mbar to ensure a collisionless plasma over the ion length scales of interest.

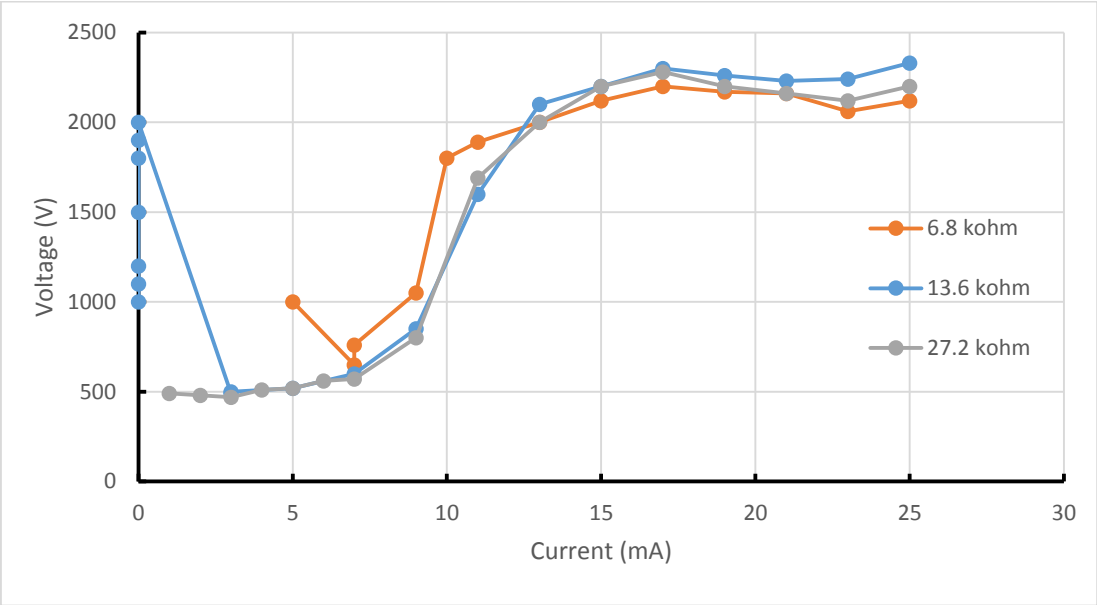

Figure 6.4 Preliminary plasma discharge I-V characteristics using a regulated anode power supply at different protection resistances at $5x10^{-4}$ mBar

Due to the regulation electronics of the higher current power supply, it is interesting to investigate the impact of the resistance in series with the Penning trap. Figure 6.4 shows the discharge characteristics at a fixed pressure at three different ballast resistances.

At higher currents (>13mA) the behaviour is broadly similar, however, with the lower load resistance of 6.8kΩ the system begins to become very unstable below 13mA making measurements difficult. At the higher load resistance of 27.2kΩ the lower currents become significantly more stable. This implied that higher load resistances yielded more stable behaviour from the regulated power supply as expected. In fact, the load resistance is fairly small compared to the discharge impedance, however the resistors (wire-wound on a ceramic frame – specifically built to dissipate significant heat whilst supporting high voltages) also provide a degree of inductance. The discharge has relatively complicated and dynamical I-V characteristics and the feedback regulation electronics of the power supply are designed for a primarily stable resistive or RC (resistor-capacitor) type load. It seems likely that the enhanced stability

arises from the resistors inhibiting the power supply regulation circuit responding to minor transient changes in the plasma.

6.3 Preliminary pulsed plasma I-V characteristics

In order to attain higher current levels on the discharge without causing too much degradation of the Penning trap, particularly the insulating components, many of which are in close proximity to the electrodes, it was necessary to attempt to pulse the anode current. It was found, in general, when the background gas pressure was lower, the behaviour of the apparatus could also become unstable at higher currents so all preliminary pulsed plasma tests were conducted at a pressure of $1x10^{-3}$ mBar. These measurements were also conducted with a magnetic field of 0.32T.

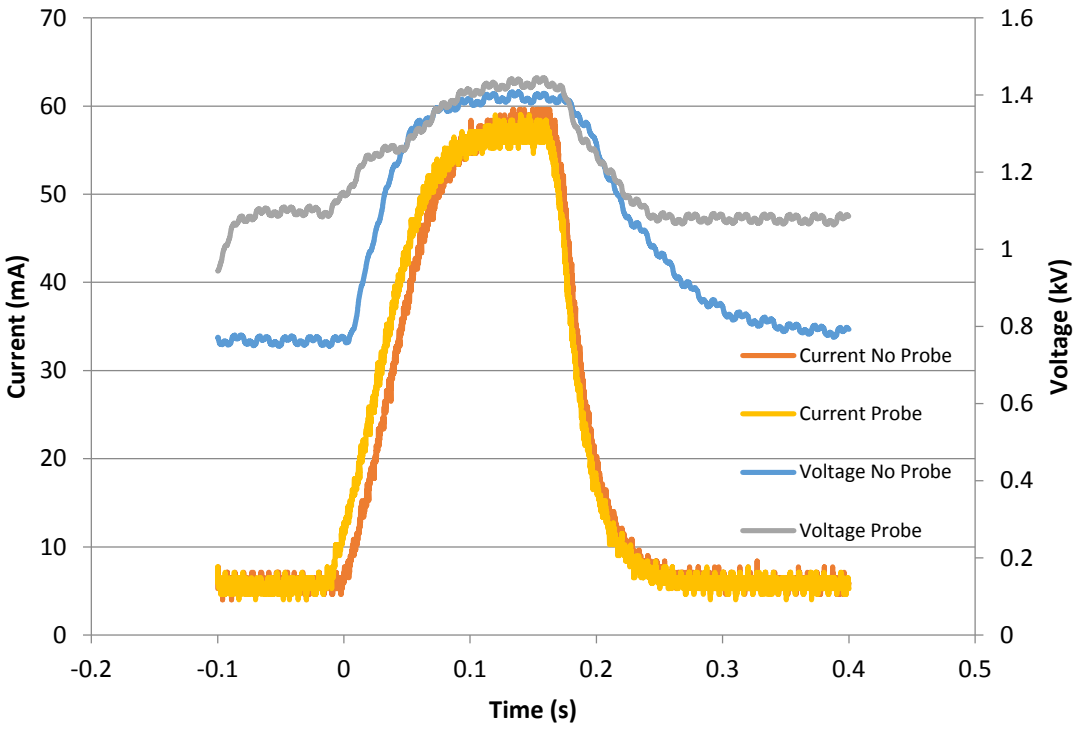

Figure 6.5 Preliminary pulsed plasma discharge voltage and current measurements of a pulse rising from 5mA to 60mA with and without the plasma probe inserted at $1x10^{-3}$ mBar

As noted previously, a higher load resistance in series with the Penning trap gave a more stable discharge, particularly at low current levels. However, for the pulse

measurements it was necessary to reduce the resistance back to 13.6kΩ as at higher current values the power supply could not ramp the current fast enough to follow the desired pulse trace. Figure 6.5 shows the typical voltage and current measurements for a pulse where the current increased from 5mA to 60mA. This plot also shows the behaviour both when there were no probes within the plasma discharge and when a probe has been inserted approximately 3cm into the plasma column. As can be seen, the probe insertion does not make a major change to the discharge behaviour, however the voltage required to maintain the plasma discharge at 5mA is approximately 200V higher in the presence of the probe. At higher current levels there is no sensitivity in the external circuit response of the discharge to the presence of the probe.

In order to investigate the I-V characteristics at higher currents, the above pulse measurement was repeated, increasing the pulse maximum each time for a range of 20mA to 100mA with the results shown in figure 6.6.

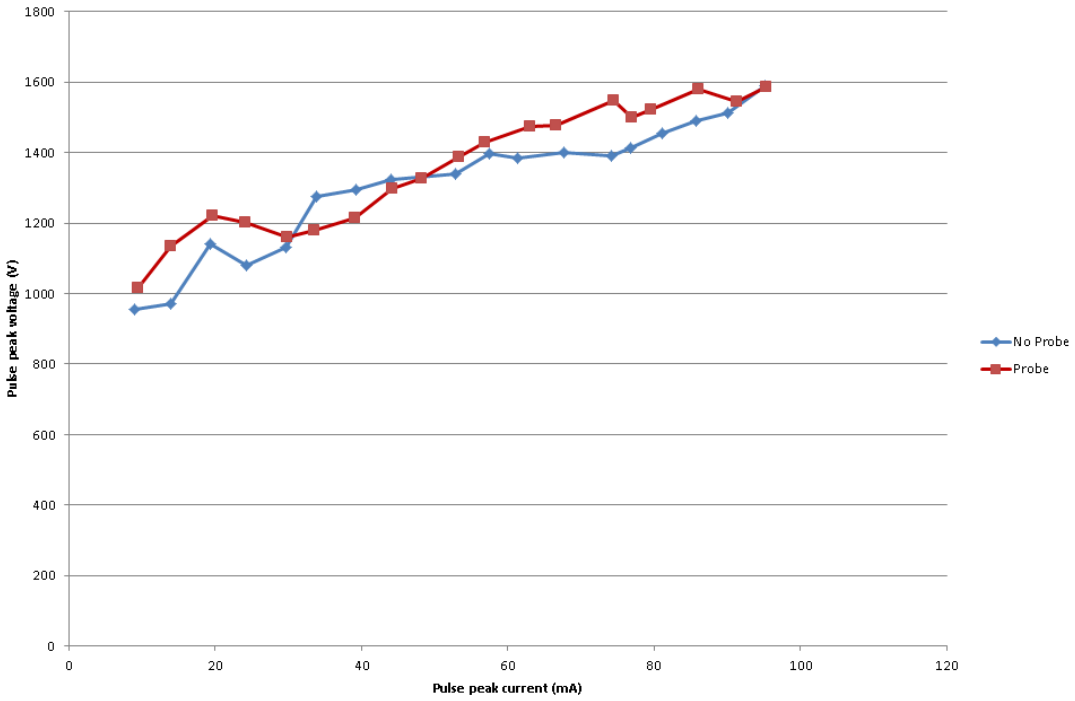

Figure 6.6 Preliminary pulsed plasma discharge, peak pulse I-V characteristics, comparing the behaviour with and without probe insertion at a pressure of $1x10^{-3}$ mBar

The I-V characteristics of the plasma above 20mA appears to be relatively linear in its response both with and without the probe inserted. There does not appear to be a particularly significant impact on the external macroscopic electrical behaviour from inserting the probe at these currents. This suggests that the probes do not seriously perturb the electro and magneto static geometry of the Penning discharge at adequately high levels of discharge current. It should be noted however, that the probe was inserted no more than a few cm from the end of the discharge anode.

6.4 Preliminary pulsed plasma Langmuir probe measurements

Langmuir probe measurements were taken by applying a bias voltage on to the probe and recording the current flowing through the probe tip. For this measurement the pulsed current in the Penning trap was modulated between 10mA and 60mA with the results shown in figure 6.7.

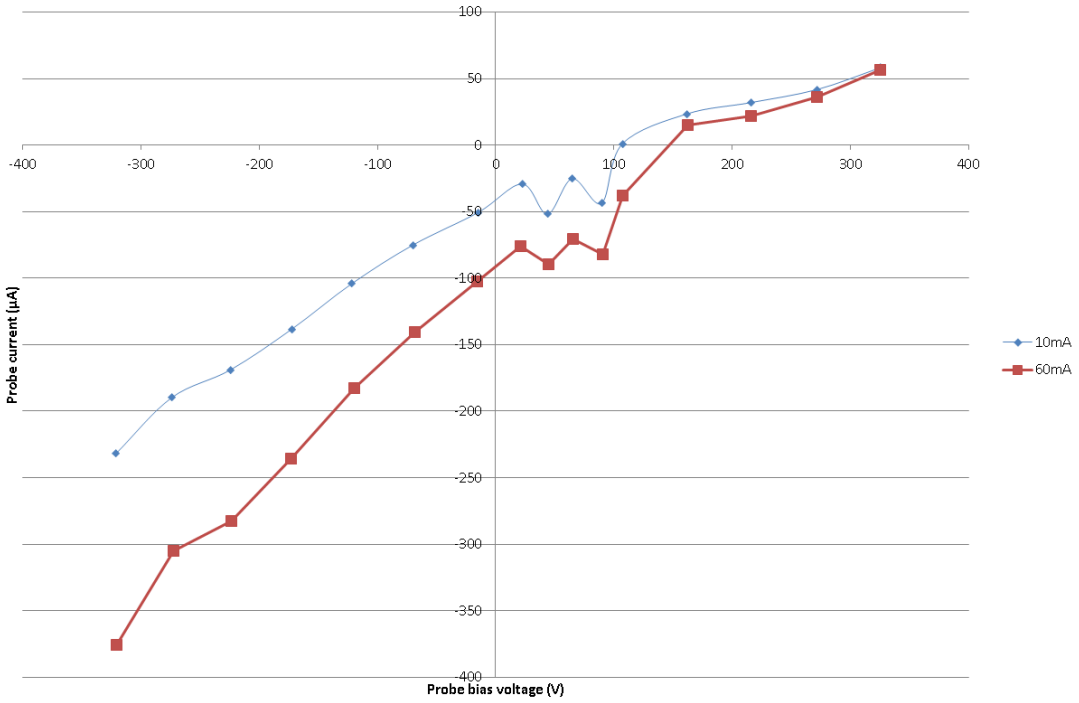

Figure 6.7 Preliminary pulsed plasma discharge Langmuir probe I-V characteristics for 10mA minimum and 60mA peak current at $1x10^{-3}$ mBar

Due to the nature of the pulse measurements, it was possible to measure the probe current for both the baseline 10mA plasma current and the peak 60mA plasma current at each bias voltage nearly simultaneously. If Langmuir probe theory were applicable, it should have been possible to take the logarithm of this plot and determine the electron temperature from the gradient of the curve, however, the results show oscillatory behaviour near the important 'knee' of the curve which suggested problems with the measurements. Moreover (and this proved to be a common issue with these measurements), the electron saturation current was fairly small, whilst the ion saturation current was not obviously found. This is thought to correspond to the differential orbital radii in the magnetic field allowing the probe to collect the ions much more freely and over a larger volume than the electrons.

6.5 Performance of electrical insulators

During the probe measurements referred above, in section 6.4, the electrical performance of the trap eventually deteriorated, with very bright arc breakdowns being observed occasionally. Ultimately the trap insulators failed short-circuit. After removing the Penning trap from the system, figure 6.8 shows the damage caused to one of the cathodes as well as its nylon insulator. Metal had been deposited onto the insulator which created an electrical connection to the anode, resulting in the short-circuit. Discolouration of areas on the copper cathode also indicated regions where electrical breakdown may have occurred. The observation of the aging of these components and in particular the deposition behaviour informed a new design of Penning trap for use at higher currents to inhibit the deposition of metal on key insulator surfaces.

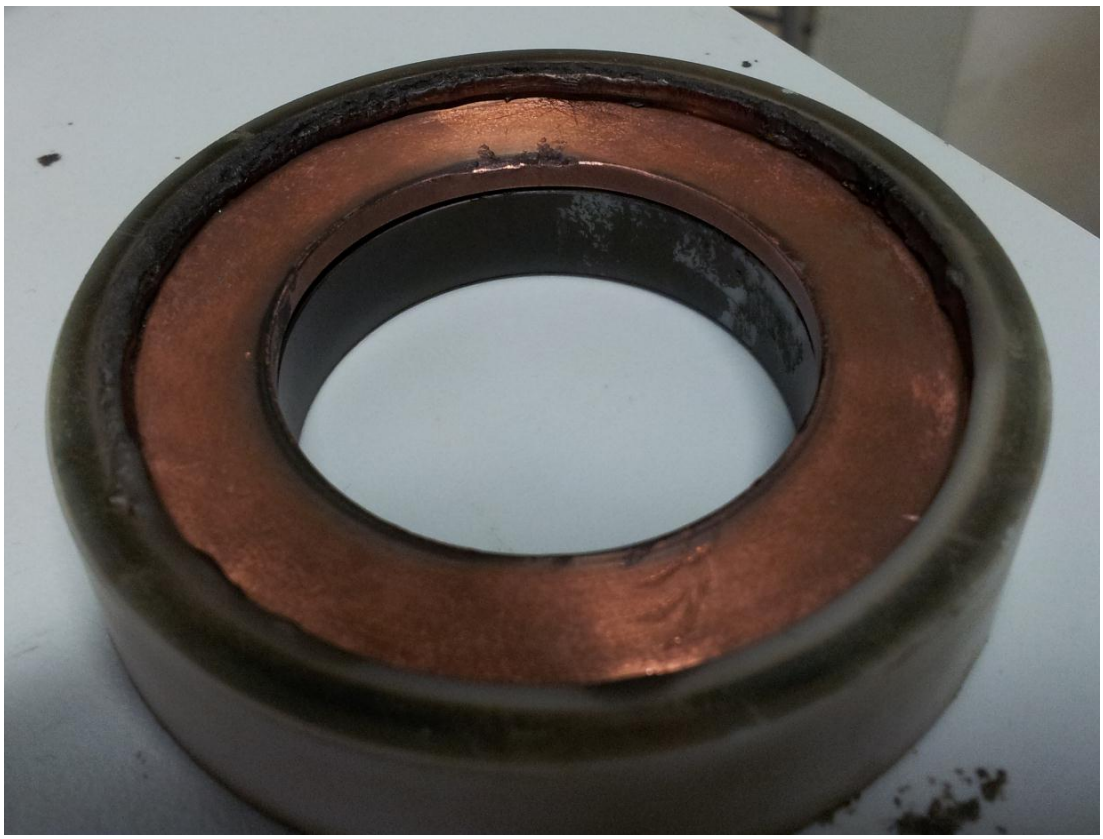

Figure 6.8 Damage caused to Penning trap cathode and insulators due to metal deposition

Figure 6.9 Damage caused to Langmuir probe due to thermal heating and electrical arcing

Figure 6.9 shows the condition of the Langmuir probe after the pulse measurements. Around the collecting face, the plastic insulator had partially melted exposing more of the inner conductor to the plasma. In addition to this, metal had been deposited onto the insulator as well. This would have led to a change in the current collection area of the probe during the experiment and may partially explain the strange behaviour of the I-V plot. For future Langmuir probes it was necessary to use a more robust material as an insulator, and a more robust conductor metal.

6.6 High current Penning trap I-V characteristics

In order to achieve a higher current discharge over a longer longitudinal length whilst minimising the issues caused by metal deposition, a new trap design was developed, as described in section 5.5. In a similar manner as before, the I-V characteristics of the discharge in the new trap were measured and plotted in figure 6.10 for varying magnitudes of confining magnetic field.

For this particular trap diameter and length, it was found that the helium pressure range for stable operation was relatively narrow between $6x10^{-4}$ and $9x10^{-4}$ mbar. Outside of this range, large current transients were common and pulsed operation, in particular, could become unstable with the discharge switching between two distinct modes of operation, one high voltage and low current, the other low voltage and high current. This behaviour was largely mitigated by choosing to operate primarily at a pressure of $7x10^{-4}$ mbar. The magnetic field selected for these experiments was ~0.3T. This was chosen as it was close to the maximum capacity of the power supply driving the system, and approached the 0.4T assumed in the simulations, providing strong transverse guidance and confinement of the electrons. Simulations were undertaken to verify that providing the magnetic field was strong enough to provide a high degree of transverse confinement to the plasma, the dynamics of the beam plasma interaction were independent of the exact value of this magnetic field.

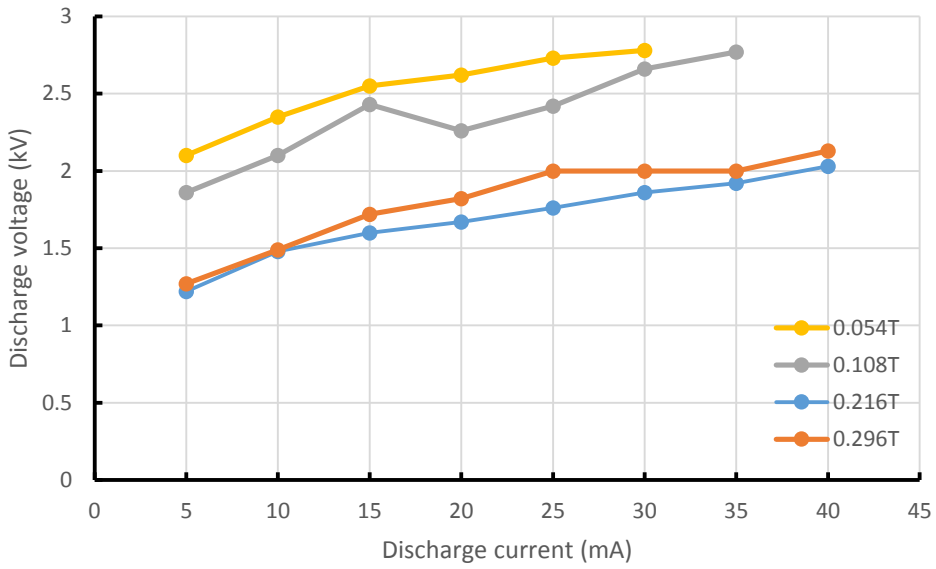

Figure 6.10 I-V characteristics of the new, high current Penning discharge as a function of insulating magnetic field

6.7 High current Penning trap Langmuir probe measurements

In a similar manner to the low current trap design, Langmuir probe measurements were attempted to diagnose the properties of the plasma. In this case the probe was formed of tungsten wire encapsulated in glass. Various different probe tip configurations were fabricated including probes with cylindrical tips and probes which only exposed the circular end of the wire, as described in section 5.9.3. The probes were inserted approximately 2cm beyond the edge of the Penning trap, with the probe axis aligned with the magnetic field. Again the probe was held at a specific bias voltage and the current in the sheath measured using an ammeter. Figure 6.11 shows the relationship that was observed between the probe bias voltage and the current that flowed through the probe. As can be seen, whilst there was a general trend that would normally be associated with Langmuir probe I-V characteristics, there were various anomalies and systematic instabilities in the measurement. The floating potential of the probe was measured as approximately 790V. When the natural logarithm of the current density was taken and the gradient determined, the resulting electron temperature was estimated to be on the order of ~100eV. This temperature is not believable for this type of discharge therefore it is not sensible to determine the plasma density from this measurement.

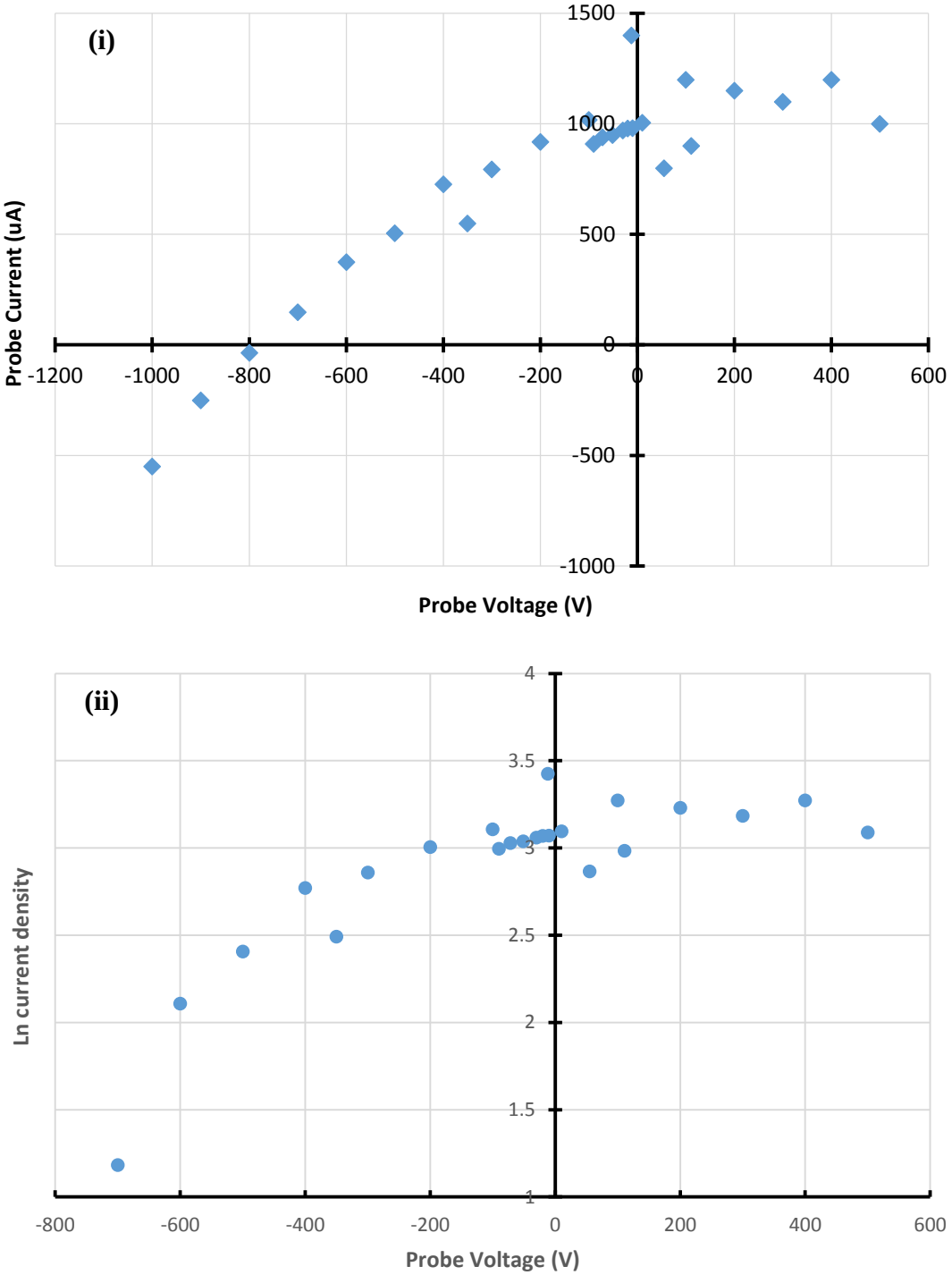

Figure 6.11 Langmuir probe measurements for high current trap design (i) current measured on the probe (ii) natural log of the current density collected on the probe

Further attempts to measure the electron density with the Langmuir probe technique were made using the different probe tip arrangements. None of these however provided any significant improvement on the measurement of the electron temperature. For a

magnetic field of 0.322T generated by the solenoid and an expected electron temperature of 5eV and an ion temperature of 0.5eV, the Larmor radius of the electrons would be ~17μm whereas the helium ions would be ~145μm. This difference in the two radii may alter the collection current of both species on the probe surface which could render the thermal assumption across the probe sheath invalid.

6.8 High current Penning trap plasma frequency measurements

As the probe I-V characteristic did not produce a reasonable curve that could be mapped to Langmuir probe theory, and therefore could not determine the electron temperature or density, an alternate measurement approach was attempted. With the probe inserted into the plasma discharge it is possible to connect the probe to a spectrum analyser to measure the longitudinal electric field oscillations within the plasma. This technique was used by [McConville, et al., 2011] and in that case it was possible to compare the results with Langmuir probe estimates of the electron density and temperature. Due to the delicacy of the spectrum analyser, and the relatively aggressive environment of the probe, the probe was connected with RG58 cable to a linear power supply, configured to hold the probe DC bias potential close to ground. A DC blocking adapter was inserted into the line connecting the spectrum analyser to the circuit, as was a co-axial RF spark gap and wide-band (~6GHz) high voltage Barth attenuators to protect against transient events on the probe reaching and potentially damaging the spectrum analyser.

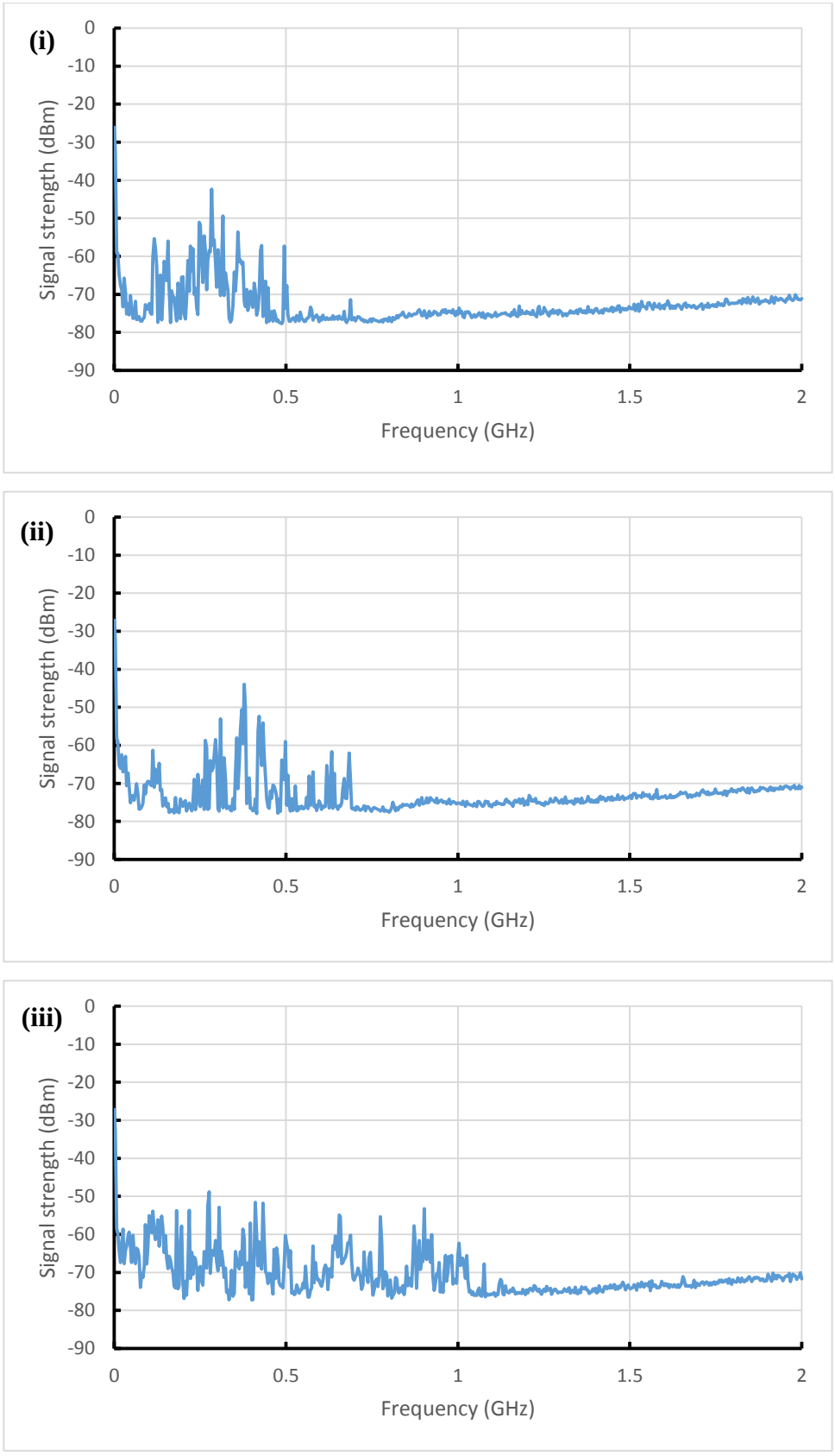

Figure 6.12 Frequency spectrum in the plasma detected by the probe at varying discharge currents (i) 8mA (ii) 12mA (iii) 25mA

From the spectra obtained, it can be seen that the highest frequency observed increases in a progressive manner as the discharge current is increased. Three example spectra are shown in figure 5.12 for increasing discharge current. The probe is polarised parallel to the static magnetic field, and would therefore tend to be sensitive to electric fields polarised in this direction. Above the plasma frequency these oscillations would correspond to O-mode type signals with relatively long wavelengths perpendicular to the static magnetic field. It would therefore seem probable that they would not be able to conform to the waveguide boundary conditions. This would suggest that the sharp cut-off in the oscillation spectrum could be interpreted as the plasma frequency at each discharge current. Figure 6.13 shows the trend of increasing maximum detected frequency with the discharge current. The cut-off frequency appears to be relatively linear with increasing discharge current until 25mA. Due to the need to accumulate the data over time and given that 25mA was viewed as the maximum appropriate current for DC operation of the plasma combined with the delicacy of the spectrum analyser, higher discharge currents were not attempted with the analyser connected.

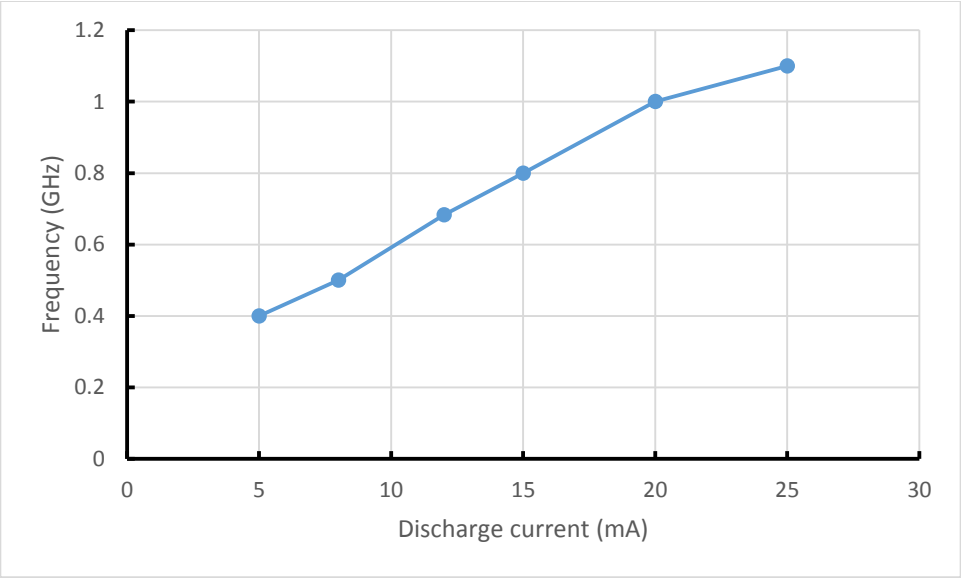

Figure 6.13 Maximum frequency detected as a function of discharge current

As a check of the validity of this method, it is possible to determine an estimate for the electron temperature by assuming the ion current to the cathode is controlled by the Bohm sheath criterion at the sheath-presheath boundary (equation 2.15). For a 1GHz

plasma frequency at a discharge current of 20mA, the electron temperature can thus be estimated as ~1eV. This value appears reasonable for a low pressure DC discharge.

Through linear extrapolation of the discharge current to a maximum of 40mA, this would generate a discharge of ~2GHz plasma frequency, corresponding to a plasma density of $\sim 5 \times 10^{16} m^{-3}$ as given by equation 2.10. This is an intermediate plasma density between the magnetically confined simulations (section 4.2.3) and the electrostatically confined simulations (section 4.2.4). Long time-scale perturbations of the ions would still be expected at this density and Penning trap anode diameter although their evolution may be impacted by the decreased density.

6.9 Electron beam characterisation

With the Penning trap removed from the system, the electron emitter was tested to determine the unperturbed electron beam performance. The velvet cathode and mesh anode were inserted into the vacuum system, positioned at a point near the plateau region of the electron emitter solenoid. The distance between the cathode and anode was set to 1.5cm, equivalent to the spacing used in the simulations. This was expected to provide sufficient electric field to cause the velvet emitter to ignite at a voltage in the range of 50-60kV, whilst requiring about 0.75μs for the plasma to close the anode-cathode gap. To provide the correct magnetic confinement of the electron beam, the two solenoids are used as described in section 5.3. The first immerses the cathode in a weaker magnetic field to focus and spatially confine the beam as the electrons are produced. The second is used to support the Penning discharge within its plateau region as well as keep the electron beam confined. The transition between the two magnet coils can potentially induce expansion, mirroring and/or scalloping behaviour into the electron beam. The magnetic field produced by the two solenoids was mathematically modelled to determine the field profile and the profile produced by this analysis was used as an input parameter in the numerical simulations of the electron beam generation and propagation (section 4.3). The numerical simulations were used to design the emitter electrodes and to adjust the parameters of the magnetic fields to attempt to minimise the predicted spread in the electron velocities caused by

transmission through the magneto-optical system. There are however aspects of the explosive electron emission process that are difficult to completely numerically model, and therefore the experimental electron emitter was tested at various magnetic field ratios to find an optimal operating regime to account for any potential real world effects not present in the simulations.

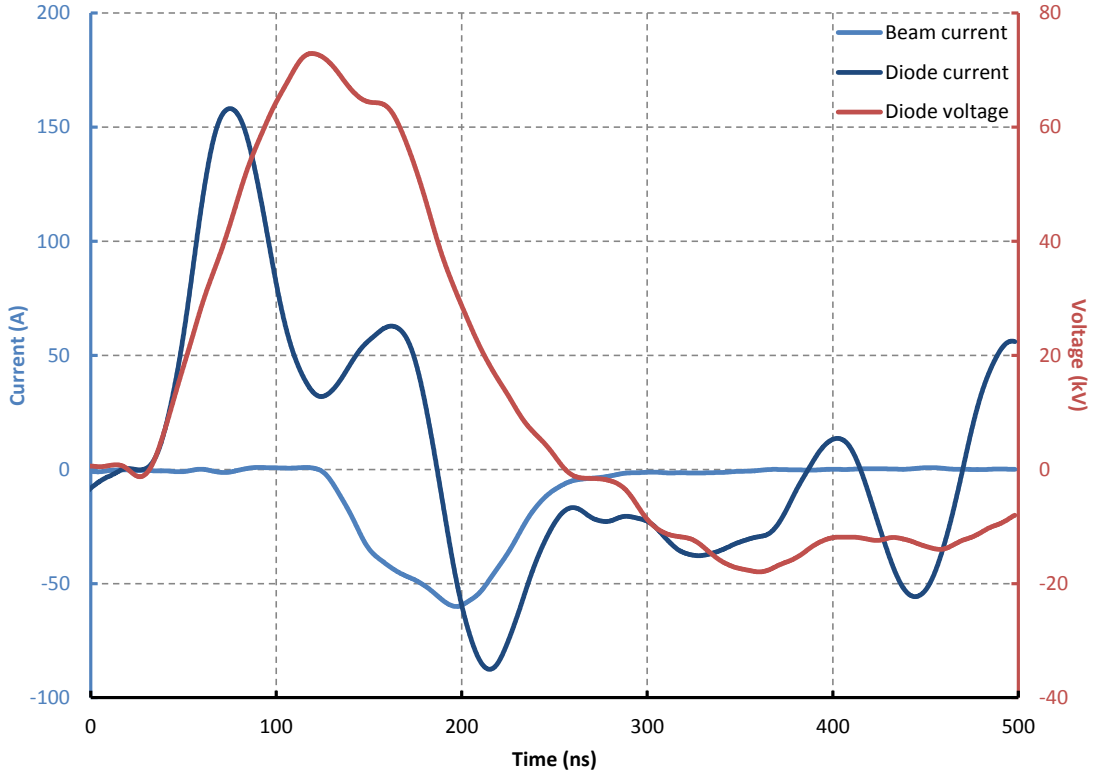

Figure 6.14 Electron beam pulse measurement illustrating the beam and diode currents and accelerating voltage pulse envelopes, accounting for calibration of all diagnostics

To determine the electron beam current, a Faraday cup was placed downstream within the plateau region of the second solenoid and connected to ground with a 50Ω resistance. This was connected to an oscilloscope (also 50Ω input impedance) through 46 to 66dB of attenuation (dependant on the expected signal level). The acceleration voltage and diode current were also measured using 1V/A Rogowski coils, as described in section 5.8, connected to an oscilloscope (50Ω impedance) with 20dB of attenuation. Figure 6.14 shows a typical measurement obtained for an electron beam, generated in this case with an emitter solenoid at 0.048T, the second (main) solenoid

at 0.3T and a charging voltage of 39kV applied to the double Blumlein HT pulse generator.

As can be seen, when the emitter HT circuit is switched, the voltage and current on the diode rise sharply together until the voltage approaches a plateau. The initial current peak occurs during the steepest point of the rise of the voltage trace and is associated with capacitive ‘displacement’ current charging the accelerator surface. As the rate of rise of the voltage pulse begins to fall off, this signal also drops, resulting in the dip in the diode current around ~120ns. At this point, the diode and beam current each begin to rise (note the current trace for the beam current is inverted in this graph) corresponding to the initiation of the explosive electron emission across the surface of the velvet. This sudden drop in the resistance of the diode appears as a drop in the total output impedance perceived by the HT pulser (recall that the accelerator is in parallel with the 206Ω matching resistor), resulting in a slight drop in the total potential across the accelerator. After some 200ns in figure 6.14, the power supply terminates its output (associated with the charge having been drained from the cables) and the potential across the diode decreases. Clearly the beam current pulse is associated only with the central ‘conduction current’ pulse in the diode current.

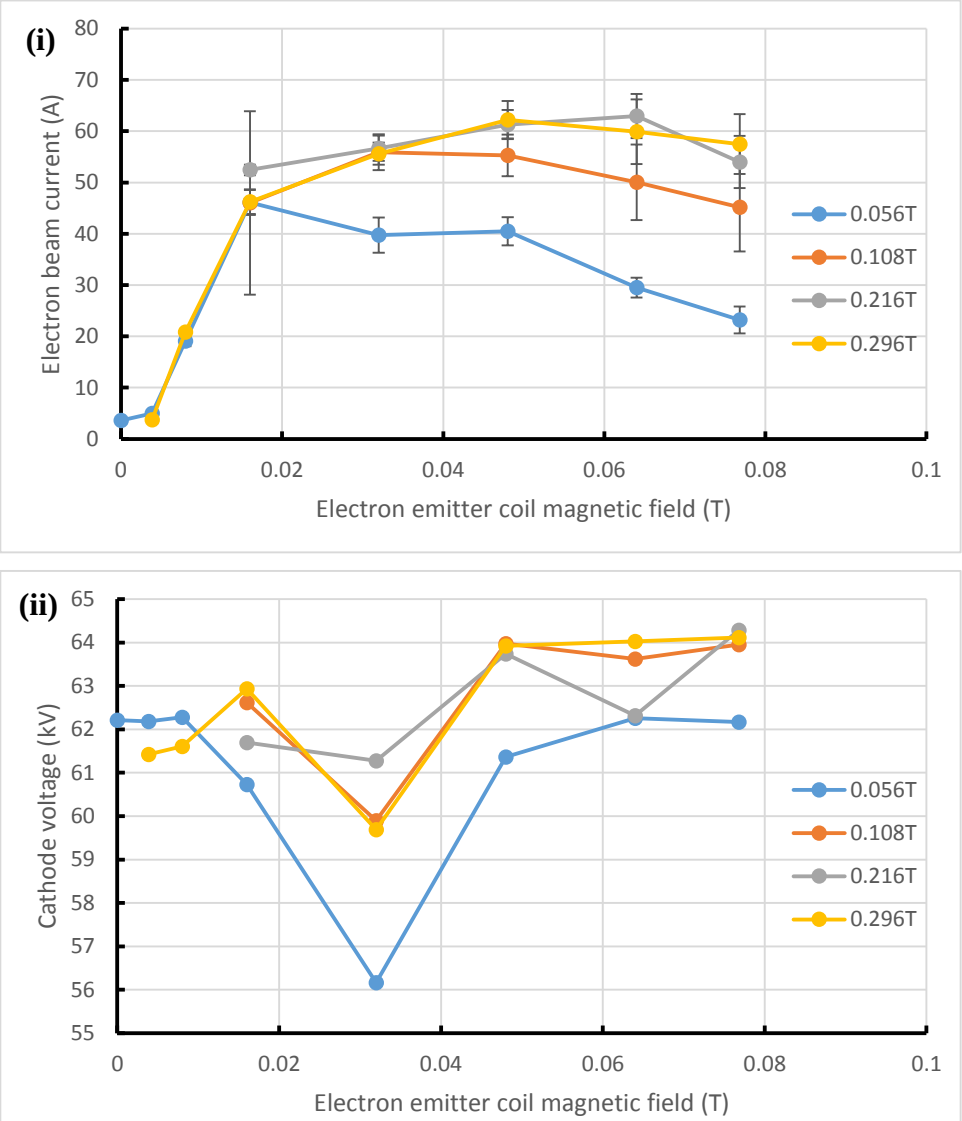

Figure 6.15 Electron beam properties as a function of emitter magnetic field (i) beam current (ii) cathode voltage for a range of downstream magnetic fields

From the data presented in figure 6.15 it can be seen that the highest beam current is produced when both of the magnets are close to maximum strength, and was fairly insensitive to the main high field coil for fields above ~0.1T When the magnetic field in the interaction space dropped to ~0.05T the transmitted current starts to drop after the emitter field is raised above B=0.01T. This is likely to be associated with the electron beam diameter becoming too large in the relatively small (55mm) diameter downstream section of the apparatus, and certainly too large to be fully intercepted by the Faraday cup due to inadequate magnetic compression. A similar but weaker

response can be observed in the measurements taken with a magnetic field of 0.1T in the main coil. An interesting (and extremely reproducible) resonance appears to occur in the electron emission region when the emission region magnetic field is set to 0.03T which causes a dip in the applied cathode voltage, corresponding to a rise in the drawn cathode current. This has no impact on the downstream electron beam current, and the cause is not clear at this time. For magnetic fields of B=0.016T and below in the electron accelerator region, the electron beam current becomes completely independent of the downstream magnetic field, but a very strong function of the emitter magnetic field. This suggests that the beam is becoming heavily scraped (i.e. the beam is colliding with the anode electrodes) in the acceleration region.

In order to characterise the diameter of the electron beam at the different magnetic field ratios, a series of beam collimators were placed in the beam path before the Faraday cup. These collimators consisted of a circular copper disk with a circular aperture machined into the centre of various diameters. If the beam diameter is greater than the machined aperture there will be a drop in beam current detected at the Faraday cup. These could therefore be used to measure the variation in the electron beam current density with radius and indeed provide control over the overall electron beam radius and total current in the beam for subsequent experiments. The results can be seen in figure 6.16 for various magnetic field arrangements. The maximum diameter detectable with no collimator was 40mm (defined by the diameter of the Faraday cup).

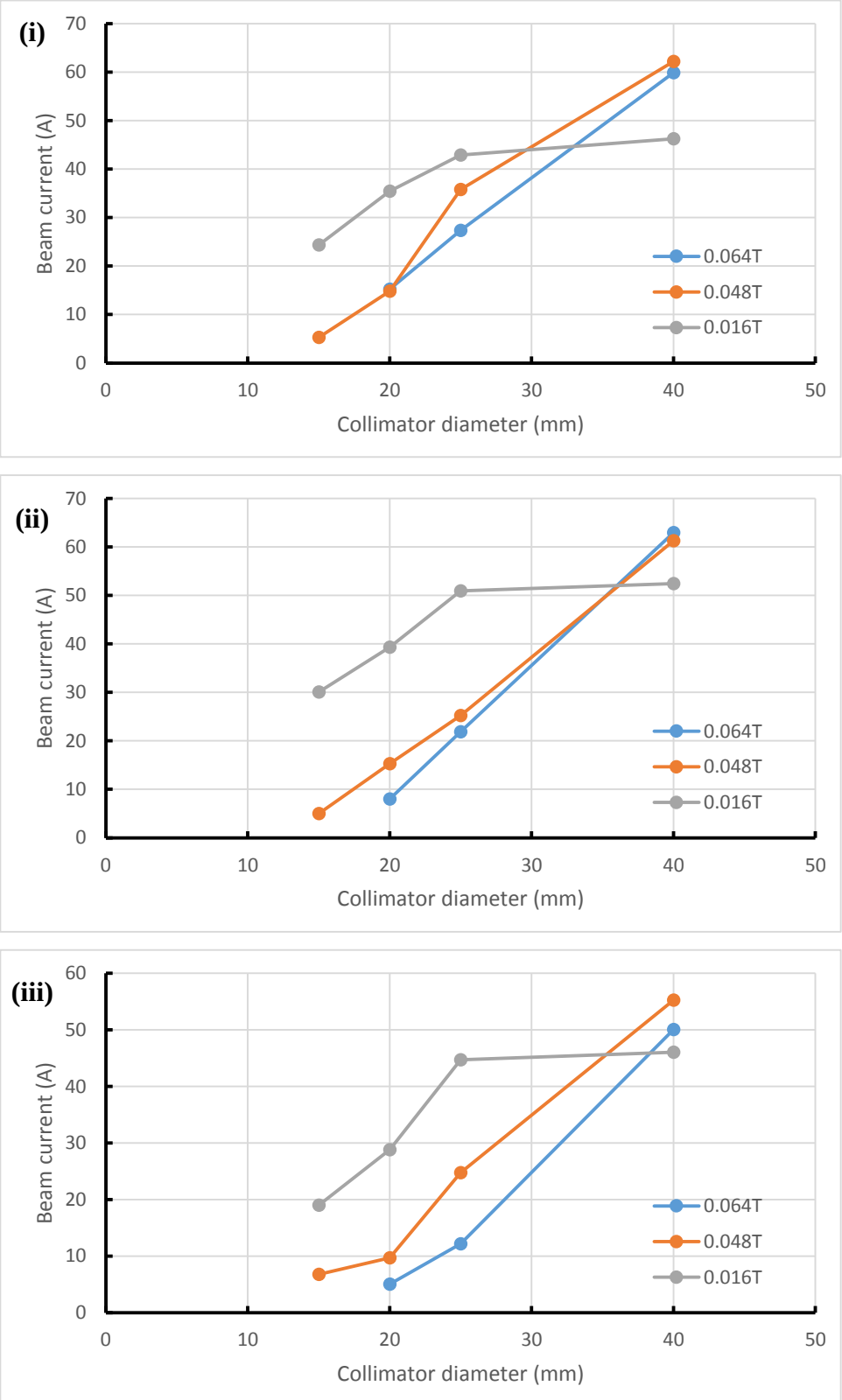

Figure 6.16 Beam current at different collimator diameter (i) Bmain=0.296T (ii) Bmain=0.216T (iii) Bmain=0.108T, for three values of the electron emitter magnetic field

For all main coil magnetic fields with an emitter magnetic field above 0.016T, there is a significant drop in beam current as the collimator diameter is reduced from 40mm to 25mm. This suggests that in these configurations the beam has expanded out to a diameter between 25 and 40mm which is larger than the simulations predicted. The near linear variation of the beam current with diameter, since the cross sectional area scales as the square of the diameter, may imply that the outer regions have a profiled rather than uniform electron density. However, when the emitter coil is set at 0.016T, almost the entire beam current is transported through the 25mm collimator, giving an estimate of the beam diameter of 20mm to 25mm for this magnetic field profile, induced by the additional magnetic compression. As the collimator is decreased beyond 25mm the beam current also begins to fall off for this magnetic arrangement. By using these collimators and altering the magnetic field arrangement, it is possible to control both how much beam current is being transmitted through the system and the beam diameter. The simulations used a beam diameter of 16mm, so a 15mm collimator was chosen as a close match to this dimension.

A general observation from the experiments suggested that the statistical behaviour of the electron beam current was very stable (for all downstream magnetic fields) when the accelerator magnetic field was less than 0.02T. This may be associated with the resonance noted when the accelerator field was tuned to 0.03T suggesting the potential for some complex behaviour in the electron accelerator when the magnetic field was set to a high value. For this reason, low emitter magnetic fields were chosen for the first experiments.

As the electron beam would be required to propagate through the Penning trap, it was also necessary to verify that the beam did not collide with any of the components of the trap assembly. By placing the Penning trap arrangement into position in the plateau of the main solenoid and with the 15mm collimator positioned between it and the electron accelerator (but also in the plateau region), measurements were taken using the Faraday cup after the electron beam had propagated through the unlit Penning trap.

These measurements were taken for three magnetic fields at the accelerator region and with a fixed main solenoid field of 0.296T.

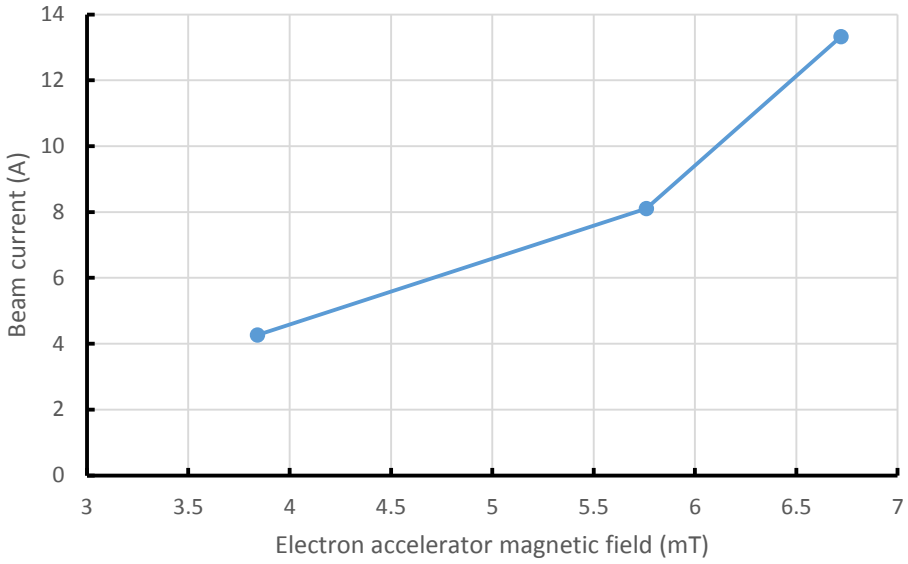

Figure 6.17 Electron beam transit through unlit Penning trap

The results shown in figure 6.17 illustrate that the electron beam is propagating through the trap with a current that can be controlled from 4 to 13A using the cathode magnetic field within a diameter of 15mm. This measurement of the beam current through the unlit Penning trap will be used as a baseline for the transit of the electron beam through the plasma. This provides a range of beam currents around that used in the numerical simulations presented in section 4.2.4. Together with a similar beam voltage and diameter this gives a beam that can be closely compared with that of the simulations.

6.10 Beam-plasma measurements

Initial tests of the effects of the electron beam on the plasma formed in the Penning discharge continued to use the Faraday cup to measure the electron beam current for different levels of accelerator magnetic field and different discharge currents. These measurements were undertaken to assess if the transit of the electron beam through the plasma has any impact upon the downstream beam current. The results for these

measurements are shown in table 6.1. Note that in all of the beam-plasma measurements, the 40mA discharge current was pulsed to prevent degradation of the trap whereas the 8mA discharge was run continuously DC. In the 40mA discharge current measurements, the beam was then triggered while the discharge current was at a maximum. This 40mA discharge current was selected as an extrapolation from figure 6.13 which suggests that this could reach a plasma density of $5x10^{16}$m-3, approximately a factor of 1.8 down on the density used in the simulations of the beam-plasma instability (section 4.2.4). It is relevant to note that in these experiments an arbitrary wave generator was employed to generate the pulsed current profile. This permitted greater control of the transfer between the high and low current states, significantly mitigating the stability issues observed in the earlier experiments where the pulse envelope was defined by a pulse generator (Section 6.3) but limited the peak current for the initial experiments to 40mA.

Electron accelerator magnetic field (mT)	**Discharge current (mA)**	**Beam current (A)**
6.72	0	13.32
6.72	8	13.43
6.72	40	12.06
3.84	0	4.26
3.84	8	4.35
3.84	40	4.42

Table 6.1 Electron beam current for different discharge currents

From the results shown in table 6.1, it can be seen that, in general, there is little impact on the transmitted beam current from the introduction of the plasma discharge. When the discharge is at 40mA and the accelerator magnetic field is at 6.72mT there is a slight dip in the beam current. This is not unexpected as although the simulations show that there is drift velocity disruption from the beam-plasma instability, the main drift of the electron beam still ensures that the majority of the beam will propagate through the entire system. The Faraday cup measurement would not be sensitive to fast modulation in the electron current potentially set up by any streaming instability.

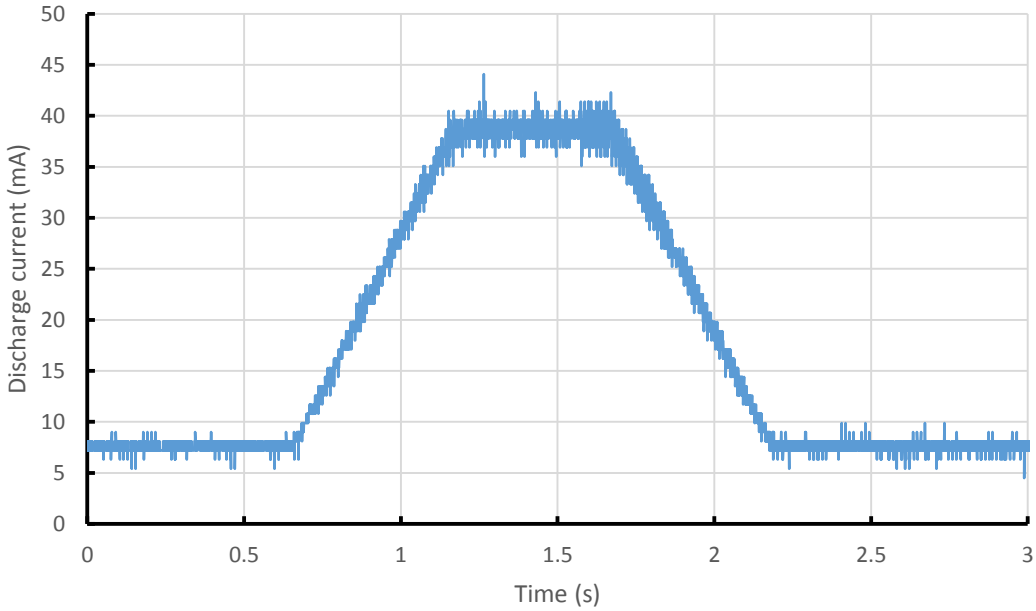

Figure 6.18 Penning trap current pulse trace

The behaviour of the discharge current was monitored during the transit of the electron beam while the discharge current was pulsed to 40mA. A typical measurement of the discharge behaviour is shown in figure 6.18. The discharge characteristics were again relatively unaffected by the transit of the electron beam. There appears to be a slight modulation of the discharge current shortly after 1.5s, the time at which the electron beam will have passed through the system. This may be the result of perturbation in the background plasma caused by the transit of the beam.

Although there remained an element of doubt about the measurement of the plasma density, it was decided that it would be sensible to attempt an initial measurement to establish the feasibility of observing the low frequency oscillations seen in the beam-plasma simulations. The Faraday cup was removed from the system and a probe inserted 1cm into the plasma column. This probe was connected to ground by a 50Ω resistor and further connected to the 50Ω input of an oscilloscope. To prevent the electron beam from intercepting the probe dielectric support, a circular copper disc with a machined slot slot was placed downstream of the Penning trap. This disc was at the same diameter of the vacuum vessels outer wall and ~3mm thick. The probe was

then inserted through the machined slot into the plasma column. This disc would ensure that the beam was intercepted before it could reach the probe connections. The probe was formed of a 0.7mm diameter tungsten wire encapsulated in glass. As previously noted it was inserted 1cm into the end of the plasma column's electrostatic confinement region, extending some 75mm from the copper shield plate and was positioned 12mm radially displaced from the axis of the experiment (and hence the centre of the electron beam path). The output from the probe was expected to indicate longitudinal oscillations in the plasma and the electric fields associated with the electron beam at the end of the plasma column.

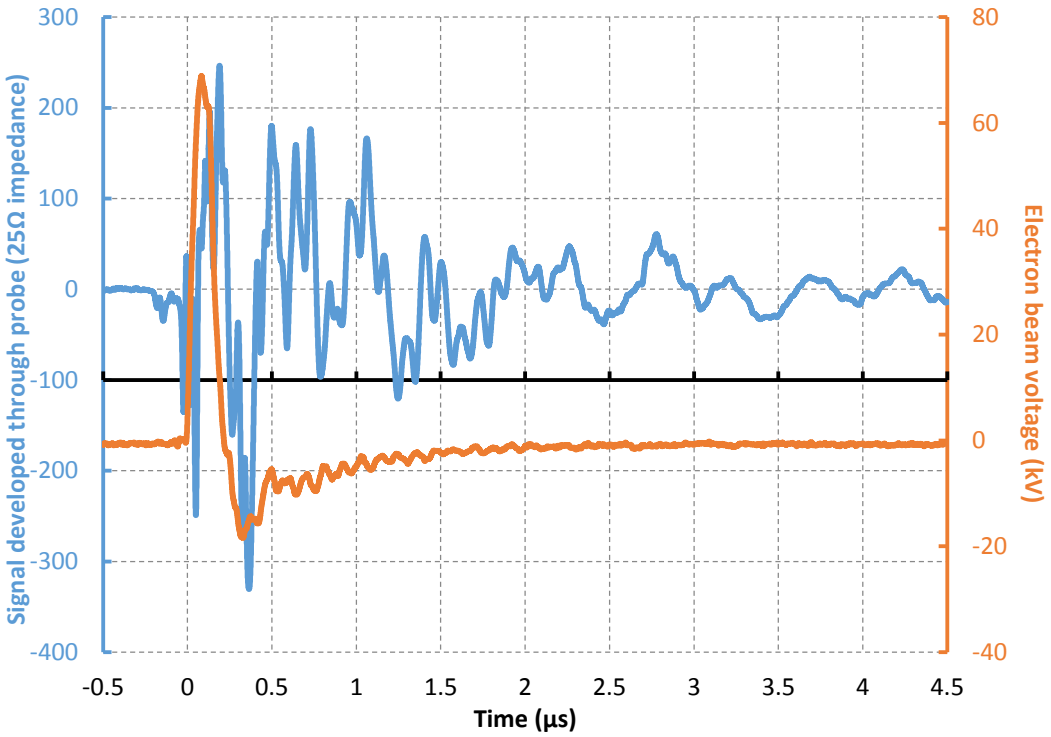

Figure 6.19 Electron beam typical pulse characteristics, showing the accelerating potential and the oscillations detected by the probe

Figure 6.19 shows the typical probe response detected during the transit of the electron beam through the plasma along with the voltage on the electron accelerator. The measurement shown corresponds to a beam current pulse of ~8A propagating through a plasma discharge at a current of 40mA. To detect the low-frequency oscillations expected due to the beam-plasma instability, the signal was recorded for approximately 4µs after the electron beam pulse has terminated. Fourier analysis could then be

performed upon the probe signal for a range of beam currents and discharge currents to investigate whether any signatures were seen that would correspond to the simulation predictions of modulation in the ions, with a maximum frequency of 2GHz and a resolution of ~250kHz. Figure 6.20 shows a comparison of the spectra observed at a beam current of ~8A for different plasma discharge currents.

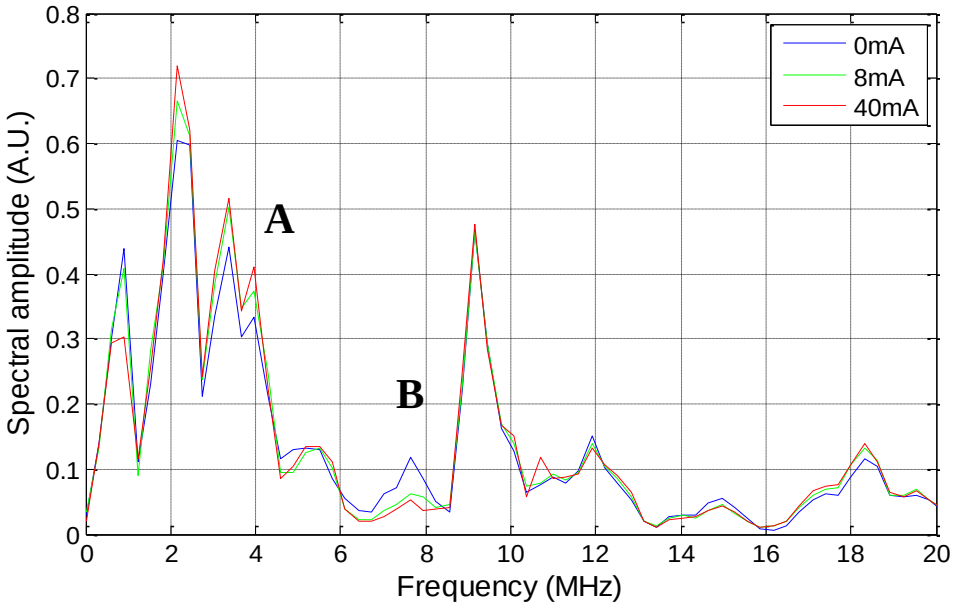

Figure 6.20 Spectra of probe signal for ~8A beam current and varying discharge currents

The spectra shown in figure 6.20, are mean results taken over a number of measurements at the same parameters, cropped to the low frequency region of interest. This aids in suppressing any statistical variation from the analysis. Despite this, the frequency spectrum detected on the probe for the electron beam propagating through the plasma does not vary significantly compared to the signals excited by the beam alone without the plasma. There are two regions (A and B on figure 6.20) where there may be indications of some low-frequency effects caused by the plasma. At a frequency of ~4MHz (A) there appears to be a slightly stronger signal recorded for both plasma discharge currents, with the 40mA fractionally larger. At a frequency of ~7.5MHz (B) there appears to be a suppression of the low-frequency oscillations that are excited by the electron beam. Again the higher discharge current shows fractionally more suppression.

After analysis of results obtained with three different electron beam currents (4A, 8A and 13A), these spectral features appear consistently, and only in the presence of a plasma and at the same frequencies. This suggests that these features are independent of both the beam and discharge current, however it should be noted that the Fourier resolution of these spectra is on the order of 0.25MHz which limits the detailed interpretation of the data. The deviations between the signal strengths at these two regions are on the order of twice the standard error in the mean of the spectral amplitudes. However, these variations in amplitude occur in a region where there is a rich and complex spectral structure with considerable variation in amplitude with frequency. This is therefore only a tentative indication of potential additional low frequency dynamics in the presence of the plasma and indicates the requirement for additional diagnostics and considerable depth of statistics.

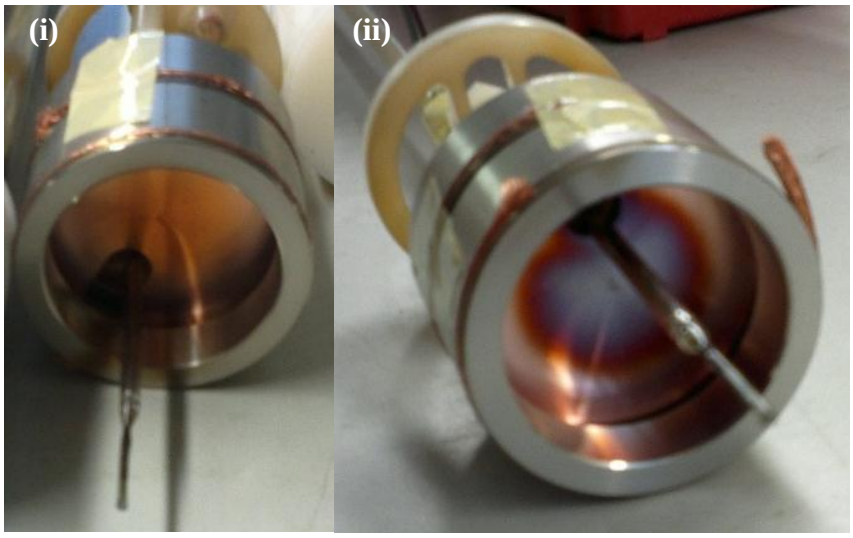

Figure 6.21 Condition of the copper probe shield after beam-plasma measurements with the probe inserted (i) 1cm (ii) 4cm into the plasma column

Repeat measurements with the probe inserted 4cm deeper into the plasma column showed no appreciable difference in low-frequency behaviour, with the exception of the case of the 40mA discharge current, 12A beam current case. In this particular case the frequency suppression at point B in the spectra was not as pronounced. Figure 6.21 however, shows the copper disc shield and its mounting that was used to protect the probe connections. The picture on the left shows the condition of the probe after it was used in the beam-plasma measurements with the probe inserted 1cm into the plasma

column. There is little damage or deposition of metal. The condition after the experiments were repeated with the probe moved 4cm deeper into the plasma are shown by the picture on the right. There is now a significant change to the surface of the copper shield (which was now only 3cm outside of the plasma column). This decolouration of copper has not been seen previously in any of the experiments conducted in this work which indicates that it is an effect associated with the beam-plasma interaction.

Chapter 7 : Discussion and future work

7 Discussion and future work

7.1 Overview

This work set out to investigate the effects of electron beams propagating through plasmas in two different configurations. This involved the numerical simulation of beam-plasma systems as well as the design and construction of a low-pressure, low temperature experimental apparatus to aid in the benchmarking of the numerical codes for their use in the simulation of beam-plasma interactions.

The first numerical study was undertaken in order to investigate the impact of a plasma in a laboratory experiment to simulate the cyclotron mechanism thought to be responsible for auroral kilometric radio wave emission from the Earth's magnetosphere. The second numerical study was an investigation of the non-linear behaviour of the two-stream/beam-plasma instability, particularly in relation to the resulting ion behaviour, with potential relevance to current fast-ignition inertial confinement fusion experiments. The laboratory experiment was designed and constructed using information gathered from the numerical investigation to provide a system that was as representative of the simulations as was possible. Tertiary numerical simulations were also carried out in the design of the electron emitter that would be used in the laboratory experiment.

7.2 Laboratory auroral kilometric radiation experiment numerical study

For the numerical investigation of the laboratory AKR experiment to be possible, the electron beam velocity distribution had to be matched to that of the electron beam produced and magnetically compressed during the laboratory experiment (intended to replicate features of the auroral electron beam observed in the magnetosphere). This was necessary as, although a parallelisable particle-in-cell code was being utilised (xOOPIC), the simulation time required to solve correctly for the emission and

magnetic compression of the electron beam (which is a large volume problem) would be prohibitive when combined with the simulation of a plasma. Furthermore, xOOPIC does not contain explosive emission routines that could reasonably be used to simulate the electron emission from the cathode. Other codes such as MAGIC do have the capacity to simulate such emission mechanisms (although in a simplified manner), however the lack of parallel computing capabilities and limited plasma simulation abilities made such a code incapable of simulating the electrons interacting simultaneously with the electromagnetic waves and the plasma. Instead, it was decided to inject the electron beam with a velocity distribution that was defined analytically and then matched to the empirical data.

The cathode surface in the AKR experimental apparatus [McConville, et al., 2008] was shaped as an annular ring with a conical electrode in the centre. This geometry would have resulted in little to no electrons with purely axial beam velocity. Analysis by [McConville, et al., 2008] showed the distribution of electrons from the experimental cathode in terms of pitch angle and it was determined that a distribution similar to that of a Maxwell-Boltzmann could adequately describe the velocity distribution produced in the experiment. The gamma distribution function was however chosen as it has a more general analytic form that could produce a flexible and configurable electron distribution encompassing the Maxwell-Boltzmann distribution with a certain set of parameters as described in section 3.2.1.

The algorithms to produce a gyrating electron beam of any particular velocity distribution did not exist in xOOPIC and so had to be added (Section 3.2.1). Once added, the simple case of a gyrating electron beam in xOOPIC was compared with a similar beam in MAGIC, which had inbuilt gyrating beam capabilities. The comparison was virtually identical for the same input parameters. As an additional test, the gyrating beam was used in a simple gyrotron simulation to verify that the new routines in xOOPIC would produce a beam supporting similar output radiation to MAGIC. MAGIC is a commercial code that has been used previously in the design and development of gyrotron oscillators and amplifiers. The two simulations compared reasonably. Temporally the cyclotron maser instability grew and saturated at the same

rate in both simulations, but the total output power predicted by xOOPIC was ~30% higher and there was an upward shift in output frequency of ~50MHz. This may be due to the different meshing algorithms in use by MAGIC and xOOPIC. MAGIC uses an adaptive meshing that is determined by the boundaries of the defined objects. This will adjust the meshing to ensure the objects are on the boundaries of the mesh. Conversely xOOPIC uses a simple uniform grid and will approximate any defined boundaries to that grid. This may result in a change in the cut-off frequency of the resonant waveguide, resulting in a different detuning value for the applied magnetic field that may provide a change in the efficiency of the coupling.

With the electron injection algorithms thus demonstrated, it was necessary to match the gamma distribution function parameters to that of the experiment. Through the comparison with magnetic mirroring measurements made in the experiment it was possible to tailor a gamma distribution function to artificially generate a beam with a velocity distribution that gave the same transmitted current response as a function of magnetic field ratio as observed in the experiments. This was undertaken for three different experimental configurations (relating to different cathode currents and magnetic fields immersing the cathode) that correspond to transmitted beam currents of 12A, 35A and 60A.

Simulations were undertaken of the emissions from the 35A electron beam in the absence of a background plasma and compared to the experimental measurements. The frequency was predicted at 5.31GHz in comparison to the measured 5.4GHz in the experiment. Similar efficiency levels were also found with the simulation at ~1% compared with ~1.5% from the experiment. The differences between the simulations and experiment may stem from slight differences in the exact geometry used in the experiment with those in the simulation. The simulations optimised the resonant cavity length within a range of ~1cm to produce the highest output efficiency. In addition, the previous experimental measurements of output power contain a degree of uncertainty that may also account for the efficiency disparity.

For the 60A electron beam current, it was possible to compare the impact of a plasma in the interaction region of the simulation to that of the experiment. It was first found that the efficiency was ~0.9% without the plasma, but that the efficiency was degraded by the presence of the plasma until the instability would not grow at all with a plasma frequency over 400MHz. This was similar to the behaviour seen in the laboratory measurements, where the output power fell with increasing plasma frequency (from a similar initial estimate of the efficiency) but in this case there was little emission measured at 300MHz. There was also a stochastic element to the experimental data, whereby there would be no emission observed at all even at lower plasma frequencies. No such stochastic behaviour was observed in the simulations. It was however found in the numerical simulations that the growth rate and time to saturation of the cyclotron maser instability was affected by the presence of the plasma. In the experiment the electron beam pulse was limited to ~100ns in length. During the experimental investigations in the present work, it was noted that the Penning discharge could change operating mode. It may be in fact that the stochastic effects observed in the AKR experiment were associated with such a process. More definitively, it had been supposed that an axial 'two-stream' type instability might be responsible for destroying the transverse particle distribution that provides the population inversion for the emission to occur. No evidence of this was seen in these simulations and therefore alternative explanations should now be sought.

7.3 Numerical investigations of the two-stream/beam-plasma instability

To begin to investigate the two-stream instability in xOOPIC, it was first necessary to ensure that the code could correctly model the well understood linear theory. Simulations were carried out using two co-propagating electron beams of similar current but different initial velocities allowing observation of the growth of the two-stream instability in the simplest form. These gave relatively good agreement to the linear theory and also showed the development of a degree of phase velocity mixing and trapping once the instability had saturated. This leads to the growing longitudinal electric fields of the instability beginning to break-up into more complicated

behaviour. It is the impact of this non-linear behaviour that leads to modulated ion dynamics that is of primary interest in this numerical study.

Simulations were then undertaken that consisted of injecting an electron beam into a plasma that was confined by a magnetic bottle. The confinement of the plasma, keeping the particles from interacting with the ports proved to be important for the stability of the PiC codes. Therefore a magnetic bottle arrangement was initially used to limit the number of particles reaching the ports of the simulation. This was eventually replaced with an electrostatic confinement as this was the method to be used in the laboratory experiment. Additionally, a small conducting block was added to the end of the simulation to ensure the electron beam did not interact with the exit port.

The beam-plasma instability in the magnetic bottle confinement also compared well with analytic theory in the linear regime, albeit with a faster temporal growth rate. Once the instability saturated the longitudinal electric field behaviour became much more complicated in comparison to that of the co-propagating beams. Regions of a standing wave type structure in the longitudinal electric field eventually began to form in the area where the initial phase velocity vortices occurred due to the saturation of the beam-plasma instability. These waves appeared to increase in amplitude, resulting in electron and ion density cavities forming. This behaviour seems consistent with the modulational instability described in section 2.5.2. The ions (and electrons) that propagate from the cavities travel in density perturbations which propagate along the simulation axis in both the positive and negative directions, with a propensity for the positive direction. Similar motion of ion density perturbations were reported experimentally by [Franck, et al., 2001] where periodic ion bunches were injected into a plasma discharge. However, the excitation mechanism in this experiment differs; ion density perturbations are formed by a modulated ion beam which excite density perturbations propagating at the acoustic velocity.

Fourier analysis was performed on the temporal behaviour of the longitudinal electric fields that occurred within the system. This discovered that the standing wave structures appeared to oscillate at a frequency of ~1GHz which is close to both the

frequency of maximum growth of the beam-plasma instability and the electron plasma frequency. This suggests that these waves consist of Langmuir oscillations. In addition to this, there appears to be a low frequency oscillation at ~10MHz that occurs in the same region as the density cavities. It is possible that this low frequency behaviour corresponds to ion acoustic wave oscillations. Assuming that the wavelength of the acoustic wave relates to the spacing between the ion density perturbations (~3cm) and that the ion acoustic velocity is defined by the electron temperature in the cavity structures ~300eV, this would give an ion acoustic frequency of ~10MHz. This lends further support to the suggestion that the modulational instability is responsible for forming the 'ion bunches' in the plasma as typically for this instability to occur there is a coupling between Langmuir oscillations and ion acoustic waves. Furthermore, the turbulence parameter defined in equation 2.77, was determined to be larger than $3k^2/k_D^2$ for wavelengths greater than ~2mm. As the structure size of the ion density perturbations were ~3cm it is possible for wave trapping to have occurred in this system and for the modulational instability to grow. Similar spectral structures were also seen in observations of type-III solar radio bursts and linked to a two-stream instability [Thejappa, 2012], although this has been challenged [Graham, 2012]

Simulations undertaken at a range of electron beam voltages and currents to investigate using electrostatic confinement for the background plasma continued to exhibit long term modulation of the ions. It was noted that, in general, for most electron beam voltages the velocity of these density perturbations was higher than that of the average ion acoustic velocity in the system at that time. When investigating the electron temperature variation in space (e.g. figure 4.37 (iii)), it was found that within the density cavities that formed, the electron temperature was significantly higher than that of the surrounding temperature. The temperature was analysed taking the mean of the distribution of macro-particle speeds within each simulation mesh cell. As there are ~100 macro-particles per cell of each species this would give a reasonable approximation of local electron temperature. The ion acoustic velocity related to this localised temperature appeared to be close to that of the drift velocity of the ion perturbations propagating from the cavities. Furthermore, the trend of the maximum ion acoustic velocity (figure 4.42) found in these cavities tended to follow that of the

ion perturbation drift velocity as the energy of the driving electron beam was varied. These observations would suggest that the ion perturbations leaving the density cavity propagate at a velocity dependent upon the electron heating that occurs within the cavity. This could be important for enhancing heating in collisional plasmas, such as a compressed deuterium-tritium pellet, as these density perturbations could potentially be damped by the ion-ion collisions leading to an overall increase in ion temperature. Further study on the collisional behaviour of these waves could be useful, discussed in section 7.5. In this collisionless case the ion perturbations also appear to exhibit behavioural characteristics of solitons [Ikezi, Taylor and Blake, 1970], insofar as they seem to travel at a fairly constant velocity and do not merge as they cross in space. Electron solitary structures have been observed in the earth's magnetotail [Matsumoto, et al., 1994], auroral zone [Ergun, et al., 1998a] and high-altitude magnetosphere [Franz, et al., 2005]. The behaviour seen in the numerical simulations could potentially be of relevance to the formation of some of these structures.

Furthermore, in measurements of solar radio bursts, zebra-like structural patterns have been observed in the radiation and absorption spectra of type III and IV bursts [Chernov, 2010]. A proton beam-plasma instability has been proposed as a possible driver for these spectral signatures [Fomichev, Fainshtein and Chernov, 2009]. This instability leads to an ion sound wave with multiple harmonics which are thought to be the source of the zebra-like structures. From the numerical simulations undertaken in this work, a series of ion density structures that propagate at the sound speed have been formed from the electron beam-plasma and modulational instability. The simulations in this thesis show the excitation of waves associated with the ion behaviour, however it is not clear that the cascade to produce additional spectral components is occurring before the structures largely dissipate. It may be possible to study the excitation of acoustic waves with the ions in the simulations developed in this thesis, however this would require the addition of collisional software routines as the collisional processes are a key damping term as shown in [Fomichev, Fainshtein and Chernov, 2009].

7.4 Laboratory apparatus to investigate the two-stream/beam-plasma instability

The laboratory experiment to investigate and benchmark the effects seen in the numerical simulations was designed and built with initial measurements made. Compromises had to be made in terms of practicality for the design of the experiment. The gas species used for the plasma discharge had to be changed to helium from hydrogen due to the chemical volatility of hydrogen. This would have the impact of decreasing the frequency of potential ion oscillations by a factor of 2, assuming that the helium is only singly ionised by the Penning discharge. Additionally, the numerical simulations were artificially hot (100eV) to attempt to suppress any numerical heating effects that could occur. The Penning discharge used in the laboratory may reasonably be expected to be at a temperature of ~1-10eV (typical for such a low pressure discharges). This may also have an impact on any ion acoustic oscillations present, however, as seen in the numerical simulations it is the localised heating due to the beam-plasma instability that appears to impact upon the ion motion. Nevertheless it is entirely possible that the ion acoustic speeds are, at least initially, an order of magnitude smaller, and assuming that the spatial structure of the ion waves is dependent on the beam-plasma instability, would result in ion density perturbation frequencies up to a factor of 10 lower as well. Taking into account the increase of mass, this would result in ion acoustic frequencies of ~0.5 to 1.58MHz for electron temperatures of 1-10eV.

Performance of the components was important in undertaking these laboratory experiments. Initial tests on a previously designed Penning trap geometry led to the understanding that the coating of insulating components with metal was of particular importance for a discharge at the required level of current. This could lead to electrical shorting of the discharge requiring the insulators to be cleaned or remade. The new insulators for the redesigned Penning trap were therefore designed in such a way to maximise the electrical tracking distance that would be required for the trap to become shorted and importantly ensuring these insulators had no line of sight to the cathode surface was found to be vital. These new insulators have been exposed to higher

current discharges (20mA for sustained periods with pulses to 40mA) over many hours, and although deposition has been observed, it has never led to shorting of the electrodes to ground. Likewise, using a coaxial cable as a plasma probe was unsuitable as the insulator surrounding the probe was not resilient to the higher current plasma. Glass encapsulated tungsten probes were manufactured in a range of configurations to offer enhanced resilience to the more aggressive environment at higher discharge current levels.

The electron accelerator was constructed and tested based upon numerical modelling in MAGIC. This accelerator was designed to be able to produce a beam current of 40A and a voltage of ~50kV. The experiments show that the beam produced was up to ~60A at ~62kV. This was acceptable as the current was found to be controllable by adjusting the magnetic field in the solenoid at the electron accelerator region, whilst the transverse size of the beam could be regulated using upstream collimators to match some of the simulated beam currents and dimensions, in particular, using fairly low magnetic fields on the electron emitter allowed the experiment to produce beams that were similar to those used in the simulations in section 4.2.4.

The measurement of the plasma density using probes unfortunately proved to be inconclusive. A stable set of measurements could not be obtained that produced a reasonable electron temperature. The presence of the magnetic field complicates the probe measurement very significantly due to the cyclotron orbits of the ions and electrons. For a 1eV plasma in a 0.296T magnetic field, the Larmor orbital radius for a thermal electron would be ~10μm whereas an ion would be ~183 μm assuming the ions are at room temperature.

By using the probe instead as a RF pickup antenna, it was possible to get an estimate of the plasma frequency of the discharge and from this an estimate of the number density and temperature of the plasma. Due to the delicate nature of the spectrum analyser used in these measurements, and more importantly the fact that the spectrum analyser required to build up data over an extended period of DC operations, a maximum trap operating current of 25mA was used as operating beyond this for long

time durations could risk damage to electrodes and discharge circuit components. The frequency was observed to increase with discharge current showing an almost linear trend and therefore the preliminary experiments investigating the transit of the electron beam through the plasma was extrapolated to a discharge current of 40mA (the maximum current used in the beam-plasma experiments). This would give a plasma frequency of ~2GHz which would result in a number density of ~$5x10^{16}m^{-3}$. This density was between that used in the simulations presented in section 4.2.3 and 4.2.4 and therefore the long time-scale ion dynamics would still be expected at this density. Due to the radius of the Penning trap anode however, the evolution of the ion structures could be constrained. It should in future be possible to increase this density further. Moreover, this is an unconventional configuration for plasma diagnostics, it will therefore be important to test this estimate of plasma frequency against an alternative method. Estimates of the Bohm velocity suggest an electron temperature for this density of plasma of a few eV which appears reasonable for a plasma of this type and pressure. For investigating the formation of ion structures on the order of 3cm, operating at a pressure of ~$7x10^{-4}$mbar also ensured that the mean free-path of the helium was ~10 times longer than these structures. As these structures appear to drift up to 10cm this gave an upper operating pressure of ~$2x10^{-3}$mbar to ensure collisionless propagation.

For the electron beam parameters and plasma density generated in this system, the dynamics seen in the numerical simulations should be observable. The electron beam current and voltage range is within the range considered in the simulations presented in section 4.2.4 while the plasma density is lower this should still lead to a strong beam-plasma instability. The formation of ion structures may be close to the centre of the 1m long plasma column but, due to the impact on stability, the plasma probes could not be inserted further than 4cm from the end of the Penning trap. Nevertheless, it may still be possible to detect the modulations in the ions by the probe.

The measurements of the low-frequency oscillations that were produced during the initial beam-plasma interaction experiments were performed with the available probes inserted just beyond the downstream end of the plasma region. These measurements

showed that the plasma may be impacting on signals in the spectral range ~4MHz and ~7.5MHz. However, the oscillations due to the electron beam pulse were very strong in comparison to the size of this perturbation. The amplitude variation at these frequencies did appear relatively consistently in the presence of a plasma, although they also appeared to be independent of the discharge and beam current. Further work will be required to verify this behaviour and additional diagnostics will be required to demonstrate the formation of the streaming instability and any subsequent impact on the plasma. Nonetheless at the end of this project, all the main components required to pass an energetic electron beam through the plasma column had been built, tested and shown to work well together.

7.5 Future work

While the predicted output from the simulations of the AKR laboratory experiments provided reasonable agreement to the experimental measurements in the presence of the plasma, there still remains a need to find an explanation of the stochastic behaviour seen in the experiments. While the growth and saturation rate of the instability is a potential explanation, further numerical investigation could be undertaken. The cylindrically symmetric 2.5D simulations cannot model some configurations of instabilities that may occur during the transit of the beam in the plasma. Therefore by extending these simulations to a full 3D PiC simulation, any such behaviour could be investigated. This would require the use of another software package as xOOPIC does not support 3D simulations.

The numerical simulations of the beam-plasma two-stream instability show interesting behaviour of the ion density in the non-linear regime. This may be of relevance to the propagation of fast electrons into a compressed deuterium-tritium target in fast-ignition inertial confinement fusion experiments. This would require scaling of the numerical simulations up many orders of magnitude in density and down in simulation (and mesh) scale in order to observe the frequencies of interest. Whilst the total length of the system would decrease, this would still dramatically increase the runtime of the simulations and would require access to reasonably large computing resources.

Investigations could also be undertaken with and without an applied magnetic field as filamentation could result in the transverse breakup of the beam where no external magnetic field were applied. Also, if binary collisions could be modelled in the code (not supported in the standard xOOPIC distribution), the effect of the ion-ion collisions on the generated density perturbations could be investigated further for potential relevance to ion heating in fast-ignition fusion [Mendonça, et al., 2005] and ion acoustic wave generation in solar bursts [Chernov, 2010].

Additionally, simulations could also be undertaken at astrophysical conditions relevant to the Earth's magnetosphere, magnetotail and/or solar corona in order to observe any potential scaling of structure formation and dynamics for comparison with theoretical predictions and observations of these phenomena.

Initial measurements have been made using the laboratory apparatus designed and constructed as part of this work. These experiments show that the electron beam and the plasma column have been successfully formed and that the electron beam can be successful transported through the plasma (this was by no means certain at the outset of the project). Now that the bulk of the apparatus exists, these is an extensive parameter range which can be explored. However, there is need to improve upon the diagnostic measurements. Alternative methods for the determination of the plasma density could be designed and used. For example, a Faraday rotation technique [Hutchinson, 2002] could be used to estimate the line integrated number density (given that the magnetic field is precisely known). This operates by propagating a linearly polarised electromagnetic (in this case microwave) radiation signal through the plasma column. The magnetic properties of the plasma cause a rotation in the polarisation angle of the signal which can then be detected and measured. This angle shift can then be used to determine the properties of the plasma. Components for this method would have to be designed and constructed to facilitate the injection of the signal. This could be used to confirm the estimates from the RF pickup technique for the plasma density, without requiring the use of Langmuir probes which proved ineffective, or other disruptive insertion devices.

Other techniques for measuring the low-frequency oscillations should also be used. The probe currently used was only inserted up to a maximum of 4cm into the plasma column. This may not be close enough to the generated perturbations of interest and therefore a method of getting the probe deeper into the plasma column would need to be devised. Care would have to be taken as this could have dramatic effects on the stability of the plasma discharge. Alternatively, Penning traps of varying axial length could be used with the probe still 4cm in from the end. Numerical observations show that the modulational behaviour is independent of total plasma length as long as the beam-plasma instability has enough space to grow and saturate. As the I-V characteristics of each trap would change, they would each have to be tested separately to determine the necessary discharge currents to keep the number density the same.

Techniques for direct observation of the ion structures could also be developed. These could include spectroscopic methods that could potentially measure the Doppler shift of the moving perturbations and/or electromagnetic (microwave) scattering whereby an electromagnetic wave is injected and the signal reflected and scattered from the ion structures could be detected.

References

Allen J.E. and Phelps A.D.R., 1977, ‘Waves and microinstabilities in plasmas-linear effects’, Rep. Prog. Phys., **40**, pp1305-1368

Benson R.F., 1985, ‘Auroral kilometric radiation: wave modes, harmonics and source region electron density structures’, Journal of Geophysical Research – Space Physics, **90**, pp2753-2784

Bingham R., Kellett B.J., Cairns R.A., Dendy R.O. and Shukla P.K., 1999, 'Wave generation by ion horseshoe distributions on auroral field lines', Geophysical Research Letters, **26**, pp2713-2716

Bingham R. and Cairns R.A., 2000, 'Generation of Auroral kilometric radiation by electron horseshoe distributions', Physics of Plasmas, **7**, pp3089-3092

Bingham R., Cairns R.A. and Kellett B.J., 2001, 'Coherent cyclotron maser radiation from UV Ceti', A&A, **370**, pp1000-1003

Bingham R. and Cairns R.A., 2002, 'A New Cyclotron Maser Radiation Mechanism in Space Plasmas', Physica Scripta, **T98**, pp160-162

Bingham R., Kellett B.J., Cairns R.A., Vorgul I., Phelps A.D.R., Ronald K. and Speirs D.C, 2004, ‘Cyclotron maser radiation in space and laboratory plasmas’, contribution to plasma physics, **44**, pp382-387

Bingham R., Speirs D.C., Kellett, B.J., Vorgul I., McConville S.L., Cairns R.A., Cross A.W., Phelps A.D.R., and Ronald K., 2013, ‘Laboratory astrophysics: Investigation of planetary and astrophysical maser emission’, Space Science Review, **178**, pp695-713

Boyd T.J.M. and Sanderson J.J., 1969, ‘Plasma Dynamics’, Thomas Nelson & Sons

Boyd T.J.M. and Sanderson J.J., 2003, 'The Physics of Plasmas', Cambridge University Press

Bret A., Gremillet L. and Dieckmann M.E., 2010, 'Multidimensional electron beam-plasma instabilities in the relativistic regime', Physics of Plasmas, **17**, 120501

Buneman O., 1959, 'Dissipation of currents in ionized media', Phys. Rev. **115**, 503

Burinskaya T.M. and Rauch J.L., 2007, 'Waveguide regime of cyclotron maser instability in plasma regions of depressed density', Plasma Physics Reports, **33**, pp28-37

Burinskaya T.M., 2013, 'Ray tracing model of the auroral kilometric radiation generation in the 3-D plasma cavity', Annales Geophysicae., **31**, 1645–1652

Cairns R.A., Vorgul I., Bingham R., Ronald K, Speirs D.C., McConville S.L., Gillespie K.M., Bryson R., Phelps A.D.R., Kellet B.J., Cross A.W., Robertson C.W., Whyte C.G. and He W., 2011, 'Cyclotron maser radiation from inhomogenous plasmas', Physics of Plasmas, 18, 2, 022902

Chambers A, Fitch R.K., and Halliday B.S., 1998, 'Basic Vacuum Technology 2nd edition', Institute of Physics Publishing

Chang P.Y., Fiksel G., Hohenberger M., Knauer J.P., Betti R., Marshall F.J., Meyerhofer D.D., Se´guin F.H., and Petrasso R.D., 2011, 'Fusion Yield Enhancement in Magnetized Laser-Driven Implosions', Physical Review Letters, **107**, 035006

Chen, 2005, 'Introduction to Plasma Physics and Controlled Fusion: 2nd Edition', Springer

Chernov G.P., 2010, ‘Recent results of zebra patterns in solar radio bursts’, Research in Astronomy and Astrophysics, **10**, pp821-866

Chu K.R., 1978, ‘Theory of electron cyclotron maser interaction in a cavity at the harmonic frequencies’, Physics of Fluids, **21**, pp2354-2364

Cross A.W., Spark S.N. and Phelps A.D.R., 1995, ‘Gyrotron experiments using cavities of different ohmic-Q’, Int. J. Electronics, **79**, pp481-493

Davidson, R.C., 2002, ‘Physics of Nonneutral Plasmas’, Imperial College Press

Delory G.T., Ergun R.E., Carlson C.W., Muschietti L., Chaston C.C., Peria W. and McFadden J.P., 1998, 'FAST observations of electron distributions within AKR source regions', Geophysical Research Letters, **25**, no 12, pp2069-2072

Dendy, R.O., ‘Plasma dynamics’, 2002, Oxford science publications

Dieckmann M.E., Shukla P.K. and Drury L.O.C., 2006, ‘Particle-in-cell simulation studies of the non-linear evolution of ultrarelativistic two-stream instabilities’, Monthly Notices of the Royal Astronomical Society, **367**, 1072-1082

Eichmeier J.A. and Thumm M., 2008, ‘Vacuum electronics: Components and devices’, Springer

Eliasson B. and Shukla P.K., 2006, ‘Formation and dynamics of coherent structures involving phase-space vortices in plasmas’, Physics Reports, **422**, 225-290

Ergun R.E., Carlson C.W., McFadden J.P., Mozer F.S., Delory G.T., Peria W., Chaston C.C., Temerin M., Roth I., Muschietti L.,Elphic R., Strangeway R., Pfaff R., Cattell C.A., Klumpar D., Shelly E., Peterson W., Moebius E. and Kistler L., 1998, ‘FAST satellite observations of large-amplitude solitary structures’, Geophysical Research Letters, **25**, 12, pp2041-2044

Ergun R.E., Carlson C.W., McFadden J.P., Mozer F.S., Delory G.T., Peria W., Chaston C.C., Temerin M., Elphic R., Strangeway R., Pfaff R., Cattell C.A., Klumpar D., Shelly E., Peterson W., Moebius E. and Kistler L., 1998, 'FAST satellite wave observations in the AKR source region', Geophysical Research Letters, **25**, pp2061-2064

Ergun R.E., Carlson C.W., McFadden J.P., Delory G.T., Strangeway R.J. and Pritchett P.L., 2000, 'Electron-cyclotron maser driven by charged-particle acceleration from magnetic field-aligned electric fields', The Astrophysical Journal, **538**, pp456-466

Fomichev V.V., Fainshtein S.M. and Chernov G.P., 2009, 'A Possible Interpretation of the Zebra Pattern in Solar Radiation', Plasma physics reports, **35**, pp1032-1035

Franck C., Klinger T., Piel A., and Shamel H., 2001, 'Dynamics of periodic ion holes in a forced beam–plasma experiment', Physics of Plasmas, **8**, 4271

Franz J.R., Kintner P.M., Pickett J.S. and Chen L.J., 2005, 'Properties of small-amplitude electron phase-space holes observed by Polar', Journal of Geophysical Research, **110**, A09212

Gillespie K.M., Speirs D.C., Ronald K., McConville S.L., Phelps A.D.R., Bingham R., Cross A.W., Robertson C.W., Whyte C.G., He W., Vorgul I., Cairns R.A. and Kellett B.J., 2008, '3D PiC code simulations for a laboratory experimental investigation of Auroral Kilometric Radiation mechanisms', Plasma Physics and Controlled Fusion, **50**, pp1-11

Gilmour A.S., 1986, 'Microwave Tubes', Artech House Inc

Gilmour A.S., 2011, 'Klystrons, Travelling Wave Tubes, Magnetrons, Crossed-field Amplifiers and Gyrotrons', Artech House Inc

Gotchev O.V., Jang N.W., Knauer J.P., Barbero M.D., Betti R., Li C.K. and Petrasso R.D., 2008, 'Magneto-inertial approach to direct-drive laser fusion', Journal of Fusion Energy, **27**, pp25-31

Graham D.B., Cairns I.H., Malaspina D.M., and Ergun R.E., 2012, 'Evidence Against the Oscillating Two-Stream Instability and Spatial Collapse of Langmuir Waves in Solar Type III Radio Bursts', The Astrophysical Journal Letters, **753**, L18

Granatstein V.L. and Alexeff I., 1987, 'High-Power Microwave Sources', Artech House

Gurnett D.A., 1974, 'Earth as a radio-source - terrestrial kilometric radiation', Journal of Geophysical Research, **79**, pp4227-4238

Gurnett D.A. and Green J.L., 1978, 'Polarization and origin of auroral kilometric radiation', Journal of Geophysical Research, **83**, pp689-696

Haeff A.V., 1949, 'The Electron-Wave Tube-A Novel Method of Generation and Amplification of Microwave Energy', Proc. IRE, **37**, 4

Hill J.M., Key M.H., Hatchett S.P., and Freeman R.R., 2005 'Beam-Weibel filamentation instability in near-term and fast-ignition experiments', Physics of Plasmas, **12**, 082304

Hohenberger M., Chang P.Y., Fiksel G., Knauer J.P., Betti R., Marshall F.J., Meyerhofer D.D., Séguin F.H. and Petrasso R.D., 2012, 'Inertial confinement fusion implosions with imposed magnetic field compression using the OMEGA Laser[a)]', Physics of Plasmas, **19**, 056306

Huddlestone R.H. & Leonard S.L., 1965, 'Plasma Diagnostic Techniques', Academic Press

Humphries A.J., ‘Charged Particle Beams’, 1990, John Wiley and Sons

Hutchinson I.H., ‘Principles of plasma diagnostics’, 2002, Cambridge University press

Ikezi H., Taylor R.J., and Bake D.R., 1970, ‘Formation and interaction of ion-acoustic solitons’, Physical Review Letters, **25**, 11-14

Ikezi H., Chang R.P.H., and Stern R.A., 1976, ‘Nonlinear Evolution of the Electron-Beam-Plasma Instability’, Physical Review Letters, **36**, 1047-1051

Jackson E.A., 1960, ‘Drift instabilities in a Maxwellian plasma’, Phys.Fluids 3, 786

Kellett B.J., Graffagnino V.T., Bingham R., Muxlow T.W.B. and Gunn A.G., 2007, ‘CU Virginis - The first stellar pulsar’, arXiv: astro-ph/0701214

Key M.H., 2007, ‘Status and prospects for fast ignition inertial fusion concept’, Physics of Plasmas, **14**, 055502

Kodama R., Norreys P.A., Mima K., Dangor A.E., Evans R.G., Fujita H., Kitagawa Y., Krushelnick K., Miyakoshi T., Miyanaga N., Norimatsu T., Rose S.J., Shozaki T., Shigemori K., Sunahara A., Tampo M., Tanaka K.A., Toyama Y., Yamanaka T. and Zepf M., 2001, ‘Fast heating of ultrahigh-density plasma as a step towards laser fusion ignition’, Nature (London) **412**, 798

Kodama R., Shiraga H., Shigemori K., Toyama Y., Fujioka S., Azechi H., Fujita H., Habara H., Hall T., Izawa Y., Jitsuno T., Kitagawa Y., Krushelnick K.M., Lancaster K.L., Mima K., Nagai K., Nakai M., Nishimura H., Norimatsu T., Norreys P.A., Sakabe S., Tanaka K.A., Youssef A., Zepf M. and Yamanaka T., 2002, ‘Nuclear fusion: Fast heating scalable to laser fusion ignition’, Nature (London) **418**, 933

Kontar E.P. and Pécseli H.L., 2002, Nonlinear development of electron-beam-driven weak turbulence in an inhomogeneous plasma', Physical Review E, **65,** 066408

Kuznetsov A.A. and Vlasov V.G., 2012, 'Kinetic simulation of the electron-cyclotron maser instability: effect of a finite source size', Astronomy and Astrophysics, **539**, A141

Latham R.V., 1983, 'Pre-breakdown Electron Emission', IEEE Trans. on Electrical Insulation, **18,** pp194-203

Lawson J.D., 1957, 'Some Criteria for a Power Producing Thermonuclear Reactor' Proc. Phys. Soc. B, **70**, 6

Lindl J., 1995, 'Development of indirect-drive approach to inertial confinement fusion and the target physics basis for ignition and gain', Physics of Plasmas, **2**, 3933

Lorrain P., Corson D.P. and Lorrain F., 1988, 'Electromagnetic Fields and Waves', Freeman

Ludeking L.D. and Woods A.J., 2010, 'Well Matched Electromagnetic Boundary in FDTD-PIC for Charged Particle Penetration', The Open Plasma Physics Journal, **3**, 53-59

Marsaglia G. and Tsang W.W., 2000, 'A Simple Method for Generating Gamma Variables', ACM Transactions on Mathematical Software, **26** (3), pp363–372

Matsumoto H., Kojima H., Miyatake T., Omura Y., Okada M., Nagano I., and Tsutsui M., 1994, 'Electrostatic Solitary Waves (ESW) in the magnetotail: BEN wave forms observed by Geotail', Geophysical Research Letters, **21**, 2915

McConville S.L., Speirs D.C., Ronald K., Phelps A.D.R, Cross A.W., Bingham R., Robertson C.W., Whyte C.G., He W., Gillespie K.M., Vorgul I., Cairns R.A., and Kellett B.J., 2008, 'Demonstration of auroral radio emission mechanisms by laboratory experiment', Plasma Phys. and Control. Fusion, **50**, 074010

McConville S.L., 2009, Ph.D. Thesis, University of Strathclyde

McConville S.L., Koepke M.E., Gillespie K.M., Matheson K., Whyte C.G., Robertson C.W., and Speirs D.C., 2011, 'Characterization of a Penning discharge for investigation of auroral radio wave generation mechanisms, Plasma Phys. and Control. Fusion, **53**, 124020

McCrory R.L., Meyerhofer D.D., Betti R., Craxton R.S., Delettrez J.A., Edgell D.H., Glebov V. Yu., Goncharov V.N., Harding D.R., Jacobs-Perkins D.W., Knauer J.P., Marshall F.J., McKenty P.W., Radha P.B., Regan S.P., Sangster T.C., Seka W., Short R.W., Skupsky S., Smalyuk V.A., Soures J.M., Stoeckl C., Yaakobi B., Shvarts D., Frenje J.A., Li C.K., Petrasso R.D., and Séguin F.H., 2008, 'Progress in direct-drive inertial confinement fusion', **15**

Mendonça J.T., Norreys P., Bingham R. and Davies J.R., 2005, 'Beam Instabilities in Laser-Plasma Interaction: Relevance to Preferential Ion Heating', Phys Rev Lett, 94, 245002 (2005)

Mesyats G.A. and Proskurovsky D.I., 1989, 'Pulsed Electrical Discharge in Vacuum', Springer-Verlag

Mutel R.L., Gurnett D.A. and Christopher I.W., 2004, 'Spatial and temporal properties of AKR burst emission derived from Cluster WBD VLBI studies' Annales Geophysicae, **22**, pp2625-2632

Nakamura Y., 1970, 'Suppression of two-stream instability by beam modulation', Journal of the Plasma Physics Society of. Japan. **28**, 1315-1321

Nergaard L.S., 1948, ‘Analysis of a simple model of a two-beam growing wave tube’, RCA Rev. **9**, 585

Nishikawa K., Hojo H., and Mima K., 1974, ‘Coupled nonlinear electron-plasma and ion-acoustic waves’, Physical Review Letters, **33**, pp148-151

Noer, R.J., 1982, ‘Electron field emission from broad-area electrodes’, Applied physics A, **28**, 1-24

Pierce, J.R. 1948, ‘Possible fluctuations in electron streams due to ions’, Appl. Phys. **19**, 231

Pritchett P.L. and Strangeway R.J., 1985, ‘A simulation study of kilometric radiation generation along an auroral field line’, Journal of Geophysical Research - Space Physics, **90**, pp9650-9662

Pritchett P.L., Strangeway R.J., Ergun R.E. and Carlson C.W., 2002, 'Generation and propagation of cyclotron maser emissions in the finite auroral kilometric radiation source cavity', Journal of Geophysical Research, **107**, pp13.1 - 13.17

Ratcliffe H., Brady C.S., Rozenan M.B.C., and Nakariakov V.M., 2014, ‘A comparison of weak-turbulence and particle-in-cell simulations of weak electron-beam plasma interaction’, Physics of Plasmas, **21**, 122104

Roberson C., Gentle K.W., and Nielson P., 1971, ‘Experimental Test of Quasilinear Theory’, Physical Review Letters, **26**, 226-229

Roberts K.V. and Berk H.L., 1967, ‘Nonlinear evolution of a two-stream instability’, Physical Review Letters, **19**, 297-300

Ronald K., 1996, Ph.D. Thesis, University of Strathclyde

Ronald K., Cross A.W., Phelps A.D.R., He W., Yin H. and Spark S.N., 1998, 'Explosive cathode gyrotron experiments', IEEE Trans. on Plasma Science, PS-26, pp375-382

Ronald K., McConville S.L., Speirs D.C., Phelps A.D.R., Robertson C.W., Whyte C.G., He W., Gillespie K.M., Cross A.W. and Bingham R., 2008, 'Electron beam measurements for a laboratory simulation of auroral kilometric radiation', Plasma Sources Science and Technology, **17**, pp1-8

Ronald K., Speirs D.C., McConville S.L., Gillespie K.M., Phelps A.D.R., Bingham R., Vorgul I., Cairns R.A., Cross A.W., Robertson C.W., Whyte C.G., He W., and Kellett, B.J., 2011, 'Auroral magnetospheric cyclotron emission processes: numerical and experimental simulations', Plasma Phys. and Control. Fusion, **53**, 074015

Rosenbluth M.N. and Sagdeev R.Z., 1984, 'Handbook of Plasma Physics Vol 1', North Holland Physics Publishing

Rosenbluth M.N. and Sagdeev R.Z., 1984, 'Handbook of Plasma Physics Vol 2', North Holland Physics Publishing

Sircombe N.J., Bingham R., Sherlock M., Mendonça T. and Norreys P., 2008, 'Plasma heating by intense electron beams in fast ignition', Plasma Phys. Control. Fusion, **50**, 065005

Somerville I.C., MacGregor S.J. and Farish O., 1990, 'An efficient stacked-Blumlein HV pulse generator', Meas. Sci. Technol., **1**, pp865-868

Speirs D.C., Vorgul I., Ronald K., Bingham R., Cairns R.A., Phelps A.D.R., Kellett B.J., Cross A.W., Whyte C.G and Robertson C., 2005, 'A laboratory experiment to investigate auroral kilometric radiation emission mechanisms', Journal of plasma physics, **71**, pp665-674

Speirs D.C., McConville S.L., Gillespie K.M., Ronald K., Phelps A.D.R., Cross A.W., Bingham R., Robertson C.W., Whyte C.G., Vorgul I., Cairns R.A. and Kellett B.J., 2008, 'Numerical simulation of auroral cyclotron maser processes', Plasma Physics and Controlled Fusion, **50**, pp1-15

Speirs D.C., McConville S.L., Gillespie K.M., Phelps A.D.R. and Ronald K., 2013, 'Numerical simulations of unbounded cyclotron-maser emissions', Journal of Plasma Physics, **79**, pp999-1001

Sprangle P. and Drobot A.T., 1977, 'The linear and self-consistent nonlinear theory of the electron cyclotron maser instability', IEEE trans. on microwave theory and techniques, **25**, 6

Stix T.H., 1992, 'Waves in Plasmas', Springer

Thejappa G., MacDowall R.J., Bergamo M., and Papadopoulos K., 2012, 'Evidence for the Oscillating Two-Stream Instability and Spatial Collapse of Langmuir Waves in Solar Type III Radio Bursts, The Astrophysical Journal Letters', **747**, L1

Thode L.E. and Sudan R.N., 1975, 'Plasma heating by relativistic electron beams', The physics of fluids, **18**, 11

Tsimring S.E, 2007, 'Electron beams and microwave vacuum electronics', Wiley

Twiss R.Q., 1958, 'Radiation transfer and the possibility of negative absorption in radio astronomy', Australian Journal of Physics, **11**, pp564-579

Verboncoeur J.P., Langdon A.B. and Gladd N.T., 1995, 'An object-oriented electromagnetic PIC code', Comp. Phys. Comm. **87**, pp199-211 Code available via http://ptsg.eecs.berkeley.edu.

von Engel A., 1965, 'Ionized gases', Oxford University Press

von Engel A., 1983, ‘Electric plasmas: Their nature and uses’, Taylor and Francis Ltd.

Vorgul I., Ronald K., Speirs D.C., Bingham R., Cairns R.A. and Phelps A.D.R., 2004, ‘Analysis of a cyclotron maser instability with application to space and laboratory plasmas’, 31st EPS Conference on Plasma Physics, **28G**, pp1-4

Vorgul I., Cairns R.A and Bingham R., 2005, ‘Analysis of a cyclotron maser instability in cylindrical geometry’, Physics of Plasmas, **12**, pp1-8

Yang X.H., Borghesi M., Qiao B., Geissler M. and Robinson A.P.L., 2011, ‘Effects of external axial magnetic field on fast electron propagation’, Physics of Plasmas, **18**, 093102

Yee K., 1966, ‘Numerical solution of initial boundary value problems involving Maxwell's equations in isotropic media’, IEEE Transactions on Antennas and Propagation **14** (3), pp302–307

Zakarov, V.E., 1972, ‘Collapse of Langmuir Waves’, Sov. Phys. JETP **35**, 908

Zarka P., Treumann R.A., Ryabov B.P. and Ryabov V.B., 2001, ‘Magnetically-driven planetary radio emissions and application to extrasolar planets’, Astrophysics and Space Science, **277**, pp293-300

Zhuo, H.B., Chen Z.L., Sheng M., Yabuuchi T., Tampo M., Yu M.Y., Yang X.H., Zhou C.T., Tanaka K.A., Zhang J., and Kodama R., 2014, ‘Collimation of energetic electrons from a laser-target interaction by a magnetized target back plasma preformed by a long-pulse laser’, Physical Review Letters, **112**, 215003

Appendix 1 AKR 60A 200MHz xOOPIC script

```
AKR 200MHz 60A
{

 AKR experiment with beam current 60A with a plasma of 200MHz

}

Variables
{
// General numerical parameters

  Bpercent = 1.024

  PI = 3.14159
  eps0 = 8.854187e-12

//*****************************************************************
// General physical parameters
//*****************************************************************

  electronMassMKS = 9.1094e-31
  electronCharge  = -1.6022e-19
  speedLight      = 2.9979e8

  unitMassMKS     = electronMassMKS / 5.48579903e-04
  HeMassNum       = 4.0026
  HeMassMKS       = unitMassMKS * HeMassNum

//*****************************************************************
// Beam Parameters
```

```
//*****************************************************************

  Current = 60
  beamRadius = 0.016
  beamgrad = 0.01
  beamAnn = 0.002

  rmsElectronSpeedMKS  = 3.e+04
  electronVelocityEV = 75000
  electronVelocityMKS  = speedLight*0.41218

  beam_ramp = 5e-9

  alpha = 1.0

//*****************************************************************
// Density Parameters
//*****************************************************************

  Plasma_Freq = 200 // MHz

  Calc_Num_Density =
((Plasma_Freq*1e6*2*PI)^2)*eps0*electronMassMKS/(electronCharge^2)


  ionDensityMKS = Calc_Num_Density
  electronDensityMKS =  ionDensityMKS

  ds = 0.005 * speedLight / plasmaFrequency


//*****************************************************************
```

```
// Geometry Variables
//*********************************************************************

  Hole_rad = 0.02

  Drift_rad = 0.0279
  Drift_len = 0.1

  Waveguide1_rad = 0.0351
  Waveguide1_len = 0.3

  Waveguide2_rad = 0.0423
  Waveguide2_len = 0.1

  Taper_len = 0.13

//*********************************************************************
// Grid parameters
//*********************************************************************

  dz = 0.00025
  dr = 0.0003

  Lz = Waveguide1_len + Waveguide2_len + Taper_len + Drift_len
  Lr = Waveguide2_rad

  Nz = fabs(Lz/dz)
  Nr = fabs(Lr/dr)

  simulationVolume = Lz * Lr
  plasmaVolume = (Waveguide1_rad^2)*PI*Waveguide1_len
  numCells         = Nz * Nr
```

```
  df_cl = fabs(Drift_len/dz)
  df_cr = fabs(Drift_rad/dr)

  wg_cl1 = fabs(Waveguide1_len/dz)
  wg_cr1 = fabs(Waveguide1_rad/dr)

  wg_cl2 = fabs(Waveguide2_len/dz)
  wg_cr2 = fabs(Waveguide2_rad/dr)

  tp_cl = fabs(Taper_len/dz)

  bm_cr = fabs(beamRadius/dr)
  hl_cr = fabs(Hole_rad/dr)
  bma_cr = fabs(beamAnn/dr)

//*****************************************************************
// Particle parameters
//*****************************************************************

//
// Background electrons
//
  totalNumElectrons    = electronDensityMKS * plasmaVolume
  numElectronsPerCell  = 3
  numElectronPtcls     = numElectronsPerCell * numCells
  electronNumRatio     = totalNumElectrons / numElectronPtcls

  peakCurrentElectrons = electronCharge * electronDensityMKS * Lr *
electronVelocityMKS

//
```

```
// Background ions
//
  totalNumIons   = ionDensityMKS * plasmaVolume
  numIonsPerCell = 3
  numIonPtcls    = numIonsPerCell * numCells
  ionNumRatio    = totalNumIons / numIonPtcls
  ionMassMKS     = HeMassMKS
  ionCharge      = -electronCharge
  rmsIonSpeedMKS = 3000.

//*************************************************************
// Misc parameters
//*************************************************************

  BMax = -0.21

  ZLength = Waveguide1_len
  ZMid = Waveguide1_len+Taper_len
  BRamp_Z = 25

  BMin = 0.21 * 1.0173 * Bpercent

  d = 1. / sqrt( 1./(dz*dz) + 1./(dr*dr) )
  timeStep = 0.6 * d / speedLight

  Brampd = 0.3
  Bdis = 0.2

}

Region
{
```

```
Grid
{
  J = Nz
  x1s = 0.0
  x1f = Lz
  n1 = 1.0
  K = Nr
  x2s = 0.0
  x2f = Lr
  n2 = 1.0

  Geometry = 0        // 2D (z-r) slab geometry
}

Control
{
  dt = timeStep

// Use the multigrid electrostatic field solve
  emdamping = 0.2
  initPoissonSolve = 0
//  CurrentWeighting=1
//  DivergenceCleanFlag = 1
  NonRelativisticFlag = 0
  ElectrostaticFlag = 0

  B01analytic = BMin/(1+exp(-(x1-(Waveguide1_len+0.25))*75)) - BMin

  B02analytic = -BMin*75*exp(-(x1-(Waveguide1_len+0.25))*75)/((1+exp(-(x1-
(Waveguide1_len+0.25))*75))^2) * x2
```

```
}

Species
{
 name = electrons
 m = electronMassMKS
 q = electronCharge
}

Species
{
 name = electron_beam
 m = electronMassMKS
 q = electronCharge
}

Species
{
 name = ions
 m    = ionMassMKS
 q    = ionCharge
}

VarWeightLoad
{
 speciesName = ions
 density = ionDensityMKS
 x1MinMKS = Drift_len
 x1MaxMKS = Waveguide1_len + Drift_len
 x2MinMKS = 0.0
 x2MaxMKS = Waveguide1_rad-dr // *Per_plasma
 np2c = ionNumRatio
```

```
// specify eV units for all velocities
  units = EV

  temperature = 50
  LoadMethodFlag = 1
}

VarWeightLoad
{
  speciesName = electrons
  density = electronDensityMKS
  x1MinMKS = Drift_len
  x1MaxMKS = Waveguide1_len + Drift_len
  x2MinMKS = 0.0
  x2MaxMKS = Waveguide1_rad-dr // *Per_plasma
  np2c = electronNumRatio

// specify eV units for all velocities
  units = EV

  temperature = 5
  LoadMethodFlag = 1
}

// Load the right-going plasma electrons over the entire simulation region
VarWeightBeamEmitter
{
  speciesName = electron_beam

  I = Current
```

```
//  A1 = 0.0
//  B1 = 0.0
//  A2 = 0.0
//  B2 = beamRadius+dr

  j1 = 0
  j2 = 0
  k1 = 0 // bma_cr
  k2 = df_cr // bm_cr

  normal = 1

  xtFlag = 1
  F=((1-(step(t-beam_ramp)))*(ramp(t)/beam_ramp))+step(t-beam_ramp)



  np2c = (1.12e+15)*(beamRadius^2)*PI*Lz / Nz /256
//  np2c = 1
// specify MKS units for all velocities
  units = EV

  v1drift = electronVelocityEV

  v1thermal = 0.0
  v2thermal = 0.0
  v3thermal = 0.0

  alpha = 12  //  Gamma theta
  beta = 1.5  //  Gamma k
  gyro = 5          //  Use horseshoe model
  Bguide = -BMin
  grad = beamgrad
```

```
  C=0
}

Conductor
{
        j1 = 0
        j2 = df_cl
        k1 = df_cr
        k2 = wg_cr1

        normal = -1
}

Conductor
{
        j1 = df_cl
        j2 = wg_cl1 + df_cl
        k1 = wg_cr1
        k2 = wg_cr1

        normal = -1
}

Conductor
{
        j1 = wg_cl1 + df_cl
        j2 = wg_cl1+tp_cl + df_cl
        k1 = wg_cr1
        k2 = wg_cr2

        normal = -1
```

```
}

Conductor
{
        j1 = wg_cl1+tp_cl + df_cl
        j2 = wg_cl1+tp_cl+wg_cl2 + df_cl
        k1 = Nr
        k2 = Nr

        normal = -1
}

ExitPort
{
        EFFlag =1
        name = Output Port

        j1 = wg_cl1+tp_cl+wg_cl2 + df_cl
        j2 = wg_cl1+tp_cl+wg_cl2 + df_cl
        k1 = 0
        k2 = Nr

        normal = -1

        C=0
        A=0
}

// Define the cylindrical symmetry axis.

CylindricalAxis
{
```

```
        j1 = 0
        j2 = Nz
        k1 = 0
        k2 = 0

        normal = 1
}

Diagnostic
{
j1 = Nz-3
j2 = Nz-3
k1 = 0
k2 = Nr

save = 1
VarName = E1
HistMax = 2097152
Comb=1
integral=sum
title = Ez Field (t) End-Line
x1_Label = t
x2_Label = Electric Field
}

Diagnostic
{
j1 = Nz-3
j2 = Nz-3
k1 = 0
k2 = Nr
```

save = 1

VarName = E2

HistMax = 2097152

Comb=1

integral=sum

title = Er Field (t) End-Line

x1_Label = t

x2_Label = Electric Field

}

Diagnostic

{

j1 = Nz-3

j2 = Nz-3

k1 = 0

k2 = Nr

save = 1

VarName = E3

HistMax = 2097152

Comb=1

integral=sum

title = EPhi Field (t) End-Line

x1_Label = t

x2_Label = Electric Field

}

Diagnostic

{

j1 = Nz-3

j2 = Nz-3

k1 = 0

```
k2 = Nr

save = 1
VarName = poynting1
HistMax = 2097152
Comb=1
integral=sum

title = Poynting Z (t) End-Line
x1_Label = t
x2_Label = Poynting Z
}

Diagnostic
{
j1 = Nz-3
j2 = Nz-3
k1 = 0
k2 = Nr

save = 1
VarName = poynting2
HistMax = 2097152
Comb=1
integral=sum

title = Poynting R (t) End-Line
x1_Label = t
x2_Label = Poynting R
}

Diagnostic
```

```
{
j1 = Nz-3
j2 = Nz-3
k1 = 0
k2 = Nr

save = 1
VarName = poynting3
HistMax = 2097152
Comb=1
integral=sum

title = Poynting Phi (t) End-Line
x1_Label = t
x2_Label = Poynting Phi
}

Diagnostic
{
j1 = Nz-3
j2 = Nz-3
k1 = 0
k2 = Nr

save = 1
VarName = poyntingm
HistMax = 2097152
Comb=1
integral=sum
Ave = 50

title = Poynting Tot (t) End-Line
```

```
x1_Label = t
x2_Label = Poynting Tot
}

Diagnostic
{
j1 = wg_cl1/2
j2 = wg_cl1/2
k1 = wg_cr1-4
k2 = wg_cr1-4

save = 1
VarName = E1
HistMax = 2097152
Comb=1
integral=sum

title = Ez in plasma
x1_Label = t
x2_Label = Ez
}

Diagnostic
{
j1 = wg_cl1/2
j2 = wg_cl1/2
k1 = wg_cr1-4
k2 = wg_cr1-4

save = 1
VarName = E2
HistMax = 2097152
```

```
Comb=1
integral=sum

title = Er in plasma
x1_Label = t
x2_Label = Er
}

Diagnostic
{
j1 = wg_cl1/2
j2 = wg_cl1/2
k1 = wg_cr1-4
k2 = wg_cr1-4

save = 1
VarName = E3
HistMax = 2097152
Comb=1
integral=sum

title = Ephi in plasma
x1_Label = t
x2_Label = Ephi
}
}
```

Appendix 2 – Two-stream instability electrostatic confinement xOOPIC script

```
two_stream_beam_plasma
{
  Simulations of beam-plasma instability
  Martin King
}

Variables
{
// General numerical parameters
  PI = 3.14159
  eps0 = 8.854187e-12

//
**********************************************************************
**
// General physical parameters
//
**********************************************************************
**
  electronMassMKS = 9.1094e-31
  electronCharge  = -1.6022e-19
  speedLight      = 2.9979e8

  unitMassMKS     = electronMassMKS / 5.48579903e-04

//
**********************************************************************
**
// Beam Parameters
```

```
//
**********************************************************************
**

  Current = 10
  beamRadius = 0.008

  rmsElectronSpeedMKS  = 3.e+04
  electronVelocityEV = 50000
  electronVelocityMKS  = speedLight*0.41218

  beam_ramp = 3e-9

//
**********************************************************************
**
// Density Parameters
//
**********************************************************************
**
  Plasma_beam_ratio = 1

  Calc_Num_Density = 9e16

  ionDensityMKS = Calc_Num_Density * Plasma_beam_ratio
  electronDensityMKS =  ionDensityMKS

 Per_plasma = 0.99

  plasmaFrequency =
sqrt((electronDensityMKS*electronCharge^2)/(electronMassMKS*eps0))
  ds             = 0.005 * speedLight / plasmaFrequency
```

```
//
**********************************************************************
**
// Grid parameters
//
**********************************************************************
**
  Nz = 1280
  Nr = 64
  dz = 0.0004
  dr = 0.0004
  Lz =  Nz * dz
  Lr =  Nr * dr

  simulationVolume = Lz * Lr
  plasmaVolume = simulationVolume*Per_plasma
  numCells         = Nz * Nr

//
// streaming electrons
//
  totalNumElectrons    = electronDensityMKS * plasmaVolume
  numElectronsPerCell  = 27*4
  numElectronPtcls     = numElectronsPerCell * numCells
  electronNumRatio     = totalNumElectrons / numElectronPtcls

  peakCurrentElectrons = electronCharge * electronDensityMKS * Lr *
electronVelocityMKS

//
// background ions
```

```
//
  totalNumIons   = ionDensityMKS * plasmaVolume
  numIonsPerCell = 27*4
  numIonPtcls    = numIonsPerCell * numCells
  ionNumRatio    = totalNumIons / numIonPtcls
  ionMassMKS = electronMassMKS*1836
  ionCharge      = -electronCharge
  rmsIonSpeedMKS = 3000.

  BMax = 0.4

  Zplus = 16*0.004

  ZLength = Lz + (2*Zplus)
  BZ = BMax
  BZ_Max = BMax*8
  ZMid = Zplus +(4*dz) // * 1.25
  BRamp_Z = 100

  d = 1. / sqrt( 1./(dz*dz) + 1./(dr*dr) )
  timeStep = 0.6 * d / speedLight

  Zplus_grid = fabs(Zplus/dz)
  beamRadius_grid = fabs(beamRadius/dr)

  Nz_tot = fabs(Nz + Zplus_grid + Zplus_grid)
  Nr_tot = fabs(Nr)

}

Region
{
```

```
Grid
{
  J = Nz_tot
  x1s = 0.0
  x1f = Lz +Zplus + Zplus
  n1 = 1.0
  K = Nr_tot
  x2s = 0.0
  x2f = Lr
  n2 = 1.0

  Geometry = 0        // 2D (z-r) slab geometry
}

Control
{
  dt = timeStep

  emdamping = 0.8
  initPoissonSolve = 0
  NonRelativisticFlag = 0
  ElectrostaticFlag = 0

   B01=BMax
}

Species
{
  name = electrons
  m = electronMassMKS
  q = electronCharge
```

```
 collisionModel = 1
}

Species
{
  name = electron_beam
  m = electronMassMKS
  q = electronCharge
 collisionModel = 1
}

Species
{
  name = ions
  m    = ionMassMKS
  q    = ionCharge
 collisionModel = 2
}

MCC
{
  gas = He
  pressure=0.00075
  temperature=0.025

  eSpecies = electrons
  iSpecies = ions

  relativisticMCC = 1
}

VarWeightLoad
```

```
{
  speciesName = ions
  density = ionDensityMKS
  x1MinMKS = Lz*(1-Per_plasma) + Zplus // 4*dz
  x1MaxMKS = Lz*Per_plasma + Zplus // -(4*dz)
  x2MinMKS = 0.0
  x2MaxMKS = Lr-dr // *Per_plasma
  np2c = ionNumRatio

// specify MKS units for all velocities
  units = EV

  temperature = 10
  LoadMethodFlag = 1
}

VarWeightLoad
{
  speciesName = electrons
  density = electronDensityMKS
  x1MinMKS = Lz*(1-Per_plasma) + Zplus
  x1MaxMKS = Lz*Per_plasma + Zplus
  x2MinMKS = 0.0
  x2MaxMKS = Lr-dr // *Per_plasma
  np2c = electronNumRatio

  units = EV

  temperature = 100.0
  LoadMethodFlag = 1
}
```

```
VarWeightBeamEmitter
{
  speciesName = electron_beam

  I = Current

  j1 = Zplus_grid
  j2 = Zplus_grid
  k1 = 0
  k2 = beamRadius_grid
          normal = 1

 xtFlag = 1
 F=(((1-(step(t-beam_ramp)))*(ramp(t)/beam_ramp))+step(t-beam_ramp))*(1-step(t-
20000E-9))
  np2c = Calc_Num_Density*(beamRadius^2)*PI*Lz / 4 / Nz  /2 /4 /40
// specify eV units for all velocities
  units = EV
  v1drift   =  electronVelocityEV

  v1thermal = 500.0
  v2thermal = 0.0
  v3thermal = 0.0
}

ExitPort
{
          j1 = 0
          j2 = 0
          k1 = 0
          k2 = Nr
          normal = 1
```

```
        C=0.5
        A=0
}

Conductor
{

        j1 = Zplus_grid
        j2 = Zplus_grid
        k1 = 0
        k2 = beamRadius_grid
       normal = 1
}

Conductor
{

        j1 = Zplus
        j2 = Zplus_grid
        k1 = beamRadius_grid
        k2 = beamRadius_grid
       normal = 1
}

Conductor
{

        j1 = Nz +Zplus_grid
        j2 = Nz +Zplus_grid
        k1 = 0
        k2 = beamRadius_grid
       normal = -1
```

```
}

Conductor
{

        j1 = Nz+Zplus_grid
        j2 = Nz+Zplus_grid+Zplus_grid
        k1 = beamRadius_grid
        k2 = beamRadius_grid
       normal = 1
}

Conductor
{
       j1 = 0
       j2 = Nz+Zplus_grid+Zplus_grid
       k1 = Nr
       k2 = Nr
       normal = -1
}

ExitPort
{
       j1 = Nz+Zplus_grid+Zplus_grid
       j2 = Nz+Zplus_grid+Zplus_grid
       k1 = 0
       k2 = Nr
       normal = -1
       C=0.5
       A=0
       EFFlag=1
       name=Output
```

```
}
CylindricalAxis
{
        j1 = 0
        j2 = Nz+Zplus_grid+Zplus_grid
        k1 = 0
        k2 = 0
        normal = 1
}

Diagnostic
{

A1=(Lz+(2*Zplus))/2
B1=(Lz+(2*Zplus))/2
A2=Lr/2
B2=Lr/2

save = 1
VarName = E3
HistMax = 2097152
Comb=1
integral=sum
title = Ephi Field (t) Zpoint Mid 1/2
x1_Label = t
x2_Label = Electric Field
}

Diagnostic
{

A1=(Lz+(2*Zplus))/2
```

```
B1=(Lz+(2*Zplus))/2
A2=Lr/2
B2=Lr/2

save = 1
VarName = E2
HistMax = 2097152
Comb=1
integral=sum
title = Er Field (t) Zpoint Mid 1/2
x1_Label = t
x2_Label = Electric Field
}

Diagnostic
{

A1=(Lz+(2*Zplus))/2
B1=(Lz+(2*Zplus))/2
A2=Lr/2
B2=Lr/2

save = 1
VarName = E1
HistMax = 2097152
Comb=1
integral=sum
title = Ez Field (t) Zpoint Mid 1/2
x1_Label = t
x2_Label = Electric Field
}
```

```
Diagnostic
{

A1=(Lz+(2*Zplus))/2
B1=(Lz+(2*Zplus))/2
A2=4*Lr/5
B2=4*Lr/5

save = 1
VarName = E1
HistMax = 2097152
Comb=1
integral=sum
title = Ez Field (t) Zpoint Outer 1/2
x1_Label = t
x2_Label = Electric Field
}

Diagnostic
{

A1=(Lz+(2*Zplus))/4
B1=(Lz+(2*Zplus))/4
A2=Lr/2
B2=Lr/2

save = 1
VarName = E1
HistMax = 2097152
Comb=1
integral=sum
title = Ez Field (t) Zpoint Mid 1/4
```

```
x1_Label = t
x2_Label = Electric Field
}

Diagnostic
{

A1=3*(Lz+(2*Zplus))/4
B1=3*(Lz+(2*Zplus))/4
A2=Lr/2
B2=Lr/2

save = 1
VarName = E1
HistMax = 2097152
Comb=1
integral=sum
title = Ez Field (t) Zpoint Mid 3/4
x1_Label = t
x2_Label = Electric Field
}

Diagnostic
{

A1=(Lz+(2*Zplus))/4
B1=(Lz+(2*Zplus))/4
A2=0
B2=0

save = 1
VarName = E1
```

HistMax = 2097152

Comb=1

integral=sum

title = Ez Field (t) Zpoint Beam 1/4

x1_Label = t

x2_Label = Electric Field

}

Diagnostic

{

A1=(Lz+(2*Zplus))/2

B1=(Lz+(2*Zplus))/2

A2=0

B2=0

save = 1

VarName = E1

HistMax = 2097152

Comb=1

integral=sum

title = Ez Field (t) Zpoint Beam 1/2

x1_Label = t

x2_Label = Electric Field

}

Diagnostic

{

A1=3*(Lz+(2*Zplus))/4

B1=3*(Lz+(2*Zplus))/4

A2=0

```
B2=0

save = 1
VarName = E1
HistMax = 2097152
Comb=1
integral=sum
title = Ez Field (t) Zpoint Beam 3/4
x1_Label = t
x2_Label = Electric Field
}

Diagnostic
{

A1=Zplus+(2*dz)
B1=Zplus+(2*dz)
A2=0
B2=Lr

save = 1
VarName = I1
HistMax = 2097152
Comb=1
integral=sum
title = Current at input
x1_Label = t
x2_Label = Current
}

Diagnostic
{
```

```
A1=Zplus+ZLength-(2*dz)
B1=Zplus+ZLength-(2*dz)
A2=0
B2=Lr

save = 1
VarName = I1
HistMax = 2097152
Comb=1
integral=sum
title = Current at output
x1_Label = t
x2_Label = Current
}

Diagnostic
{

A1=Lz/2
B1=Lz/2
A2=Lr/2
B2=Lr/2+dr

save=1
VarName = species1
HistMax = 2097152
Comb=1
integral=sum

title = 1Energy_Test
x1_Label = t
```

```
x2_Label = Energy(ev)
}

Diagnostic
{

A1=Lz/2
B1=Lz/2
A2=Lr/2
B2=Lr/2+dr

save=1
VarName = species2
HistMax = 2097152
Comb=1
integral=sum

title = 2Energy_Test
x1_Label = t
x2_Label = Energy(ev)
}

Diagnostic
{

A1=Lz/2
B1=Lz/2
A2=Lr/2
B2=Lr/2+dr

save=1
VarName = species3
```

```
HistMax = 2097152
Comb=1
integral=sum

title = 3Energy_Test
x1_Label = t
x2_Label = Energy(ev)
}

SingleDump
{
 svar = C
 sFILE = IC8mm50kV10A_05Ves_2len
 sspc = 0
}

SingleDump
{
 svar = U5
 sFILE = TE8mm50kV10A_05Ves_2len
 sspc = 2
}

SingleDump
{
 svar = U5
 sFILE = TI8mm50kV10A_05Ves_2len
 sspc = 0
}

}
```

Appendix 3 Published work

King M, Bryson R., Ronald K., Cairns R.A., McConville S.L., Speirs D.C., Phelps A.D.R., Bingham R., Gillespie K.M., Cross A.W., Vorgul I., and Trines R., 2014, 'Progress towards numerical and experimental simulations of fusion relevant beam instabilities', Journal of Physics: Conference Series, **511**, 012047

King M., Speirs D.C., Bingham R., McConville S.L., Bryson R., Gillespie K.M., Phelps A.D.R., Cross A.W., Whyte C.G., Cairns R.A., Vorgul I., Trines R.M.G.M., and Ronald K., 2013, 'Computational and experimental study of beam-plasma instabilities relevant to fast-ignition inertial confinement fusion', 40th EPS conference on Plasma Physics, Helsinki, Finland

King M., McConville S.L., Speirs D.C., Bingham R., Bryson R., Gillespie K.M., Phelps A.D.R., Cross A.W., Whyte C.G., Cairns R.A., Vorgul I., Trines R.M.G.M., and Ronald K., 2013, 'Study of fusion relevant beam-plasma instabilities utilising experimental and computational methods', 40th IOP Plasma physics conference, York, UK

King M., McConville S.L., Speirs D.C., Bingham R., Bryson R., Gillespie K.M., Phelps A.D.R., Cross A.W., Whyte C.G., Cairns R.A., Vorgul I., Trines R.M.G.M., and Ronald K., 2012, 'Numerical and experimental investigations of fusion-relevant beam-plasma instabilities', 54th Annual Meeting of the APS Division of Plasma Physics, Providence, RI, USA,

King M., McConville S.L., Speirs D.C., Bingham R., Bryson R., Gillespie K.M., Phelps A.D.R., Cross A.W., Whyte C.G., Cairns R.A., Vorgul I., Trines R.M.G.M., and Ronald K., 2012, 'Numerical simulations and the development of experimental apparatus for the study of beam plasma instabilities', 39th EPS Conference on Plasma Physics, Stockholm, Sweden

King M., McConville S.L., Speirs D.C., Bingham R., Bryson R., Gillespie K.M., Phelps A.D.R., Cross A.W., Whyte C.G., Cairns R.A., Vorgul I., Trines R.M.G.M., and Ronald K., 2012, 'Numerical and experimental investigation of fusion relevant two-stream instability', 39th IEEE International Conference on Plasma Science, Edinburgh, UK

King M., McConville S.L., Speirs D.C., Bingham R., Bryson R., Gillespie K.M., Phelps A.D.R., Cross A.W., Whyte C.G., Cairns R.A., Vorgul I., Trines R.M.G.M., and Ronald K., 2012, 'Numerical and experimental study of beam-plasma instabilities relevant to fast-ignition inertial confinement fusion', 39th IOP Plasma physics conference, Oxford, UK

King M., McConville S.L., Ronald K., Speirs D.C., Bryson R., Gillespie K.M., Phelps A.D.R., Bingham R. , Cross A.W., Whyte C.G., Cairns R.A., Vorgul I., and Trines R.M.G.M., 2011, 'Investigation of beam-plasma instabilities utilising numerical and experimental methods', 38th EPS Conference on Plasma Physics, Strasbourg, France

King M., McConville S.L., Ronald K., Speirs D.C., Bryson R., Gillespie K.M., Phelps A.D.R., Bingham R. , Cross A.W., Whyte C.G., Cairns R.A., Vorgul I., and Trines R., 2011, 'Numerical and experimental investigations of beam-plasma instabilities', 38th IOP Plasma physics conference, North Berwick, UK

King M., Bryson R., McConville S.L., Ronald K., Speirs D.C., Gillespie K.M., Constable D.A., Matheson K., Phelps A.D.R., Bingham R., Cross A.W., Whyte C.G., Cairns R.A., Vorgul I., Kellett B.J., and Trines R., 2010, 'Investigations into beam-plasma interactions', 52nd Annual Meeting of the APS Division of Plasma Physics, Chicago, IL, USA

King M, Bryson R., Ronald K., Cairns R.A., McConville S.L., Speirs D.C., Phelps A.D.R., Bingham R., Gillespie K.M., Cross A.W., Vorgul I., and Trines R., 2010, 'Progress towards numerical and experimental simulations of fusion relevant beam instabilities', 15th International Congress on Plasma Physics, Chile

King M., McConville S.L., Ronald K., Speirs D.C., Bryson R., Gillespie K.M., Constable D.A., Matheson K., Phelps A.D.R., Bingham R., Cross A.W., Whyte C.G., Cairns R.A., Vorgul I., Kellett B.J., and Trines R., 2010, 'An experiment to investigate beam-plasma interactions', 37th IOP Plasma physics conference, Windemere, UK

Bryson R., Speirs D.C., King M., Phelps A.D.R., McConville S.L., Gillespie K.M., Ronald K., Vorgul I., Cairns R.A. and Bingham R., 2012, 'Numerical simulations of the anomalous Doppler resonance using pic code vorpal' Plasma Science (ICOPS), 2012 Abstracts IEEE International Conference on, UK

Bryson R., Speirs D.C., King M., Phelps A.D.R., McConville S.L., Gillespie K.M., Ronald K., Vorgul I., Cairns R.A. and Bingham R., 'PiC simulations of the anomalous Doppler resonance for a scaled laboratory experiment', 54th Annual Meeting of the APS Division of Plasma Physics, Providence, RI, USA,

Humphrey, K.A., Speirs D.C., King M., Ronald K., Phelps A.D.R., Bingham R., Trines R., Norreys P., Cairns R.A., Silva L.O., and Fiuza F., 2012, 'Beam instabilities in laser-plasma interaction relevant to fast ignition' Plasma Science (ICOPS), 2012 Abstracts IEEE International Conference on, UK

McConville, S.L., King, M., Matheson, K., Whyte, C.G., Speirs, D.C., Gillespie K.M., Phelps A.D.R., Cross A.W., Robertson C.W., Ronald K., Koepke M.E., Cairns R.A., Vorgul, I., Bingham R., and Kellett B.J., 2012, 'Laboratory experiment to investigate the impact of background plasma on cyclotron emission', Plasma Science (ICOPS), 2012 Abstracts IEEE International Conference on, UK

McConville, S. L., King, M., Speirs, D.C., Whyte, C. G., Koepke, M.E., Gillespie, K.M. and Ronald, K., 2012, 'Scaled laboratory experiments to investigate the moderation of auroral cyclotron emissions by background plasma', Infrared, Millimeter, and Terahertz Waves (IRMMW-THz), 2012 37th International Conference on, Australia

McConville, S.L., King, M., Koepke M.E., Speirs, D.C., Gillespie K.M., Phelps A.D.R., Cross A.W., Matheson, K., Cairns R.A., Vorgul, I., Bingham R., Kellett B.J., and Ronald K., 2012 'Laboratory measurement of cyclotron radiation inhibition by background plasma relevant to the polar magnetosphere', 54th Annual Meeting of the APS Division of Plasma Physics, Providence, RI, USA,

McConville S.L., Ronald K., Speirs D.C., Gillespie K.M., Phelps A.D.R., Cross A.W., Bingham R., Robertson C.W., Whyte C.G., He W., King M., Bryson R., Vorgul I., Cairns. R.A., and Kellett B.J., 2014, 'Scaled Experiment to Investigate Auroral Kilometric Radiation Mechanisms in the Presence of Background Electrons', Journal of Physics: Conference Series, **511**, 012061

Ronald K., Speirs D.C., Gillespie K.M., King M., Matheson K., McConville S.L., Phelps A.D.R., Whyte C.G., Robertson C.W., Cross A.W., Bingham R., Koepke M.E., Cairns R.A., Vorgul I., and Kellett, B., 2014, 'Laboratory and numerical investigation of mechanisms for magnetospheric cyclotron emissions', General Assembly and Scientific Symposium (URSI GASS), XXXIth URSI